Electrical properties of hot-pressed nitrogen ceramics

Rafiqul Aslam Sharif

Sharif, Rafiqul Aslam (1977) Electrical properties of hot-pressed nitrogen ceramics. Doctoral thesis, Durham University.

ELECTRICAL PROPERTIES OF HOT-PRESSED NITROGEN CERAMICS

A thesis submitted to the
University of Durham for the
degree of Doctor of Philosophy

by

Rafiqul Islam Sharif, M.Sc. (Dacca)

Department of Applied Physics and
Electronics, Science Laboratories,
Durham City, England.

August, 1977.

ABSTRACT

Some electrical properties of hot-pressed Si_3N_4, 5 W/o MgO/Si_3N_4 and two sialons, $Si_{(6-Z)} \cdot Al_Z \cdot O_Z \cdot N_{(8-Z)}$ having $Z \approx 3.2$ and $Z \approx 4.0$ have been measured, using a variety of techniques, between 18°C and 1000°C. The electrical behaviour of all the materials showed similar general features.

The d.c. conductivities were in the range of 10^{-15}-10^{-16} $\Omega^{-1}cm^{-1}$ at 18° C and rose to 10^{-6}-10^{-5} $\Omega^{-1}cm^{-1}$ at 1000° C. The current density-field (J_s-E) characteristics were ohmic in applied fields of less than 3×10^3 volt cm^{-1} ; conductivity increased with electric field above that range. Above about 280° C, σ_{dc} was independent of E, its temperature dependence following $\log \sigma_{dc} \alpha T^{-1}$. Below about 230° C conductivity fitted a $\sigma \alpha \exp ({}^{-B}/{}_{T}{}^{1/4})$ law in both low and high fields. The activation energies were in the range of 1.45-1.80 eV and 0.05-0.15 eV at above 300° C and near room temperatures respectively. Time dependent charging (I_C) and discharging (I_D) currents were observed which followed a $I(t) \alpha t^{-n}$ law with n = 0.7-0.8 at room temperature. The exponent n for I_C decreased with increasing temperature.

Hall effect and thermoelectric power measurements enabled the Hall mobility to be estimated as less than 10^{-4} $cm^2v^{-1}sec^{-1}$ at above 400° C and showed that the materials were all p-type between 400 and 900° C and n-type above 900° C. The drift mobility obtained from observations of transit time effects was 1×10^{-8} - 5×10^{-9} $cm^2v^{-1}sec^{-1}$. Various hopping models to explain the data are considered.

At room temperature the variation of conductivity ($\sigma'(\omega)$) with frequency over the range 200 Hz to 9.3 GHz followed the $\sigma'(\omega) \alpha \omega^n$ law with n = 0.9. The dielectric constant (ε') and loss ($\tan\delta$) both fell slightly over this frequency range, the average values at 10^5 Hz being about 9.5 and

5×10^{-3} respectively. At temperatures up to 500° C the data fits well with the 'Universal dielectric law' $\varepsilon''(\omega) \propto \omega^{n-1}$ and approximately fits the Kramers-Kronig relation $\varepsilon''(\omega)/_{\varepsilon'(\omega) - \varepsilon_{\infty}} = \cot ({}^{n\pi}/_{2})$ with $0.5 < n < 1$. The exponent n decreases with increasing temperature. The effects may be caused by either non-Debye dipolar or hopping charge phenomena.

Similar studies of electrical properties for 30 m/o Li-sialon and 14.3 m/o Y-sialon were also made in an attempt to relate the electrical properties and compositions of pure and doped sialons.

ACKNOWLEDGEMENTS

I am most grateful to my supervisor, Dr. J S Thorp, for his enthusiastic guidance, advice, encouragement and every possible help throughout the work and the preparation of this thesis.

I would like to thank the University of Dacca for the award of a research scholarship and for the grant of study leave from October, 1973 to September, 1977.

I am indebted to Professor K H Jack (University of Newcastle-upon-Tyne) and members of his group for supplying specimens and for many helpful discussions ; to Dr. M J Morant, Dr. E G Nice and members of Dr. J S Thorp's research group for many useful discussions.

My thanks are due to Professor G G Roberts for allowing me to use the facilities of the Department, and to the technical staff of the Department headed by Mr. F Spence for their assistance. In particular, I am grateful to Mr. R T Harcourt for cutting and polishing specimens ; to Mr. R Waite, Mr. C Savage and Mr. P Friend for assistance in the construction of apparatus.

I specially thank my wife, Mujida, whose long patience and encouragement made it possible for me to undertake this work.

Finally, I wish to thank Mrs. S Mellanby for her careful typing of the script and Mrs. E Johnston for the tracing of the diagrams.

CONTENTS

LIST OF TABLES

LIST OF FIGURES

Preceding page

Preceding page

Preceding page

Preceding page

CHAPTER 1

INTRODUCTION

1.1 THE NATURE OF NITROGEN CERAMICS:

Silicon nitride (Si_3N_4) has been established for some years as a leading refractory ceramic. It has been more attractive than other ceramics for its exceptional properties as high strength, thermal shock resistance, wear resistance, high decomposition temperature, oxidation resistance, low co-efficient of friction and resistance to corrosive environments. Therefore, it is at present a leading contender for a wide range of high temperature engineering applications, especially for gas turbines, flame cans, high temperature gas bearings, welding jigs and containers for molten metal. It is often difficult to make a particular design of component with these refractory properties. Silicon nitride is a covalently bonded solid and has a high elastic modulus, low density, small co-ordination number and high melting temperature. The self-diffusivity of the material is extremely small with the result that it cannot be sintered to maximum density by firing alone. Two processes of preparing solid silicon nitride are now used ; these are called "reaction bonding" and "hot-pressing".

In reaction bonding, a silicon powder compact is first made in the required shape and is then nitrided. This process is carried out in molecular nitrogen at about 1400°C and gives a product consisting of a mixture of α and β silicon nitride. Very little change is observed in the original dimensions of the silicon compact during nitriding, and so intricate shapes can be made by the reaction bonding method. However the desired density cannot be achieved by this method due to the presence of porosity.

Reaction sintered silicon nitride is always porous on a micro-scale (about 20%). This material can be fabricated easily and is relatively cheap to make, though unfortunately the presence of porosity causes low density. Also, the oxidation resistance and the resistance to corrosive environments decreases because the porosity leads to a higher effective surface area. The low density material is not strong enough for many engineering applications.

The second method of making silicon nitride is hot-pressing. The starting material for pressing is silicon powder which is nitrided to give directly α-silicon nitride powder. This is then hot-pressed in air at between one to two tons psi in a graphite die at about 1700°C for one hour. This gives a maximum density, β-silicon nitride product with higher strength and greater chemical resistance than that of reaction-bonded materials. This yields a pore-free material. However, the machining processes such as milling, cutting, and grinding, are more difficult than with reaction bonded material ; further this method of preparation is more expensive than the reaction bonding method.

Several broad studies to establish the engineering properties for its major applications have been made. Silicon nitride in the hot-pressed β-form attains a density approaching the theoretical value of 3.2×10^3 kgm^{-3}, an elastic modulus of 310×10^3MN m^{-2} and a modulus of rupture of 1.03×10^3 MN m^{-2} (1-2). The corresponding figures for the reaction sintered, less dense, α-type are 2.5×10^3kgm^{-3}, 170×10^3MN m^{-2} and 170 MN m^{-2}. In addition both types possess a low coefficient of expansion ($3 \div 3.5 \times 10^{-6}$°C^{-1}). Many of the physical properties of hot-pressed silicon nitride, such as high temperature creep and tensile strength (3-4), thermal shock and high temperature oxidation resistance (5), have been fairly extensively studied. It is realised that even hot-pressed material contains impurities which result from the hot-pressing additive usually magnesium oxide. This additive material reacts with the silica which is always present as a surface layer on the silicon nitride powder and gives a glass or a second crystalline phase. As a result their presence impairs the high temperature properties. Improvements are continuously being made in both hot-pressed and reaction-bonded silicon nitrides by reducing their impurity content. Recently advances in silicon nitride technology have demonstrated the improvements to the high temperature mechanical properties and the oxidation resistance of the both types of materials which can be made by removing impurities (6).

Alternative materials can be made by similar methods. The crystal lattice of silicon nitride can accommodate other atoms, both metallic and non-metallic, in large amounts. The recent work at Newcastle (5) and also in Japan has shown that aluminium and oxygen can enter the β-silicon nitride lattice to give a solid solution of Al_2O_3 in the nitride ; also, it has been established that the metal atoms of low valency, such as lithium, magnesium and yttrium can enter as well, in a charge compensating role. The latter products are known as "sialons" depending on the phases of the combining elements silicon-aluminium-oxygen-nitrogen and other related systems. Silicon nitride is the first of a wide range of nitrogen ceramics, in which it is possible to design the material and these are being made by using both reaction bonding and hot-pressing techniques. These new nitrogen ceramics are reported by Jack(5) to be superior to silicon nitride in mechanical properties.

1.2 THE PREPARATION OF HOT-PRESSED NITROGEN CERAMICS

The method of hot-pressing has been used by the research workers at the Department of Metallurgy, University of Newcastle,to manufacture the nitrogen ceramics investigated in the present work (7). The starting materials shown in Table1.1were in the form of α- Si_3N_4, MgO and Al_2O_3. These materials were thoroughly mixed with the required additive using wet milling in butanol, isopropanol or acetone in polythene jars or by dry mixing in bottles on a pascal ball mill. The grinding medium used in wet milling operations was either Cyl-peb alorite or tungsten carbide balls. The use of tungsten was always observed to give an added impurity in the products. After a few hours the initial milled slurry was evaporated for dryness at 56°C-120°C. The dry powder was then vibro-mixed for a short time and finally the product was vacuum dried at 100°C over phosphorous pentaoxide to absorb water vapour. The dry and thoroughly mixed powders were cold-compressed in a steel die at pressures of about 180 to 300 bars. In order to hot-press these mixtures, 1 to 2 W% MgO was usually added to the starting materials to produce densification. The cold-pressed pellet was buried in boron nitride and placed in a graphite boat. The boron nitride minimized the reducing effects of graphite on the sample. A pressure of about 1 ton/$_{in}2$ (154 bars) was applied to the graphite die which was then heated to a temperature of 1700°C. This temperature was maintained for one hour after which the system was allowed to cool naturally.

1.3 THE STRUCTURE OF NITROGEN CERAMICS

It is essential to know the structure of silicates as a basis for understanding the complex nitride systems. The complex structures of many silicates are derived from silica SiO_2, in the same way a range of nitrogen ceramics can be developed from silicon nitride, Si_3N_4. The basic building unit of all silicates and in the various forms of silica itself is the SiO_4 group, carrying four negative charges (Fig. 1.1). In this the central silicon atom is bonded to oxygen atoms at each of the four corners. The SiO_4 tetrahedra can be joined in various ways by sharing oxygen corners and give many different structures of silicates. Some of the arrangements in which tetrahedra can be

Sample Reference	Nominal Composition	Phase Identified	Unit Cell dimensions of β or β' phase	Unit Cell dimensions of other phases
1	Si_3N_4 (washed with NaOH) hot-pressed at 1700° C for 1 hr.	β - Si_3N_4 with glass impurity	a = 7.61 Å c = 2.91 Å	-
2	5 W/o MgO/Si_3N_4 hot-pressed at 1700° C for 1 hr.	β - Si_3N_4 with Mg-Si-Oxynitride glass impurity	a = 7.61 Å c = 2.91 Å	Forsterite (Mg_2SiO_4) a = 4.756 Å b = 10.195 Å c = 5.981 Å
3	Z = 3.2 sialon hot-pressed at 1700° C for 1 hr.	β' sialon with trace amounts of X-phase and a glass	a = 7.68 Å c = 2.97 Å	X- phase a = 9.728 Å b = 8.404 Å c = 9.572 Å β = 108.96 °
4	Z = 4.0 sialon hot-pressed at 1700° C for 1 hr.	β' sialon with glass impurity	a = 7.7 Å c = 3.05 Å	-

Table 1.1 Composition and unit-cell dimensions of the specimens ; phases identified by X-ray diffraction and electron microscopy (after ref. 5,7).

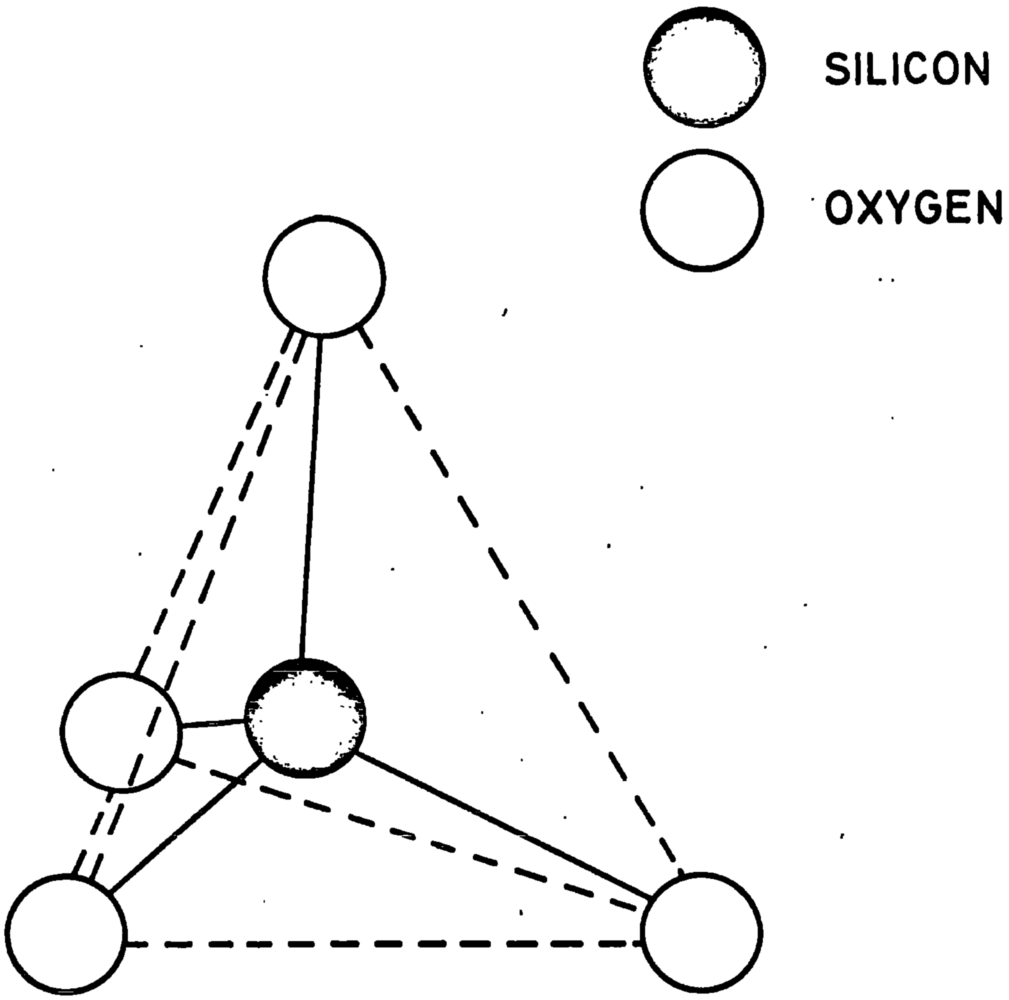

FIG. 1·1 The tetrahedral unit in the silicates (SiO_4) and nitrogen ceramics (after reference 5) linked are shown in Figure 1.2. On the other hand, a random array of tetrahedra gives rise to an amorphous structure as in the glasses.

In a similar way, nitrogen can build up a tetrahedra structure with four nitrogen corners surrounding a central silicon atom (Fig.1.1). For example, silicon nitride exists in two modifications, alpha and beta, of which β-silicon nitride is structurally in the form of SiN_4 tetrahedra joined in a three dimensional network by corners ; each nitrogen corner is common to three tetrahedra (Fig. 1.3). The α-Si_3N_4 can be transformed to β-Si_3N_4 above 1450°C by loss of silicon monoxide. The α-Si_3N_4 prepared by nitriding silicon with molecular nitrogen has about one in every thirty nitrogen atoms replaced by an oxygen atom in its structure. It is now believed that α-silicon nitride is a defect structure in which a few nitrogen atoms are replaced by oxygen ; this suggests that more nitrogen atoms can be replaced by reactions with suitable compounds, without changing the structure.

Aluminium also plays a very special role in the silicate structures, due to the AlO_4 tetrahedron in the same way, as does silicon. This time AlO_4 has an overall negative charge of five units as compared with the -4 units of SiO_4 but they are of the same size. Therefore, it is possible to replace SiO_4 by AlO_4 in the rings, chains and networks if valency or charge compensations can be made elsewhere in the structure. Thus, the work at Newcastle (5,7) and also in Japan (8) has established that Si^{4+} in silicon nitrdde can be replaced by an Al^{3+} in Al_2O_3 of O^{2-} is substituted for a N^{3-}. Other metal ions, e.g. Li^+, Na^+, Mg^{2+}, Y^{3+} can be introduced in addition to Al^{3+} in a charge compensation role. A wide range of materials, both glassy and crystalline, are now being made by using α-Si_3N_4 and silicon-aluminium-oxygen-nitrogen with the addition of other metals as mentioned above in a way corresponding to that found in the range of silicates built from

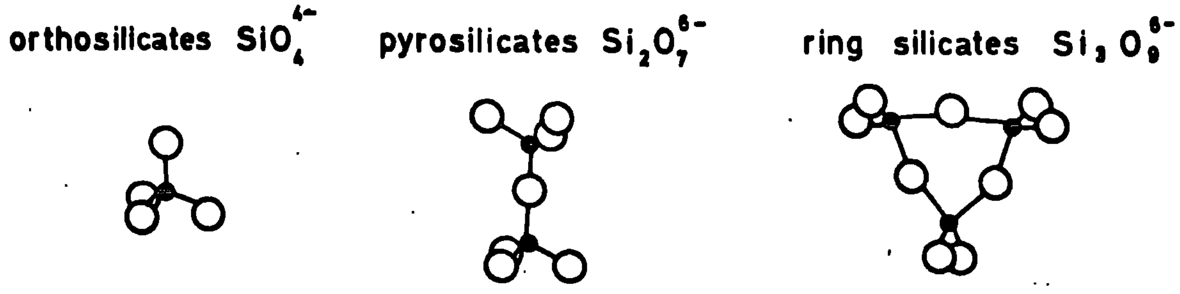

orthosilicates SiO_4^{4-} pyrosilicates $Si_2O_7^{6-}$ ring silicates $Si_3O_9^{6-}$

eg olivine eg melilite eg wollastonite

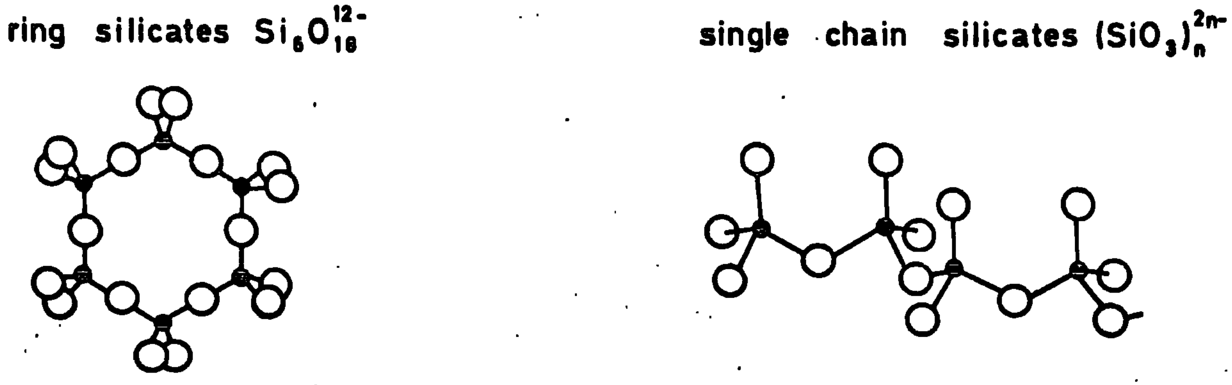

ring silicates $Si_6O_{18}^{12-}$ single chain silicates $(SiO_3)_n^{2n-}$

eg beryl eg pyroxene

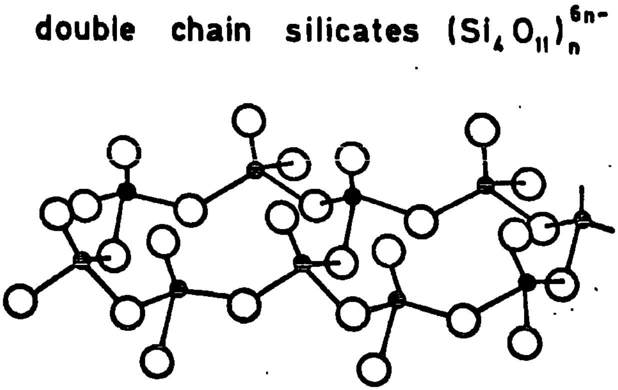

double chain silicates $(Si_4O_{11})_n^{6n-}$

eg amphibole

FIG.1.2 The Silicate structures.

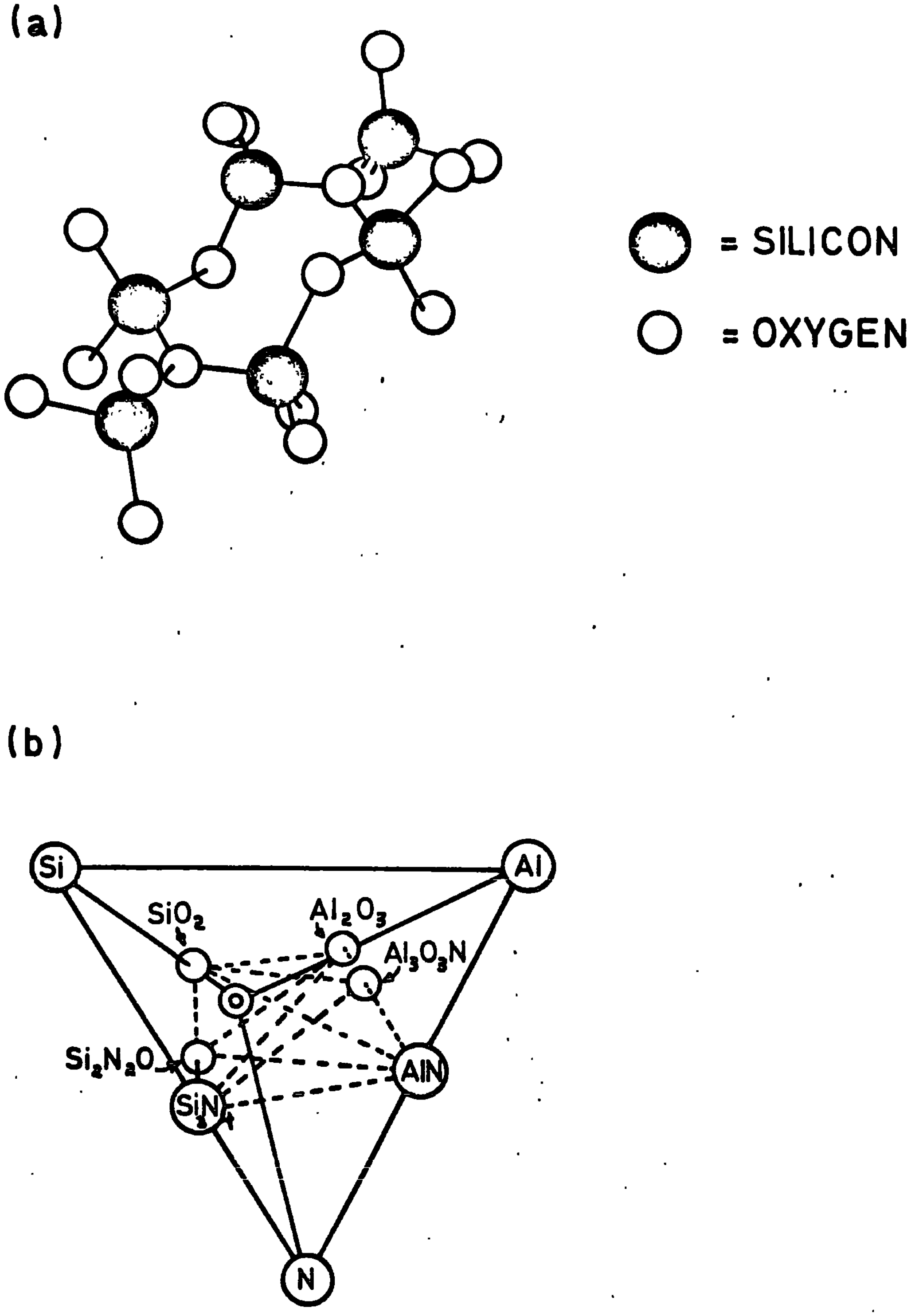

FIG. 1·3 (a) The crystal structure of β-Silicon nitride. (b) The tetrahedral representation of the Si-Al-O-N system (after reference 5) silica and silicon-aluminium-oxygen tetrahedra. In a broad sense these are known as "nitrogen ceramics" and the name sialon is given to all materials based upon the structural unit (Si, Al) $(O,N)_4$ or more generally (Si,M) $(O,N)_4$, where M is one or more of the above mentioned charge compensation metals.

1.4 MICROSTRUCTURAL ANALYSIS OF HOT-PRESSED NITROGEN CERAMICS

Extensive studies of the microstructure of nitrogen ceramics have been made in the last five years. From x-ray powder photographs, Jack (5) and Wilson (7) have shown that hot-pressed Si_3N_4 contains mostly β-Si_3N_4, a hexagonal crystalline phase, with glass impurity. The addition of 5W/o MgO with α-Si_3N_4 converts most to β-Si_3N_4 and MgO reacts with some Si_3N_4 to form a non-crystalline silicate phase i.e. MgO-Si-oxynitride glass impurity. Evan (9) has mentioned that about 80% of crystalline material is β-Si_3N_4 with the remainder consisting roughly of α-Si_3N_4, silicon carbide and another unidentified phase, probably silicate. From electron microscope analysis it has been shown that the microstructure of hot-pressed silicon-nitride consists mostly of small angular grains of β-Si_3N_4 with some larger irregular grains of the same β-phase. Some non-crystalline regions are observed between certain of the small angular grains. Small angular grains vary in length from 0.1 to 2 μm and some larger irregular grains may be up to 8 μm in length. Some grains also show dislocations and the dislocations generally occur along the C-axis of the β-phase (9-10).

Early experiments to produce sialons were made by adding together silicon nitride and alumina and hot-pressing at 2000°C (11). From x-ray analysis it was found that the structure of the resulting sialon remained almost identical to that of hexagonal β-Si_3N_4, but the β' unit-cell dimensions of the homogeneous sialon were increased relative to the β-phase due to the increase of the metal : non-metal atom bond-lengths. This, also contains a defect structure with metal atom vacancies which results in other phases as well as β′. Previously Jack and Wilson (11) proposed a general formula for crystalline β′-sialon solid solutions as :

$$Si_{6-\frac{3}{4}x}.Al_{\frac{2}{3}x}.O_x.N_{8-x} \qquad (1.1)$$

where x is the number of oxygen atoms replacing nitrogen in the silicon nitride unit-cell. Thus when one oxygen atom replaces a nitrogen atom, three-quarters of one silicon atom must be replaced by two-thirds of an aluminium atom. On the basis of this composition, Drew (12) also identified from microscopy studies that the microstructure of hot-pressed sialon materials contained single phase β′ with a few isolated grains of x-phase, and grain boundary glassy phase, where x is a monoclinic phase. The typical grain size of β′ was 0.2 to 1 μm; the grain size became smaller with addition of decreased amount of Al_2O_3 to the mixture based on the above composition. Subsequent work has proved that the composition based on the above equation does not form a single phase (11,13). Consequently, alternative compositions for β′ were considered. The formula, corresponding to x has been modified (13) and the correct general formula of the sialon is known as

$$Si_{6-z}.Al_z.O_z.N_{8-z} \qquad (1.2)$$

where z has the same meaning as x above and can vary from 0 to about 4.2. A homogeneity range of solid solutions in the above equation are obtained only by reacting metal : non-metal elements in the ratio of 3M: 4X. Compounds may also be used, for example, Al_2O_3N with α-Si_3N_4. The derivation of the true sialon formula has been explained by Jack (5) on the basis of phase diagrams (Fig. 1.4). In moving from the left-hand to the right-hand side of this diagram, $3Si^{4+}$ is gradually replaced by $4Al^{3+}$ and from the bottom to

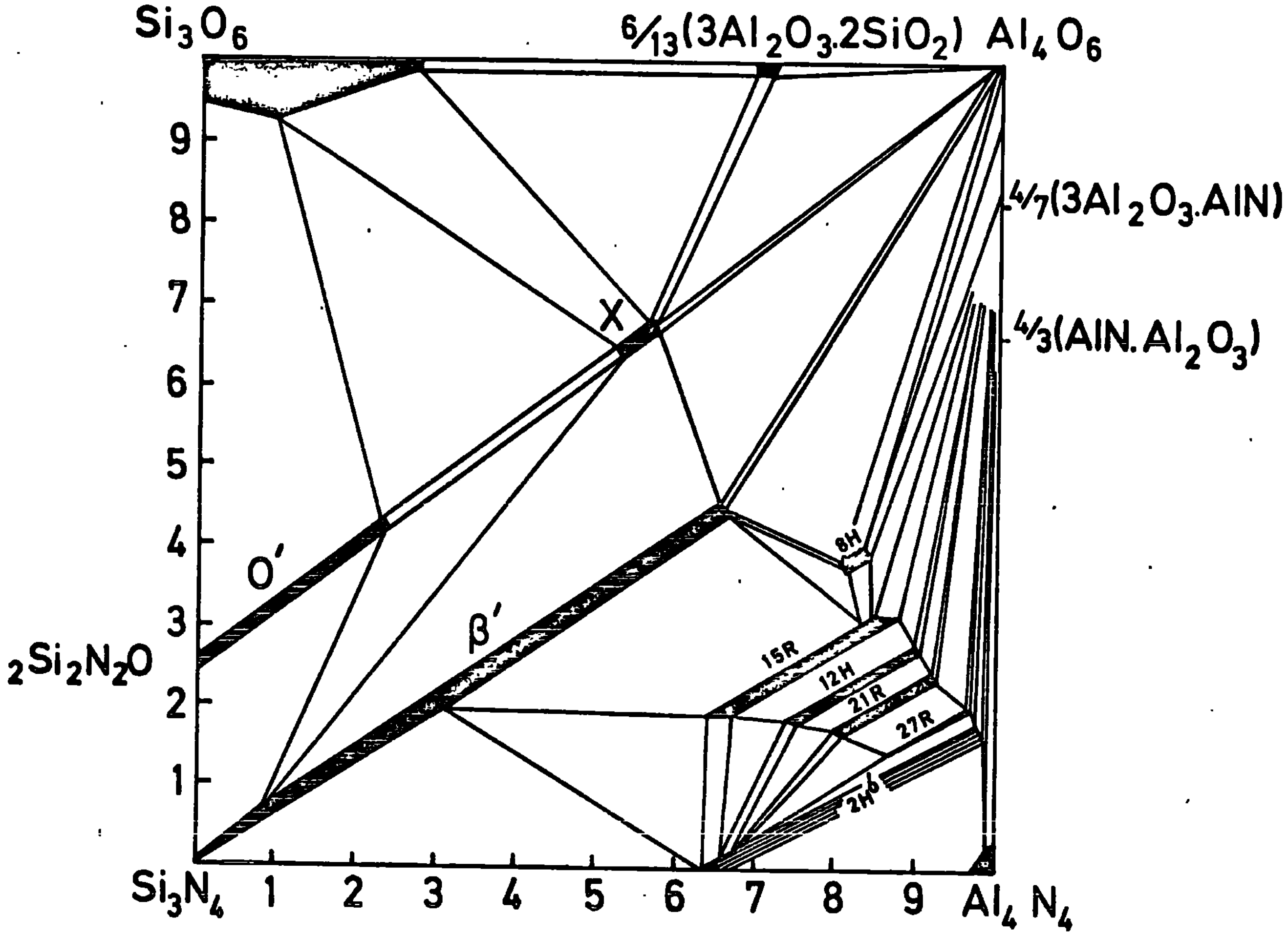

FIG. 1·4 The Si_3N_4-AlN-Al_2O_3-SiO_2 system based on research at Newcastle (after reference 5) the top, $4N^{3-}$ is replaced by $6O^{2-}$. The central region of the square is a material of composition $Si_{1.5}.Al_2O_3N_2$ for homogeneous single phase β′-sialon. The variation of the hexagonal unit-cell dimensions with z value is shown by Figure 1.5. The β′-phase and the silica rich x-phase are usually produced by the reaction of silicon nitride and alumina but the latter gradually decreases as the hot-pressing temperature is increased above 1800°C. The presence of x-phase is produced from the excess surface SiO_2 which has not been balanced by addition of AlN to the Si_3N_4-Al_2O_3 mixture. The presence of x-phase can be minimized by keeping the composition near to the M:X = 3:4 ratio ; an almost single phase β′ crystal sialon can be obtained. This is identified with the general formula given above. High temperature creep properties of sialons have demonstrated the marked increase in creep resistance as the balanced composition is approached (13). These results were used as indirect evidence for a progressive decrease in the amount of grain boundary glassy phase on going from x to z compositions. In Figure 1.6 the transmission electron micrograph clearly shows that many of the grains have hexagonal prism shapes with occasional disturbance of neighbouring grains in a hot-pressed sialon material (14). Figure 1.7 demonstrates the typical faceted grain morphology and associated inter-crystalline glassy phase (corresponding to an x formula composition). The presence of irregular grain boundaries and absence of inter-granular glass (corresponding to a z formula balanced composition)are shown in Figure 1.8. The structure and phases present in the sialons, having z = 3.2 and 4.0 (which are used in the present work) have been provided by Jack (5) and Wilson (7). These sialons contain β′-phase which remains essentially the same as that of hexagonal β-silicon nitride but with increased lattice parameters. In addition to that z = 3.2 sialon has contained trace amount of x-phase with glass and z = 4.0 sialon has contained glass impurity only.

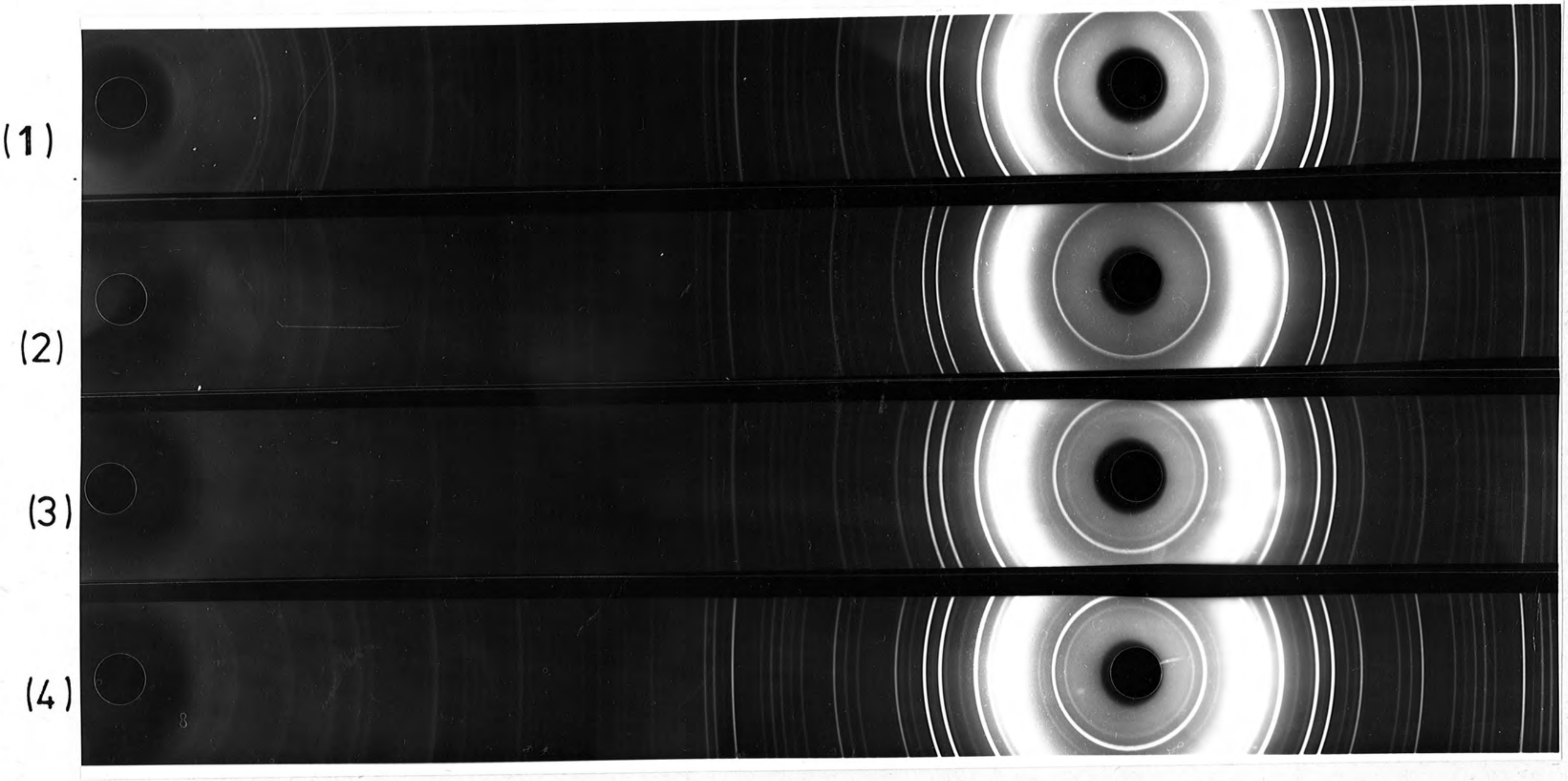

FIG.1.9 X-ray diffraction patterns of (1) Si_3N_4, (2) 5w/o MgO/Si_3N_4, (3) z = 3.2 sialon and (4) z = 4.0 sialon.

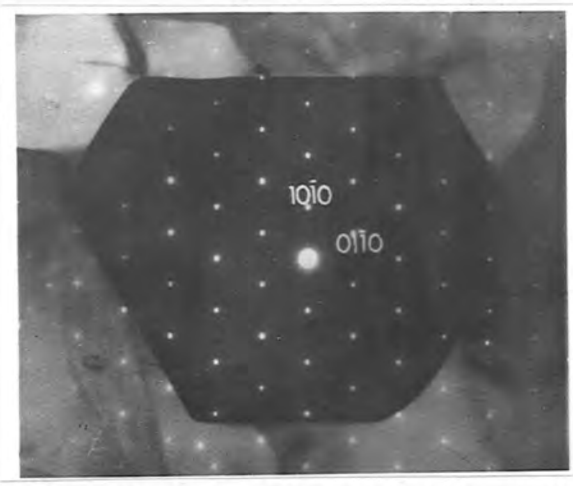

FIG. 1.6 Transmission electron micrograph and superimposed diffraction pattern from a single faceted grain in a hot-pressed sialon specimen showing the hexagonal prismatic cross-section in the β' crystal (after ref. 14)

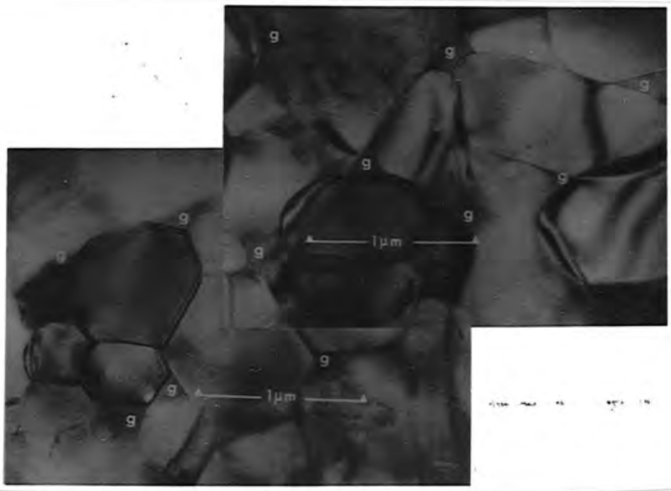

FIG. 1.7 Transmission electron micrograph showing typical faceted grain morphology and associated inter-crystlline glass phase (g) in a sialon specimen (corresponding to an x formula composition) (after ref. 14)

FIG. 1.8 Transmission electron micrograph showing irregular (non-faceted) grain boundaries and absence of inter-granular glass in a sialon specimen (corresponding to a z formula "balanced" composition) (after ref. 14)

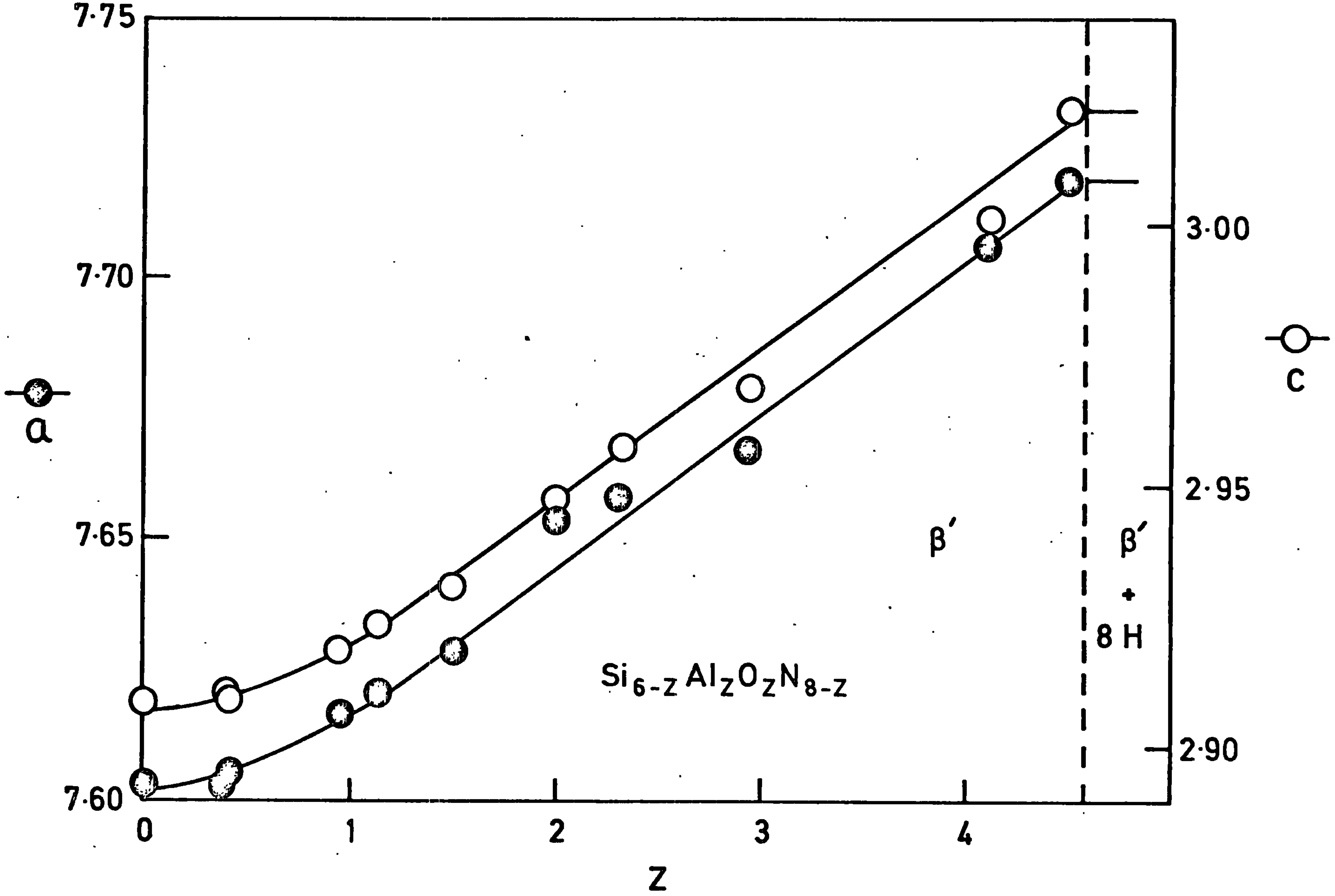

FIG. 1·5 Unit-cell dimensions of β′ (after reference 5)

The unit-cell dimensions and the presence of phases of the materials are listed in Table 1.1. Some X-ray powder photographs of the materials used in the present work were taken in our laboratory by using a standard method as shown in Figure 1.9. It is noticed in this diagram that the diameters of the successive rings for 5 w/o MgO/Si_3N_4 and two sialons in low θ region are slightly greater than that of Si_3N_4; this indicates that the structures of β'-sialons are similar to that of hexagonal crystal of β-Si_2N_4 but with increased lattice parameters. There are also numerous weak lines adjacent to strong lines which may be due to the presence of other phases. Precise X-ray data and a knowledge of the phases present in these specimens are provided by Jack (5) and Wilson (7), these are listed in Table 1.1.

We have come to know that the materials used in the present work have contained at least two phases in addition to glass impurity. The presence of a non-crystalline phase and impurities cannot be eliminated fully by using the method of preparation and composition mentioned above. Their presence has the added disadvantage that when silicon nitride is used as a starting material for making nitrogen ceramics, the silica layer prevents the production of a homogeneous single phase. Every particle of starting Si_3N_4 powder is always coated with a layer of silica. After washing in caustic soda, the presence of silica can be reduced but a certain amount is left behind. The Newcastle research workers estimated 4 W/o of silica in the starting material due to this effect. The addition of increased amount of AlN to Si_3N_4-AlN-SiO_2 mixtures reduced the amount of second phase.

1.5 PROPERTIES OF β'-SIALON

It is not certain whether the intrinsic advantageous properties of β' sialon can be achieved in practice because of the impurity content. However, even with these impurities the mechanical and physical properties of sialons are similar to those of β-silicon nitride while its chemical behaviour is closer to that of aluminium oxide. Its thermal expansion coefficient (2.7×10^{-6}) is less than that of β-Si_3N_4 (3.5×10^{-6}). The oxidation resistance is greater than silicon-nitride. Moreover, sialon is undoubtedly better than silicon nitride in fabrication ; the required shapes can be made and can be fired, in an inert atmosphere at about 1600°C to theoretical density.

The mechanical, physical and chemical properties of nitrogen ceramics are fairly well known. On the other hand their electrical properties are almost unknown. The materials potential for electrical and technological applications, such as high temperature insulators, high frequency dielectrics etc. is uncertain without a fundamental understanding of their electrical properties. In fact, many of the basic advances in the characterization and fabrication of ceramic materials have been primarily motivated by the compositional and microstructural requirements imposed on them by electrical property applications.

The aim of the present work was to investigate the electrical properties of some hot-pressed nitrogen ceramics especially in d.c. and a.c. applied electric fields at temperatures between 18°C and 1000°C, to ascertain the conduction mechanism applicable at low and high temperatures and to relate these properties to composition and structure of the materials.

CHAPTER 2

SUMMARY OF THEORY

2.1 ENERGY BAND AND STRUCTURE

It is believed that the crystalline band structure model remains substantially unchanged as long as the environment and co-ordination remains almost unchanged. The distance between atoms in a crystalline lattice is such that no overlap between electron energy bands appears and there is a gap between them ; the conduction and valence bands represent continuous bands of allowed energy levels in which electrons and holes move freely in the lattice (except for scattering). The disappearance of crystalline long range order in disordered solids has important consequences for transport and the band gap model cannot be applied. Many theoreticians (15-19) have made a number of approaches on the energy level structures of amorphous semiconductors and insulators. According to their opinions the conduction and valence bands of allowed levels in which electrons may move in crystalline insulators are basically preserved, but the forbidden energy gap is replaced by a "pseudo gap" ; it means that the conduction and valence band edges (E_c,E_v) become blurred by the presence of a distribution of localized states extending into the band gap as band tails (Figure 2.1). Structural disorder is the basic cause of the formation of localized levels. Several mechanisms of charge carrier localization are known (16,20). In general the localization occurs for the following reasons : (a) a random potential at each atom, (b) fluctuation in the density or mean interatomic distance, (c) absence of long range order. Three types of disorder are found in disordered materials. The first is a continuously connected long-range disorder, i.e. no bonds are broken and no foreign impurities are present. This type of disorder is formed by random small perturbations in the nearest

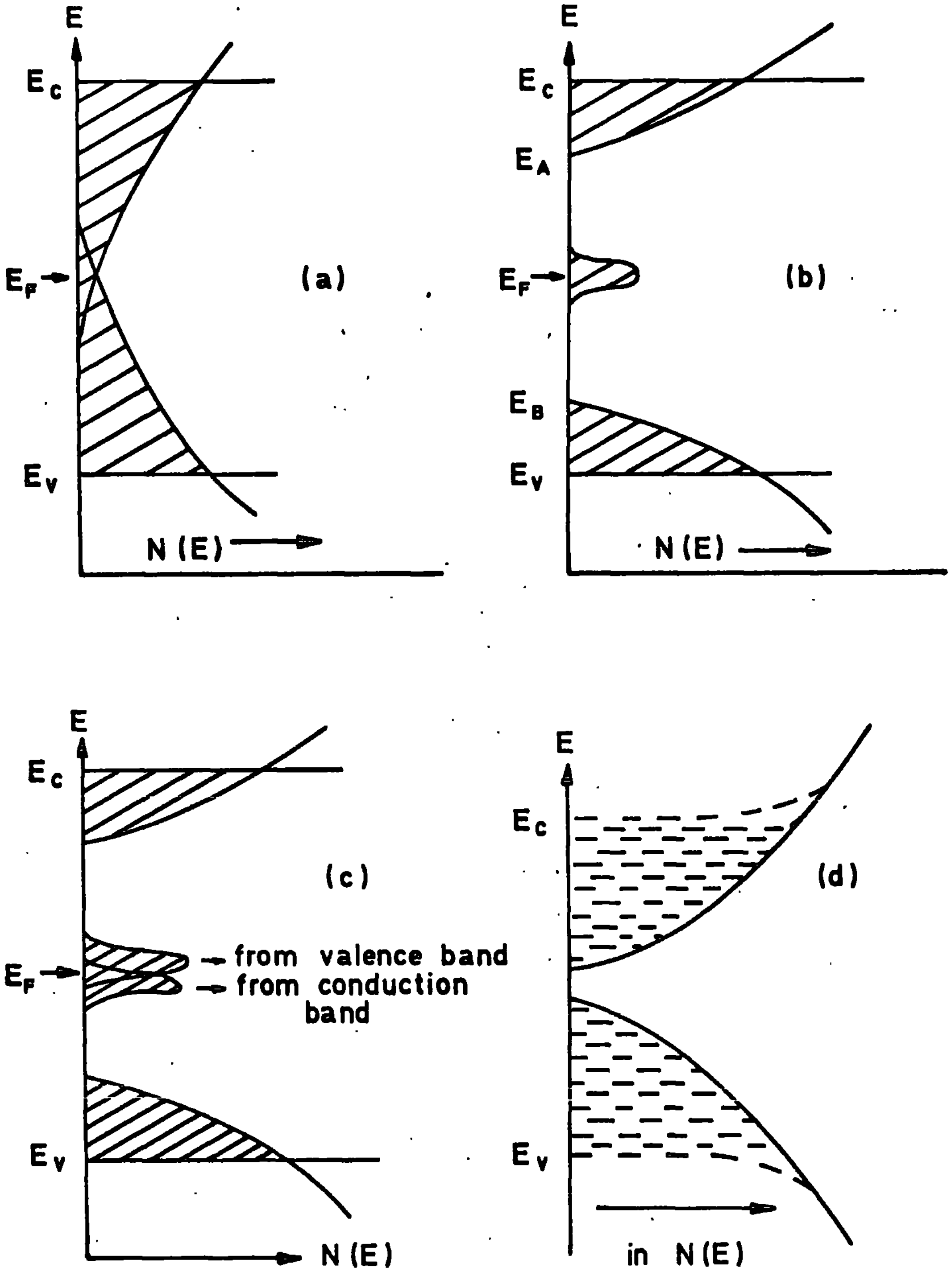

FIG. 2·1 Tails of localized states in the band gap (shaded area) for disordered solids. (a) CFO model (ref. 17.) (b) Mott and Davis model (ref. 18.) (c) Mott model (ref. 16.) (d) Jonscher and Hill model (ref. 19.)

neighbour bonding. The second type of disorder arises in relatively rigidly bonded materials which contain a large density of broken bonds forming "grain boundaries" ; these separate well-ordered small crystallites giving a discontinuous structure with a rather lower density than a single crystal. The third type of disorder is due to structural defects, for example dangling bonds, foreign impurities, etc., incorporated interstitially or substitutionally in the disordered lattice. These impurities may have originated in the initial process of manufacture of the material (19). Most recently, Anderson (21) developed the idea of the electron-lattice interaction and suggested that it produces a strong attractive interaction between electrons in non-metallic glasses that outweighs the coulombic repulsion of two electrons in a localized state. As a consequence, most localized states in the gap would be doubly occupied. Except for the states very close to the edges, the states in the gap are due to impurities or defects. The simplest defect is broken bond. Two electrons (↑↓) are shared in a chemical bond between two atoms. In some structural configurations the atoms are not able to share the electrons and the bond is broken, which is known as a dangling bond. Dangling bonds occur in glasses as well as in crystals ; for example, on internal surfaces of microvoids and in vacancies and in multivacancies. Opinions about the concentration and distribution of localized states in the gap of disordered solids differ greatly.

A density of states distribution as shown in Figure 2.1a was suggested in certain glasses by Cohen and Fritzche (17). The conduction and valence band have tails of localized states sufficiently extensive to overlap near the centre of the mobility gap. Electrons from states at the top of the valence band are transferred into states at the bottom of the conduction band, ensuring that the Fermi level lies on the region of overlap. An alternative model suggested by Davis and Mott (18) is shown in Figure 2.1b. In this model a narrow band of localized states near the centre of the gap and the localized states at the band edges have been considered. These localized states may have arisen in the third type of disordered materials as discussed above. In Figure 2.1c a dangling bond can provide a donor below the middle of the gap and an acceptor above it, as suggested by Mott (16). The disorder, and particularly random fields due to charge cavities, gives a range of energies for both so that the two bands overlap and some dangling bonds acquire a positive and some a negative charge. The density of states, $N(E_F)$ is finite and the Fermi energy is pinned. Jonscher and Hill (19) have suggested a band model for the first type of disordered material which is expected to lead to a wide distribution of localized levels in the forbidden gap (Fig.2.1d). This form of disorder is expected to lead to a decrease in the density of states with distance from the band edges and may lead to overlap between the states.

If, the material contains impurities, on the other hand, a good fraction of these impurities will satisfy the valence bonds by choosing their favourite co-ordination environment ; however a sufficient number might fail to do so, giving rise to internal fields and spatial potential fluctuations. Even without invoking impurities and dangling bonds, charge and potential fluctuation variations are expected from variations in electronegativity. These are a consequence of spatial fluctuations in structure, density and composition. So this effect directly or indirectly gives rise to localized states.

Transport via the localized states leads to the concept of hopping as an alternative conduction mechanism. The concept of hopping is related to the idea of localized levels in the forbidden gap of disordered solids. Depending upon the ratio of localized radius to the intersite spacing, it has been suggested in (19) that it is possible to distinguish the following four types of transport ; (1) hopping conduction in the region of strong localization, (2) percolation paths of easy transitions between selected sites as the ratio approaches unity, (3) impurity band formation where the ratio is larger than unity and, (4) the limit of free band conduction where the localization does not occur at all.

The field dependence, frequency dependence and temperature dependence transport experiments give direct evidence to distinguish between free band

and hopping conduction. In addition to that it can give further information of the energetic position of the localised levels in which the hopping conduction takes place.

2.2 LOW-FIELD CONDUCTION PHENOMENA

When a constant electric field is applied to a material, the current rapidly or slowly reaches an equilibrium direct current value. This current can be represented in terms of the number of charged particles present and their drift velocity in the presence of an electric field. The electric current density, J is defined as the charge transported through a unit area in a unit time. If the number of charge carriers of species i per unit volume is N_i with a drift velocity V_i and a charge per particle is Z_ie, where Z is the valence and e the electronic charge, then the electrical current density is given by

$$J_i = N_iZ_ieV_i \tag{2.1}$$

The electrical conductivity σ is defined by the general relationship

$$\sigma = {}^{J}/_{E} \tag{2.2}$$

Consequently, σ_i is defined from the relations (2.1) and (2.2)

$$\sigma_i = (N_iZ_ie)\,\frac{V_i}{E} \tag{2.3}$$

The drift velocity is directly proportional to the locally acting electric field strength and this ratio is defined as the drift mobility

$$\mu_i = {}^{V_i}/_{E} \tag{2.4}$$

The conductivity is then the product of the concentration and mobility of charge carriers,

$$\sigma_i = (N_iZ_ie)\mu_i \tag{2.5}$$

In the case of crystalline materials in which the transport is clearly attributable to free carriers, the expression of conductivity σ may be written in the simple form (19).

$$\sigma = \Sigma_r \sigma_r = \Sigma_r q_r \mu_r N_r \qquad (2.6)$$

where the summation extends over all species r of available carriers and processes. Equation (2.6) implies a clear distinction between the available carrier densities N_r and their mobilities. This distinction arises naturally in the case of conduction by free carriers. In the case of localized conduction the situation is different. The hopping conduction occurs by transitions from occupied to empty levels and this very fact precludes a clear distinction between the number of available carriers and their mobilities. The transition probabilities of all the localized electrons (at all energies) which correspond to mobility are partially dependent on the availability of neighbouring empty sites. The expression for conductivity in this situation is given

$$\sigma = eN_e \mu \qquad (2.7)$$

where N_e, the effective density of localized carriers, μ the hopping mobility in terms of drift velocity V_d in the applied field E. This equation corresponds to conduction in localized states at the Fermi level and it represents one of the cases covered by equation (2.6). Other processes which may be involved are conduction in excited or extended states.

The effect of variables such as composition, structure and temperature, is to change the concentration of charge carriers and their mobility for conduction. However, the temperature dependence of the direct current (d.c.) conductivity $\sigma_{dc}(T)$ under a small external applied field gives information on activation energies which distinguishes between free carrier and hopping conduction (18, 22, 23).

Mott and Davis (18) have suggested that, in general, in the case of amorphous semiconductors and insuators the conductivity expression over the whole temperature range is expected to contain three terms. The temperature dependence of conductivity can be expressed by the following relation

$$\sigma = C \exp\left\{{}^{-E}/_{KT}\right\} + C_1 \exp\left\{{}^{-E_1}/_{KT}\right\} + C_2 \exp\left\{{}^{-E_2}/_{KT}\right\} \quad (2.8)$$

The following details may be noted :-

(a) The first term is due to intrinsic behaviour and the conduction is assumed to take place at the extremities of the conduction band. The value of $C \sim 10^3 - 10^4\ \Omega^{-1}\ \text{cm}^{-1}$ is expected. If this condition for the magnitude of the first term is satisfied then one can usually consider $E_A = \Delta E \leqslant \frac{1}{2} E_o$ where E_o is the optical gap. (24). In the case of intrinsic behaviour the number of electrons, n is equal to the number of holes, p. This condition determines the position of Fermi level E_F in terms of the conduction and valence band parameters so that

$$\sigma\ (\text{intrinsic}) = \text{const.} \exp\left[\frac{-\{E_c - E_v\}}{KT}\right] \quad (2.9)$$

In disordered materials $n \neq p$ because of the much larger number of electrons and holes in localized tail states and gap states. So the equation (2.9) cannot be valid at low temperature. The energy separation $E_c - E_v$ between the mobility edges for electrons and holes has no immediate relation with the optical gap E_o. The slope of the Arrhenius plot of the conductivity yields a quantity ΔE_o from which one may obtain the distance of the Fermi energy from the mobility edge of the predominant conduction. The optical gap E_o may be larger or smaller than the ΔE_o.

(b) The second term of equation (2.8) is due to transport by carriers excited into the localized states at the edges of the conduction or valence band and for this $C_1 \sim I\Omega^{-1}\text{cm}^{-1}$.

(c) The last term of equation (2.8) is due to hopping conduction by electrons with energies near E_F. In this situation $C_2 << C_1$ and $E_2 << E_1$. At low temperatures $\exp(^{-E_2}/KT)$ is replaced by $\exp\frac{(-\text{const.})}{T^{\frac{1}{4}}}$. As the temperature is lowered, the activation energy, ΔE_A will fall, i.e. the predominant hopping path in the localized state distribution moves progressively closer towards the Fermi energy and the conductivity variation is expressed in the form (16,18).

$$\sigma \;\alpha\; \exp(^{-B}/T^{\frac{1}{4}}) \qquad (2.10)$$

where B is constant, depending on the density and the degree of localization of states through which hopping transport of carriers take place. This law is based on variable range hopping between states with energy near Fermi level. The theoretical basis of the $T^{-\frac{1}{4}}$ law has been extensively discussed in the literature (20,25 and 26). Many theoreticians (18,20,25) have given the value of B as

$$B = 2.1 \left\{ \alpha^3 / KN(E_F) \right\}^{\frac{1}{4}} \qquad (2.11)$$

where α is the decay constant of the localized wave function $e^{-\alpha R}$, and $N(E_F)$ is the density of states at the Fermi energy. The temperature vatiation of the average hopping distance, R, can be calculated from the relation

$$R = \left\{ ^9/8\pi\alpha N(E_F)KT \right\}^{\frac{1}{4}} \qquad (2.12)$$

and the average hopping energy, W is expressed in the form

$$W = 3/4\pi N(E_F)R^3 \qquad (2.13)$$

In semiconductors in which there is a range of localized states leading to a mobility edge E_C in the conduction (or valence band) as shown in Figure (2.1c) the conductivity is expected to be of the form (27).

$$\sigma \; \alpha \; C \exp\left\{(E_F - E_A + W)/KT\right\} + D \exp\left\{-(E_F - E_C)/KT\right\} \qquad (2.14)$$

Here E_A is the energy which corresponds to the predominant hopping path through the material, W is the associated hopping energy, $D \sim 200 \; \Omega^{-1} \; cm^{-1}$ is the minimum metallic conductivity and $^C/_D \sim 10^{-3}$. The $\log\sigma - 1/_T$ plot should show a kink.

Figure 2.2A shows the variation of N(E), μ(E), and f(E) with E for energies above E_F, and the manner in which $\sigma_{(E)}$ may vary with temperature. The temperature variations of the above mentioned three conductivity mechanisms are also shown on a plot of lnσ against $^1/_T$ in Figure 2.2B. If the density of defect states is high then process (b) will not dominate in any temperature range and a direct transition from (a) to (c) will occur.

In (20,28-29) a similar dependence of σ(T) in disordered system has been investigated on the basis of an application of the percolation theory to the current flow in the random resistor network for the hopping probability between sites. The schematic representation of the actual current paths in a disordered system taken from (30) is shown in Figure (2. 3).

In the case of conduction in localized states distributed widely in space and in energy (Fig. 2.1d), the Arrhenius plots are not necessarily linear (19), and the activation energy is a function of temperature. The condition that the conductivity occurs away from the Fermi energy can be expressed as $\Delta E_A >> KT$. The conduction near the Fermi level occurs at low temperature and E_A should be a small multiple of KT, i.e. $E_A < 10KT$.

2.3 HIGH-FIELD D.C. BEHAVIOUR

The mechanism of low-field conduction described in Section 2.2 applies to quasi-equilibrium conditions where the distribution in energy of the localized carriers does not depart significantly from the thermal equilibrium distribution.

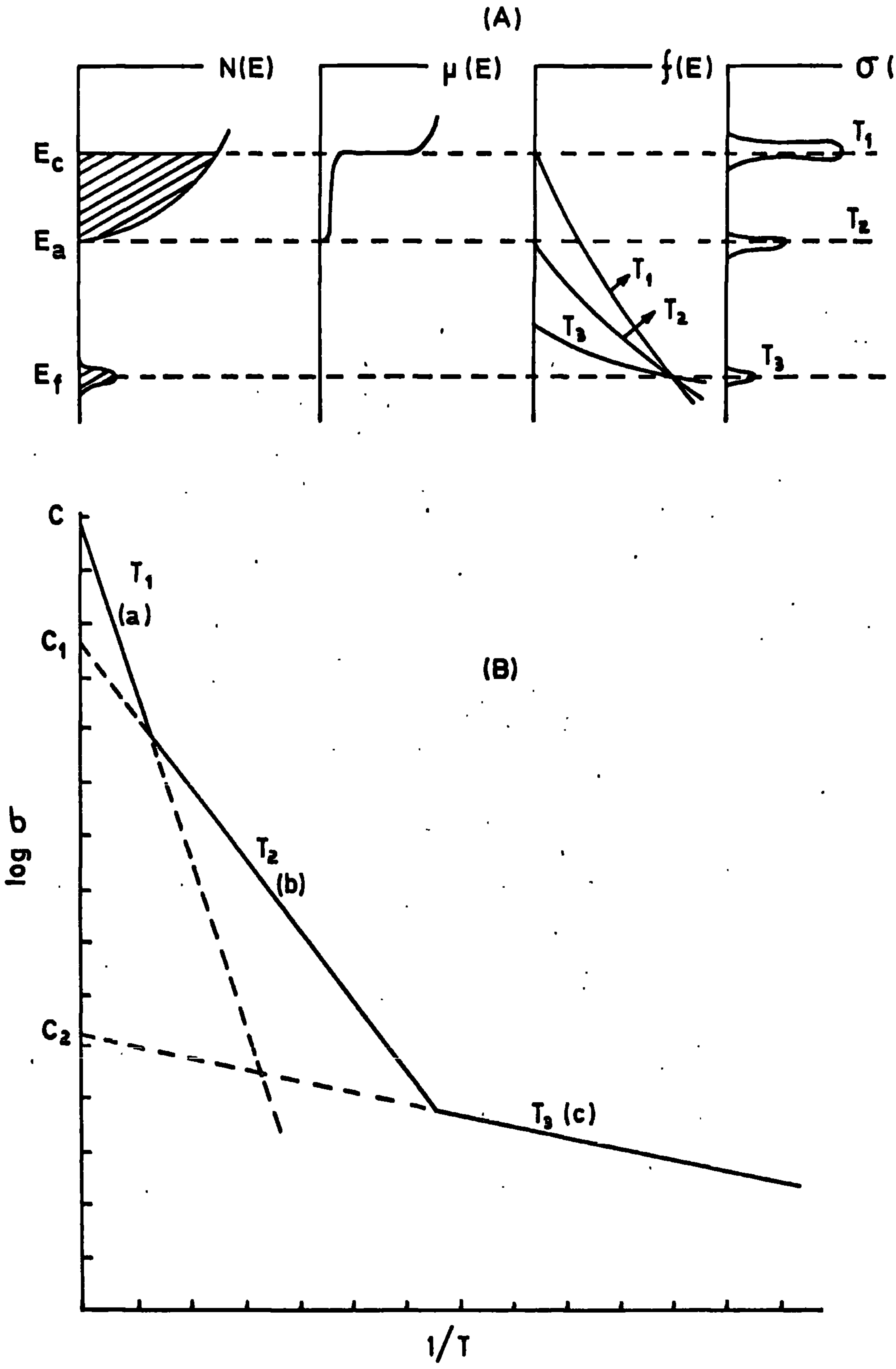

FIG. 2·2 (A) Illustration of the effect of temperature on the mode of conduction. $\sigma(E) = eN(E)\mu(E)f(E)$; $T_1 > T_2 > T_3$ (B) The temperature dependence of conductivity expected on the model of FIG.2·2 (A) (after reference 18).

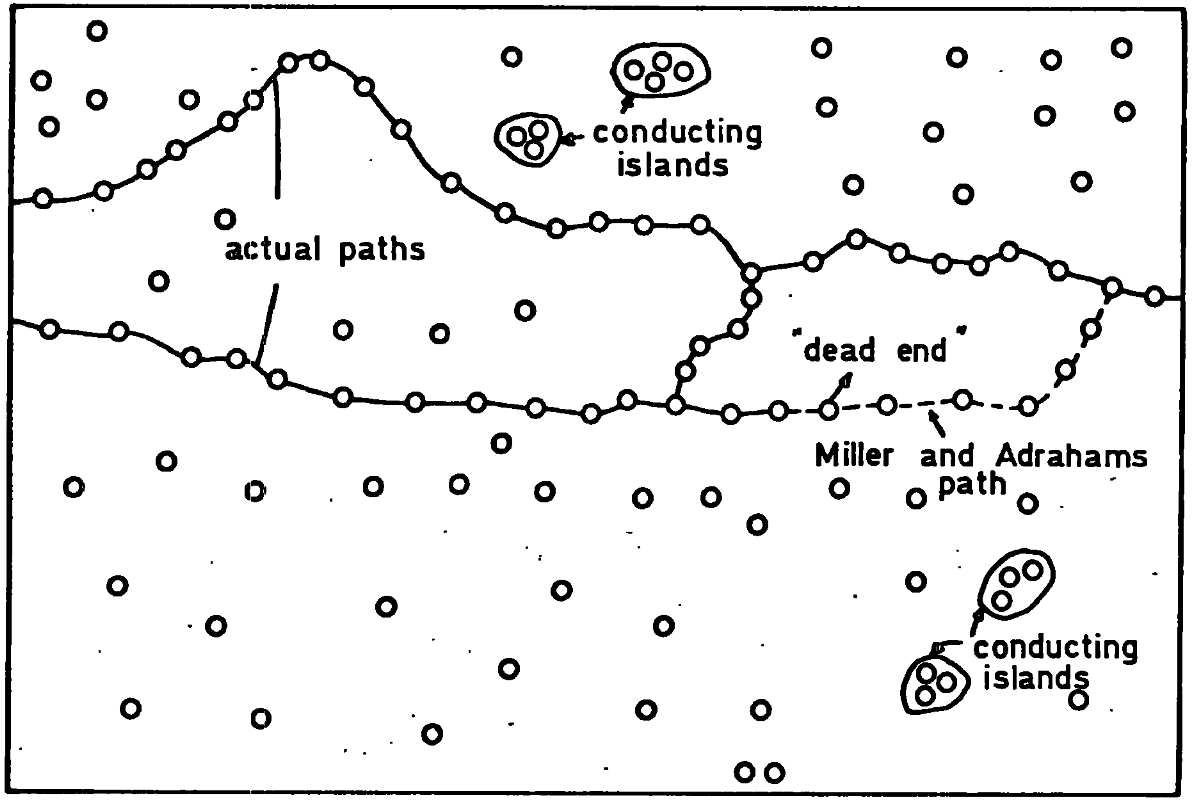

FIG. 2·3 Schematic representation of the actual current paths in a disordered system and of current path according to Miller and Abrahams, which does not by pass "dead ends." The conducting islands marked do not contribute to the d.c. conductivity, but they play an important role for a.c. conductivity. (after reference 30)

When the applied fields exceed some $10^3 - 10^4$ V/cm several types of phenomena may arise which are not present at low fields. All amorphous semiconductors and insulators exhibit a non-linear region of steady current-field dependence at fields in excess of $5 \times 10^3 - 10^5$ V/cm. Several bulk effects of this non-linear behaviour have been described in the literature. In (31-32) the field dependence of conductivity at low temperatures under moderate applied fields ($10^3 < E < 10^5$ v/cm) is obtained as

$$\sigma \; \alpha \; \exp\left\{ {}^{eaF}/_{KT} \right\} \tag{2.15}$$

where F is a linear function of electric field and "a" is the characteristic hopping length. This behaviour is interpreted on the basis of percolation theory as well as variable range hopping conduction near the Fermi energy. The temperature dependence of conductivity in equation (2.15) follows the $T^{-\frac{1}{4}}$ law. The effect of field is greater as the average hopping distance R increases ; i.e. for lower temperatures and for lower densities of states. At high temperatures σ becomes independent of field and this effect is not considered. A deviation from $T^{-\frac{1}{4}}$ behaviour is suggested with increasing field, until at sufficiently high fields and low temperatures the conductivity becomes temperature independent. The characteristic hopping length "a" is less than the average hopping distance R of equation (2.12) and decreases with increasing temperature. In (33-34) the field dependence of the current is investigated for very low temperatures and for not too strong fields. It is found that

$$J\ (E) \sim e^{BE} \tag{2.16}$$

where B is constant. In the presence of a high field, an electron in a state with ionization energy E_i near the Fermi energy can jump to a state with energy lowered by the field to a value below E_i with the emission of a phonon as shown in Figure 2.4a.

In (19) the field dependence of hopping conduction has been described as due to enhancement of hopping probabilities by a high field. The mechanism is

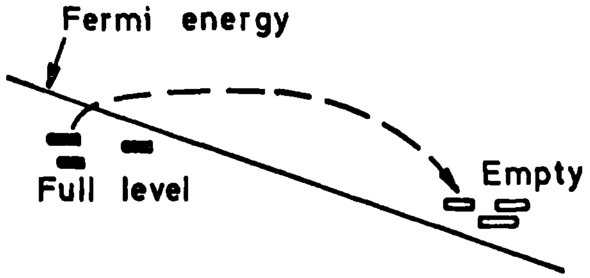

FIG. 2·4 (a) High field emission hopping conduction in a state with energy E_i near the Fermi energy. (ref. 33)

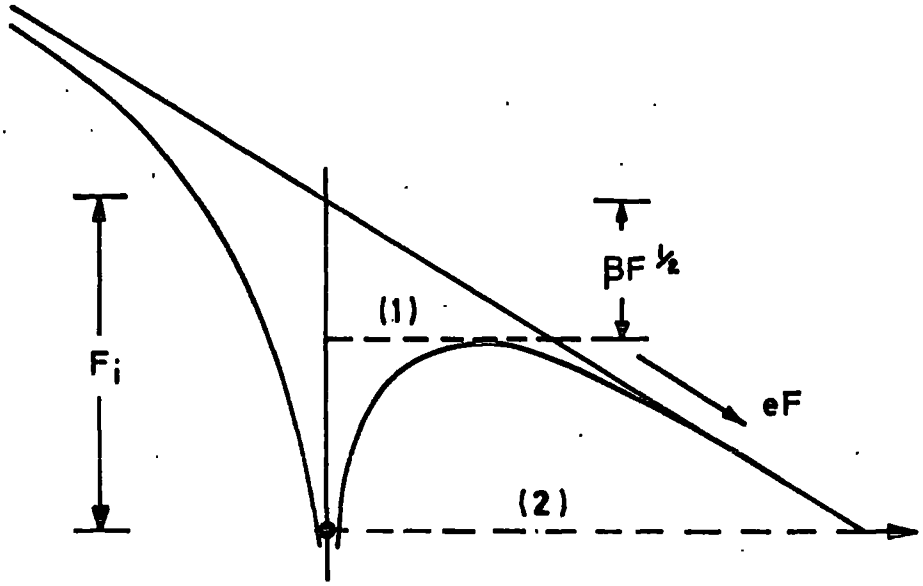

FIG. 2·4 (b) The Poole - Frenkel effect. The ionization energy E_i is decreased by the applied field F, in the direction of the field by $\beta F^{1/2}$. Electron emission can take place over the top of the reduced barrier as in (1), or by tunnelling as in (2). (ref. 19.)

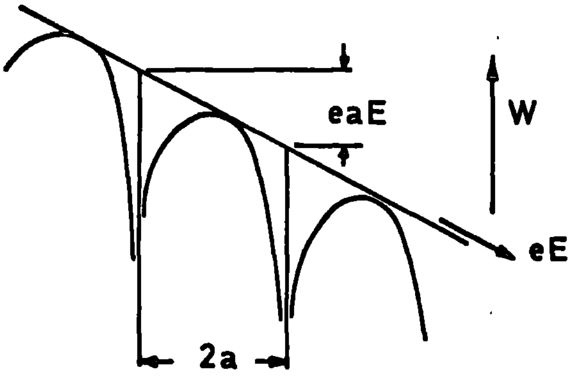

FIG. 2·4 (c) The Poole effect. Barrier lowering by a high field in a closely spaced coulombic centers. (ref. 19.)

a lowering of the hopping barriers for electrons on donor-like centres (Fig. 2.4b). With centres spaced sufficiently far apart for their Coulomb potentials not to overlap significantly. This mechanism gives a field dependence of current due to the Poole-Frenkel effect.

$$J_{PF} \quad \alpha \quad \exp\left\{ e\,\beta\,E^{\frac{1}{2}}/_{KT} \right\} \tag{2.17}$$

This expression is also written in the form

$$J_{PF} = \sigma_o\,E\,\exp\left\{ \frac{e\beta E^{\frac{1}{2}}}{KT} - \phi_t \right\} \tag{2.18}$$

where $\beta = ({}^{e}/_{\pi\varepsilon'\varepsilon_o})^{\frac{1}{2}}$ is the Poole-Frenkel constant ; ε' is the high frequency dielectric constant of the material, ϕ_t is the activation energy into the extended states of the electron and σ_o is a constant. This shows that a graph of logJ versus $E^{\frac{1}{2}}$ ought to give a straight line with a slope $e\beta/_{KT}$. This mechanism has been observed in a range of amorphous materials and insualators. In some cases the experimental β is rather less than the expected β_{pf} by a factor of between ½ and 1. This discrepancy is a general feature of much of the experimental material and it is suggested that it is due to Schottky emission from the electrode which should give an identical characteristic but with the coefficient (19).

$$\beta_s = \left\{ {}^{e}/_{4\pi\varepsilon'\varepsilon_o} \right\}^{\frac{1}{2}} = \frac{1}{2}\,\beta_{pf} \tag{2.19}$$

A different situation arises if the Coulombic centres are situated so close together that their fields overlap (19). In this case the lowering of the barrier is given by eEa, where 2a is the distance between centres as shown in Figure 2.4c. This model is characterised by a current-field dependence of the type

$$\log J = \text{constant} + eaE/_{KT} \tag{2.20}$$

and is known as the Poole effect. This characteristic is well known in ionic conduction but this has been also observed in amorphous materials.

The non-linear behaviour in I-V characteristics may also arise from contact induced effects, e.g. presence of non-equilibrium carriers resulting from injection of space-charge limited currents into insulators(35-36).

2.4 MOBILITY

The mobility of carriers in crystalline semiconductors is much higher than that of disordered solids. In the case of disordered materials the mean free path is much lower than the interatomic spacing which suggests a breakdown of free carrier theory. The classical transport theory, which is based on the assumption of a band mechanism of transport is inapplicable to solve the problem of the materials with low mobilities (less than 10^{-1} cm^2/V sec).

Many theoreticians (16,19,37) have suggested a lower limit for the free band mobility $\mu > 0.1 cm^2/V$ sec ; for hopping conduction, on the other hand the mobility is less than 0.1 $cm^2 v^{-1} sec^{-1}$. The direct mobility measurements at one temperature can distinguish band from hopping conduction. The experimental determination of mobility in hopping systems is based on two different methods. These are known as drift mobility μ_D and Hall mobility μ_H techniques.

The drift mobility provides a measure of the response of a carrier to the application of a small electric field E

$$\mu_D = {}^{V_D}/_E \qquad (2.21)$$

where μ_D and V_D are respectively the drift mobility and drift velocity associated with a charge carrier.

The Hall mobility on the other hand, provides a measure of the response of a charge carrier to an applied magnetic field. If one creates a net current flow via the application of an electric field and in addition applies a small magnetic field perpendicular to the current direction, the carriers will experience a net deflection which is perpendicular to both the magnetic field and the current direction.

The Hall mobility μ_H is then defined as

$$\mu_H = V_1 \Big/ \frac{V_D H}{C} = \frac{C\,\mu_{xy}}{H\,\mu_{xx}} \qquad (2.22)$$

where V_1 is the component of carrier velocity which is perpendicular to the electric field direction and $(V_D H/C)$ is due to the effective electric field.

In general one should not expect the carriers response to an electric field to be the same as that of a magnetic field hence usually $\mu_H \neq \mu_D$. In the hopping regime the Hall and drift mobilities (in a small polaron model) have turned out to differ appreciably from one another, in contrast to the regime of free band conduction (18). The Hall mobility in the transition regime between hopping and band regimes has been investigated in (38). It is known that the validity of equation (2.22) in hopping systems is not at all obvious both as regards the magnitude and the sign of the effect (39-40), since the concept of the classical Lorentz force does not apply. In disordered systems the experimentally determined sign of the Hall effect is in general negative. This applies also in those cases where the conductivity is realised by holes (a phenomenon termed"the p-n anomaly "). The sign of the Hall effect is then of an elemental (three site) jump process. In (41) it has been shown that the relative sign of the Hall effect for holes as compared to the sign for the electrons is given by the factor $-(-1)^n$ where n is the minimum number of sites in a closed path. Taking triangular closed paths (n=3) it follows that the sign of the Hall effect for holes should be the same as that for electrons, namely negative. Thus, if the conduction is predominantly hole-like, the sign of the Hall effect is also negative. Therefore, the Hall effect is no longer considered a useful tool for either determining the sign of the carriers or calculating the carrier density. Moreover, the mobilities in hopping materials are generally far too low to be detected from conventional Hall effect measurements.

The mobility in hopping systems is determined by other methods such as drift measurements. The drift mobility method consists of measuring the transit time t_t required by a sheet of injected charge to traverse the known thickness d of a sample in a given electric field E. Then

$$\mu_D = {}^{d}/_{t_t E} \qquad (2.23)$$

Several techniques have been used to measure the very low values of mobility (42-43).

In hopping systems it is generally expected that the Hall mobility should be less than the drift mobility and essentially temperature independent (40). On the small polaron hopping model, on the other hand, the Hall mobility is found to be typically much larger than the drift mobility (41).

In view of high density of localized states in the model of amorphous semiconductors, the drift mobility is thermally activated, i.e. it obeys the relation

$$\mu_D = A \exp \left\{ {}^{-E}/_{KT} \right\} \qquad (2.24)$$

If the localized states are at the edges of the conduction and valence bands the drift mobility is expected to be temperature independent (18).

2.5 THERMOELECTRIC POWER

When a conductive material is placed between electrodes at different temperatures, a potential difference ΔV is produced. This potential difference per degree temperature difference is termed the thermoelectric power or the Seebeck coefficient, which is given by the following expression

$$S = {}^{dV}/_{dT} \qquad (2.25)$$

When measured under experimental condition such that no current follows through the specimen, the equation can be taken as

$$S = \frac{V_h - V_c}{T_h - T_c} \quad . \tag{2.26}$$

where $V_h - V_c$ and $T_h - T_c$ are the emf and temperature differences between the hot and cold ends of the specimen. The maximum value of $|\Delta T|$ should not exceed approximately 10° C. The sign of S may be determined from the polarity of the cold end of the sample.

In the case of crystalline semiconductors with a single type of charge carrier, the Seebeck coefficient can be written (18, 44-45)

$$S = \frac{K}{e} \left\{ \frac{E_c - E_F}{KT} + A \right\} \tag{2.27}$$

where E_c is the energy of the conduction band edge and A is the energy transport term which depends on the nature of the scattering process and is normally a small constant between 2 and 4. If current is carried by holes, the sign of S is reversed and $(E_c - E_F)$ is replaced by $E_F - E_V$. In the case of amorphous semiconductors and insulators, no major change of equation (2.27) is required. For current carried in extended states, A is expected to be equal to unity and E_c or E_V refers to the appropriate mobility shoulder. For current carried in localized states at the band edges, A will again be small and E_c and E_V are replaced by E_A and E_B respectively. Measurements of S as a function of temperature provide the most direct way of determining the temperature coefficient γ of the activation energy for conduction. The activation energy for conduction is written for n-type carriers as (18)

$$\left. \begin{aligned} E &= E_c - E_F = E(o) - \gamma_T \\ \text{and} \quad S &= -\frac{K}{e} \left\{ \frac{E(o)}{K_T} - \frac{\gamma}{K} + 1 \right\} \end{aligned} \right\} \tag{2.28}$$

A plot of S against $1/_T$ has a slope that yields E(o) (as does a plot of $\ln\sigma$ against $1/_T$) and the intercept on the S axis at T = o yields γ.

In the case of high temperatures where KT>>E, i.e. KT exceeds the band width, one obtains (18,20)

$$S = \frac{K}{e} \ln \left\{ {}^{n}/_{(N-n)} \right\} \qquad (2.29)$$

where n denotes the concentration of the charge carriers, and N the concentration of the sites ($n=N_D-N_A, N = N_D$). According to equation (2.29) the sign of the thermoelectric power determines the type of conduction. If $n<N/2$, then $S<o$ and the conduction is caused by electrons, whereas for $n>N/_2$, $S>o$ it is caused by holes. Therefore, for $n = N/_2$ the sign of the thermoelectric power changes (whereas the Hall effect in the hopping region may preserve its sign). The sign of S is a much more reliable indication than the Hall effect of whether the material is n-type or p-type. The change of sign S at high temperature is suggested due to the minority carriers which play an increasingly important part in the conduction (18,20).

The low temperature region, where the conductivity is realized by hops near the Fermi level and the $T^{-1/4}$ law holds, is investigated in (18,44,46-47) In this case the appropriate formula is

$$S = \frac{\pi^2}{3} \frac{K^2T}{e} \left\{ \frac{d \ln\sigma'(E)}{dE} \right\}_{E = E_F} \qquad (2.30)$$

A change of sign of the thermopower at low temperature is a common phenomenon and is interpreted as a change in the mechanism from charge transport by excited carriers (whether in extended or localized states) to conduction due to electrons in some kind of defect band.

2.6 ALTERNATING CURRENT BEHAVIOUR

The band and hopping conduction mechanisms have a basically different non-steady state behaviour. For band conduction, current is associated with electronic states and electrons (or holes) do not change their states in order to carry current. In hopping conduction, on the other hand, current is produced only by hopping carriers. The conductivity of a hopping process is an increasing function of frequency ; this is in contrast to band conduction which exhibits a slow decrease due to free movement of charge carriers through a periodic lattice (48). The frequency dependence of conductivity in a hopping system was first reported by Pollak and Geballe (49) for compensated crystalline silicon in the impurity conduction range. The frequency dependence of the real part of conductivity is represented in the form

$$\sigma(\omega) = \sigma_o + \sigma'(\omega) \tag{2.31}$$

where σ_o is the dc conductivity and the true ac conductivity $\sigma'(\omega)$ has been represented by an empirical relation of the form

$$\sigma'(\omega) \propto \omega^n \tag{2.32}$$

where n = 0.8.

The theory of this phenomenon is treated by Pollak in several papers (4) ; this dependence is based on a pair approximation in which the carriers are assumed to hop between pairs of localized sites, with an average being taken over all pairs of sites. These are distributed randomly in space and in energy in a disordered solid. The probability for hopping between two centres is proportional to

$$\sigma'(\omega) = \sigma(\omega) - \sigma_o \propto \frac{\omega^2 \tau}{1+\omega^2\tau^2} \tag{2.33}$$

where τ is the mean of the times taken to jump back and forth. The polarization, resulting from hopping carriers depends not only on the hopping distance (i.e. on τ) but also on the energy separation Δ between the two member states of a pair in which hopping occurs. The time τ is an exponentially increasing function of the jumping distance ; the need to average over all possible pairs leads to domination by pairs for which $\omega\tau=1$ and hence the conductivity is proportional to ω. On the idea of two-centre hopping many other theoreticians (18,51-52) have predicted a similar frequency dependence of conductivity for amorphous semiconductors and disordered solids. At $\omega \neq o$ a charge carrier contributing to the current has not to move across the specimen from electrode to electrode. The main contribution to the current comes from electronic transitions within well conducting clusters of atoms. At sufficiently high frequencies these clusters are pairs of atoms with a small spacing. However, with decreasing frequency the sizes of the clusters increase (53) and a pair approximation becomes inadequate. The frequency down to which a pair approximation holds, lowers with decreasing concentration of atomic sites (54). There are two methods for understanding the idea of a pair approximation. The first approach consists of calculating the current due to a pair of atoms on which one electron is placed. Then the result is multiplied by the probability of finding one electron on the selected pair and it is averaged over all the contributions from all the pairs (49-52, 54-57). The second approach consists of neglecting all the sites except the sites of the selected pairs (58-60). The ac conductivity in the pair model consists of the phonon contribution $\sigma^{(1)}(\omega)$, and the phononless one $\sigma^{(2)}(\omega)$, At low temperatures for ${}^{\nu}\mathrm{ph}/_{\omega} >> 1$ with $\nu\mathrm{ph} = 10^{12}$ Hz, $\mathrm{Re}\sigma^{(1)}(\omega)$ is expressed in the form (20)

$$\mathrm{Re}\sigma^{(1)}(\omega) = \frac{\pi^4}{12}\, e^2 N(E_F)\, \omega KT (2\alpha)^{-5} \ln^4 ({}^{\nu}\mathrm{ph}/_{\omega}) \qquad (2.34)$$

where α is the effective radius of the localized states wave function and $N(E_F)$ is the density of states with energy near the Fermi level. An expression of such a type is found in (50,52,59), but the results are different from each other. In this situation the main contribution to the conductivity comes from pairs with a spacing between the atoms of order $\frac{1}{2}\,\alpha$ (this arises by taking the average over the hopping distance R). According to the relation (2.34) the frequency dependence $\mathrm{Re}\sigma^{(1)}(\omega) \sim \omega \ln^4 (\nu_{ph}/\omega)$ holds, which over a large frequency range may be expressed by the empirical relation (2.32). In (18) it is suggested that two kinds of hopping mechanisms may be responsible for $\mathrm{Re}\sigma^{(1)}(\omega) \alpha\ \omega^{0.8}$ behaviour in the low frequency range near room temperature. These are :

(a) transport by hopping carrier excited into the localized states at the edges of the valence or conduction band,

(b) hopping by carriers with energies near the Fermi level with finite $N(E_F)$.

The two processes can be distinguished by observing the temperature dependence of $\sigma(\omega)$ and the frequency at which $\omega^{0.8}$ behaviour begins, i.e. the onset from the d.c. level of the $\mathrm{Re}\sigma^{(1)}(\omega) \alpha\ \omega^{0.8}$ law. In case (a), where multiple hopping is occurring, the temperature dependence of the a.c. component of $\mathrm{Re}\sigma'(\omega)$ should be the same as that of σ_o and the onset of $\mathrm{Re}\sigma(\omega)\ \alpha\ \omega^{0.8}$ occurs at higher frequencies. In case (b) the a.c. component of $\mathrm{Re}\sigma(\omega)$ is weakly dependent on temperature and the $\mathrm{Re}\sigma(\omega)\ \alpha\ \omega^{0.8}$ law is followed from the lowest frequencies upwards. Pollak and Pike (61) have raised a point that the conductivity of many glasses is due to ionic hopping and the significant information is considered in the departures of the exponent n from unity. In (62) the exponent n is shown to be temperature dependent under certain conditions ; n is close to unity if the wave functions are highly localized or if the temperature is low, while n becomes progressively smaller as the wave functions become more spread out and the temperature increases. Scher and Lax (63) have developed a theory of time dependent diffusion in hopping systems which gives n = 1 as the limit of temperature-independent behaviour, in agreement with experimental observations. They show that the conduction process can be regarded as a continuous-time random-walk of a classical particle on a lattice ; this interpretation is not included in the pair approximation.

At higher frequencies mechanisms of various kinds such as the phonon contribution due to correlated hops, phononless contributions and other mechanisms may lead to a dependence (18,49)

$$\sigma(\omega) \propto \omega^2 \qquad (2.35)$$

and at still higher frequencies $\sigma(\omega)$ becomes frequency independent. A saturation region often occurs when the applied frequency exceeds the hopping frequency of the pair i.e. $\omega > 1/\tau$. In ω^2 behaviour one could assume that the centres are well separated pairs so that $\omega\tau = 1$ cannot apply and the equation (2.33) follows the ω^2 behaviour, which is characteristic of isolated two centre case. The phononless contribution originates from resonance transitions between sites with energy difference which is approximately equal to $\hbar\omega$. This contribution yields generally the well-known dependence (64-65), $\sigma^{(2)}(\omega) \sim \omega^2 \ln^4 \omega$ which follows the relation (2.35). Such a quadratic dependence is also considered for phonon contributions due to correlation effects, i.e. the dependence of the occupation probability of a site on the occupation of the neighboured sites (50). The correlation effect increases as the pair separation decreases ; such a dependence is obtained also in (66-67) by investigating hops within clusters. Both linear and square law dependencies correspond to transport near the Fermi level. According to the predictions of the pair model the phonon contribution to the conductivity dominates in the low frequency range ($<10^8$Hz) and $\sigma'(\omega) \propto \omega^n$ with $n \leqslant 1$ holds. The upper part of this variation shows a continuous curvature convex upwards (18,20). The frequency dependence of $\sigma(\omega)$ on pair model approximation is shown in Figure 2.5a.

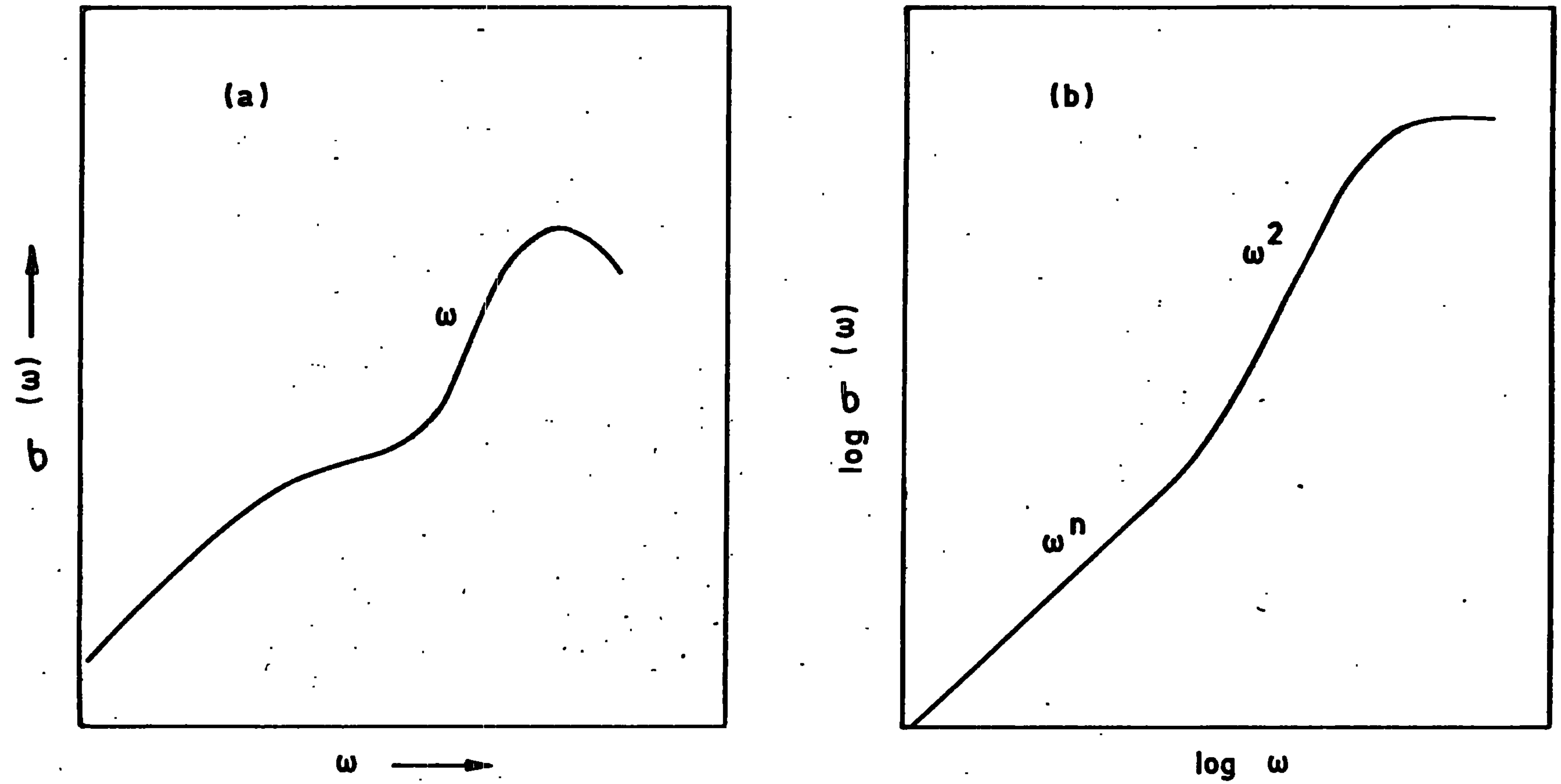

FIG. 2·5 Schematic representation of the frequency dependence of the real part of the electrical conductivity, $\sigma(\omega)$ for disordered systems. (a) after reference 20. (b) after reference 35.

Interpretation of the frequency dependence of $\sigma(\omega)$ on the pair model has been investigated in most detail in chalcogenide glasses (68,69). In such materials a dependence ω^n with $0.7 < n < 1$ has been observed at frequencies up to 10^6 to 10^8 Hz. At higher frequencies an ω^2 dependence followed by a saturation region at $\omega = 10^9$ Hz has been reported. In amorphous Ge the frequency dependence of $\sigma(\omega)$has also been extensively studied (70-73). A dependence ω^n with $n = 0.8 - 0.95$ is observed in the frequency interval 10^4 to 2×10^5 Hz. A similar dependence is observed in phosphate glasses (74) and in some other amorphous materials (50). A ω^2 dependence followed by a saturation region at higher frequencies is observed in the solid polymer (75) and in semiconducting NiO doped with Li (76). Recently it has been pointed out that the experimentally observed ω^2 law may be affected by contact effects on the electrodes and other spurious effects (24,77).

Jonscher (77) has pointed out that this frequency dependence of $\sigma(\omega)$ is found not only in disordered, glassy and amorphous solids but also in ordered molecular solids. The carriers involved are not necessarily electrons, but may be polarons,protons or ions. The principal drawback of all the previous theories of frequency dependence of $\sigma'(\omega)$ is that they are based on the pair approximation of hopping conduction. Moreover, it is difficult to obtain an adequate physical insight into the mechanisms involved, especially in view of the extremely wide range of physical systems which other people are considering. He has suggested the Universal law of dielectric loss (77).

$$\varepsilon''(\omega) = \frac{\sigma'(\omega)}{\varepsilon_0 \omega} \propto \omega^{n-1} \qquad (2.36)$$

$$\text{or} \qquad \sigma'(\omega) \propto \omega^n$$

with $n<1$. A wide range of materials follow this law over a wide range of frequencies (between sub-audio and microwave). It is pointed out that the exponent n is not a constant for all systems but is a function of temperature, approaching unity at low temperatures and decreasing to 0.5 or less at higher temperatures. In general, there seems to be no correlation between the values of σ_o and $\sigma'(\omega)$ for various materials. This type of frequency dependence is found in both hopping and dipolar systems. In many materials it is not certain whether the observed behaviour should be interpreted by dipolar or by charge hopping mechanisms(78). Jonscher (35) has interpreted the frequency dependences $\sigma \propto \omega^n$ and $\sigma \propto \omega^2$ by a branched network of hopping sites and a separate set of dipole-like pairs with a much shorter relaxation time respectively, in contrast to the pair approximation model discussed above. According to this the frequency dependence of $\sigma(\omega)$ is as shown in Figure (2.5b). It is pointed out that the ω^n behaviour is temperature dependent though the effect is weaker than for dc conductivity at low fields. At high frequencies the occurrence of ω^2 followed by saturation at very high frequencies is relatively temperature independent. The low frequency mechanism is the extended hopping over many localized centres but avoiding the "bottlenecks" which arise for dc conduction due to difficult long hops.

With electron hopping there is a relatively small contribution to dielectric constant ε'. The value of ε' increases with temperature but the change is smaller at higher frequency (78-79).

In the Debye dipolar mechanism the frequency dependence of the complex permittivity (ε',ε") is expressed in the form (80)

$$\begin{aligned} \varepsilon''(\omega) &\propto \omega\tau/(1+\omega^2\tau^2) \\ \text{and} \quad \varepsilon'(\omega)-\varepsilon_\infty &\propto 1/(1+\omega^2\tau^2) \end{aligned} \qquad (2.37)$$

and their ratio is

$$\frac{\varepsilon''(\omega)}{\varepsilon'(\omega) - \varepsilon_\infty} = \omega\tau \qquad (2.38)$$

where ε_∞ is the dielectric constant at high frequency. The a.c. electrical conductivity corresponding to the dipolar process can be represented by

$$\sigma'(\omega) \;\alpha\; {}^{\omega 2}\!/_{(1 + \omega^2 \tau^2)} \qquad (2.39)$$

and shows a rise proportioned to ω^2 at frequencies below $1/_\tau$ and a saturation region above. The term τ is the relaxation time, which is equal to the reciprocal jumping frequency. This situation is exactly analogous to the case of two-centre hopping. Therefore, hopping of a charge carrier between two centres is both physically and mathematically indistinguishable from a dipole jumping between two orientations.

Recently Jonscher (81) has suggested that according to the Kramers-Kronig relation, the empirically observed law of equation (2.36) for $\varepsilon''(\omega)$ implies the same frequency dependence for the real part $\varepsilon'(\omega)$ which thus takes the form

$$\varepsilon'(\omega) - \varepsilon_\infty \;\alpha\; \omega^{n-1} \qquad (2.40)$$

The ratio $\varepsilon''/_{\varepsilon'-\varepsilon_\infty}$ is independent of frequency. This is in stark contrast with the Debye dipolar behaviour of equation (2.38) where this ratio is equal to $\omega\tau$. The consequence of this is that,

$$\frac{\varepsilon''(\omega)}{\varepsilon'(\omega) - \varepsilon_\infty} = \text{Cot}\left\{\frac{n\pi}{2}\right\} \qquad (2.41)$$

with n <1. This Universal law of dielectric response is characteristic of either non-Debye dipolar systems or hopping charge carriers, electronic or ionic (82). The detailed physical mechanisms which lead directly to the criterion (2.41) are suggested in (81-82). It is difficult to obtain conclusive evidence of the dipolar or hopping charge carrier from the expression (2.41). There is a general lack of good correlation between d.c. conductivity and $\sigma'(\omega)$. It has been suggested that the correlation between the magnitudes of σ_o and $\sigma'(\omega)$ and especially a similarity between the respective activation energies would provide strong evidence for the hopping charge origin of the polarization. On the other hand if the polarization is dipolar, the d.c. and a.c. response will not be correlated at all.

CHAPTER 3

PRELIMINARY CONDUCTIVITY STUDIES

3.1 INTRODUCTION

The d.c. electrical properties of amorphous thin film silicon nitride have been reported by many authors (83-86). Silicon nitride has been used for semiconductor devices both as a diffusion mask and for passivation of electrical junctions. Three conduction processes in silicon nitride are suggested ; these are Poole-Frenkel emission, field ionization and trap hopping. All of the processes are bulk limited. The steady state d.c. conduction properties of silicon nitride films in the range of 50-100 Å are reported in (86). The current through this material was time dependent, and started decreasing from the moment of application of a voltage. A period of 10-15 minutes was necessary for the current to reach its final value after each increment in voltage. These nitride films were made by vapour deposition on degenerate silicon substrates using the silane-ammonia reaction. The temperature, thickness and field dependences of current indicated that a transition in current mechanisms occurred at a film thickness of approximately 80 Å. Below this thickness, the current was characterized by a small temperature dependence and a marked thickness dependence. At film thicknesses above this value, high field conduction showed non-ohmic behaviour. The conductivity increased with applied fields (above 10^4 v cm^{-1}) and the current-voltage characteristic was represented in the form $\sigma \sim \exp\left[\frac{q\Phi}{KT} - \beta_F E^{\frac{1}{2}}\right]$ which is evidence of Poole-Frenkel effect. Recently Sullivan and Card (87) have reported that amorphous thin films of silicon nitride with dissimilar (aluminium and silicon) electrodes exhibited conduction properties with a consistent dependence on the polarity of the applied electric field and film thickness ; the conduction in these films was by a bulk controlled process. The temperature dependence of current at high field did not give a linear log J versus T^{-1} plot. The activation energy varied from 1.5 eV at high temperature (above 250 K) to 0.09 eV at intermediate temperature (between 250 K and 170 K). It has been suggested that Poole-Frenkel emission is into the band tails at E_a and E_b at high temperatures and at high fields. Conduction in these tails is by hopping with very small activation energy. At intermediate temperature, hopping conduction (thermally assisted tunnelling) between localized states in the defect band near mid-gap is suggested. The low temperature results are associated with field ionization of localized states in the defect band. It has been further suggested that localized states in the Si_3N_4 (presumably in the defect band near mid gap) were changed by injection at distances $\gtrsim$ 100 Å from the electrodes. Thin film silicon nitride is a good insulator; the electrical conductivity of this material being 10^{-15} $ohm^{-1} cm^{-1}$ at room temperature.

The a.c. electrical properties of thin film silicon nitride have been reported by Jonscher in (88). A frequency dependence of conductivity was observed which followed the $\sigma(\omega) \propto \omega^2$ law over a frequency range extending over six decades. He also pointed out that the activation energy was 10^{-2} eV and that there was very little change of permittivity with frequency. The strongly pronounced square law dependence in Si_3N_4 coincided with a very low d.c. conductivity suggesting the absence of spurious effects. It has been suggested that the conduction processes are due to electron hopping in view of the very low activation energies and the absence of any departures from ω^2 law even at frequencies as high as 1 MHz and above.

Only in (89) are some electrical conductivity data of reaction bonded Si_3N_4 found. The d.c. conductivity value of this material was given as 10^{-13} ohm^{-1} cm^{-1} at room temperature and rose to about 5 x 10^{-6} ohm^{-1} cm^{-1} at 1000° C. It has been found, however, that the resistivity of high density specimens is poor (i.e. a low resistivity), owing to the presence of unreacted free silicon.

Equally, only one paper has appeared on the electrical properties of reaction bonded materials of the MgO-Si_3N_4 system by Andreava et al (90). With increase in the content of magnesium oxide in the initial mixture, the d.c. electrical resistivity of the sintered specimens increased in the range 20-900° C by two orders of magnitude as a result of the fact that the resistivity of MgO in this temperature range was higher than that of silicon nitride. In the range 1000-1400° C the electrical resistivity for specimens of three of the compositions (20,40 and 80 m/o MgO) was practically the same, while that of the specimen containing 60 m/o MgO was an order of magnitude higher ; this might be due to the presence of the Ortho silicate Mg_2SiO_4 with a distorted lattice formed during sintering as suggested by them. In specimens of the remaining compositions the following compounds occurred : Si_2ON, Mg_2SiO_4 and $MgSiO_3$, which led to a reduction in the electrical resistivity at high temperatures. Conductivity of these materials were in the range $3 \times 10^{-12} - 10^{-13}$ ohm^{-1} cm^{-1} at room temperature and rose to 4×10^{-6} - 10^{-5} ohm^{-1} cm^{-1} at 1400° C. It has been suggested that materials of the system MgO-Si_3N_4 may be used as insulators at temperatures up to 1400° C.

To the author's knowledge there have been no previous reports of the electrical properties of hot-pressed nitrogen ceramics, and the work described in this Chapter was undertaken primarily to investigate the salient features of electrical conductivity in hot-pressed silicon nitride, 5 w/o MgO/Si_3N_4 and two compositions of sialon ceramics.

3.2 EXPERIMENTAL

Most of the materials were supplied as discs and specimens were cut with a diamond wheel into rectangular blocks with plane surfaces ; typical specimen dimensions were 1.5 cm x 0.5 cm x 0.2 cm which gave a conveniently defined shape for conductivity and thermoelectric power measurements. Similar shapes of specimen were used for Hall effect studies. It was known from previous studies of techniques that the current electrodes of the specimen tend to short out the Hall field if a suitable shape of the specimen is not used. Consequently the length-to-width ratio of the specimen was always made greater than 4 in order to minimize this shorting effect.

3.2.1 D.C. AND A.C. CONDUCTIVITIES

For both d.c. and a.c. conductivity measurements, a two probe method was employed using platinum/platinum paste electrodes as contacts. The apparatus and circuit arrangements are shown in Figure 3.1. The platinum paste was first painted on the small end faces of the specimen and pt. wire was then attached to the electrode material for making connecting leads. The contacts were held to the specimen by mechanical pressure (for firing). The assembly was fired at 300° C to achieve good mechanical bonding between electrodes and specimen. The pt. wire strips led through separate bores in a silica rod to an external circuit ; a second set of twin bores in another rod carried the pt/pt. 13% Rh thermocouple wires which monitored the temperature of the specimen. A compact furnace surrounding the specimen was used. All the measurements were made in air as it was known that there was no risk of oxidation up to 1000° C. For d.c. measurements a constant voltage (60 V) was applied across the specimen from a stabilised power supply and the resulting current (I) was measured on a galvanometer (sensitivity 0.009 μA per mm deflection). A decay of current was observed after sudden application of a voltage. Measurements were made when the current had attained a steady value.

For a.c. measurements a voltage was applied across the specimen from an A.F. Generator at different frequencies. The current was then measured from the voltage developed across a standard resistance (connected in series with specimen) by the relation $I = {}^{V}s/_{R_s}$. No decay of current was observed in a.c. measurements.

With a constant low applied field (less than 40 v cm^{-1}) the

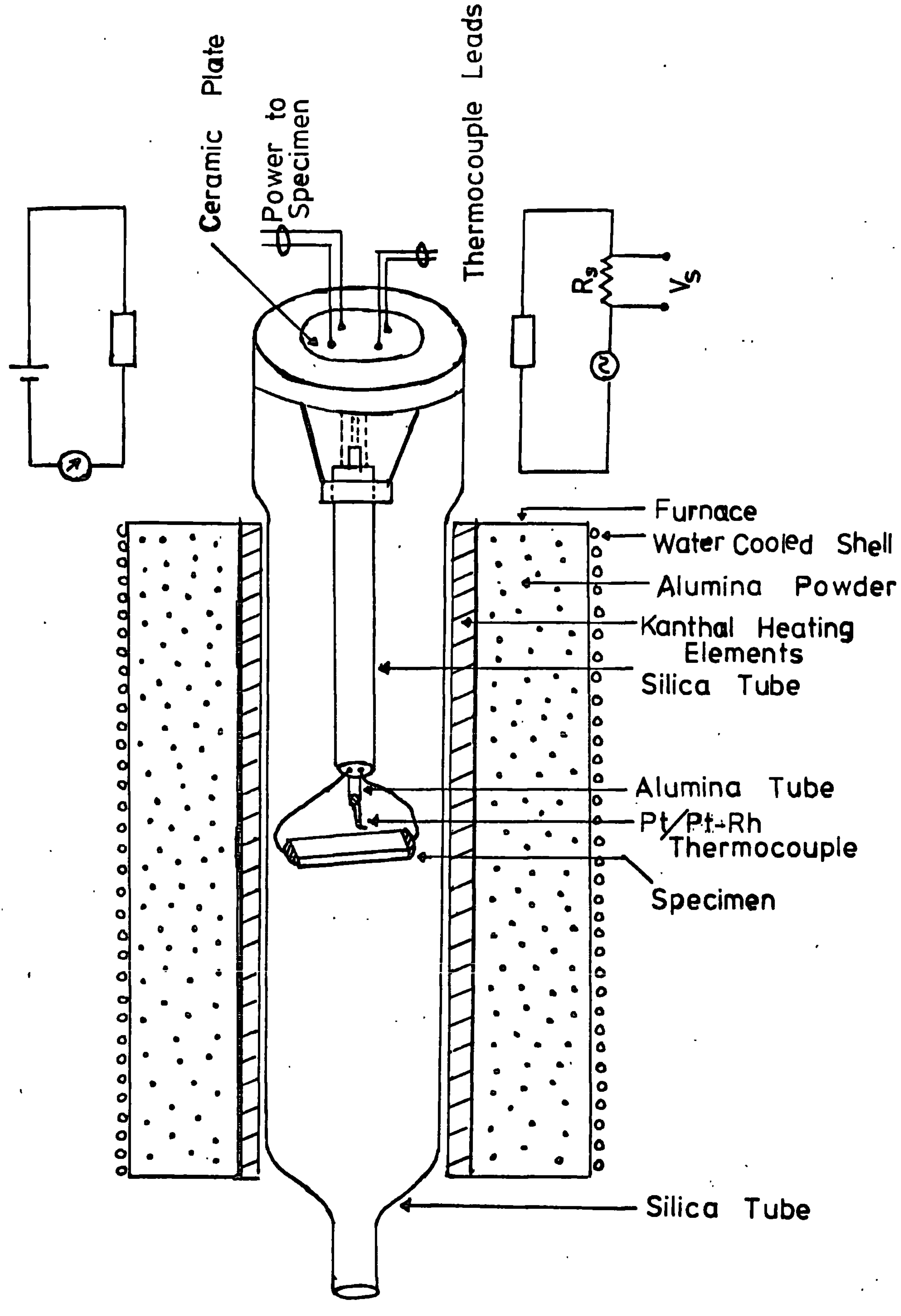

FIG. 3.1 Apparatus for measuring d.c. and a.c. electrical conductivities at high temperatures.

conductivity was derived from

$$\sigma = \frac{d}{A} \cdot \frac{I}{V} \tag{3.1}$$

where d and A, the length and cross-sectional area respectively, were obtained accurately from the measured dimensions of the rectangular specimen. The impedance of all the specimens was very high at room temperature ($\sigma < 10^{-12}\,\Omega^{-1}\,\mathrm{cm}^{-1}$) ; consequently, measurements were made over the temperature range 400 to 1000°C, the lower limit being determined by the onset of measurable conductivity and the upper by the furnace. A.C. measurements were made over the frequency range 15 Hz to 5 KHz.

3.2.2 D.C. HALL EFFECT

The d.c. Hall effect was investigated, using a conventional five probe method, over the same temperature range as mentioned above. The experimental assembly is illustrated in Fig.3.2. Platinum/platinum paste contacts were again used. The furnace was mounted between the poles of a Newport Type D electromagnet with which magnetic fields of up to IT could be obtained. A constant voltage (50 v) was applied across the electrodes 1 and 2 from a stabilized power supply and the resulting current (I_x)was monitored in a sensitive scalamp galvanometer. A potential divider (10 MΩ) was used across Hall probes A and B of the specimen to eliminate the residual Hall voltage (Fig. 3.2). By adjusting the position of the moving contact C on the potentiometer the voltage between C and D was reduced to zero at the value of magnetic field H = 0. By using a Keithley Type 149 nanovolt null detector for increasing the sensitivity of a pye precision decade potentiometer, into which the output of a high input impedance ($10^{12}\,\Omega$) d.c. amplifier was fed, fairly high sensitivity was obtained and Hall voltages of as little as 0.01 μV could be detected.

According to experimental investigation of the Hall effect for obtaining

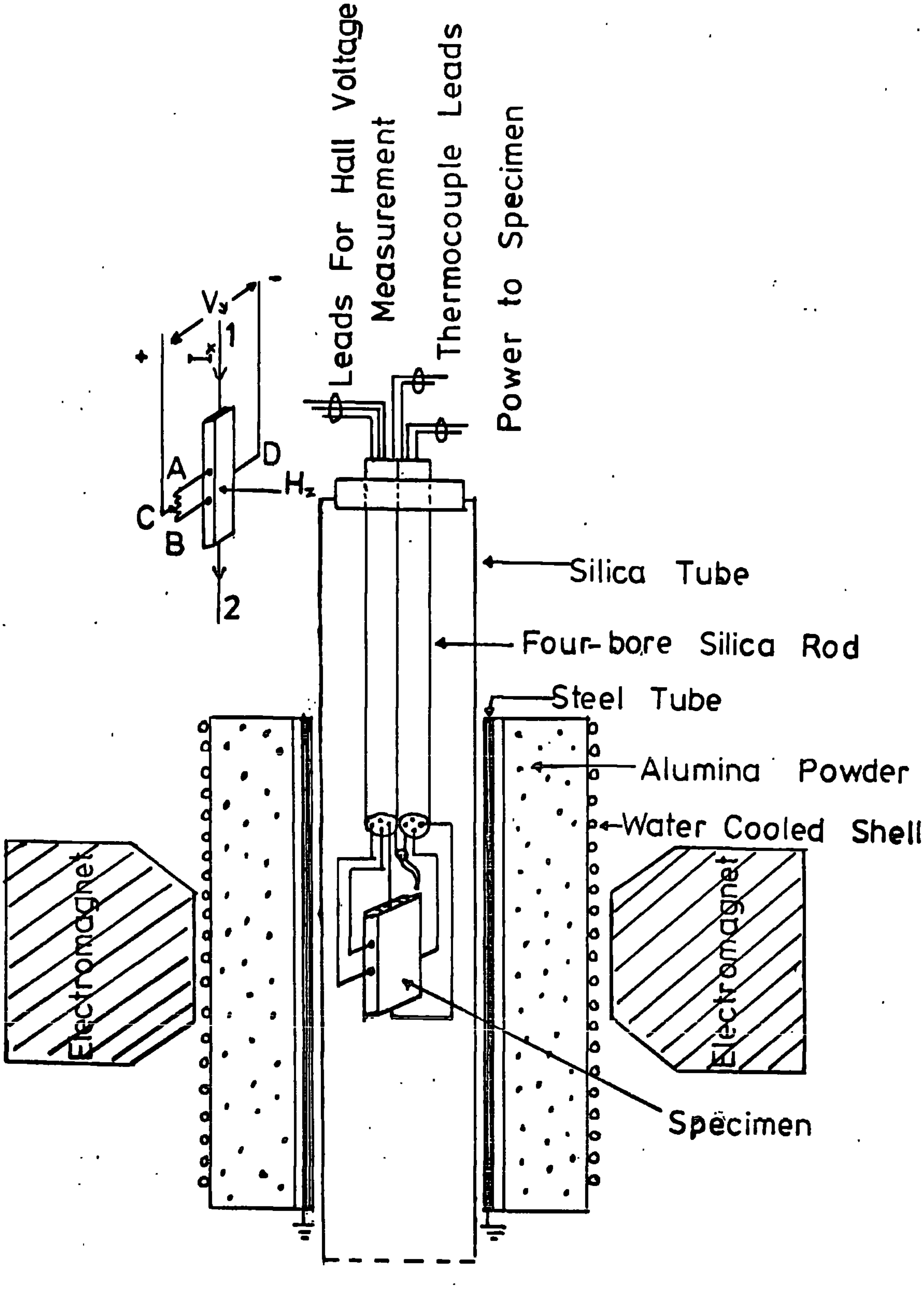

FIG. 3.2 Apparatus for measuring d.c. Hall-effect at high temperatures.

the mobility of charge carrying species, the Lorentz force F on a charge e is given by

$$F = e\ (E + V \times H) \qquad (3.2)$$

where e is the charge and V is the velocity of the particle which is subjected to an electric field E and a magnetic field H. If an n-type specimen is subjected to an electric field E_x and magnetic field H_z (Fig.3.2), a transverse electric field is given by

$$eE_y = H_z eV_x \qquad (3.3)$$

where V_x is the velocity with which the carriers drift in the X-direction under the applied field E_x. The current-density can be represented by

$$\frac{I_x}{w.t} = neV_x \qquad (3.4)$$

where w is the width of the specimen in the y-direction and t is the thickness of the specimen in the H direction. From equations (3.3) and (3.4) E_y is eliminated and $w.E_y = V_y$ called the Hall voltage, obtained from

$$V_y = W.E_y = \frac{H_z I_x}{ent} \qquad (3.5)$$

The Hall coefficient R_H is defined as the transverse Hall field per unit current density, i.e.

$$V_y/W = R_H\ H_z\ \frac{I_x}{w.t}$$

$$\text{or} \quad R_H = \frac{V_y.t.10^8}{H_z.I_x} \qquad (3.6)$$

where H is in gauss and the thickness t is in cm. The Hall mobility is given by

$$\mu_H = |R_H| \sigma \qquad (3.7)$$

where $R_H = \frac{1}{ne}$ (using the conventional one carrier relationship) and σ is the electrical conductivity of the material.

3.2.3 THERMOELECTRIC POWER

The thermoelectric effects were also investigated over the same temperature range. The apparatus and sample holder for measuring thermal emf at high temperatures are shown in Fig. 3.3. The two longitudinal end faces of the specimen were situated between two steel blocks under compression. The lower block was supported by a steel rod (thread marked) which insured that specimen and blocks were aligned for uniform contact pressure at all times. Two thermocouples of pt/pt-13% Rh were attached in two separate points on a broad face of the specimen using platinum plaste. The assembly was fired at 200° C for two hours to achieve good mechanical bonding between electrodes and specimen. All the wires were carried through separate bores in two alumina tubes to an external circuit. A steel tube in the inner wall of the furnace and two steel jacket tubes to cover the alumina tubes (containing thermocouple wires) were used to avoid pick up thermal noise signal. A small subsidiary heater was used at the top end of the specimen for controlling the temperature gradient ΔT (less than 10°C) between two points of the specimen. Thermocouple leads were connected to a precision potentiometer through a two-way key for measuring temperature between two junctions of the specimen and the common platinum wires were connected to digital millivoltmeter through a high input impedance ($10^{12}\Omega$) d.c. amplifier for measurement of the thermoelectric voltages as a function of ΔT. The thermoelectric power or Seebeck coefficient was calculated from the relation (Chapter 2, Sect.2.5)

$$\alpha = \frac{V_h - V_c}{T_h - T_c} \qquad (3.8)$$

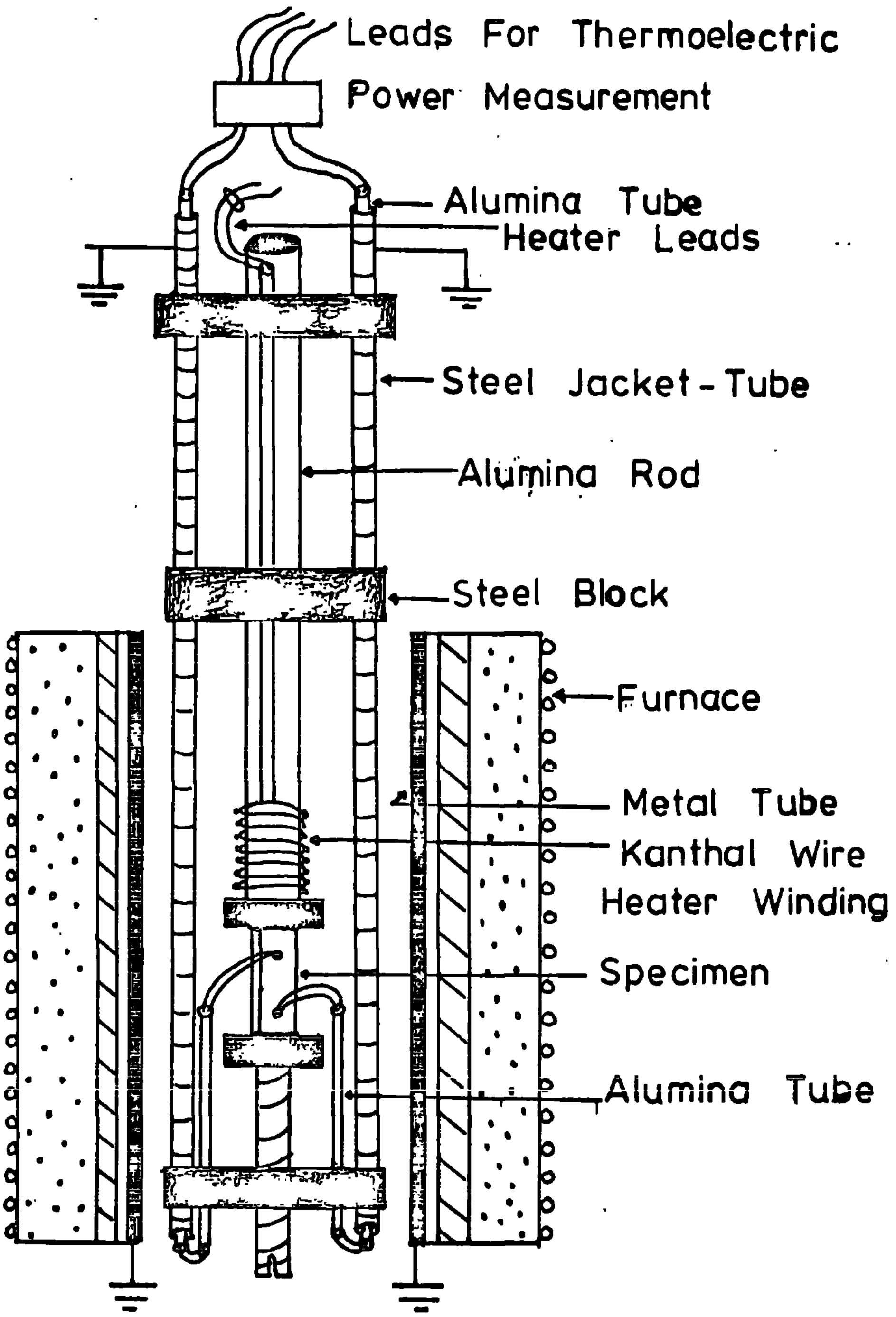

FIG.3.3 Apparatus for measuring thermoelectric power at high temperatures.

The sign of the carriers was determined by observing the polarity of the lower temperature end of the specimen.

3.3 RESULTS

3.3.1 D.C. AND A.C. CONDUCTIVITIES

Application of a d.c. voltage to all of the specimens resulted in current flow which was initially large and then decayed, over a period of some minutes, to a steady value. A typical decay of current for z = 4.0 sialon at 841° C under a constant applied 10 v is shown in Fig. 3.4. To avoid these polarization effects all the d.c. conductivity measurements were made only after equilibrium conditions had been attained. No polarization effects were observed when using a.c. voltages. Some conductivity data are given in Figs. 3.5 to 3.7 in which the logarithms of the conductivities are plotted as functions of inverse temperature.

As regards the d.c. conductivity (σ_{dc}) curves readings were taken both on heating and cooling. The curves show that the behaviour was reversible, indicating that there were no significant changes in either the specimens or the contacts during temperature cycling. There is a striking similarity between the form of the results for the four different materials (Table 3.1). The relationship between log σ_{dc} and 1/T is linear between 1000 and about 700° C and becomes non-linear at lower temperatures ; consequently the activation energy in the higher temperature region (i.e. 1000 to 700° C) is constant, but below 700° C it decreases slowly with decreasing temperature. Values for activation energy (E_A) were calculated from the d.c. conductivity results using the relation

$$\sigma_{dc} = \sigma_o \exp\left\{ {}^{-E}A/KT \right\} \qquad (3.9)$$

in the linear high temperature region and from the slopes of the curves at lower temperatures (Table 3.1). A value of the pre-exponential factor

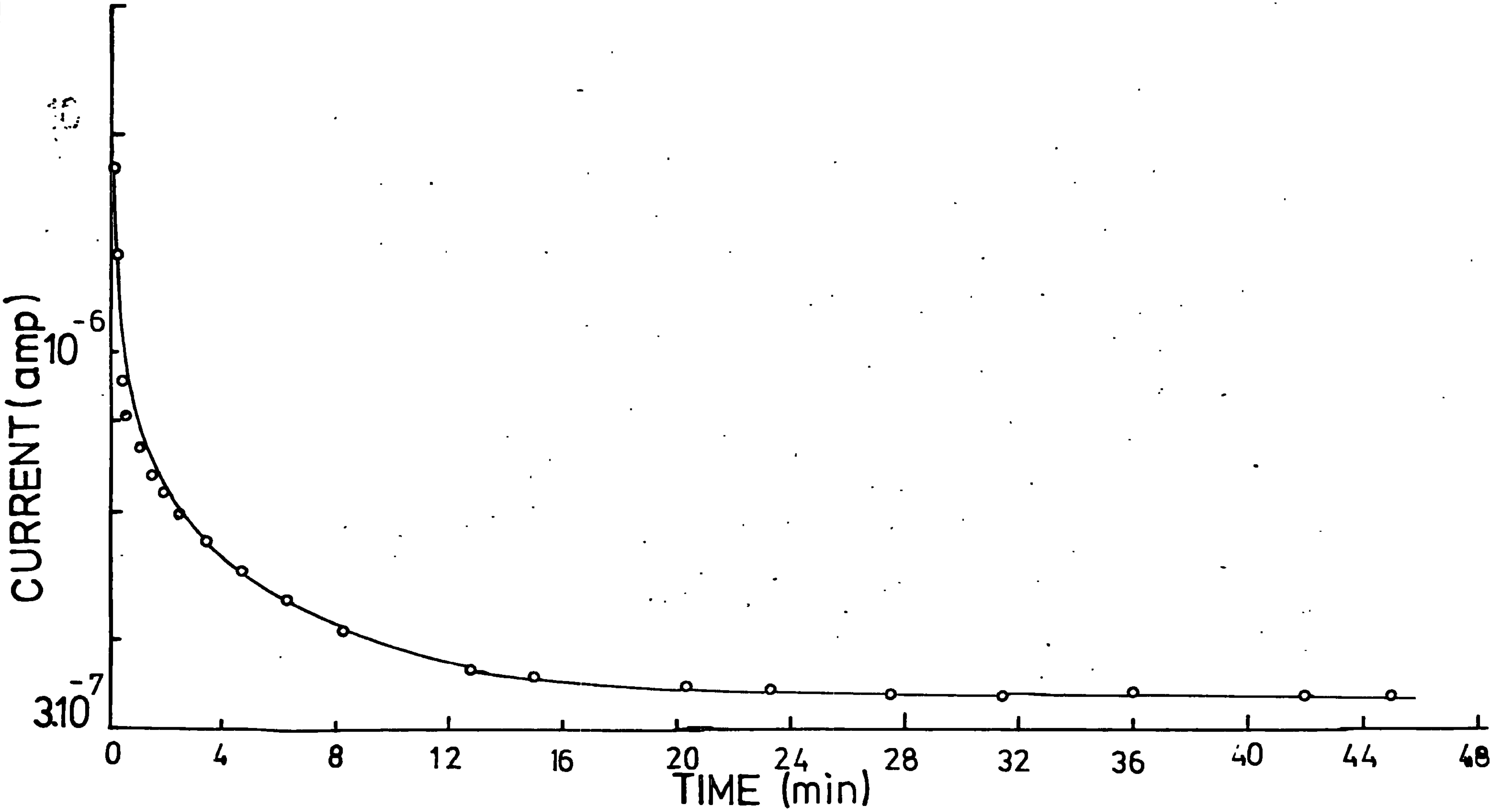

FIG. 3.4. Typical decay of current for z=4 sialon at 841 °C under a constant applied voltage (10V).

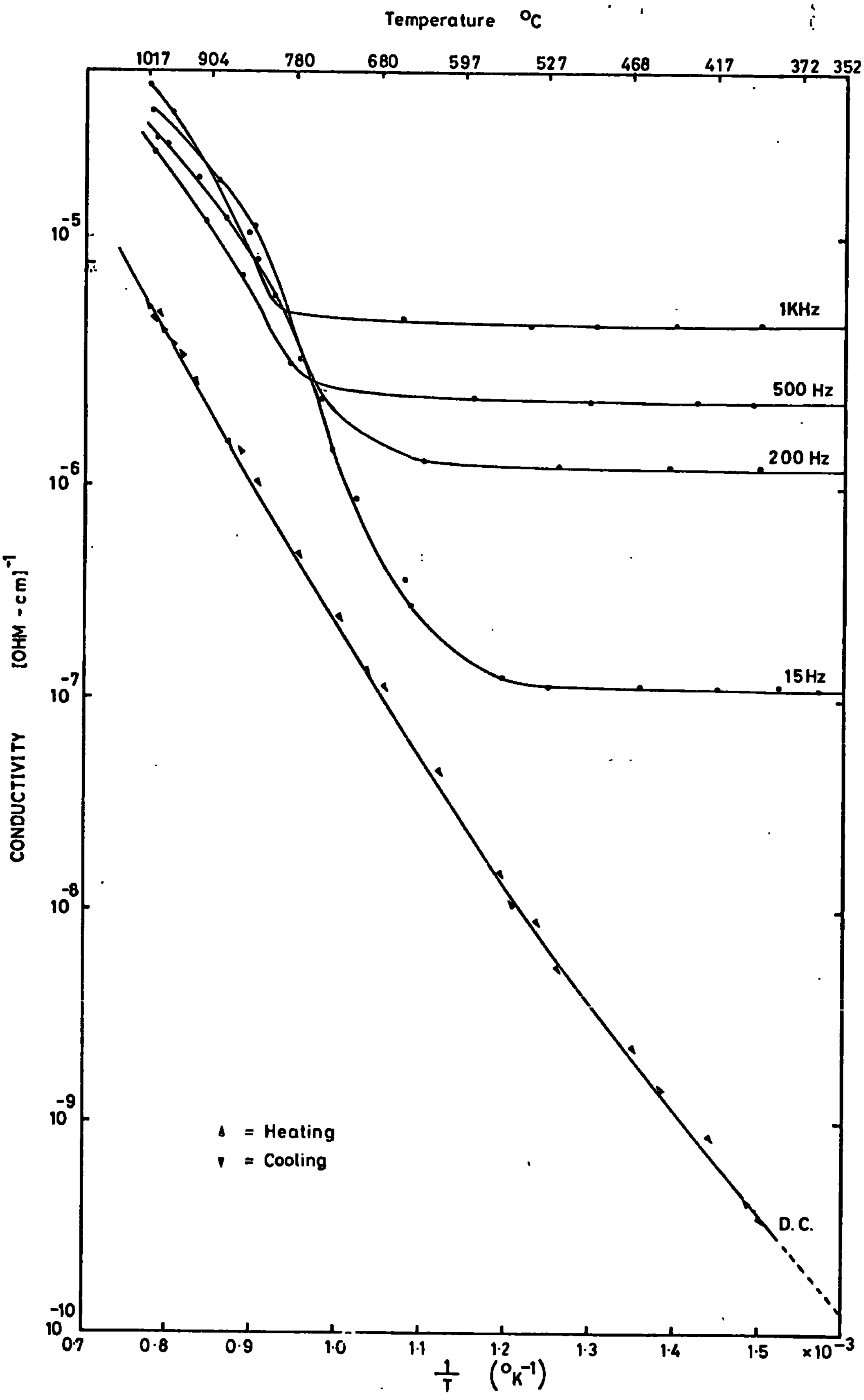

FIG 3.5. Variation of d.c. and a.c. conductivity with reciprocal temperature for hot - pressed Si_3N_4

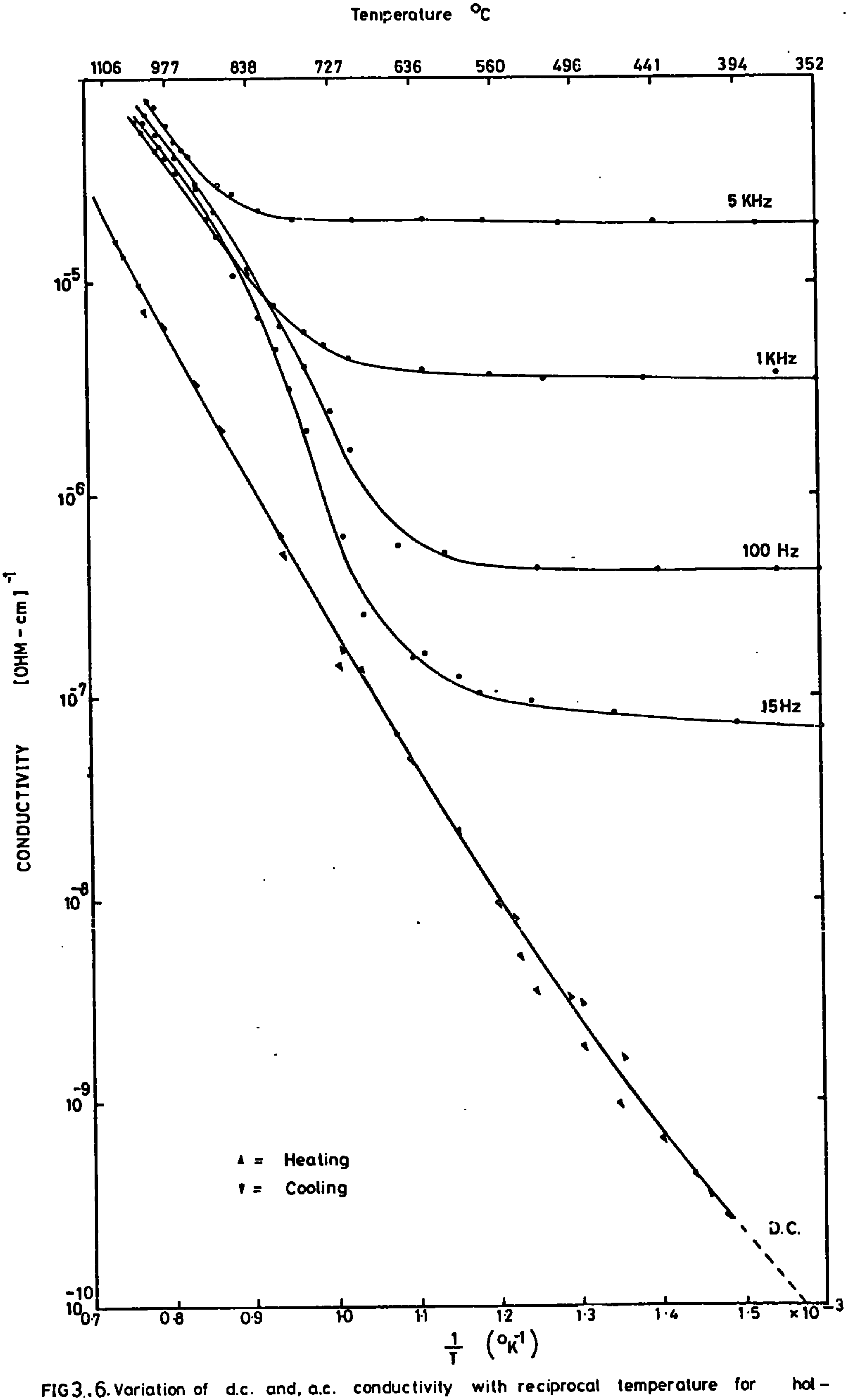

FIG 3..6. Variation of d.c. and, a.c. conductivity with reciprocal temperature for hot-pressed 5 w/o MgO. - Si_3N_4

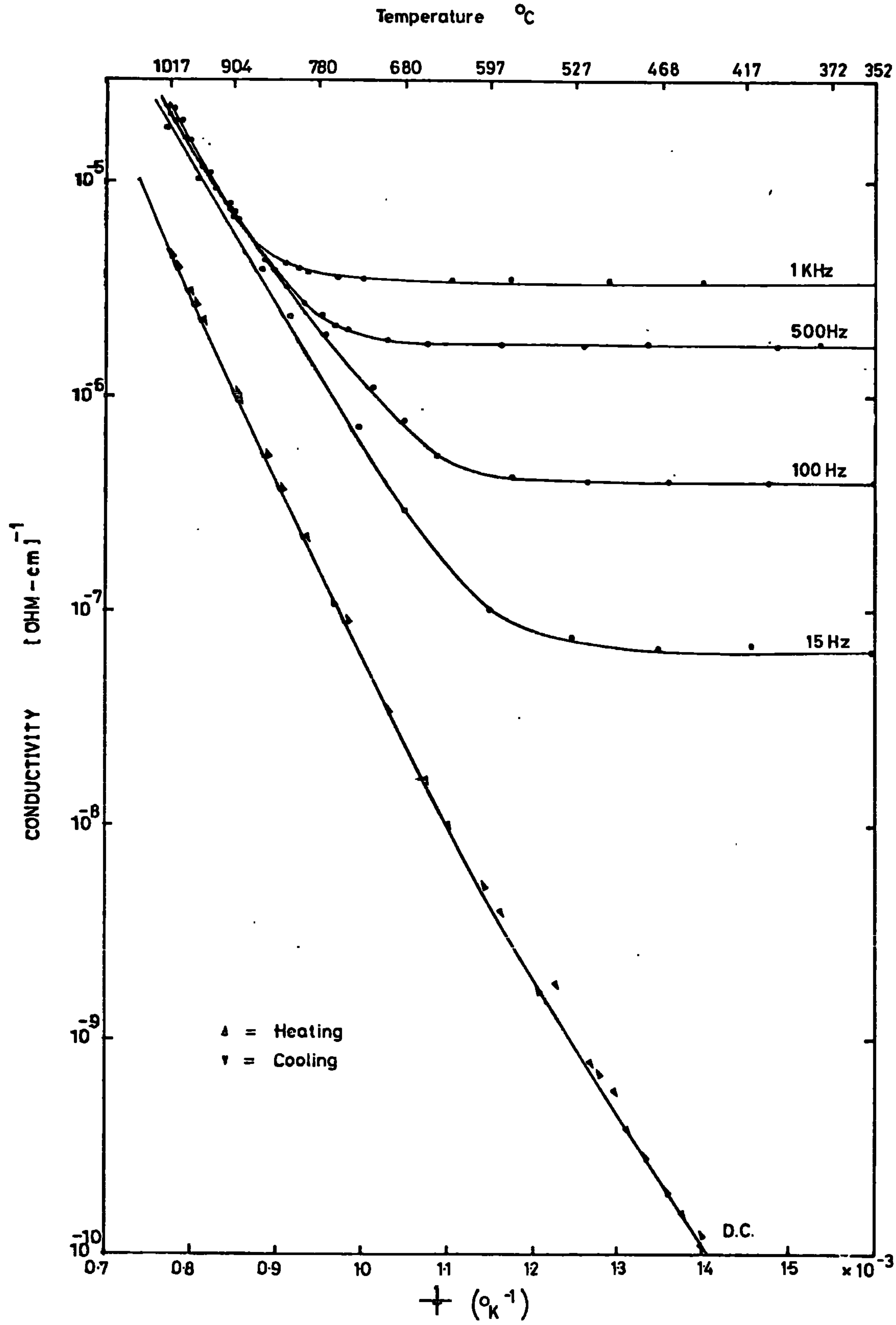

FIG 3.7. Variation of d.c. and a.c. conductivity with reciprocal temperature for hot-pressed z=4 Sialon.

Specimen No.	d.c. Results					a.c. Results		
	Conductivity $(\Omega cm)^{-1}$		Activation energy (eV)		σ_o $(\Omega\ cm)^{-1}$	Activation energy (eV)	n	A
	1000°C	400°C	1000 - 700°C	500 - 400°C	1000-700°C	1000-800°C	468°C	468°C
1. Si_3N_4	$6.5x10^{-6}$	$4.6x10^{-10}$	1.28	0.94	0.77	1.23	0.91	$1.1x10^{-8}$
2. 5W/oMgO/ Si_3N_4	$8.2x10^{-6}$	$2.65x10^{-10}$	1.38	1.01	2.41	1.15	0.93	$6.81x10^{-9}$
3. $Z \simeq 3.2$ sialon	$4.3x10^{-6}$	$9.25x10^{-11}$	1.55	1.05	1.78	-	-	-
4. $Z \approx 4.0$ sialon	$4.0x10^{-6}$	$3.8x10^{-11}$	1.64	1.22	9.50	1.32	0.93	$5.66x10^{-9}$

TABLE 3.1 : Numerical values of conductivities, activation energies and the parameters σ_o, n and A for nitrogen ceramics between 400° C and 1000° C.

$(\sigma_o)$was also calculated from the linear high temperature region (Table 3.1).

The a.c. behaviour shows several features which are common in the results from each of the specimens. In the lower temperature region, (below about 600^o C), the complex conductivity, $\sigma_{ac}(\omega)$ is strongly dependent on frequency but is almost independent of temperature. At higher temperatures $\sigma_{ac}(\omega)$ for a given specimen was found to be the same at all frequencies but it became temperature dependent giving a log $\sigma_{ac} - T^{-1}$ variation very similar to that found for σ_{dc} at high temperatures. The activation energies derived from these high temperatures a.c. results agreed closely with the estimates based on the d.c. data. At low temperatures the activation energy decreases with increasing applied frequencies and decreasing temperatures. It is noticeable that in the high temperature region the a.c. conductivity can also be fitted to a relation of the form of Equation (3.9) and the activation energies so derived are also given in Table 3.1.

3.3.2 HALL EFFECT AND THERMOELECTRIC POWER

No Hall voltage was observed in any of the specimens between 400 and 1000^o C and below 400^o C the high impedance of the specimens preclude measurement by the apparatus available. As the equipment would have detected a Hall voltage of greater than 0.01 µv, this observation implied that the Hall mobility in the specimens was very low. The mobility was estimated from the following data by using the relations (3.6) and (3.7).

$I_x = 4 \times 10^{-10} - 2 \times 10^{-5}$ amps between 400 and 1000^o C ;

$H = 10^4$ gauss ; $t = 0.2$ cm ; $V_H \sim .01$ µv ;

$\sigma_{dc} = 10^{-10} - 5 \times 10^{-6}\ \Omega^{-1}\ cm^{-1}$ between 400 and 1000^o C ;

therefore $$\mu_H = |R_H|\ \sigma = \frac{V_H.\ t.\ 10^8}{H.\ I} \times \sigma_{dc}$$

or $$\mu = \frac{10^{-8} \times .2 \times 10^{8} \times 10^{-10}}{10^{4} \times 4 \times 10^{-10}} = 5 \times 10^{-6}\,\mathrm{cm}^{2}\mathrm{v}^{-1}\mathrm{sec}^{-1} \text{ (at } 400^{\circ}\text{ C).}$$

From this estimation it can be assumed that the mobility of the materials was probably less than $10^{-5}\mathrm{cm}^{2}\mathrm{v}^{-1}\mathrm{sec}^{-1}$ over the temperature range explored.

Some difficulties were encountered in attempts to measure thermoelectric powers. In the first place the voltage, ΔV, developed across the specimen was measured as a function of the temperature gradient, ΔT, at various fixed temperatures between 400 and 1000 °C; in evaluating the data, ΔV was taken to be positive if the hotter electrode was positive. Preliminary measurements showed that even at $\Delta T = 0$ a finite voltage difference (ΔV_o) was observed. As the presence of this prevented actual thermoelectric power determinations an attempt to remove ΔV_o was made by annealing in air at 1000° C for 48 hr. Treatments of this kind have proved successful in overcoming similar effects in potassium chloride (91) and some other materials (92). With the nitrogen ceramics, however, annealing reduced the value of ΔV_o considerably, but did not remove it completely, and thus it was possible only to deduce the sign of the carriers from the sign of ΔV. Some results for Si_3N_4 are given in Fig. 3.8 ; below 900° C the material is p-type and above 900° C it is n-type. Similar behaviour was observed in all the other ceramics examined. The change in the sign of the carriers is revealed also by the temperature dependence of ΔV_o, the voltage developed with zero temperature gradient. This variation is shown for Si_3N_4 in Fig. 3.9 which shows that ΔV_o changes sign near 900° C. Again similar effects were found in the other materials.

3.4 DISCUSSION

The measurements of a.c. conductivity as a function of frequency at low temperatures suggest immediately that hopping processes may be involved. Data was taken from Figs. 3.5 to 3.7 at 468° C, below which temperature $\sigma_{ac}(\omega)$

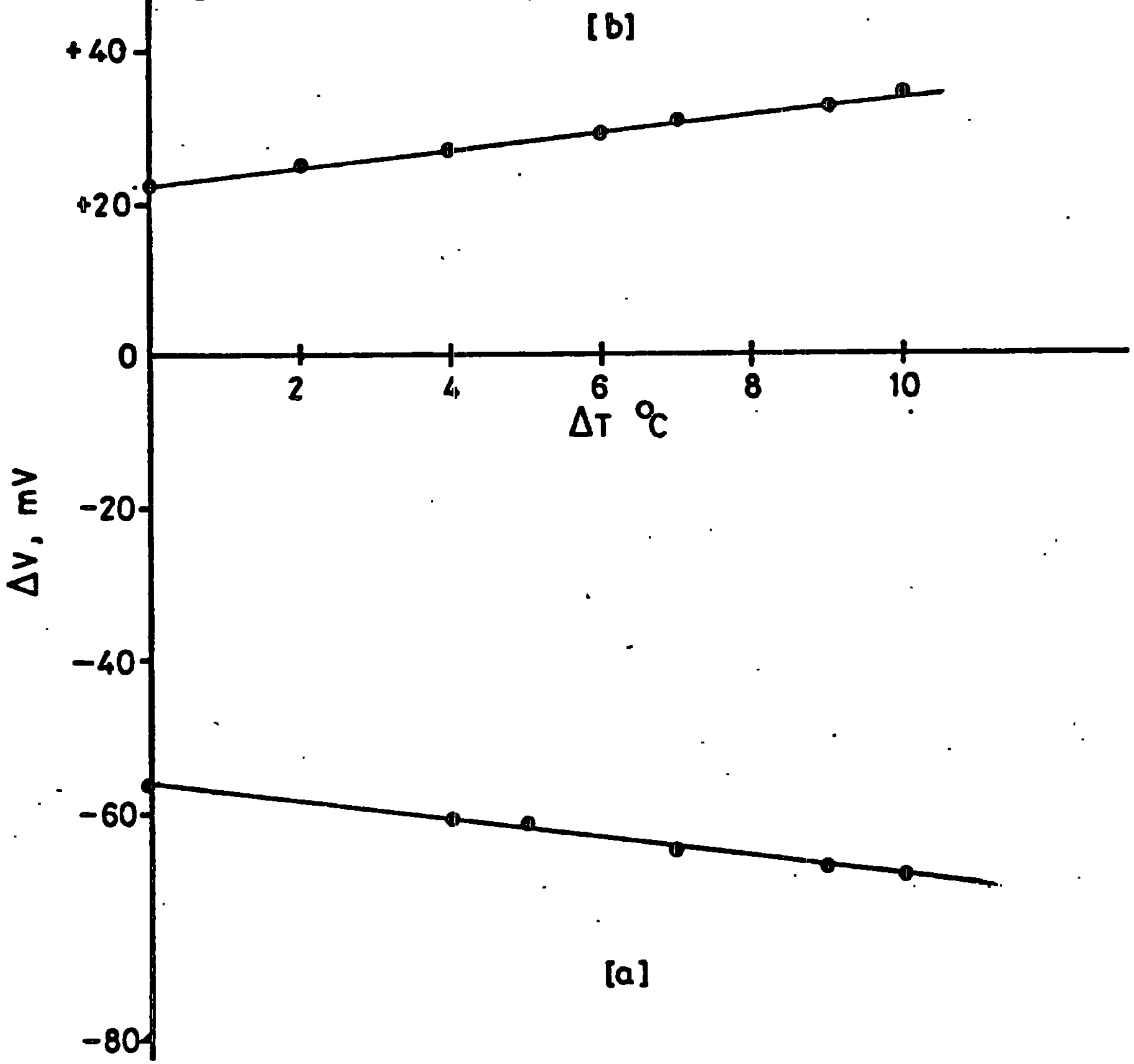

FIG 3.8. Variation of ΔV with temperature gradient ΔT at [a] 690 °C and [b] 932 °C for hot-pressed Si_3N_4.

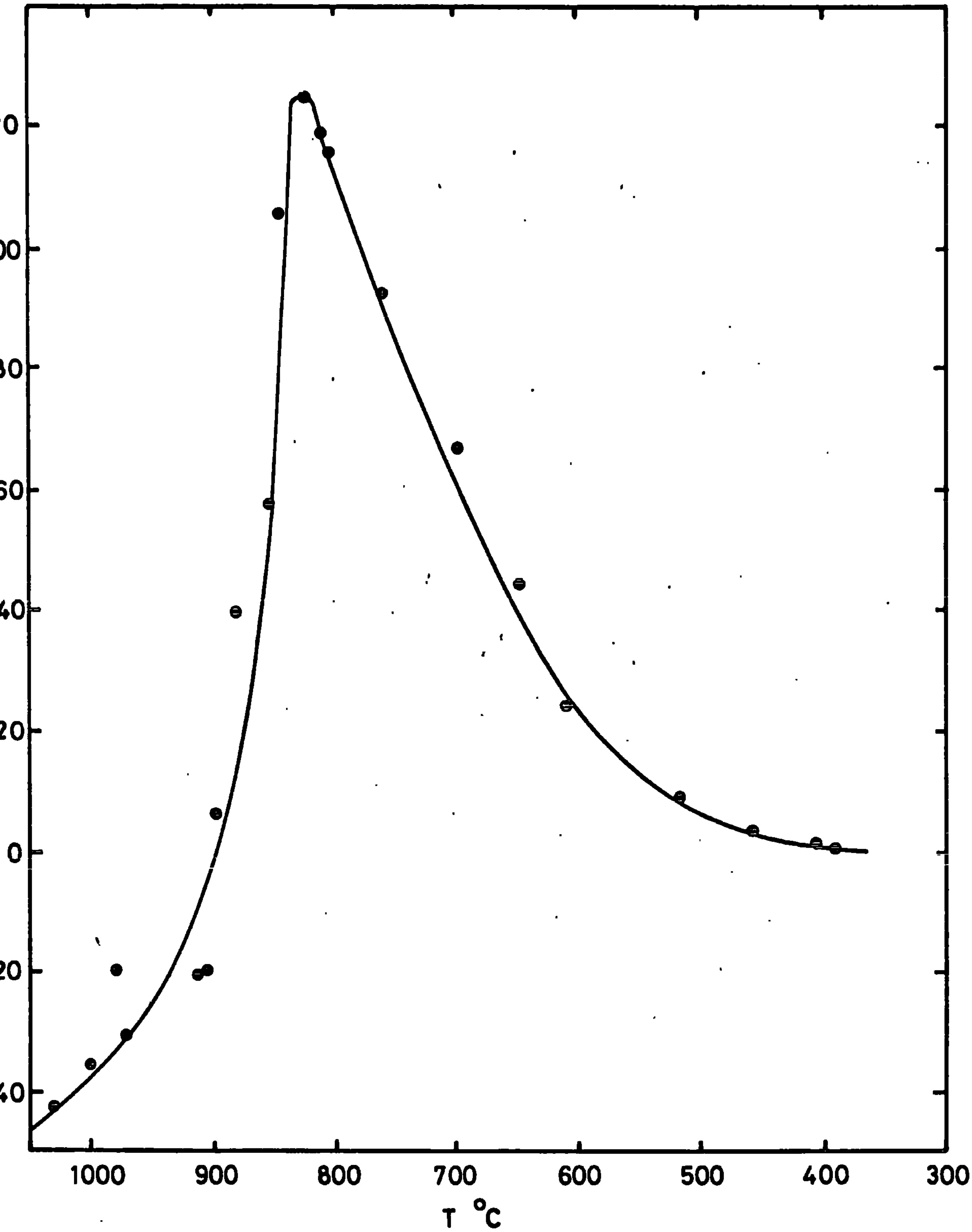

FIG 3.9. Temperature dependence of ΔV_o, for hot-pressed Si_3N_4.

was independent of temperature,and this was used to plot log $\sigma_{ac}(\omega)$ versus ω. As Fig. 3.10 shows, linear variations were obtained for all the materials. In the low temperature range the a.c.conductivity increases with angular frequency ω following a relation of the form (Chapter 2, Sect. 2.6)

$$\sigma_{ac}(\omega) = A.\omega^{n} \tag{3.10}$$

The values of n and A derived from Fig. 3.10 are listed in Table 3.1 and it is found that $n \approx 0.9$. This type of frequency dependence was first observed by Pollak and Geballe (49) for impurity conduction in silicon ; for this material their analysis, based on the assumption that hopping occurred exclusively between pairs of majority impurities, yielded an $\omega^{0.8}$ dependence over several decades of frequency. Similar behaviour has also been observed in many glasses containing transition metal ions (52) and many disordered materials as mentioned in Section 2.6. Austin and Mott suggest that in these glasses the conductivity is due to the presence of ions of more than one valency ; an electron can then pass from one ion to another and the mechanism gives a frequency dependence similar to that for impurity conduction. It may be noted also that in both chalcogenide glasses (93) and other amorphous semiconductors (52,94) values of n in the range $0.7 < n < 1.0$ have been reported. Details of the physical source of this behaviour have been discussed in Section 2.6.

As regards the d.c. conductivity data we find that, for all the specimens, the log σ versus 1/T plots are not linear below about 700° C. The data were plotted in the form of graphs of log σ_{dc} versus $T^{-1/4}$,(Fig.3.11) ; these were straight lines indicating that the variation in $\sigma_{d.c.}$ followed the relation (Chapter 2, Section 2.2)

$$\sigma_{d.c.} = A \exp\left\{-B/T^{1/4}\right\} \tag{3.11}$$

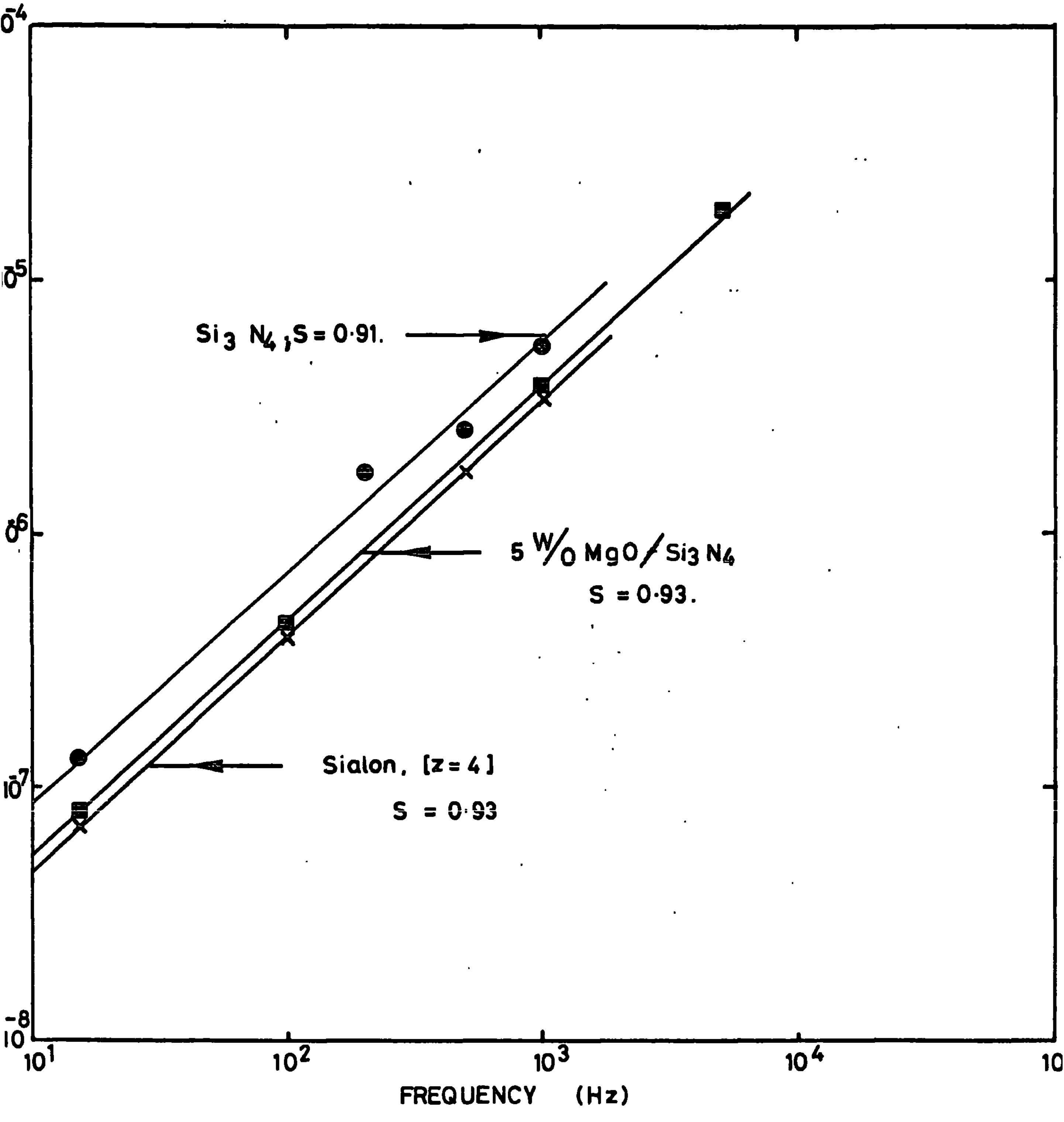

IG 3.10. Frequency dependence of a.c. conductivity for hot-pressed Si_3N_4, 5 W/O MgO/Si_3N_4 and z=4.0 sialon.

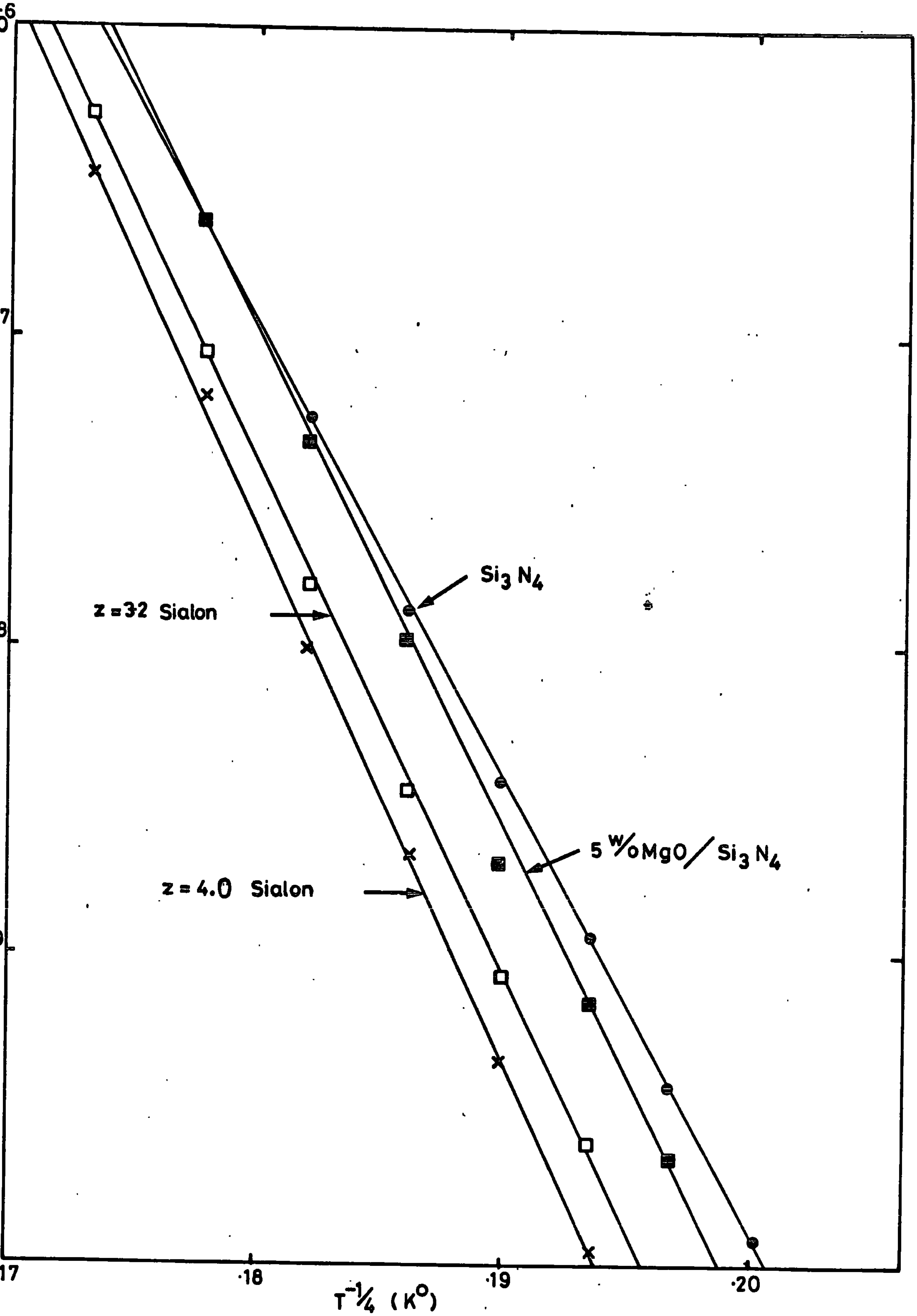

IG 3.11. Variation of σ_{dc} with $T^{-1/4}$ in the low temperature range.

This type of variation has been shown to hold in several substances in which hopping mechanisms occur, e.g. in nickel oxide (52) and in AS_2Se_3 (93) and supports the view that hopping dominates in the nitrogen ceramics in the lower temperature range. This behaviour is further discussed in Chapter 5 in more detail. In the higher temperature region $\sigma_{d.c.}$ and $\sigma_{a.c.}$ both follow a T^{-1} variation which shows that hopping is no longer the dominent mechanism. This behaviour is similar to that of intrinsic materials and the mechanism for both a.c. and d.c. conductivity appears to be the same. It is interesting to note also that here the carriers are n-type as distinct from p-type at lower temperatures. It is known that in semiconducting glasses (95-96) and other amorphous materials the sign of the thermoelectric power is positive in the hopping region. It has also been stated earlier (Chapter 2, Section 2.5) that the change of sign of the carriers at high temperature suggests a transition of the conduction mechanisms which are likely to be associated with localized states and impurity conduction. According to the theory presented in (Chapter 2, Section 2.4) it is known that hopping is one of the usual transport mechanisms in low mobility materials. The very low value of mobility determined from Hall-effect measurements indicates that the conduction mechanism is presumably hopping in the temperature range explored.

The effect of changes in the composition of the materials examined are indicated by Fig. 3.12 which includes for comparison the available data on reaction-bonded ceramics of similar composition. In Si_3N_4, the hot-pressed material has, at all temperatures, a greater conductivity than that of reaction-bonded material (89). The addition of magnesia to silicon nitride (5w/oMgO/Si_3N_4) produced a small decrease in conductivity relative to Si_3N_4 hot-pressed without MgO additive but pre-washed with alkali ; it seems probable that traces of alkali are not completely removed. With the hot-pressed 5w/o MgO/Si_3N_4 the conductivity was an order of magnitude higher than that

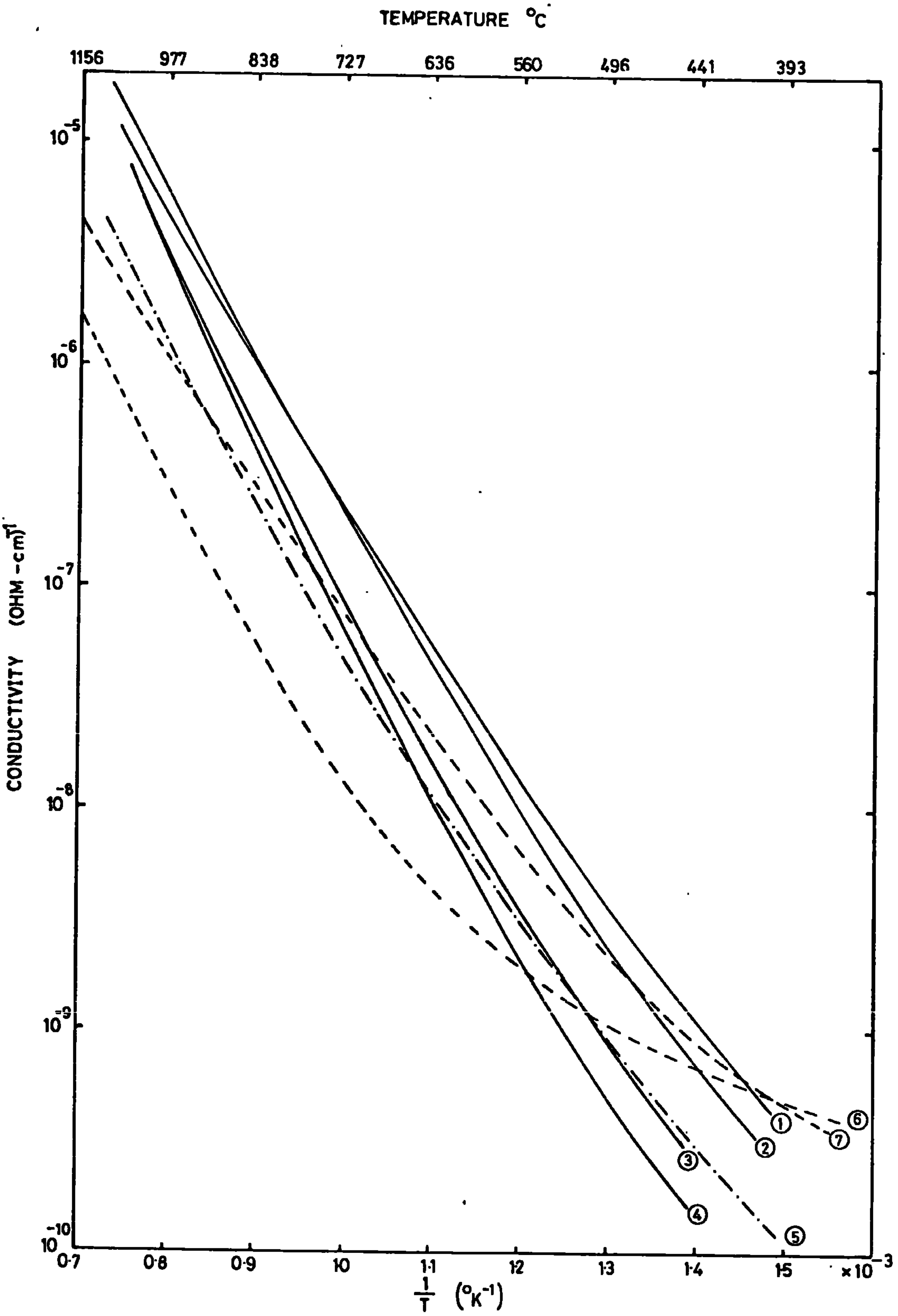

FIG 3.12. Comparison of d.c. conductivity data for hot-pressed and reaction-bonded ceramics. Key :- hot-pressed materials, ① Si_3N_4, ② 5 w/o MgO/Si_3N_4, ③ z = 3·2 Sialon ④ z = 4 Sialon ; reaction bonded materials, ⑤ Si_3N_4, ⑥ 6·72 w/o MgO/Si_3N_4, and ⑦ 16·1 w/o MgO/Si_3N_4.

reported (90)for 6.7w/o MgO/Si_3N_4 made by reaction bonding. As regards the sialons both gave lower conductivities than either the hot-pressed Si_3N_4 or 5W% MgO/Si_3N_4 and the $z \approx 4.0$ sialon had a lower conductivity than the $z = 3.2$ sialon. In the preparation of nitrogen ceramics by hot-pressing techniques there is a likelihood of the formation of a glassy phase ; the presence of such phases has been directly demonstrated by X-ray and electron microscope studies (5,9-12) which have also shown that the materials are not homogeneous and contained both defects in structure and impurities. The occurrence of a thermoelectric electromotive force at zero temperature gradient, (which has also been reported elsewhere (91), supports the view that the materials contain uneven distributions of impurities. It is likely that the reaction-bonded ceramics would contain a smaller amount of glassy phase than the hot-pressed materials. If the glassy phase had a relatively high conductivity, as might be expected, this could account for the higher observed conductivities of the hot-pressed materials. Alternatively, this higher value of $\sigma_{d.c.}$ could have been due to the presence of surface contribution which could not be reduced in this technique of measurements (Fig. 3.1). Conductivity measurements, using more refined techniques, are described in Chapter 5. All the electrical properties presented here appear to be consistent with the presence of a glassy phase and impurities, and it seems probable that these determine the conductivity behaviour.

CHAPTER 4

DIELECTRIC PROPERTIES

4.1 INTRODUCTION

The series of measurements described in Chapter 3 were not completely unambiguous in so far as the measurements made were of complex conductivity, $\tilde{\sigma}(\omega)$. It is known from theory that when an a.c. voltage is applied across a specimen at any particular frequency, the resultant current through the specimen is a function of admittance, $\gamma(\omega)$. The complex conductivity $\tilde{\sigma}(\omega)$ is defined as follows, $\gamma(\omega) = G_p(\omega) + i\omega C_p(\omega) = A\tilde{\sigma}(\omega)$ where $G_p(\omega)$ and $C_p(\omega)$ are the equivalent parallel circuit conductance and capacitance, respectively, while A is a geometrical factor equal to the electrode area divided by length in the case of a rectangular specimen. The complex conductivity $\tilde{\sigma}(\omega)$ can be expressed as $\tilde{\sigma}(\omega) = \sigma_{dc} + i\omega\varepsilon(\omega) = \sigma_{dc} + \sigma'(\omega) + i\omega\varepsilon'(\omega)$ where σ_{dc} is d.c. conductivity and $\sigma'(\omega)$ is the "pure" alternating current (ac) conductivity, related to the dielectric loss through $\sigma'(\omega) = \varepsilon_o\omega\varepsilon''(\omega)$. Therefore, the previous measured conductivity contained all types of current component. Moreover, the surface contribution to bulk conduction could not have been reduced in that type of electrodes arrangement. The conductivity was also measured only over a limited range of frequency (15 Hz to 5 Hz) at temperatures between 400° C and 1000° C.

Dielectric measurements on the other hand permit the separate determination of the real and imaginary parts of the conductivity and so allow a more reliable comparison with theory to be made. Several theories of hopping conduction (Chapter 2, Sect. 2.6), for example those of Pollak (49-50), and Mott and Davis (18), indicate that a frequency dependence of the real part of the conductivity following a $\text{Re}\sigma(\omega) \propto \omega^n$ law should be observed where $n < 1$. Caution should be used before interpreting all cases of rising conductivity with frequency as evidence of hopping conduction. Similar relations may be observed for various dielectric loss mechanisms (24, 97-98). It is necessary to measure the $\mathrm{Re}\,\sigma(\omega)$ over a wide frequency range (between sub-audio and microwave frequencies) to take into account this behaviour. More recently Jonscher (80-82) has suggested that several hopping models may lead to the ω^n law and has shown further that a wide range of materials follow the universal dielectric laws' according to which $\varepsilon''(\omega) = \frac{\sigma'(\omega)}{\varepsilon_o \omega} \alpha\ \omega^{n-1}$ and $(\varepsilon'(\omega) - \varepsilon_\infty) \alpha\ \omega^{n-1}$ where again $n < 1$. The value of n is also a function of temperature and decreases with increasing temperature. This behaviour is characteristic of either non-Debye dipolar or hopping charge carrier (ionic or electronic) systems.

Some data on dielectric constant, ε' and tanδ of reaction bonded silicon nitride are found in (89, 99). The values of ε' = 5.8, 7.2 and 9.4 and tanδ = 2×10^{-2} are mentioned in (99). Walton (100) found the value of ε' ∿ 5.6 and tanδ ∿ 2×10^{-3} for reaction sintered Si_3N_4 over the frequency range 8-10 GHz at temperatures up to 800^o C. He suggested that this material could be produced with satisfactory dielectric properties for high temperature radome applications. Andreeva et al (90) reported the measurements on ε' and tanδ of the system MgO-Si_3N_4 (reaction bonded material) over the frequency range 50 KHz to 30 MHz at room temperature. The values of ε' and tanδ in for example 20 m/o MgO - 80 m/o Si_3N_4 were in the range of 8.4-6.8 and $4.7 \times 10^{-3} - 1 \times 10^{-3}$ respectively ; and decreased with increasing frequency. They pointed out that the frequency dependence of tanδ was complicated character due to inhomogeneous specimens containing several phases.

The work described in this Chapter was to establish the frequency variations of dielectric constant and loss over a wide frequency range. Although the majority of the measurements were made at room temperature a preliminary study was also made of the temperature dependencies of the frequency variations.

4.2 EXPERIMENTAL

The specimens examined in this investigation were of the same compositions as studied previously (Chapter 3). Most of the specimens were supplied as discs from which thin plates were cut with a diamond wheel cutting machine ; the large area faces of the specimens were polished to a 0.25 micron finish using a precision polishing machine. Specimens were typically 15 mm x 15 mm x 0.3 mm and circular gold electrodes of 1 cm diameter were evaporated on to the opposite polished faces to ensure good electrical contact. In this electrode arrangement, the bulk path length (thickness) for current flow was made much shorter than the surface path length (Fig. 4.1 (a)).

4.2.1 BRIDGE METHOD

The dielectric properties of the specimens were measured over the frequency range 200 Hz to 50 KHz using a Wayne-Kerr bridge (Type B.224) at room temperature and at high temperatures up to 500° C. At room temperature, a dielectric testing jig, made with perspex insulators, was used to hold the specimen during measurements (Fig. 4.1 (b)). In this method, the bridge was first balanced to reduce the capacitance and conductance present in the circuit (without mounting specimen in the dielectric jig). The specimen was then inserted between the electrodes (Fig. 4.1 (b)) and the measurements were made. The conductance , G and capacitance, C, were determined directly as functions of applied frequency and the data was used to derive the real part of the conductivity (Reσ), the loss tangent (tanδ) and the dielectric constant (ε') from the relations (101)

$$\mathrm{Re}\sigma\ (\omega) = \frac{d}{A} \cdot G \tag{4.1}$$

$$\tan\delta = \frac{G}{\omega C} = \frac{\varepsilon''}{\varepsilon'} \tag{4.2}$$

and

$$\varepsilon'(\omega) = \frac{C}{\varepsilon_0} \cdot \frac{d}{A} \tag{4.3}$$

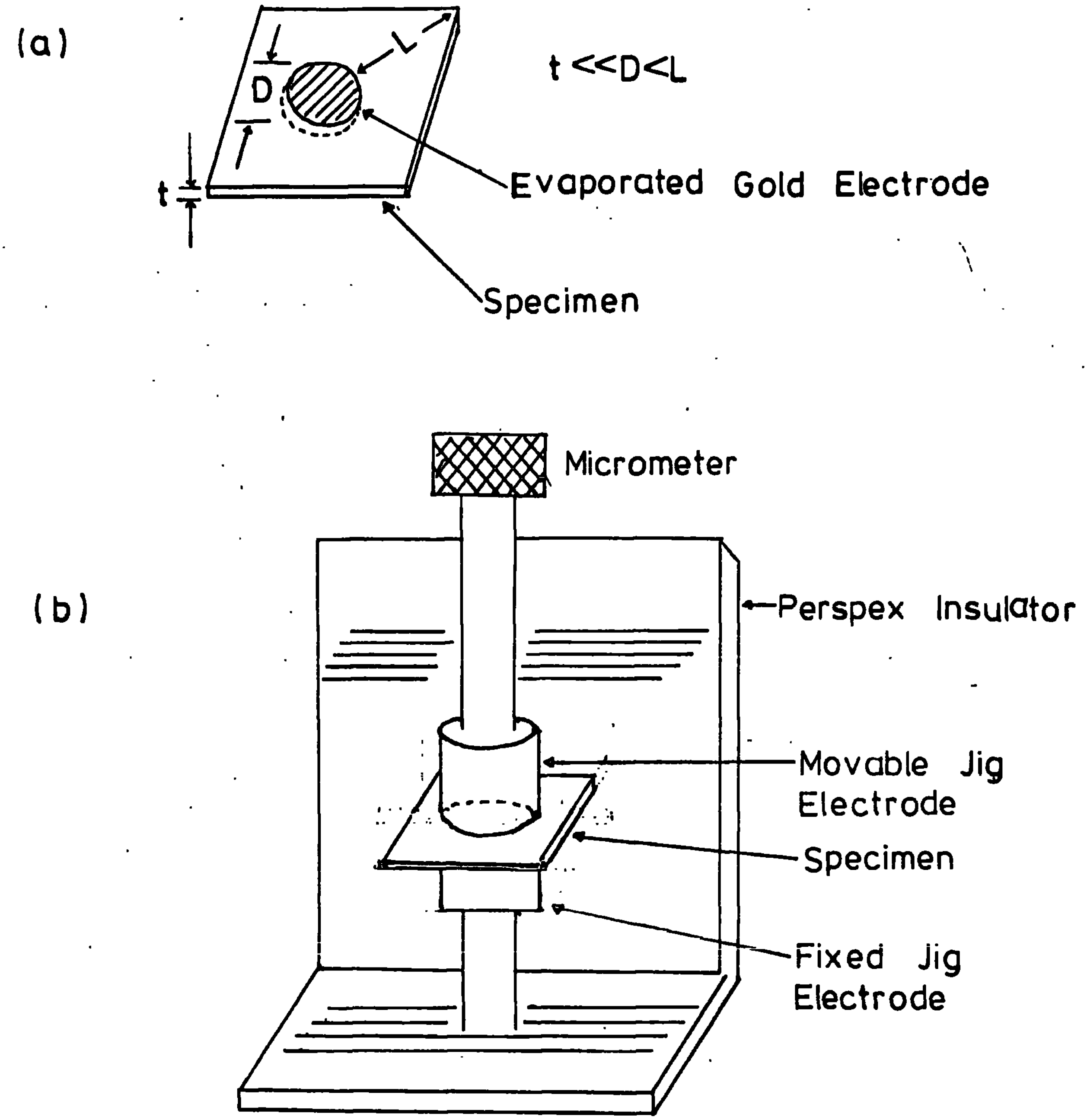

FIG. 4.1.(a) Electrode arrangement to minimize contributions from surface conduction.
(b) Dielectric jig for measuring dielectric properties at room temperature.

where ω is the angular frequency, d the specimen thickness in centimetres and A the area of the electrode in square centimetres. The ε_o is called the permittivity of free space having a value of 8.85×10^{-14} F/cm. In all the specimens both G and C decreased slightly with time (by about 1%) from their initial values at frequencies below 5 KHz but attained equilibrium values within ten minutes. In the present experiments, the specimens were cut in the form of square plates which projected beyond the circular jig electrodes. Due to this, an edge correction for dielectric constant was applied using an edge correction formula (102). In this method, equation (4.3) was modified by

$$\varepsilon' = \frac{C}{C_o + C_e} \qquad (4.4)$$

where
$$C_e = \frac{1.113D}{8\pi}\left[\ln \frac{8\pi D}{d} - 3\right] \qquad (4.5)$$

and
$$C_o = \varepsilon_o \cdot \frac{A}{d}$$

in which D is the diameter of each electrode in centimetres. The overall accuracy of the measurements was ± 6%.

The high temperature measurements were made in air with a specially designed jig and furnace arrangement in which the insulator supporting the electrodes, located external to the furnace, could be kept cool (Fig.4.2). Particular care was necessary both in furnace design and in shielding in order to minimize pickup signals due to thermal noise and the atmosphere around the specimens. The measurements were made over the frequency range 500 Hz to 50 KHz and the parameters G and C were found, at any particular frequency, first at room temperature and then as the specimen was heated. For temperatures below 150° C it was found that on returning to room temperature G and C had both increased by about 5% ; these effects, attributed

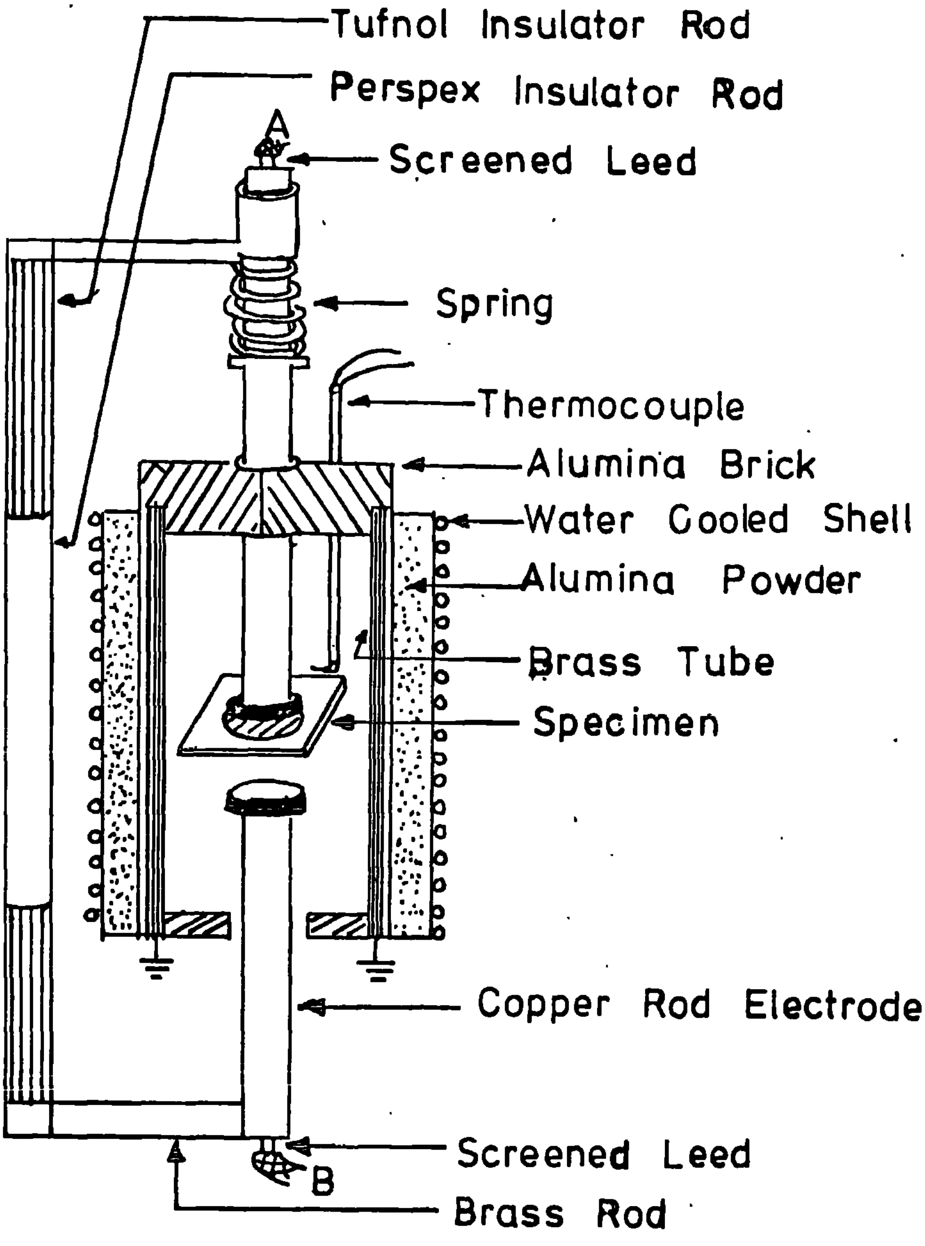

FIG.4.2. Apparatus for measuring dielectric properties at high temperatures.

to space charge (Chapter 3, Sect. 3.3.2), were overcome by heat treating the specimens in air for 12 hours at 65° C between successive measurements at different frequencies.

4.2.2 Q-METER METHOD

The high frequency measurements were made in air at room temperature over the frequency range 100 KHz to 75 MHz, using a standard Q-meter (Marconi TF 1245) and two oscillators (Marconi TF 1246 and 1247). The same dielectric testing jig and the specimens of similar type to those described above, were used also in this technique. The capacitance and Q-value were measured firstly with the specimen mounted in the jig and secondly (at the same electrode spacing) without the specimen under resonance conditions at a constant applied frequency. The difference in capacity was a function of dielectric constant, and the change in Q-value was a function of the loss factor of the specimen. The process of measurement was then used at different applied frequencies. The data was used to derive the dielectric parameters from the corresponding set of relations (103-104)

$$\left.\begin{aligned} \varepsilon'(\omega) &= \frac{C_1 - C_2}{C_o} + 1 \\ \left\{ C_o \right. &= \left. \varepsilon_o \cdot \frac{A}{d} \right\} \end{aligned}\right\} \qquad (4.7)$$

$$\left.\begin{aligned} \tan\delta &= \frac{Q_1 - Q_2}{Q_1 \cdot Q_2} \cdot \frac{C_1}{C_1 - C_2} = \frac{\varepsilon''}{\varepsilon'} \\ \text{and} \quad \mathrm{Re}\,\sigma(\omega) &= \frac{d}{A} \cdot \frac{1}{R} \\ \text{where } R &= \frac{Q_1 \cdot Q_2}{Q_1 - Q_2} \cdot \frac{1}{\omega} \cdot \frac{1}{C_1} \end{aligned}\right\} \qquad (4.8)$$

in which C_1 and C_2 and Q_1 and Q_2 are the capacitances in micro-micro farads and Q-values observed by the Q-meter at resonance respectively without and with the specimen. At higher frequencies a correction was applied for circuit inductance (L_R) using the relation (103)

$$C \text{ effective} = \frac{C^*}{1 + \omega^2 L_R C^*} \tag{4.9}$$

where C^* refers to C_1 and C_2 in turn and L_R = 2.8 mμH ; this correction amounted at most to about 8%. Q-meter measurements were not possible above 75 MHz because of the difficulty in obtaining sufficiently thin, large diameter specimens. An edge correction for dielectric constant was also applied in this technique using a similar edge correction formula (102). Equation (4.7) was modified by

$$\varepsilon' = \frac{C_1 - C_2}{C_o + C_e} + 1 \tag{4.10}$$

where the parameters C_o and C_e were already defined in Section 4.2.1. This correction term was amounted to ± 5%.

4.2.3 MICROWAVE METHOD

Some measurements were also made at 9.3 GHz by the perturbation method using a resonant type cavity (105-108).

In general, perturbation methods are utilized in studying the effects of a small change, i.e. when a resonant cavity is perturbed by the introduction of a small dielectric specimen its resonant frequency is lowered. The change in frequency is a function of the dielectric constant, ε' and the change in cavity Q is a function of the loss factor, ε" of the material. The quantities which must be measured are the resonance frequency and the loaded Q of the cavity without and with the dielectric sample respectively. The results of the perturbation theory are expressed in the form (105-106)

$$\frac{\Delta f}{f_o} - \frac{j\Delta}{2}\left\{\frac{1}{Q}\right\} = \frac{(\varepsilon-1)\int_{V_s} E_o E_s dV}{\int_{V_o} E_o^2 \, dV} \tag{4.11}$$

where $\Delta f = f_o - f_s$ = difference in cavity frequency without and with sample.

f_o = resonant frequency of empty cavity

V_s = volume of sample

V_o = volume of cavity

E_o = microwave field strength in empty cavity

E_s = microwave electric field strength inside sample

Q = loaded Q of cavity

$\varepsilon = (\varepsilon' - j\varepsilon'')$ = relative (complex) dielectric constant of the sample

For a rectangular or cubical cavity operating in the TE_{10n} mode equation (4.11) can be reduced in the form (106-107)

$$\left.\begin{aligned} \frac{\Delta f}{f_o} &= 2\,(\varepsilon' - 1)\,.\,\frac{V_s}{V_o} \\ \text{or } \varepsilon' - 1 &= \frac{1}{2}\,.\,\frac{\Delta f}{f_o}\,\frac{V_o}{V_s} \end{aligned}\right\} \tag{4.12}$$

$$\left.\begin{aligned} \Delta\left\{{}^{1}/_{Q}\right\} &= 4\varepsilon''\,\frac{V_s}{V_o} \\ \text{or } \varepsilon'' = \frac{\mathrm{Re}\sigma}{\omega\varepsilon_o} &= {}^{1}/_{4}\,.\,\frac{V_o}{V_s}\left\{\frac{1}{Q_s} - \frac{1}{Q_o}\right\} \end{aligned}\right\} \tag{4.13}$$

$$\text{and } \tan\delta = \frac{\varepsilon''}{\varepsilon'} \tag{4.14}$$

where ε', ε'' and $\mathrm{Re}\sigma$ are the dielectric constant, the dielectric loss and the real part of conductivity (ohm^{-1} cm^{-1}) of the same respectively.

In this method the following conditions should be satisfied

(i) the Q of the cavity must be greater than 2,000

(ii) $\Delta f/_{fo}$ must be smaller than 0.005

(iii) the ratio of the volume of the specimen to cavity should be less than 1/20.

A cubical cavity, whose internal dimension was 2.23 cm, was made of copper (Fig. 4.3). The Q of the cavity was about 2640. The specimen whose dimensions were typically 5 mm x 5mm x 1mm, was mounted at the centre of the cavity with the help of a quartz rod in order to locate it at a position of maximum electric field. The choice of cavity was partly determined by the available shape and size of the specimen to be used and also to satisfy the conditions of the perturbation method described above. The block diagram of the microwave apparatus is shown in Figure 4.4. The modulated microwave power from a klystron source was allowed to pass to the cavity through a coupling hole. The incident and reflected power traces were displayed on dual beam oscilloscope with respect to the klystron mode from the output of the crystal detectors X_1 and X_2 respectively (Fig. 4.4). The resonance curve of the cavity was monitored by adjusting the frequency tuner and reflector voltage of the klystron. The incident power trace was used to measure the frequencies of the resonance curve using a calibrated wavemeter. The resonant frequency of the cavity was found by marking the wavemeter absorption marker to the maximum amplitude peak point of the displayed resonance curve and the frequency interval f_1-f_2 between the 3 db points respectively of the curve were also noted in a similar way. These results were used to calculate the Q-value of the cavity from the relation $Q = {}^{f}o/_{f_1-f_2}$. The quartz rod was first inserted up to the centre position of the cavity through a hole (Fig.4.3) and its actual length inside the cavity was marked carefully. The resonant frequency f_o and Q_o of the cavity with the rod in position was measured. The specimen with rod (exactly of the same length as marked before) was then

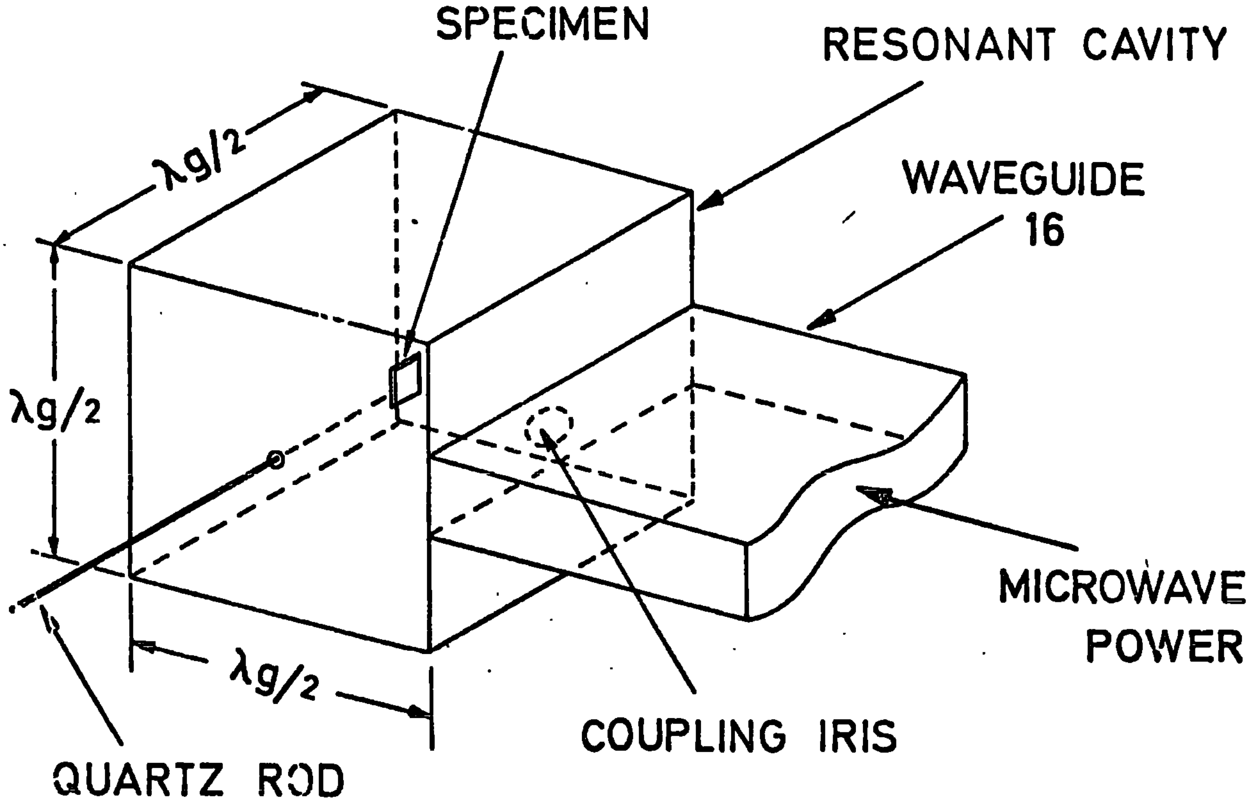

FIG.4.3 Cavity and specimen arrangement for measurement of dielectric properties at 9·3 GHz

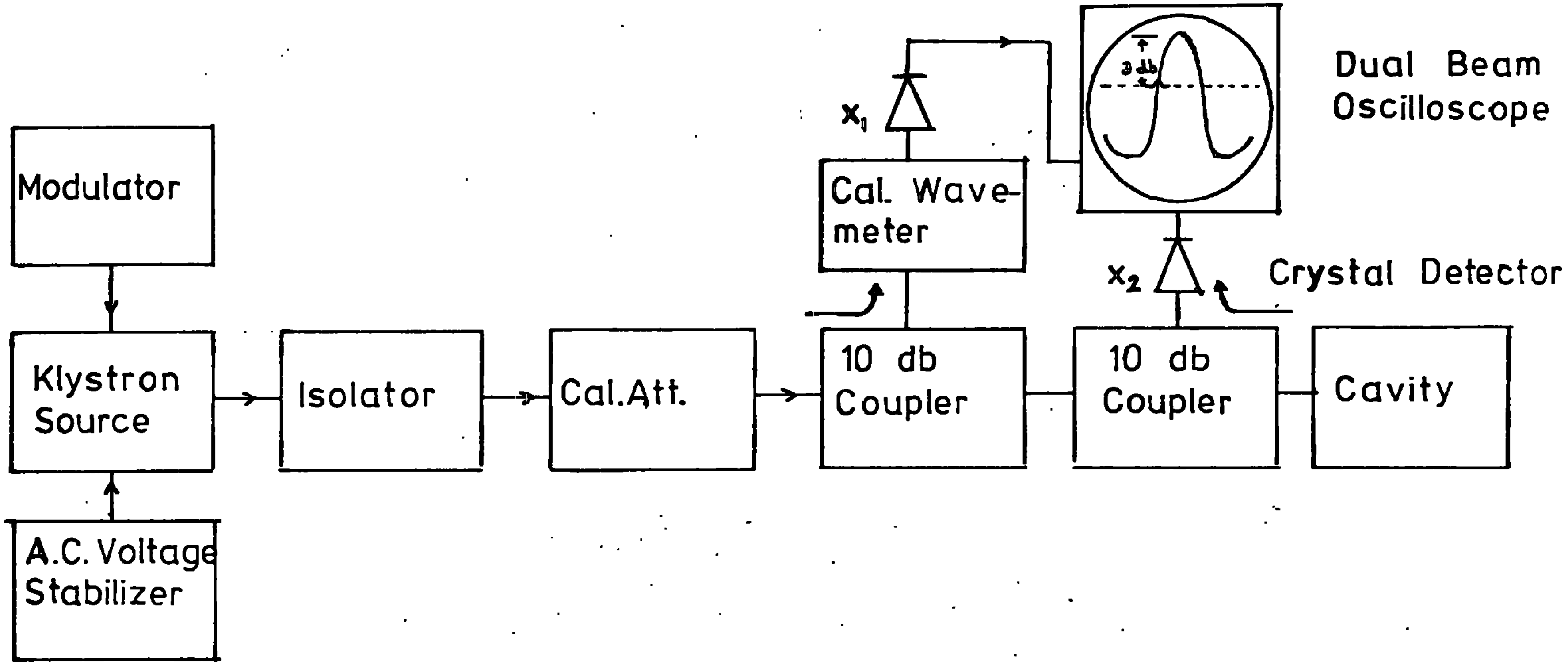

FIG 4.4 Schematic diagram of microwave apparatus for measuring dielectric properties at room temperature.

placed at the centre of the cavity. The shifts of the corresponding resonant frequency f_s and Q_s were noted. The measurements were then repeated several times. The values of f_o, $\Delta f = f_o - f_s$, Q_o and Q_s were noted carefully and the data was used to derive the dielectric parameters from the equations (4.12, 4.13 and 4.14). The estimated accuracy of the microwave results, all of which were made in air at room temperature, was ± 10%.

4.3 RESULTS

4.3.1 ROOM TEMPERATURE DATA

It was found that the frequency variations of conductivity, $\mathrm{Re}\sigma(\omega)$, dielectric constant, ε' and loss, $\tan\delta$ were very similar in both form and magnitude for all three materials. The conductivity variation, derived directly from the experimental data assuming, as proved below, that the d.c. contribution was negligible, is shown by the full lines of Figure 4.5. Over the frequency range 200 Hz to 5MHz, this fits well with the relation

$$\mathrm{Re}\sigma\,(\omega) \quad \alpha \quad \omega^{n} \qquad (4.15)$$

where n has the value 0.9. Several authors (e.g. 77,82) have noted that high frequency bridge and Q-meter measurements may be misleading because of the effects of small series resistances or inductances originating in the contacts and leads to the specimen. Here it is noticeable that the data obtained by the microwave cavity technique, (which is free from this shortcoming) lies close to the extrapolation of the low frequency variation. Thus the apparent ω^2 variation above 5 MHz appears to be spurious and the experimental data is interpreted as indicating that a $\omega^{0.9}$ variation holds over the whole frequency range from 200 Hz to 9.3 GHz.

The observed variations of ε' and $\tan\delta$ with frequency are shown by the full lines of Figures 4.6 (a) and (b). The values of both ε' and $\tan\delta$

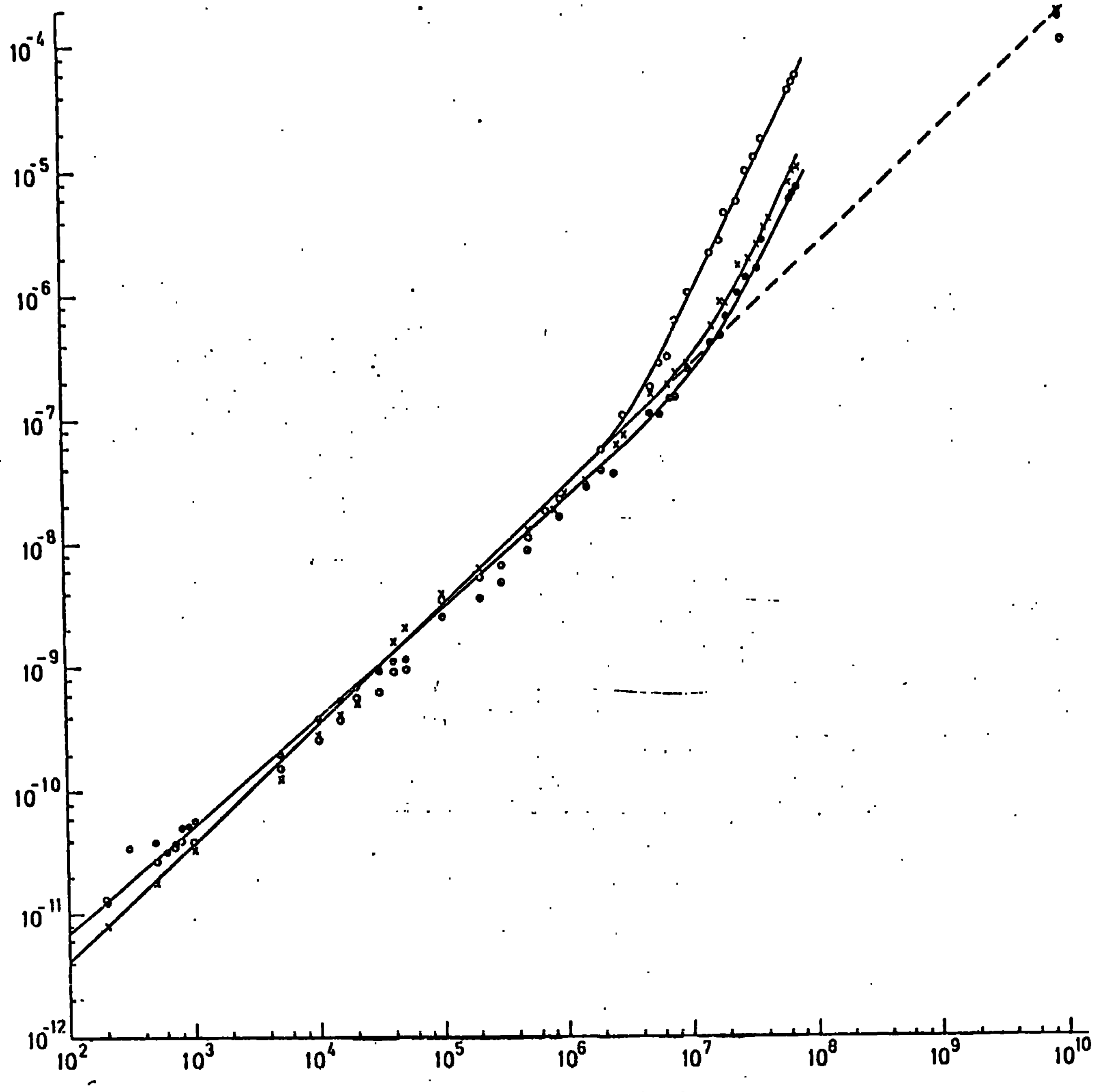

FIG. 4.5 The frequency dependence of the real part of the conductivity, Reσ for Si_3N_4 (•), z = 4 sialon (×) and 5 W/o MgO/Si_3N_4 (∘) at room temperature.

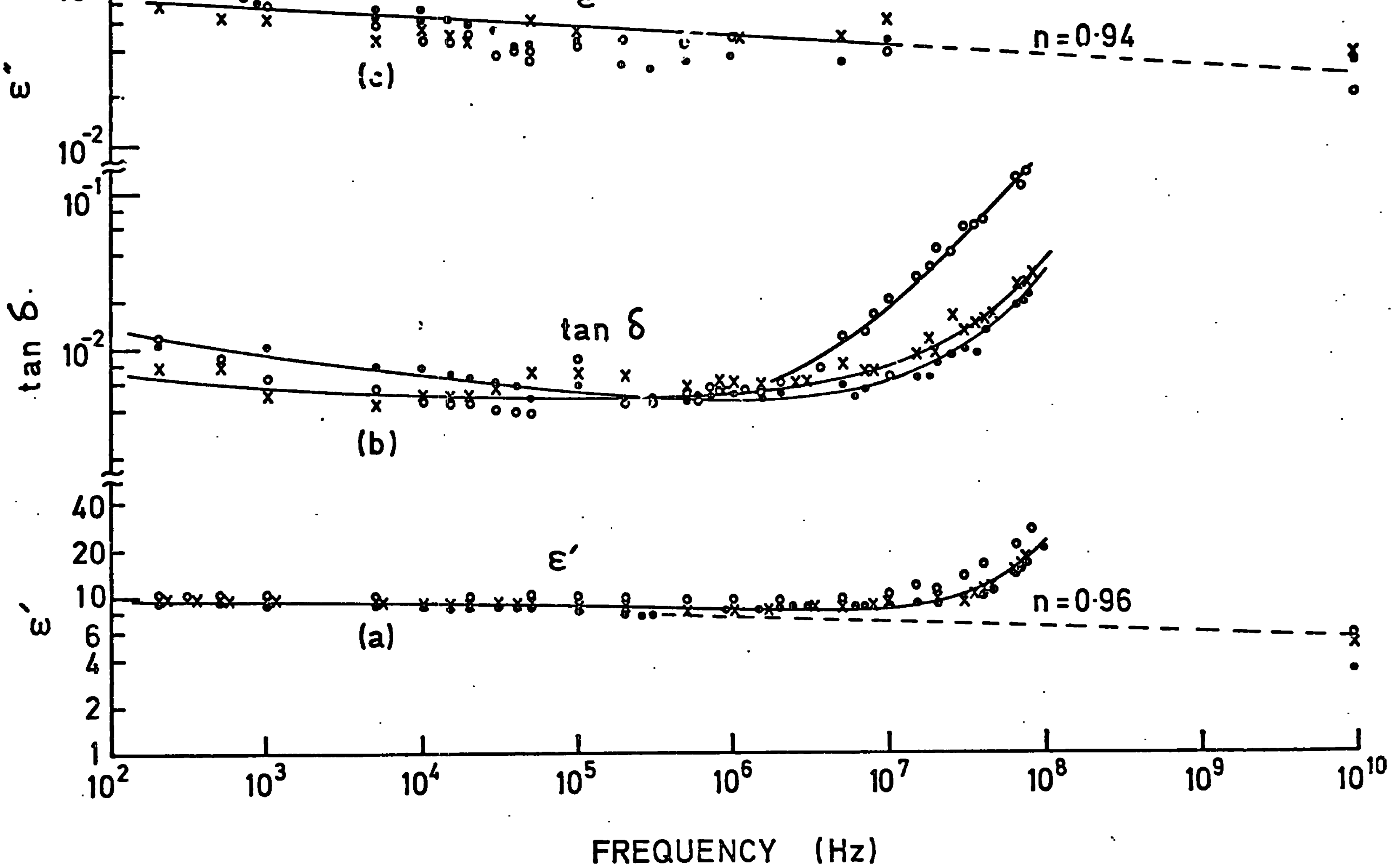

FIG. 4.6 The frequency dependence of dielectric loss, ε'', tan δ and dielectric constant, ε', for Si_3N_4 (•), 5 w/o MgO/Si_3N_4 (∘) and z = 4 sialon (x) at room temperature.

decrease slightly with increasing frequencies up to about 5MHz. The experimental Q-meter data shows increases in both above 5 MHz, and these apparent rises are again thought to be spurious because the microwave data fits reasonably well on the extrapolation of the low frequency ε' variations. There is good agreement between the present data and that reported (Table 4.1) on reaction bonded materials of similar composition. The variation of $\varepsilon''(\omega)$ with frequency was derived from Figure 4.5 by the relation $\varepsilon''(\omega) = \frac{\mathrm{Re}\sigma(\omega)}{\omega\varepsilon_o}$, assuming linear variation in each case ; this is given in Figure 4.6 (c).

4.3.2 HIGH TEMPERATURE DATA

Because of the occurrence of errors in the high frequency measurements noted above, measurements were restricted to frequencies below 10^5 Hz. Figure 4.7 illustrates the type of temperature dependence found for both σ_{dc} and $\mathrm{Re}\sigma(\omega)$; it refers specially to the Z = 3.2 sialon, but the other two ceramics (Si_3N_4, 5 W/o MgO/Si_3N_4) gave similar results though with less good linearity in Arrhenius plots at high temperatures. The general pattern confirms the observations made in the earlier conductivity studies (Chapter 3) and shows that whereas a single activation energy may be used at high temperatures this does not apply at lower temperatures ; here the activation energy is finite though small and decreases with increasing frequency. In general two distinct temperature variations of $\mathrm{Re}\sigma(\omega)$, above and below about T_t = 550 K, are observed and the values of E_A, derived from $\log\mathrm{Re}\sigma(\omega)$ versus T^{-1}, were 1.3 eV and 0.08-0.02 eV above 550 K and near room temperatures respectively. The salient feature is that the d.c. contribution to the $\mathrm{Re}\sigma(\omega)$ is negligible even at high temperatures (Fig. 4.7).

The temperature variations of $\tan\delta$ for 5 W/o MgO/Si_3N_4 and Z = 3.2 sialon at different applied frequencies are plotted as log $\tan\delta$ against T^{-1} in Figure 4.8. The high temperature data fits almost linearly on the log $\tan\delta$ versus T^{-1} plot. At lower temperatures, i.e. below 475 K, there are

Sample reference	Nominal Composition	Q-meter at 10^5 Hz		Microwave at 9.3 GHz	
		ε'	tan δ	ε'	tan δ
1	Si_3N_4 (washed with NaOH) Hot pressed at 1700°C for 1 hr.	7.98	5.9×10^{-3}	3.2	1.05×10^{-2}
2	Si_3N_4 - 5 W % MgO Hot-pressed at 1700°C for 1 hr.	9.58	5.0×10^{-3}	5.65	4.02×10^{-3}
3	z ≈ 4.0 sialon hot pressed at 1700°C for 1 hr.	8.71	6.02×10^{-3}	5.07	3.69×10^{-2}
4	z ≈ 3.2 sialon hot-pressed at 1700°C for 1 hr.	8.2	4.0×10^{-3}	-	-
Reported data on reaction-bonded materials		ε'	tan δ	ε' (8 - 10 GHz)	tan δ (8 - 10 GHz)
S J Godfrey review (9)	Si_3N_4	(a) 7.2 (b) 9.4 (c) 5.8	2×10^{-2} (average)	-	-
J D Walton (10)		(frequency uncertain but < 10^6 Hz)		5.6	2×10^{-3}
T V Andreeva et al (11)	6.72 W % MgO - Si_3N_4	8 to 7 between 5×10^4 & 3×10^7 Hz	5×10^{-3} to 1×10^{-3} between 5×10^4 & 3×10^7 Hz	-	-

Table 4.1 Dielectric data for nitrogen ceramics at room temperature.

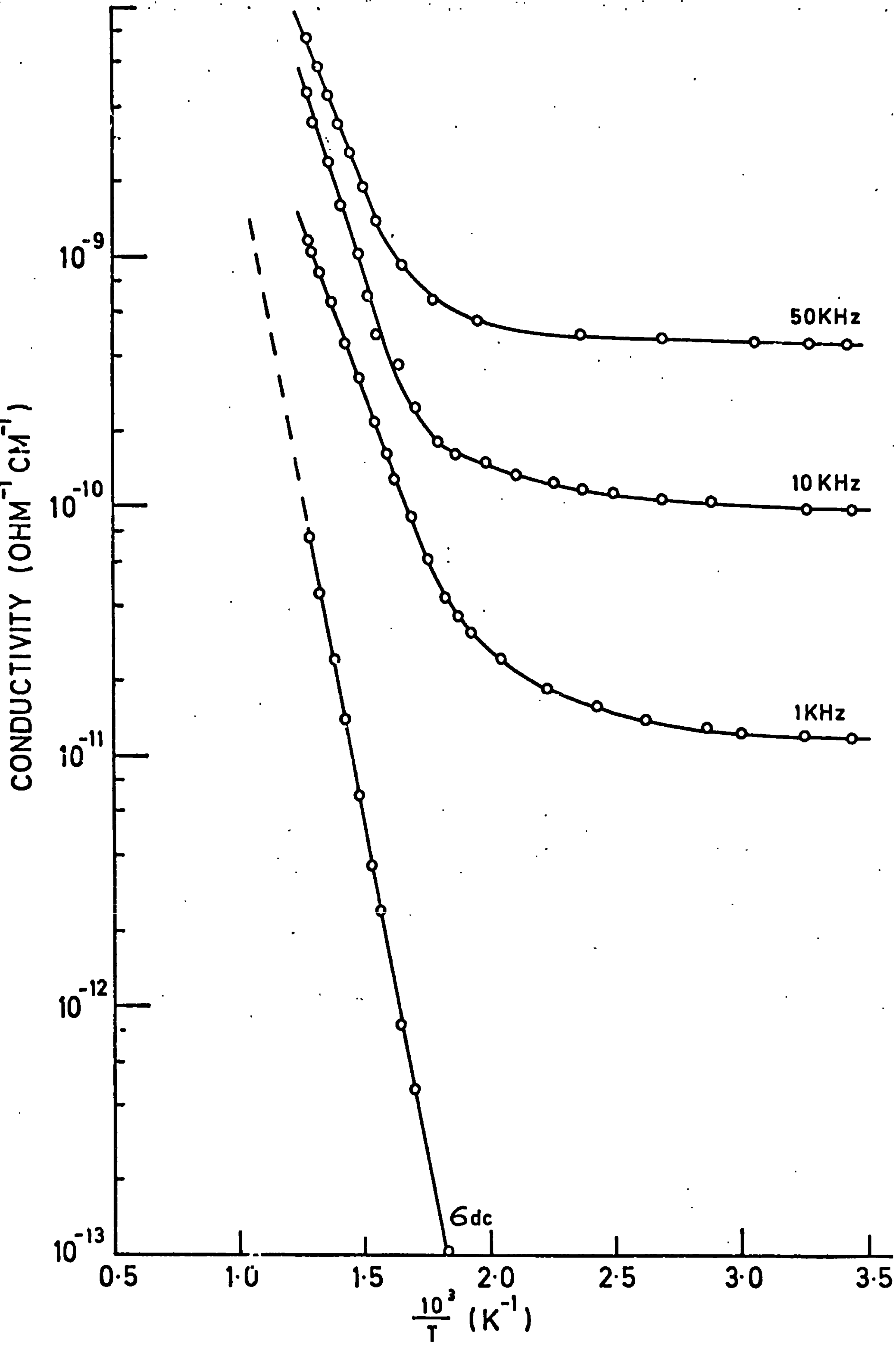

FIG. 4.7 Temperature and frequency variation of the real part of conductivity for $z = 3{\cdot}2$ sialon.

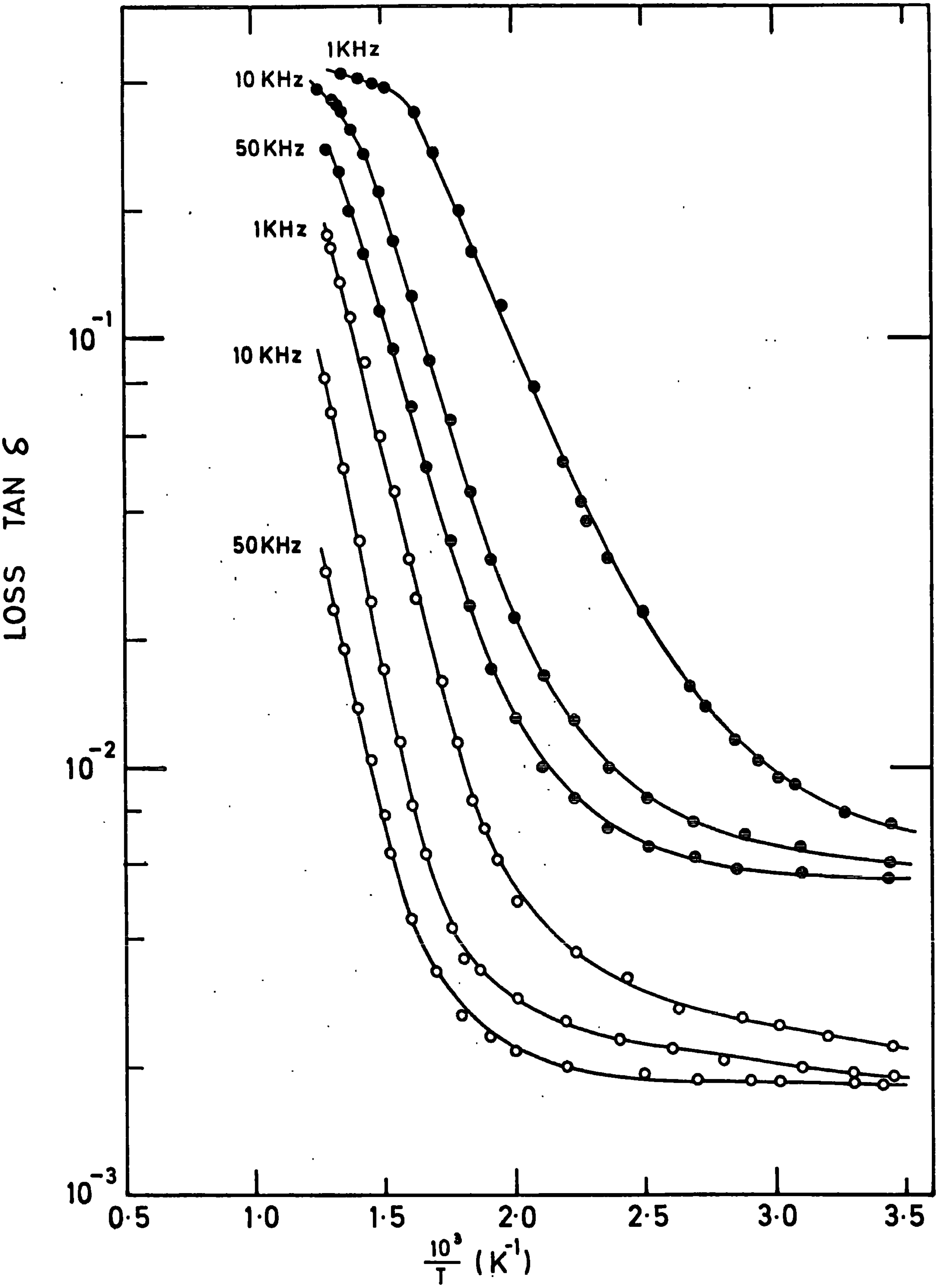

FIG. 4.8 Temperature variation of the loss tangent for z = 3·2 sialon (○) and 5 w/o MgO / Si_3N_4 (●) at different applied frequencies.

departures from linearity. The loss tanδ decreases slowly with increasing frequency ; this applies at all temperatures. The temperature variation of ε' for the same specimens is shown in Figure 4.9 in which ε' is plotted against T. The dielectric constant ε' and loss tangent both rise slowly with temperature below 500 K and rise rapidly with temperature above about 500 K. At higher temperatures the rise is more rapid at lower frequencies. A more pronounced rise of ε' with temperature is observed in MgO/Si_3N_4 than in either sialon or silicon nitride. The dielectric constant data suggested that ε'(ω) followed log ε'(ω) α T rather better than log ε"(ω) α T^{-1} (Fig.4.10). It is noticed that there is no significant difference in the values of the dielectric parameters for the three materials at temperatures below about 500 K. Above this transition temperature (T_t) the values of σ(ω), tanδ and ε'(ω) for sialon are much lower than for both Si_3N_4 and 5 W/o MgO/Si_3N_4; the values for Si_3N_4 are generally higher than those for 5 W/o MgO/Si_3N_4.

4.4 DISCUSSION

In a wide range of low conductivity materials it is generally found that the frequency dependence of the conductivity involves two components such that the measured real part of conductivity Reσ(ω) is related to the true conductivity σ'(ω) by the relation (Chapter 2, Sect. 2.6)

$$\mathrm{Re}\,\sigma(\omega) = \sigma'(\omega) + \sigma_{dc} \qquad (4.16)$$

and the frequency variation of σ'(ω) follows

$$\sigma'(\omega) \ \alpha \ \omega^n \qquad (4.17)$$

where usually $0.7 < n < 1$ at low temperature. There is general agreement that the a.c. conductivity in hopping systems will follow equation (4.17) but there are several approaches, e.g. those of Mott and Davis (18), Pollak (49-50) and Jonscher (80-82) to the detailed physical sources of the mechanisms involved. With the present materials the experimental

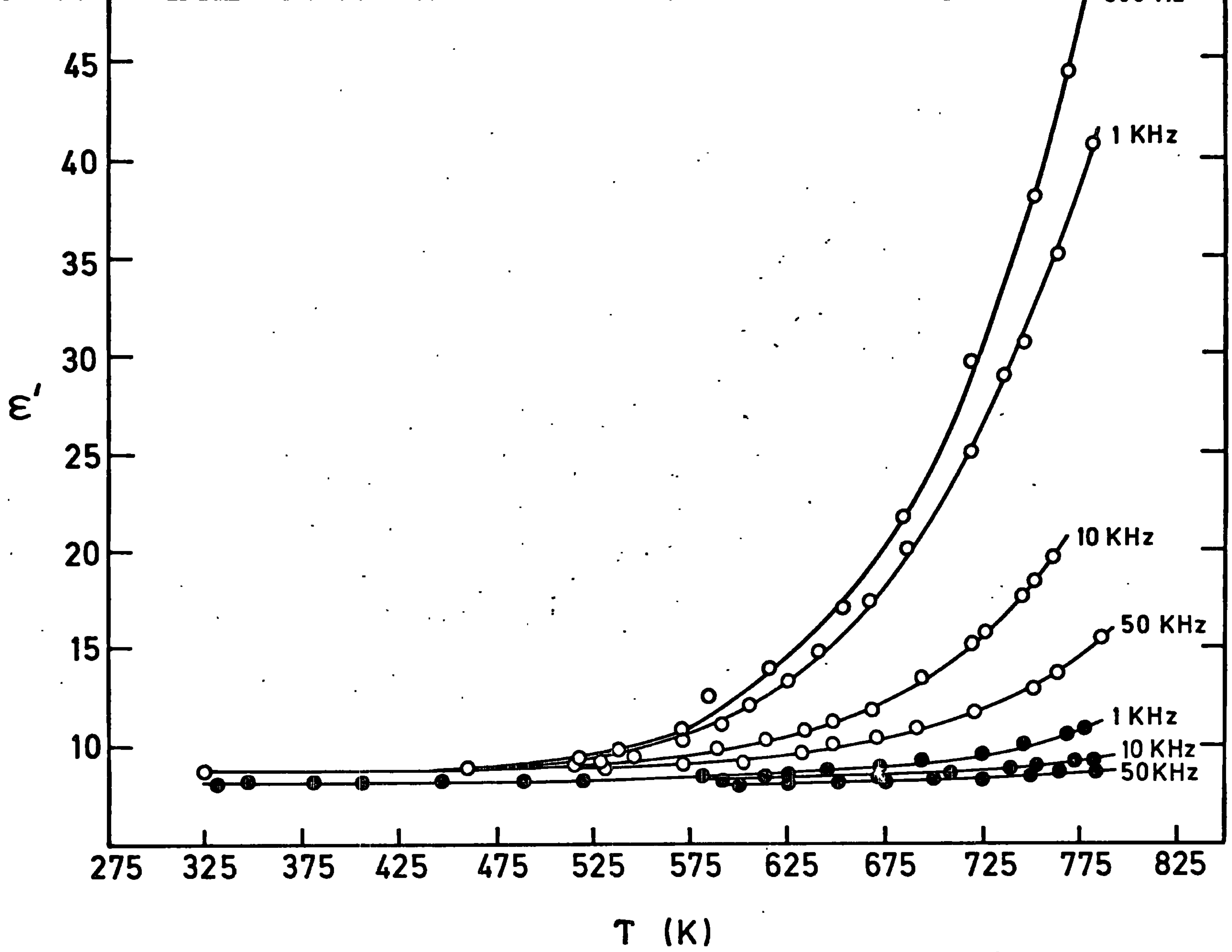

FIG.4.9 Temperature variation of the dielectric constant ε' for 5w/o MgO/ Si_3N_4 (○) and Z = 3·2 sialon (●) at different applied frequencies.

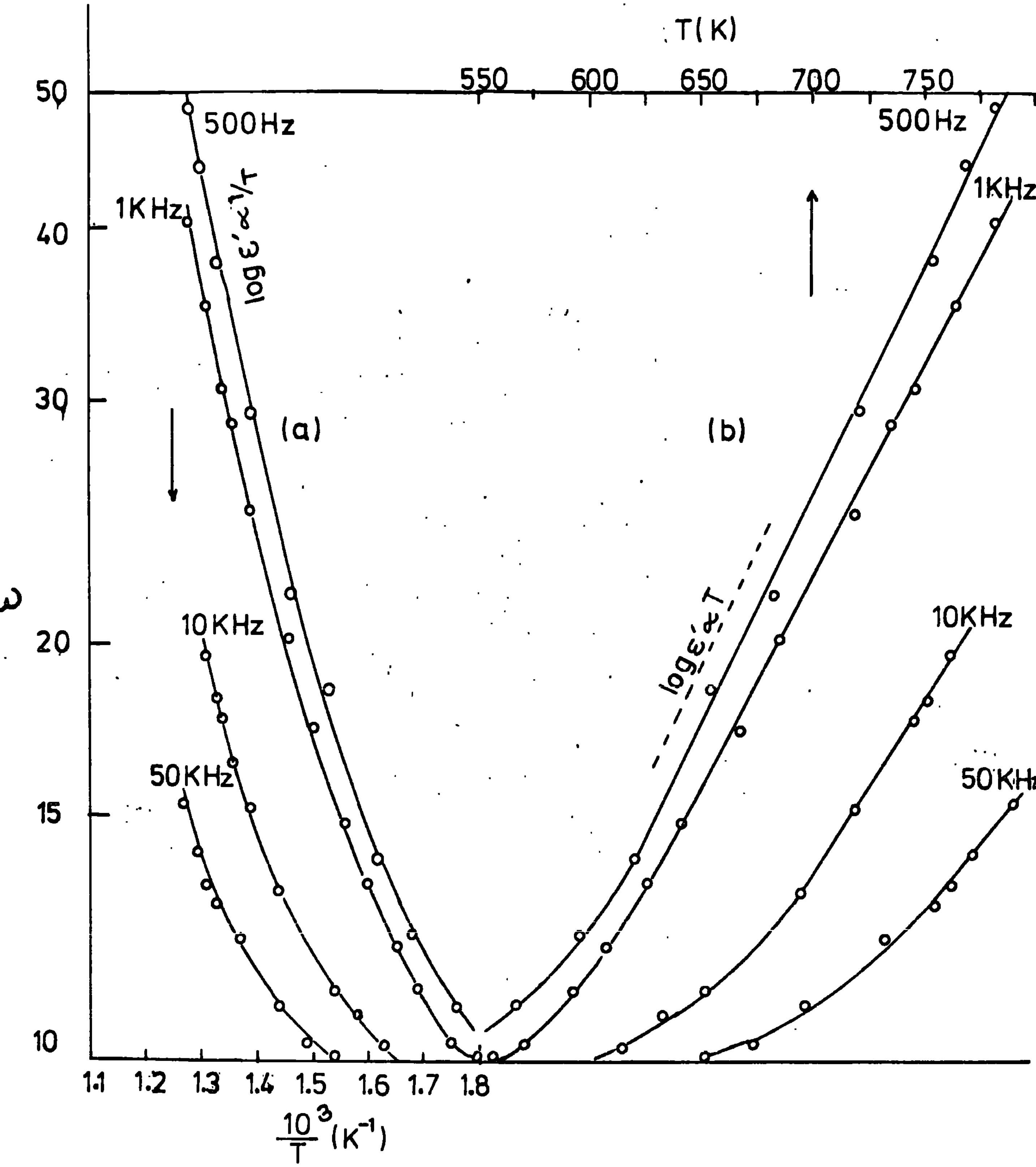

FIG. 4.10 Temperature and frequency variation of the dielectric constant for 5w% MgO/Si_3N_4 in both (a) log ε′ – T^{-1} and (b) log ε′ – T plots. Data replotted from FIG. 4.9

evidence indicates that σ_{dc} is negligible at low temperature (Fig.4.7) and that $\sigma'(\omega)$ is proportional to ω^n with n = 0.9 at room temperature over eight frequency decades up to 9.3 GHz. The precise details of the hopping mechanism involved are not yet clear although it appears that Mott's law (18) cannot apply since the Mott formulae predict a continuous curvature convex upwards which is not observed.

The room temperature dielectric loss data fit well with the "universal law" suggested by Jonscher (81-82) according to which

$$\varepsilon''(\omega) \quad \alpha \quad \omega^{n-1} \tag{4.18}$$

where $n < 1$

$$\varepsilon''(\omega) \quad \frac{\sigma'(\omega)}{\varepsilon_o \omega} \tag{4.19}$$

In many disordered materials, amorphous semiconductors and insulators, this law is obeyed and a striking feature is that in all these materials the loss falls in a narrow band only two decades wide on the loss axis. The room temperature variation for the nitrogen ceramics covers only one decade in loss (Fig. 4.6 (c)). The law is also obeyed at temperatures up to at least 770 K, although the value of n falls progressively, as shown in Figure 4.11 (a), as the temperature increases in agreement with theory (Chapter 2, Sect. 2.6). It was noted that the contribution of σ_{dc} to $\mathrm{Re}\sigma(\omega)$ was not completely negligible at high temperatures and therefore, the values of $\varepsilon''(\omega)$ above 550 K were calculated using the relations (4.16) and (4.19). The exponent n for Z = 3.2 sialon changes from n = 0.94 at 291 K to n = 0.44 at 770 K and for 5 W/o MgO/Si_3N_4 from n = 0.90 at 291 to n = 0.57 at 770 K (Fig. 4.6 (c) and 4.11 (a)).

The effects of temperature on the frequency variations of $\varepsilon'(\omega)$ are again shown in Figure 4.11 (b) in which log ε' is plotted against logf at different temperatures. The data fit linearly in this plot but the slope

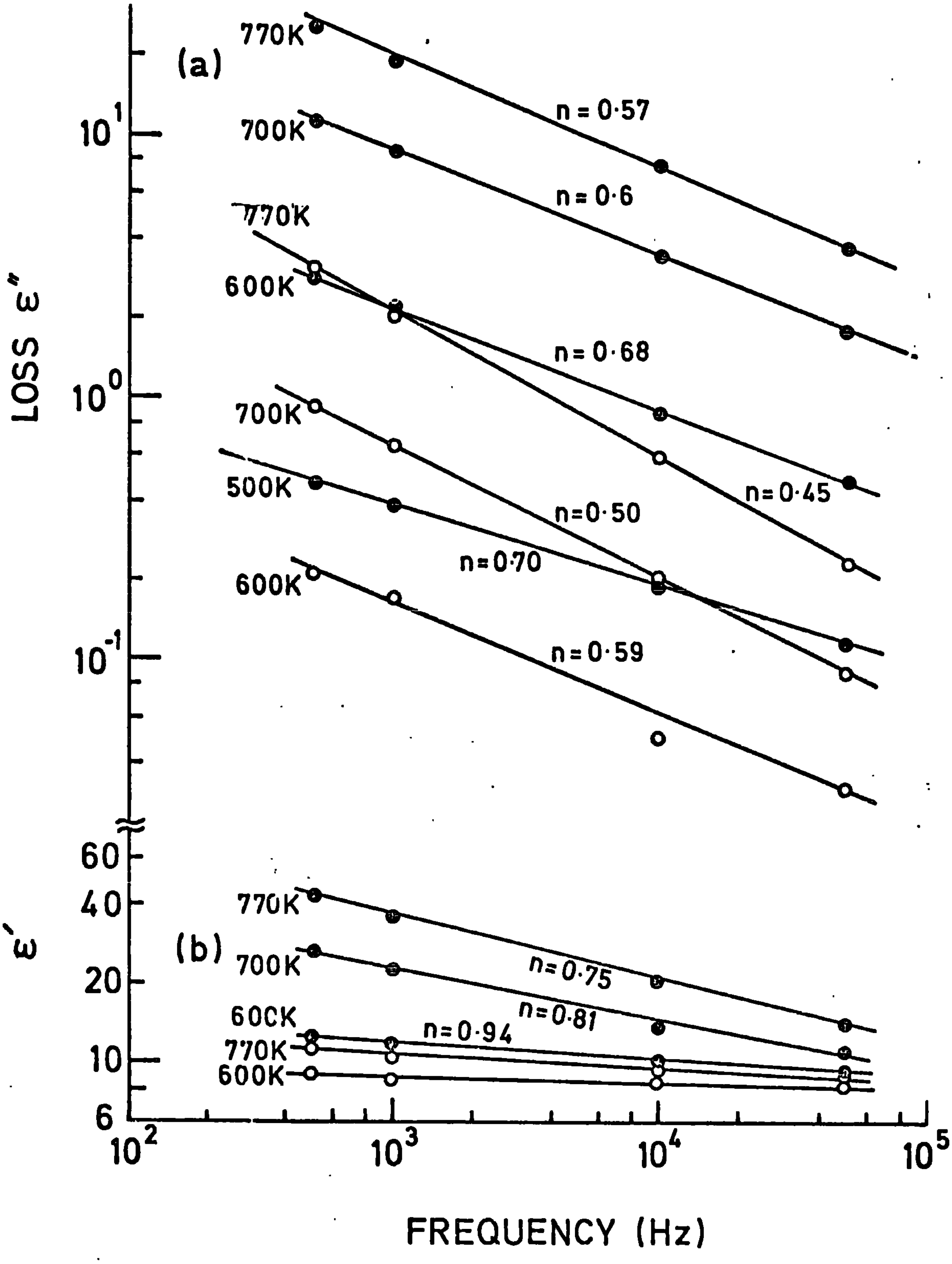

FIG. 4.11 Typical temperature variations of the power law characteristics of (a) $\varepsilon'' \propto \omega^{n-1}$ and (b) $\varepsilon' \propto \omega^{n-1}$ for 5 w/o MgO/Si_3N_4 (●) and Z = 3·2 sialon (○)

increases with increasing temperature. A tentative analysis of the dielectric constant data has been attempted in the following way. An estimate of the limiting value ε_∞ (high frequency dielectric constant) was made by extrapolation of the variation at each individual temperature (Fig. 4.11 (b)) to 9.3 GHz. The values of $(\varepsilon'(\omega) - \varepsilon_\infty)$ so obtained are plotted in Figure 4.12 as log $(\varepsilon'(\omega) - \varepsilon_\infty)$versus logf at different temperatures. It is found that these follow the $(\varepsilon'(\omega) - \varepsilon_\infty) \alpha\ \omega^{n-1}$ law (Chapter 2, Sect. 2.6) with values of n decreasing from 0.95 at room temperature to 0.65 at 770 K. At any temperature the value of n in the $(\varepsilon'(\omega) - \varepsilon_\infty)$ variation is higher than the corresponding value in the $\varepsilon''(\omega)\ \alpha\ \omega^{n-1}$ law. The ratio of $\varepsilon''(\omega)$ to $(\varepsilon'(\omega) - \varepsilon_\infty)$ approximately satisfies the Kramers-Kronig relation (Chapter 2, Sect. 2.6)

$$\frac{\varepsilon''\ (\omega)}{(\varepsilon'(\omega) - \varepsilon_\infty)} = \cot\ (n.\pi/_2) \qquad (4.20)$$

Equation (4.20) can apply to a very general property of both non-Debye dipolar and hopping carriers (electronic or ionic)systems in solids which satisfy two conditions (81-82):

(i) carriers or dipoles move by discontinuous hops or jumps between stationary positional or orientational states,

(ii) other charges or dipoles present in the system produce a finite extent of screening which cannot follow instantaneously the discontinuous movements of individual charges and dipoles. These criteria are in contrast with those for the free-carrier band model of a semiconductor or for Debye dipolar mechanisms (Chapter 2, Sect. 2.6). This is illustrated by Table 4.2 in which a comparison is made, for different temperatures, of the values of n obtained from the $\varepsilon''(\omega)$ and $(\varepsilon'(\omega) - \varepsilon_\infty)$ variations with those derived from Equation (4.20) by substitution of the experimental values of the ratio

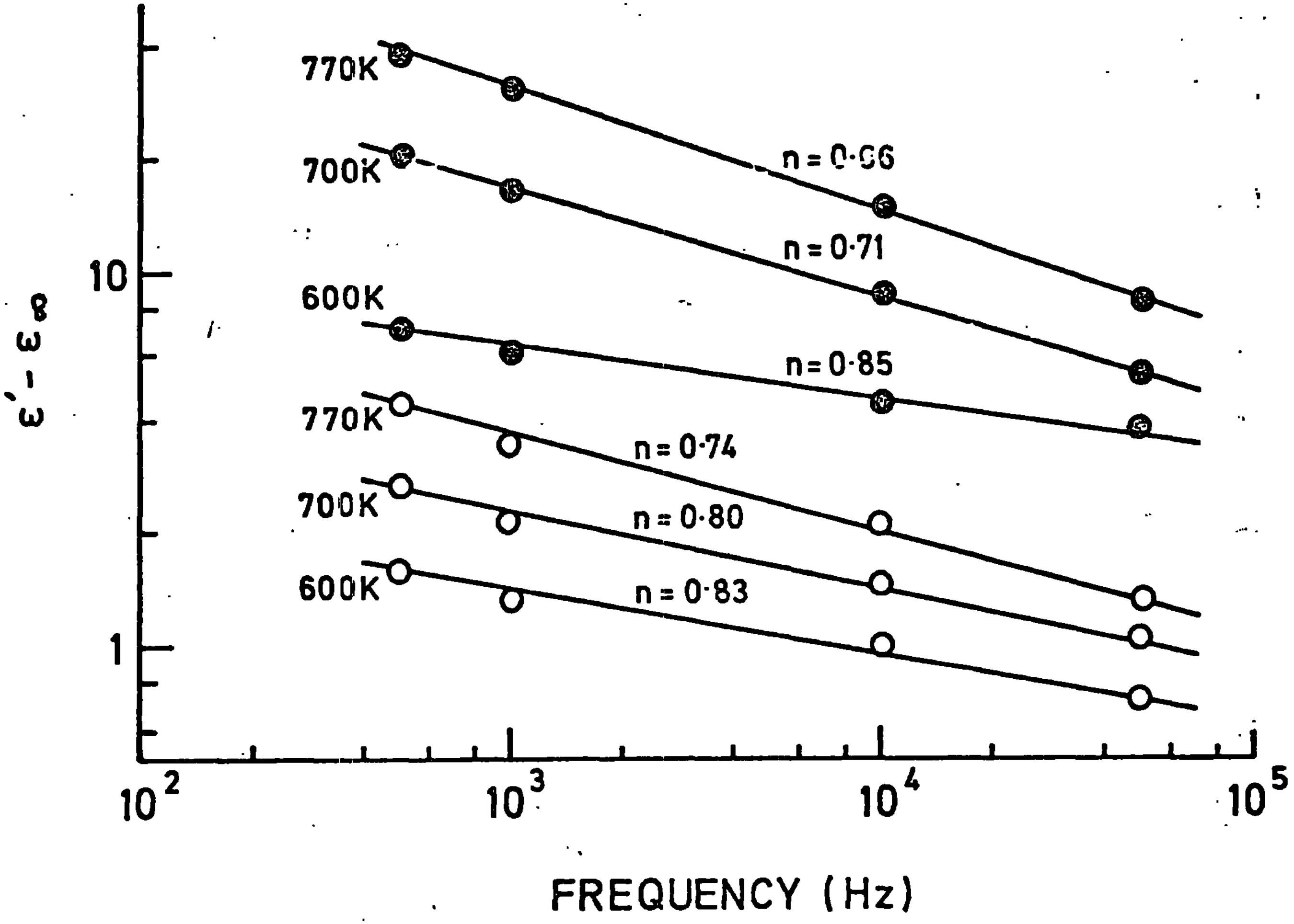

FIG.4.12 Temperature variations of the power law characteristics of $\varepsilon' - \varepsilon_\infty \propto \omega^{n-1}$.

Temperature (K)	n from $\varepsilon' - \varepsilon_\infty$		n from ε''		Measured average $\varepsilon''/\varepsilon' - \varepsilon_\infty$		Expected value of n $(2/\pi)\ \mathrm{Cot}^{-1}\left[\varepsilon''/\varepsilon' - \varepsilon_\infty\right]$	
	MgO/Si_3N_4	Z=3.2 sialon	MgO/Si_3N_4	Z=3.2 sialon	MgO/Si_3N_4	Z=3.2 sialon	MgO/So_3N_4	Z=3.2 sialon
291	.96	.96	.92	.93	1.58×10^{-2}	1.26×10^{-2}	.98	.99
500	.88	-	.70	.77	.12	-	.92	-
600	.85	.83	.68	.59	.31	.103	.81	.93
700	.71	.8	.60	.50	.49	.30	.71	.81
770	.66	.74	.57	.45	.61	.51	.65	.70

Table 4.2 Comparison of values of the exponent n obtained by different methods at various temperatures.

$\varepsilon''(\omega)/_{\varepsilon'(\omega) - \varepsilon_{\infty}}$. The effects of both frequency and temperature variations are noticeably smaller on $\varepsilon'(\omega)$ than on $\varepsilon''(\omega)$; this implies that the carriers make a relatively small contribution to $\varepsilon'(\omega)$, a feature characteristic of the hopping mechanism suggested recently by Jonscher (78). Such a behaviour of dielectric constant also supports the electronic hopping model, if the centre pair with one electron is considered to be a dipole. As the temperature rises, the number of such dipoles increases and the dielectric constant increases too, but the change is smaller with the increase of frequency (79).

CHAPTER 5

D.C. ELECTRICAL PROPERTIES

5.1 INTRODUCTION

The precise nature of the conduction mechanisms was not established from the previous high temperature d.c. conductivity measurements between 400° C and 1000° C (Chapter 3). In those measurements the decay of current was observed but a detail study was not made to elucidate the origin of this behaviour. It was known from Hall-effect investigations that the mobility of the materials was very low although the actual magnitude could not be obtained. However, these d.c. electrical data indicated that the materials were of high restivity and low carrier mobility. For high resistivity materials, a very low value of mobility can be obtained from transit time measurement of ejected carriers (109). The frequency variations of the dielectric parameters between 18° C and 500° C suggested that the conduction was due to either non-Debye dipolar or hopping processes (Chapter 4). It is generally very difficult to obtain conclusive evidence of the dipolar or charge hopping origin of the mechanisms from only this dielectric measurement without a knowledge of temperature and field variations of the d.c. conductivity data (19,82), (Chapter 2, Section 2.2). Further information can be obtained from the time dependence of the charging and discharging currents at different temperatures which generally follow the empirical law $I(t) \alpha t^{-n}$ with $0.5 < n < 0.8$, (n decreases with increasing temperature) ; this is also known as the "Universal law of dielectric response. These effects have been analysed by Jonscher (78, 82) and Lewis (110). High field effects give further confirmation of the mode of conduction inferred from low field measurements (Chapter 2, Sect. 2.3). The purpose of the work described in this Chapter was to investigate the d.c. electrical properties especially in the range from room temperature to 500° C using refined experimental techniques omitted in the previous measurements. Here the time variations of the charging and discharging currents were studied, together with their field and temperature dependencies.

5.2 EXPERIMENTAL

In this investigation, thin plate specimens with circular gold electrodes were used as before (Chapter 4). This type of specimen and electrode arrangement made the surface path greater than the thickness so that the surface contribution in the total conduction was reduced considerably (111). The d.c. electrical properties of the specimens in applied fields up to about 1.1×10^4 volt cm^{-1} were measured using two probe pressure-contact methods over the temperature range between 18° C and 500° C in an ambient of air, the upper temperature limit being determined by the need to avoid gold diffusion into the specimen. The apparatus and the special jig arrangement for measurement at the above mentioned temperature range are shown in Figure 5.1. Special precautions, as described by Tallan (111), were taken to minimize possible errors in the results. Signals due to thermal noise and the atmosphere around the specimens, as well as the circuit arrangement, were minimized by using a brass tube as the inner wall of the furnace and shielded earthing connections. The perspex insulator used to separate the electrodes was outside of the furnace, where it could be kept cold. The apparatus was first tested by measuring the resistance of a standard high value resistor of 10^{13} ohms. Small currents of about 5×10^{-14} amp were able to be measured with the d.c. amplifier (Elliott Process Inst.Ltd.). With the voltages applied (<350 volt) across the jig and the split electrodes the total leakage current (without specimen) between them was less than 1×10^{-13} amp. Under all circumstances the experimental error did not exceed about ± 10%.

The decaying, steady and discharging currents, were measured under different applied fields up to about 1.1×10^4 V cm^{-1} between 18° C and 500° C.

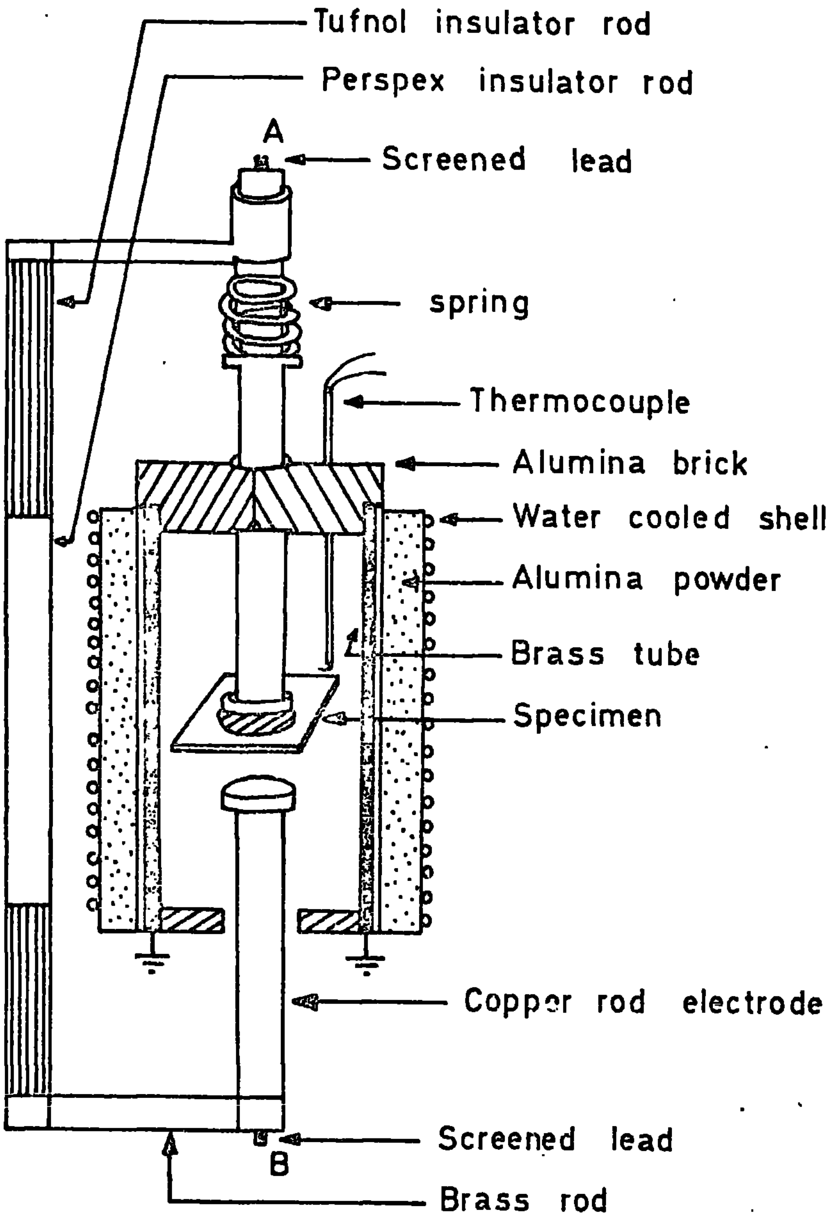

FIG. 5.1 Apparatus for measuring d.c. electrical properties at high temperatures.

Two series of measurements were performed on each specimen. In the first, a voltage was applied and the current allowed to reach a steady value I_s. The applied voltage was then removed and the specimen was short-circuited via the current measuring unit until the observed reverse current had decayed. The next higher voltage was then applied and the process repeated at each increment. The whole series of measurements took more than 6 days per specimen. In the second method once the steady current was reached, the next voltage was applied without discharging. The times taken to reach subsequent steady current values were much shorter. The steady currents obtained by the two methods at room temperature were the same within the limits of experimental error. The second method was used to measure the steady currents at room temperature and the high temperature measurements were made using the first method. Both the decaying and discharging variations of current with time were noted carefully without making any disturbance of the environment and the atmosphere around the apparatus. The temperature variation of the steady current was found by first allowing equilibrium to be reached at room temperature and then raising the temperature successively. This data was used to derive the temperature variation of conductivity. Specimens which had previously been heated often showed space-charge effects at temperatures below about 130° C. This behaviour was reduced by giving the specimen a heat treatment in air (65° C for 20 hours) while short-circuited between successive sets of measurements at different fields. Similar treatments were applied to measure the temperature and field variations of the decaying and discharging currents in order to discharge the specimen completely between successive stages of measurement.

5.3 RESULTS

5.3.1 STEADY CURRENT BEHAVIOUR

Particular interest attaches to the variations of the steady current with field and temperature. The electrical properties were very similar in all the materials examined. The variation of steady current with applied field at room temperature is shown in Figure 5.2 in which the current density J was obtained from I_s by division by the known electrode area. In Fig.5.2(a) the plot of log (J) versus log (E) is linear at low electric fields (<3Kv cm^{-1}) but is not at high electric fields. The same data are replotted in Fig. 5.2 (b) which shows that log (J) versus $E^{\frac{1}{2}}$ is a straight line in the high electric field region. The conductivity is almost independent of E in the low applied fields but in the high field region varies as log $\sigma \propto$ E (Fig. 5.3). The temperature variations of conductivity for the three specimens at a low applied field are shown in Figure 5.4 in which log σ is plotted as a function of inverse temperature. The relationship between log σ and T^{-1} is linear between 773 K and about 550 K and becomes non-linear at lower temperatures ; consequently the activation energy in the higher temperature region is constant, but below 550 K it decreases slowly with decreasing temperature. Values for activation energies (E_A) were calculated from the relation

$$\sigma = \sigma_o \exp \left({}^{-E_A}/_{KT} \right) \qquad (5.1)$$

in the linear high temperature region and from the slopes of the curves at lower temperatures (near room temperatures) ; these are listed in Table 5.1. The pre-exponential factor was calculated from the linear high temperature region and gives $\sigma_O \sim 1$ ohm^{-1} cm^{-1}. In Figure 5.5 the effect of different applied fields on the temperature variations are shown for Z = 3.2 sialon. The conductivity is independent of applied fields at temperatures above about 550 K ; below that, the conductivity increases with applied field and is weakly dependent on temperatures. The slopes of the logσ versus E plots decrease slowly with increasing temperatures. It is noticeable that the conductivity of sialon is less than that of MgO/Si_3N_4 below 525 K and the former is higher above that temperature. The conductivity of Si_3N_4 is more than one order of magnitude higher than both sialons and MgO/Si_3N_4 throughout

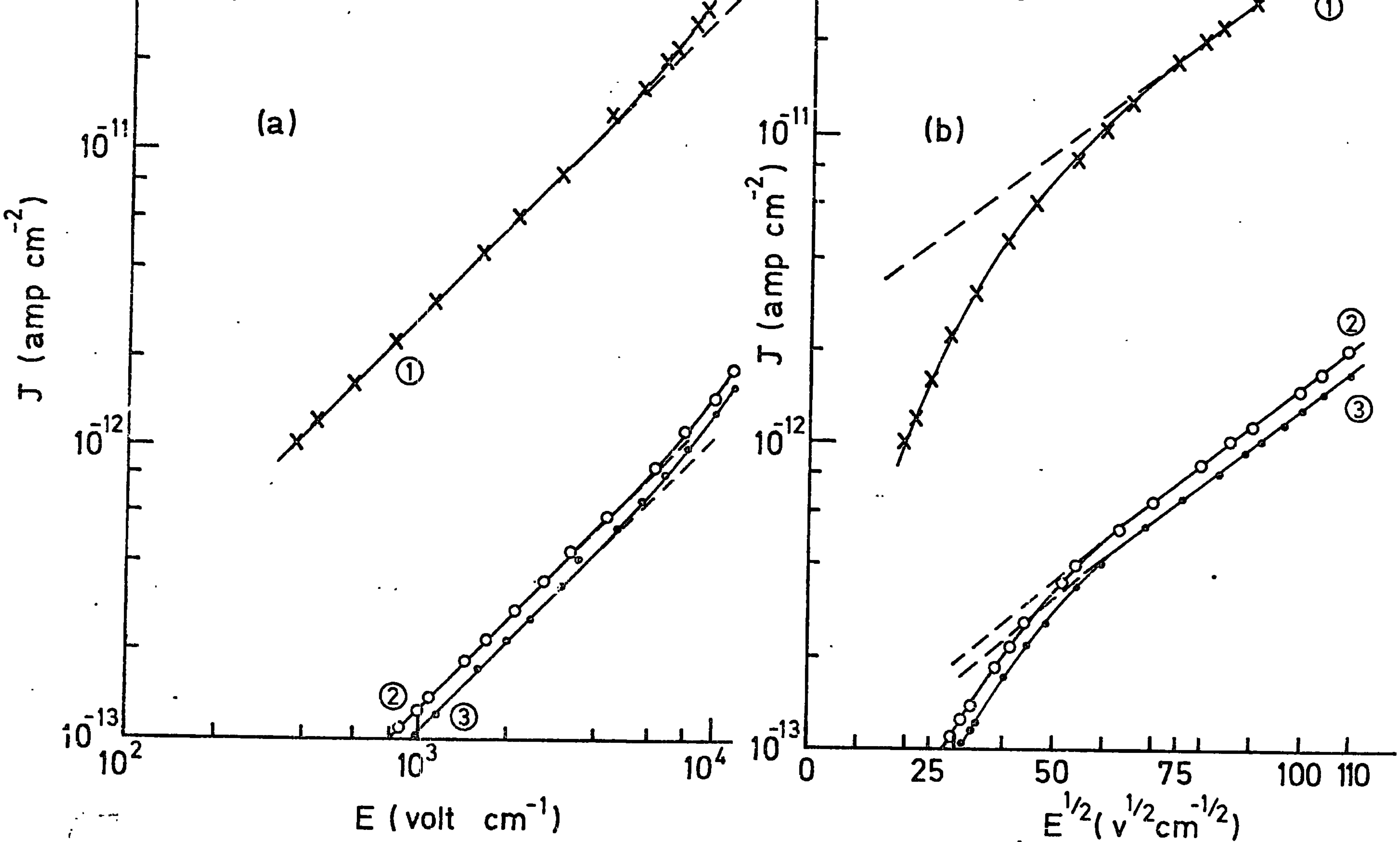

FIG.5.2 (a) Log J versus log E and (b) Log J versus $E^{1/2}$ for ① Si_3N_4 (x); ② 5 w/o MgO/Si_3N_4 (o) and ③ z = 4·0 Sialon (•) at room temperature.

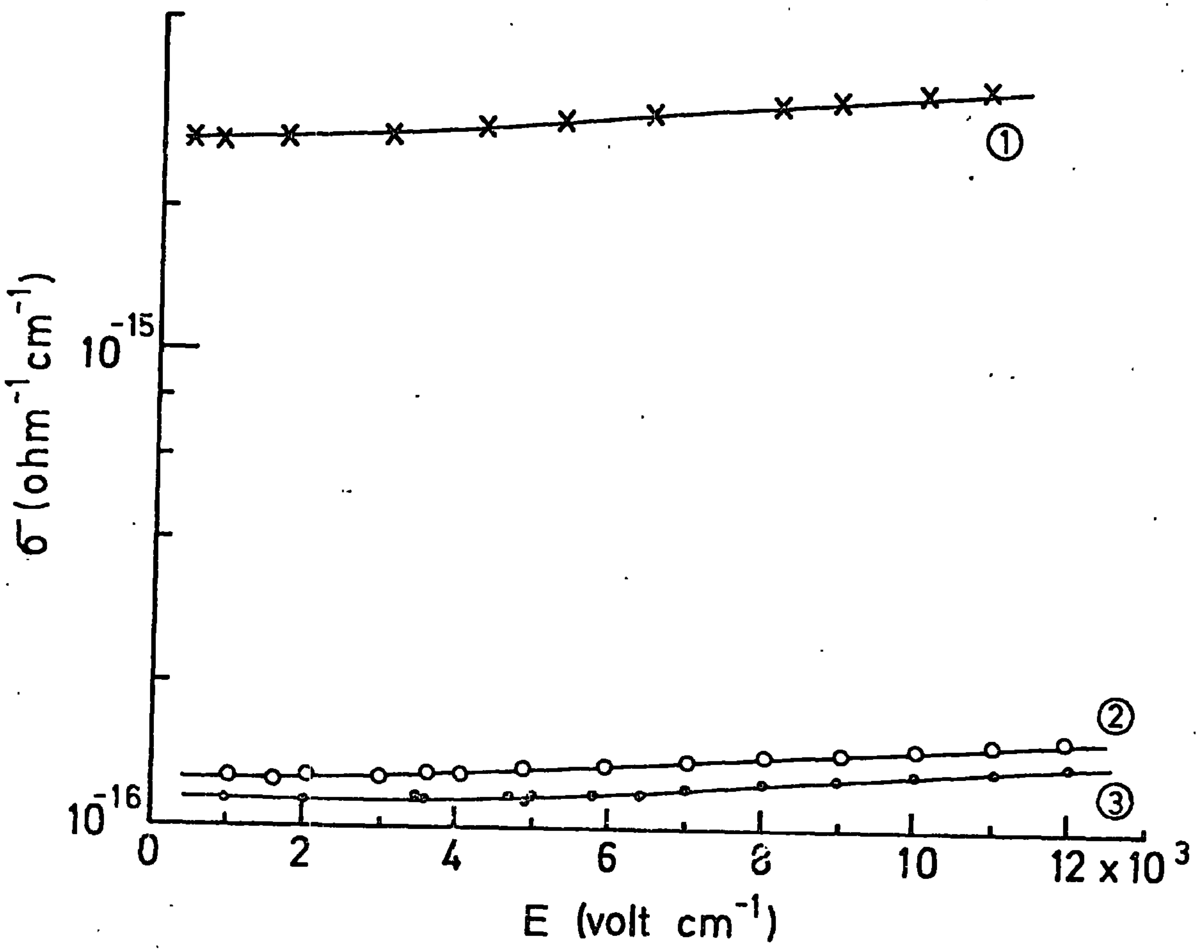

FIG. 5.3 Log σ versus E for ① Si_3N_4(x) ; ② 5 w/o MgO/ Si_3N_4 (○) ; and ③ z=4·0 Sialon (•) at room temperature.

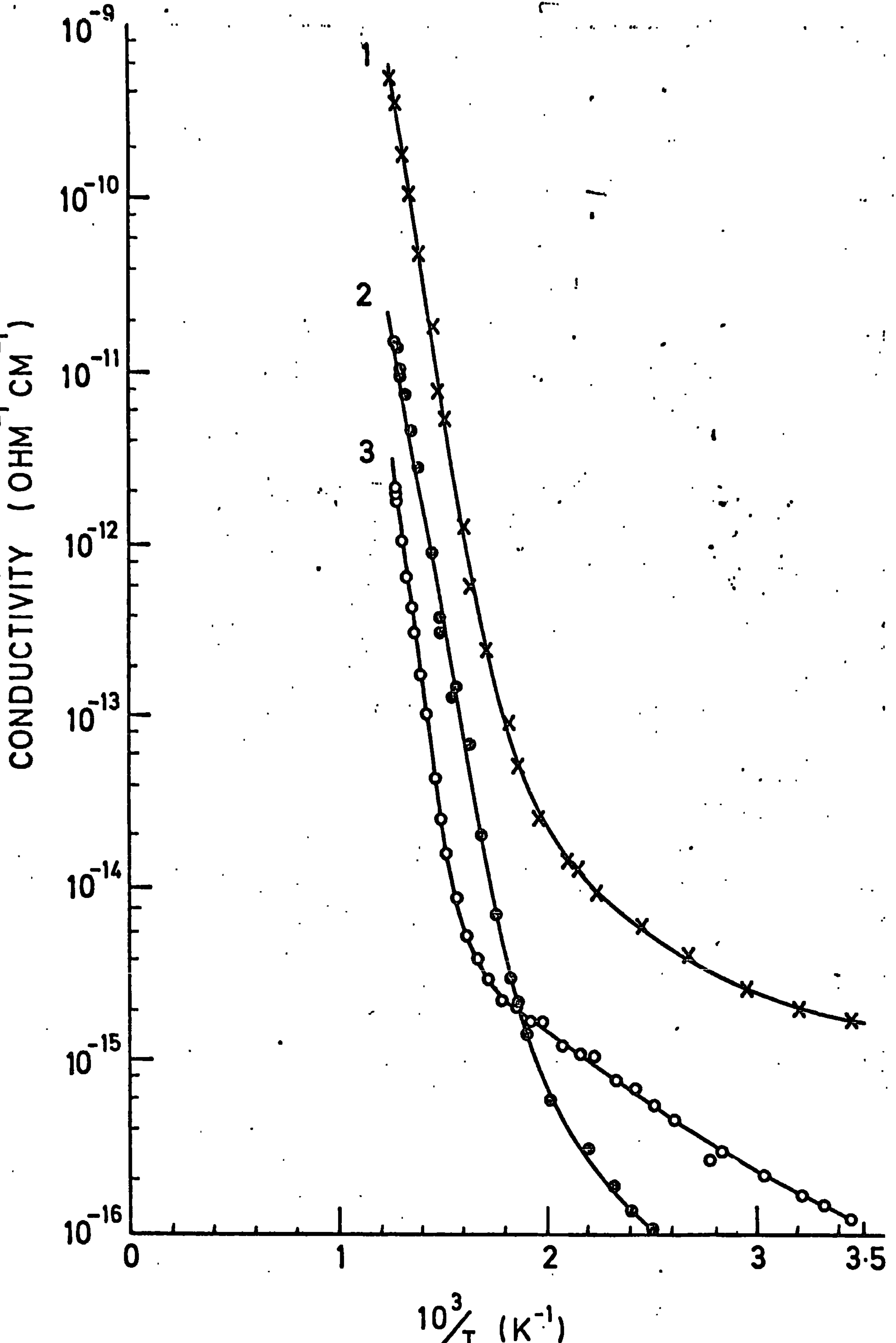

FIG. 5.4 Temperature variation of d.c. conductivity for (1) Si_3N_4 (x); (2) 5 w/o MgO/Si_3N_4(○) and (3) z = 3·2 sialon(⊙

Sample reference	Nominal Composition (hot-pressed)	D.C. Conductivity (Ω^{-1} cm^{-1})		High temperature region		Low temperature		Characteristic hopping length 'a'	μ_D ($cm^2 v^{-1} sec^{-1}$)	Exponent n at 18°C	
		500°C	18°C	E_A (eV)	σ_o (Ω^{-1} cm^{-1})	E_A (eV)	B			I_c	I_d
1	Si_3N_4	3×10^{-10}	1.8×10^{-15}	1.46	1.0	.08	75	72 Å	1.7×10^{-8}	0.80	0.80
2	5W% MgO/Si_3N_4	2×10^{-12}	1.2×10^{-16}	1.8	1.0	.15	83	58 Å	5.4×10^{-9}	0.85	0.80
3	Z = 3.2 sialon	1.5×10^{-11}	7×10^{-17}	1.45	0.05	.05	53	-	7.35×10^{-8}	0.70	0.80
4	Z = 4.0 sialon	-	1×10^{-16}	-	-	-	-	62 Å	6.15×10^{-8}	0.70	0.80

Table 5.1 D.C. electrical parameters of nitrogen ceramics used in this investigation between 18° C and 500° C.

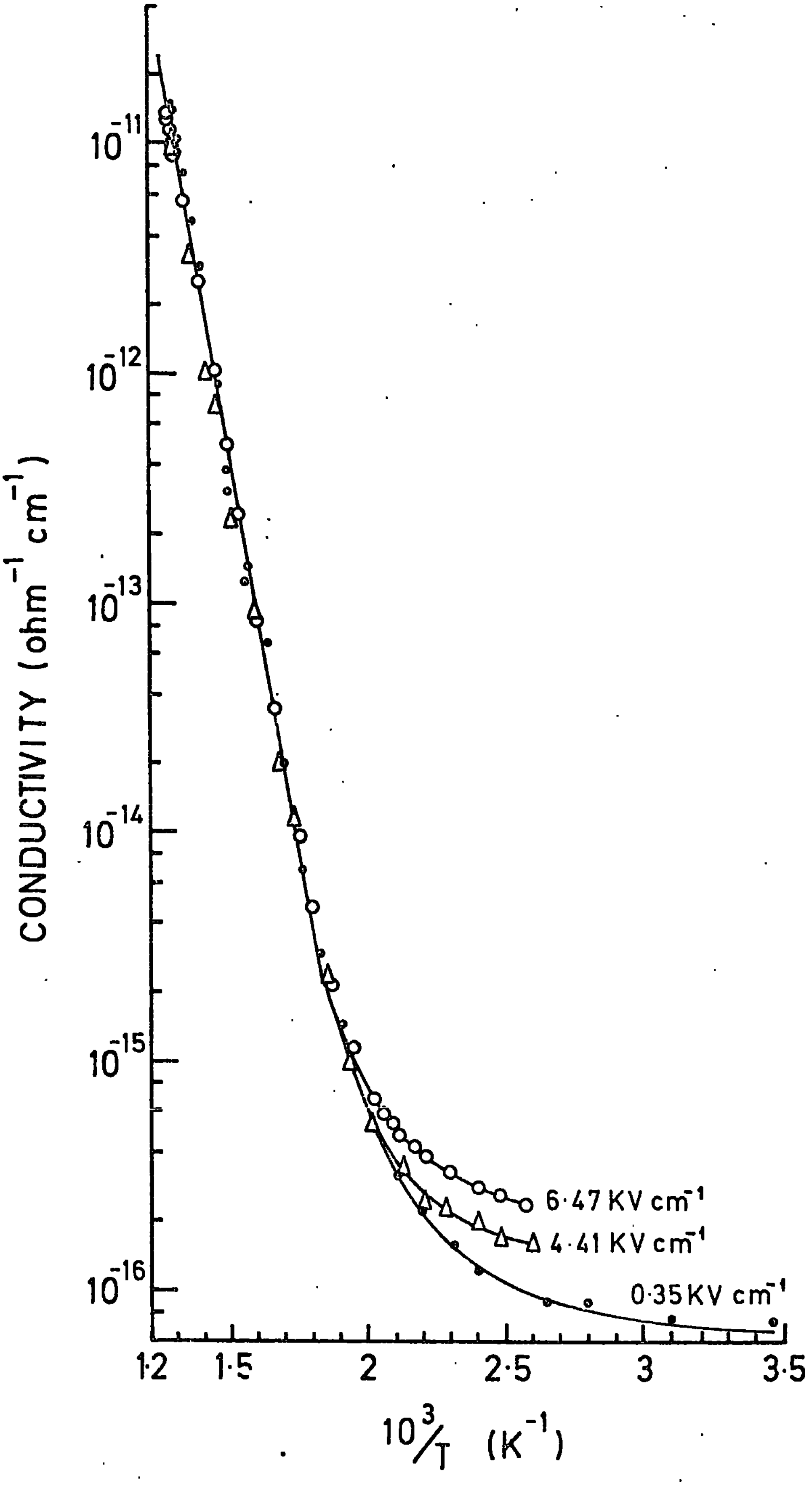

FIG. 5.5 Temperature dependence of conductivity for z=3·2 sialon at different applied fields.

the temperature range. The comparison of these results with available data on reaction bonded materials shows that the conductivity of hot-pressed materials is at least two to three orders of magnitude lower than that of reaction bonded Si_3N_4(89) and MgO/Si_3N_4 (90) materials of similar compositions at temperatures between 18° C and 500° C. Therefore, in the previous d.c. conductivity data between 500° C and 1000° C (Chapter 3, Figure 3.12), a higher value of σ for the hot-pressed materials was due to the surface contribution in the bulk current. The present result confirms that hot-pressed materials are better insulators than that of reaction bonded materials.

5.3.2 TIME DEPENDENT BEHAVIOUR

The charging and discharging currents of 5 W/o MgO/Si_3N_4 and Z = 3.2 sialon at different temperatures under a constant field are shown in Figure 5.6 (a) and Figure 5.7 respectively. The time for the current to decay to the steady value (I_s) varied from 2 to 15 hours, depending on the temperature ; the shortest times were for high temperatures. Initially the charging current followed a $I \propto t^{-n}$ law but during the subsequent slower decrease the characteristic showed a fluctuation for all materials, before levelling off to a steady value. The time of occurrence of the fluctuation region is almost independent of temperature. The exponent n lies between 0.70 and 0.80 at room temperature and decreases with increasing temperature to about 0.4 at 400° C.

The discharging currents were always of opposite polarity to the charging current, following the same t^{-n} law with n = 0.8, almost independent of temperature. The temperature variation of I_c and I_d for 5 W/o MgO/Si_3N_4 after t = 0 , i.e. 90 sec and 120 sec (Fig. 5.6 (a)) is replotted in log I versus T^{-1} (Fig. 5.8 (a)). Two distinct temperature dependences of both I_c and I_d are observed, the transition occurring at 555 K. Although the log I_d versus T^{-1} plots are linear in both the high and low temperature parts the slopes differ ; the log I_c versus T^{-1} plots show a similar transition but

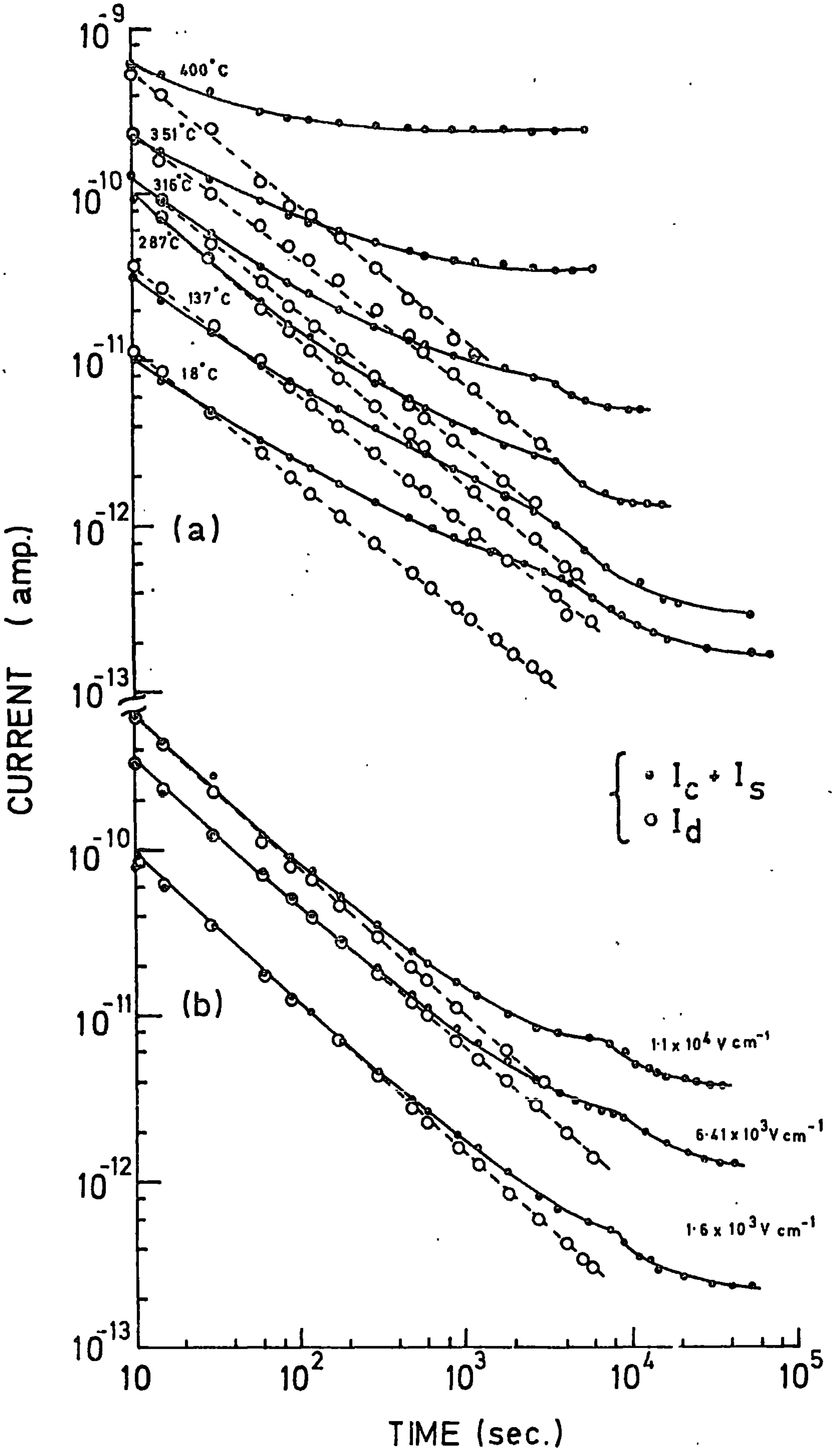

FIG.5.6(a) Typical charging and discharging currents for 5 w/o MgO/Si_3N_4 at different temperatures under an electric field 1·6 KVcm^{-1} (b) Field dependence of charging and discharging currents for the same specimen at 232°C.

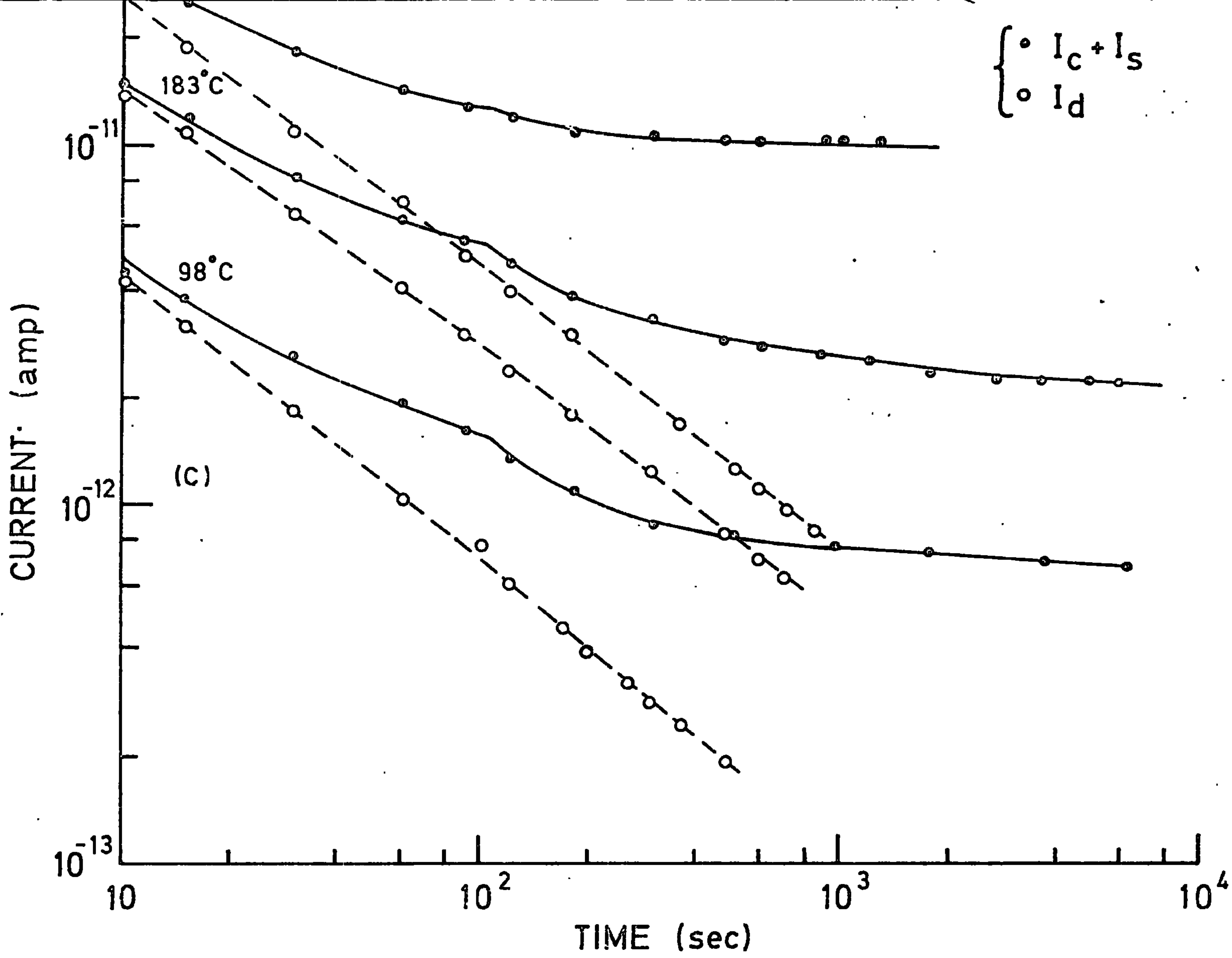

FIG. 5.7 Typical charging and discharging currents for $z = 3{\cdot}2$ sialon at different temperatures under a constant applied field ($1{\cdot}7$ KV cm^{-1})

are not quite so linear. The temperature variation of I_c is very similar to that of I_s (Fig. 5.4) and the activation energies derived from the temperature variation of I_c agreed well with those derived from I_s.

The charging and discharging currents for the same specimen in different applied fields at a constant temperature are given in Figure 5.6 (b). This shows that n is almost independent of applied field and that the time taken to reach a steady value of the charging current decreases slightly with increasing field. At high fields I_c follows the t^{-n} law for a longer time. Similar fluctuations are observed at high fields but the times at which they occur become shorter with increasing field. This behaviour is significant and its effect will be discussed in Section 5.4.2. In general I_c is higher than I_d at high temperatures and at high fields. Some typical values of I_c and I_d after 90 sec, 3×10^2 sec, 10^3 sec and 3×10^3 sec, taken from Figure 5.6 (b), are replotted as log I versus log E in Figure 5.8 (b). The log I_c - log E plot is initially linear at both low and high fields and gradually becomes non-linear with increasing time in the high field region. The variation of log I_d is linear throughout, which implies that I_d obeys ohm's law to much higher fields than does I_c. The slopes of I_c and I_d and their variations with E are exactly the same as those of I_s (Fig. 5.2 (a)). Similar effects were noted in other specimens, though the times involved varied somewhat.

5.4 DISCUSSION

5.4.1 STEADY CURRENT BEHAVIOUR

(a) Low Fields

The low field steady-current behaviour shows that the log J versus log E characteristic is linear (Fig. 5.2 (a)) and the slope (1.01) shows that ohm's law is obeyed. The temperature dependence of conductivity in this region shows that the activation energy, E_A is constant at temperatures above about 555 K ; below that temperature E_A decreases slowly with decreasing

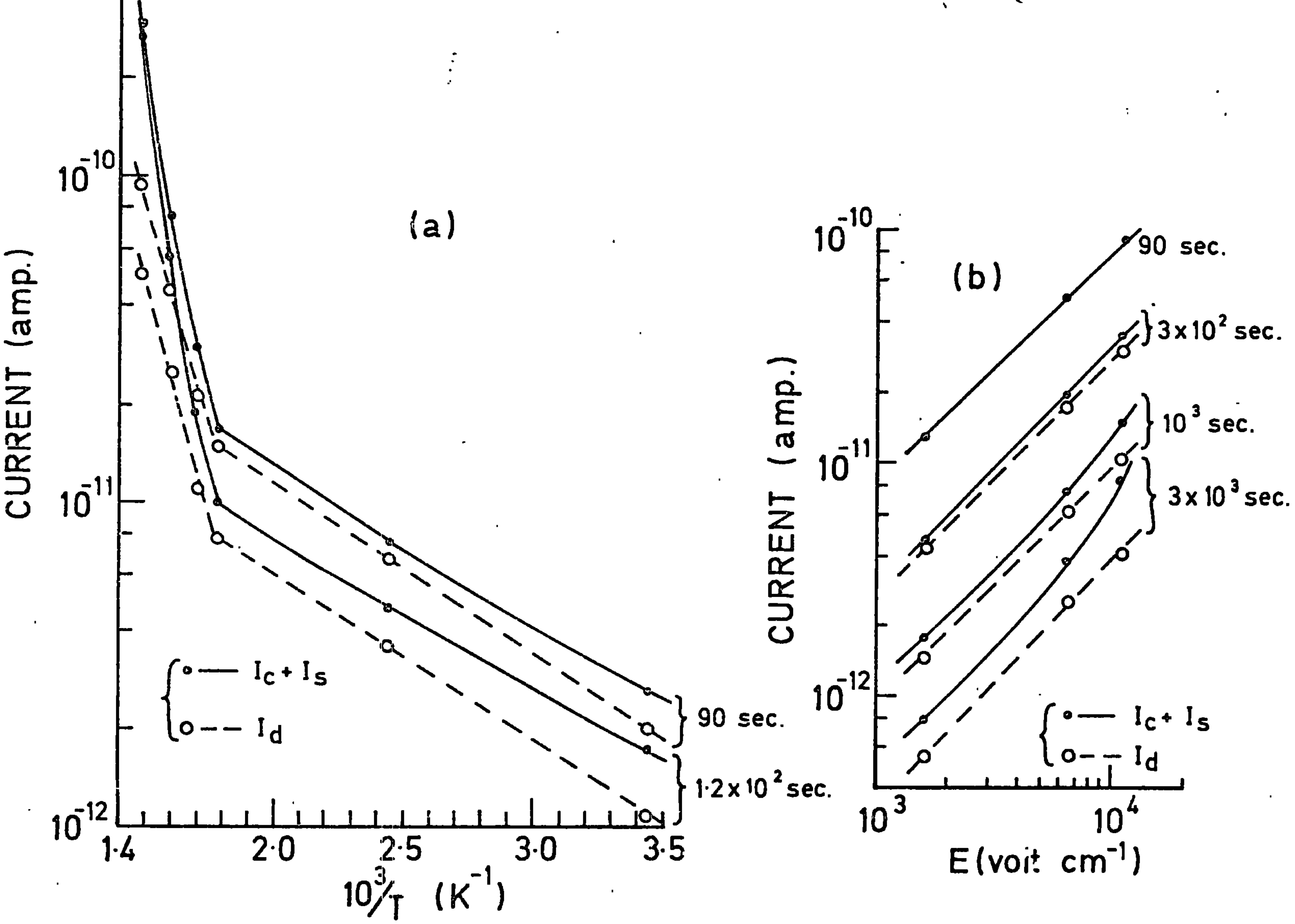

FIG.58(a) Temperature dependence of charging and discharging currents. (b) Field dependence of charging and discharging currents.. Data re-plotted from Fig. 6(a) and 6(b) respectively.

temperature and reaches finite values near room temperature in the range of 0.06 - 0.09 eV for different materials. One would expect a $\sigma \alpha \exp(^{-B}/_{T^{1/4}})$ law to be followed at low temperatures (18-19,26), where B is a constant which depends on the density of states at the Fermi level and on the spatial extent of the electronic wave-functions. Within experimental error the conductivity data below about 525 K agrees well with log $\sigma \alpha T^{-1/4}$ (Fig.5.9). Above that temperature the conductivity data deviates from linearity and a kink is observed at about 530 K in this plot. The value of B calculated from the slope of lnσ versus $T^{-1/4}$ was in the range of 50-80 for the four materials. This behaviour is characteristic of variable range hopping conduction by carriers with energies near the Fermi level (Chapter 2, Sect. 2.2). Similar values of E_A and B have been observed in many amorphous semiconductors. According to theory, the $T^{-1/4}$ law occurs at low temperatures and requires $E_a < 10$ KT ; therefore, this condition is met in the present results where 10 KT $\simeq$ 0.3 eV below 400 K and E_A was less than 0.09 eV. In the previous work (Chapter 3) however, although the data fits to a $T^{-1/4}$ law an interpretation on the same basis does not seem to be valid in the range 600 K to 900 K because $E_A \sim 1.0$ eV. At high temperatures, the value of E_A(approx.1.5 eV) and the pre-exponential factor $\sigma_o \sim 1$ ohm^{-1} cm^{-1} favour interpretation as hopping by carriers excited into the localized states near the edge of the conduction or valence bands (Chapter 2, Sect. 2.2). According to theory, conduction in extended states is not expected even at high temperatures up to 1273 K (Chapter 3, Sect. 3.4.1) as the value of σ_o did not exceed 1 ohm^{-1} cm^{-1} and the value of E_A was almost the same between 600 K and 1273 K.

(b) High Fields

The departure from a log J α log E variation in the J - E characteristic may be due to several effects (Chapter 2, Sect. 2.3). In the case of percolation theory and variable range hopping conduction near the Fermi level, the field dependence of conductivity can be expressed as (31-32)

$$\sigma \ \alpha \ \exp\left\{ e\ F\ a/_{KT} \right\} \qquad (5.2)$$

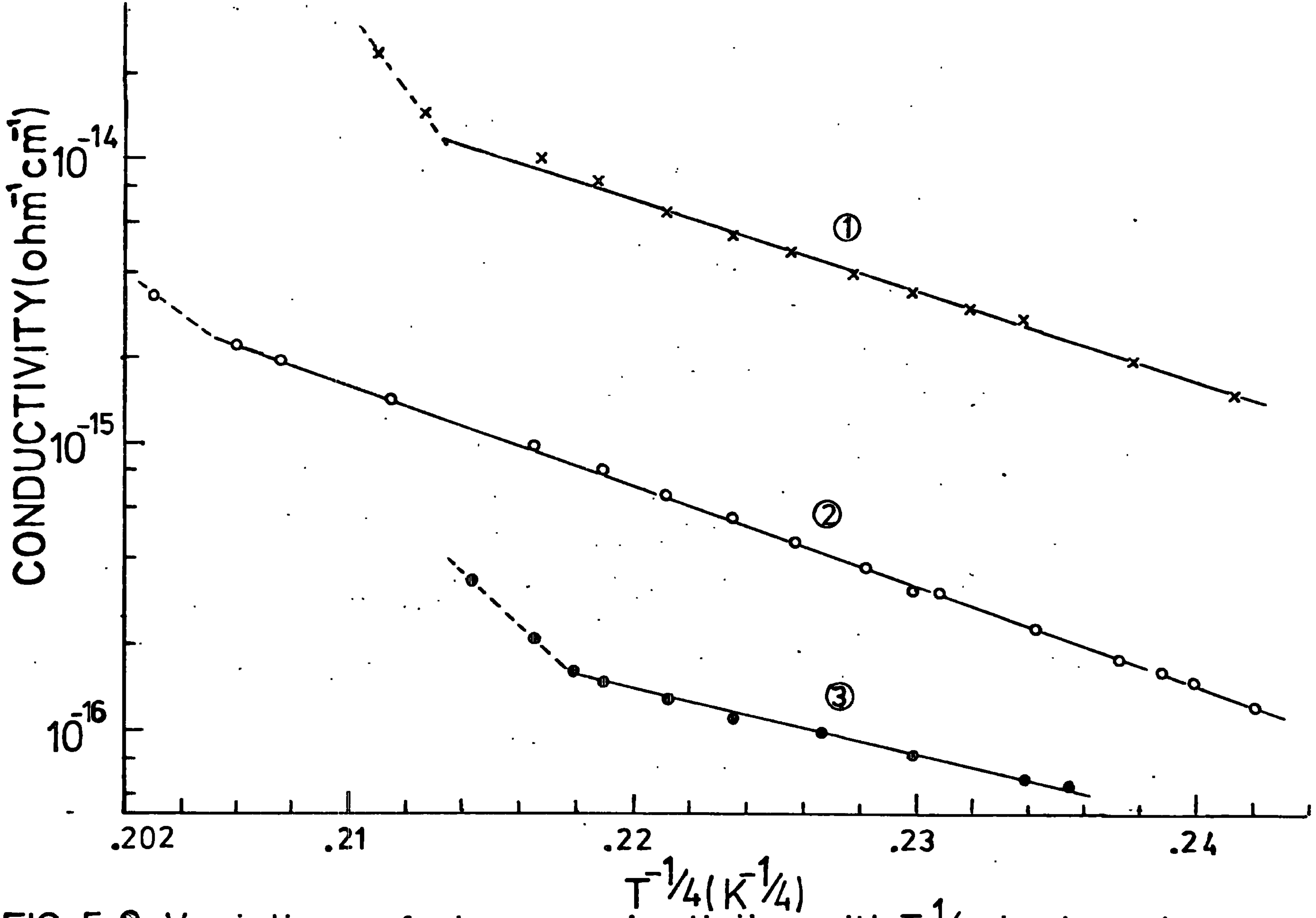

FIG. 5.9 Variation of d c conductivity with $T^{-1/4}$ in low temperature for ① Si_3N_4(×), ② 5w/o MgO/Si_3N_4(○) and ③ z=3.2 sialon(●). Data replotted from FIG. 5.4

where 'a' is the characteristic hopping length and F is a linear function of applied field. The log σ versus E plots are linear at room temperature (Fig. 5.3), fitting well with equation (5.2). This relation also applies at temperatures up to 550 K but the slope log σ versus E decreases with increasing temperature (Fig. 5.5). The values of 'a' calculated from the slopes at room temperature were in the range of 60 Å - 72 Å ; these are listed in Table 5.1. The data from Figure 5.5 shows that 'a' decreases with increasing temperature. This behaviour may correspond to the extension of the low field $T^{-1/4}$ law beyond the ohmic region (Chapter 2, Sect. 2.3). The effect of the field should be greater as the average hopping distance increases ; i.e. for lower temperatures and for low densities of states.

An alternative explanation would suppose that there may be a field-assisted contribution to the bulk dominated current due to the Poole-Frenkel effect (Chapter 2, Sect. 2.3) given by

$$\log J_{PF} = \text{constant} + \frac{e\,\beta^{\frac{1}{2}}}{KT} \qquad (5.3)$$

where $\beta = (^{e}/\pi\varepsilon'\varepsilon_{o})^{\frac{1}{2}}$ is the Poole-Frenkel constant and ε' is the high frequency dielectric constant of the material. This shows that a graph of log J versus $E^{\frac{1}{2}}$ ought to give a straight line with a slope $e\beta/_{KT}$. A fit to log J versus $E^{\frac{1}{2}}$ for nitrogen ceramics is observed at room temperature (Fig. 5.2 (b)), but the value of $\varepsilon' = 1.2$ derived from the relation (5.3) is smaller than experimentally measured microwave value $\varepsilon' = 4.5$ (Chapter 4, Sect. 4.3). Although the value of ε' at optical frequencies may be somewhat less than the microwave value quoted, the fit to equation (5.3) does not seem good. Moreover, at temperatures above 550 K, σ is independent of E (Figure 5.5) which implies that there is no field-assisted contribution.

5.4.2 DECAYING AND DISCHARGING CURRENTS BEHAVIOUR

The time-domain of step-response decaying and discharging currents follows the empirical law

$$(I_c(t) - I_s) = I_d(t) \propto t^{-n} \qquad (5.4)$$

with n<1, which is the "Universal law of dielectric response" suggested by Jonscher (78,82). The charging current, I_c is normally higher than the discharging current. It is known that $I_c(t) - I_s = I_d(t)$ is not always satisfied, the difference $I_c(t) - I_d(t)$ being itself a function of time and tending to I_s only in the steady state limit. The present measurements give values of n derived from I_c (without I_s subtracted) and I_d between 0.7 and 0.8 at room temperature ; from the I_c data it was found that n decreased to 0.45 at 673 K. The exponent n is almost independent of applied field up to 10^4 volt cm^{-1} (Fig. 5.6 (b)). Further analysis of the data shows that the charging current I_c (after I_s is subtracted) follows the t^{-n} law more linearly for a longer time up to the region of fluctuation. The idealised relation $I_d(t) = I_c(t) - I_s$ is not always satisfied in some data ; the value of $I_c(t) - I_s$ is sometimes slightly higher than I_d. Figure 5.10 illustrates the type of relation between the total charging current $(I_c + I_s)$, the charging current after subtraction of the steady value current I_s and the discharging current I_d for all four specimens. This behaviour has been observed in many amorphous materials and insulators. Jonscher (78,82) and Lewis (110) have sugggested that equation (5.4) provides an alternative treatment equivalent to the frequency domain approach which results in the Universal law of dielectric loss $\varepsilon''(\omega) \propto \omega^{n-1}$ or $\sigma'(\omega) \propto \omega^n$ with n<1 (Chapter 2, Sect. 2.6). This type of loss behaviour was observed in these materials (Chapter 4). Comparison of the n values obtained by both methods shows very close agreement, both in respect of the room temperature magnitudes and the temperature variations. Further analysis shows that the temperature dependences of I_c and I_d (Fig. 5.8 (a)) are very similar to that of I_s (Fig. 5.4). Two distinct temperature dependent regions of I_c and I_d,

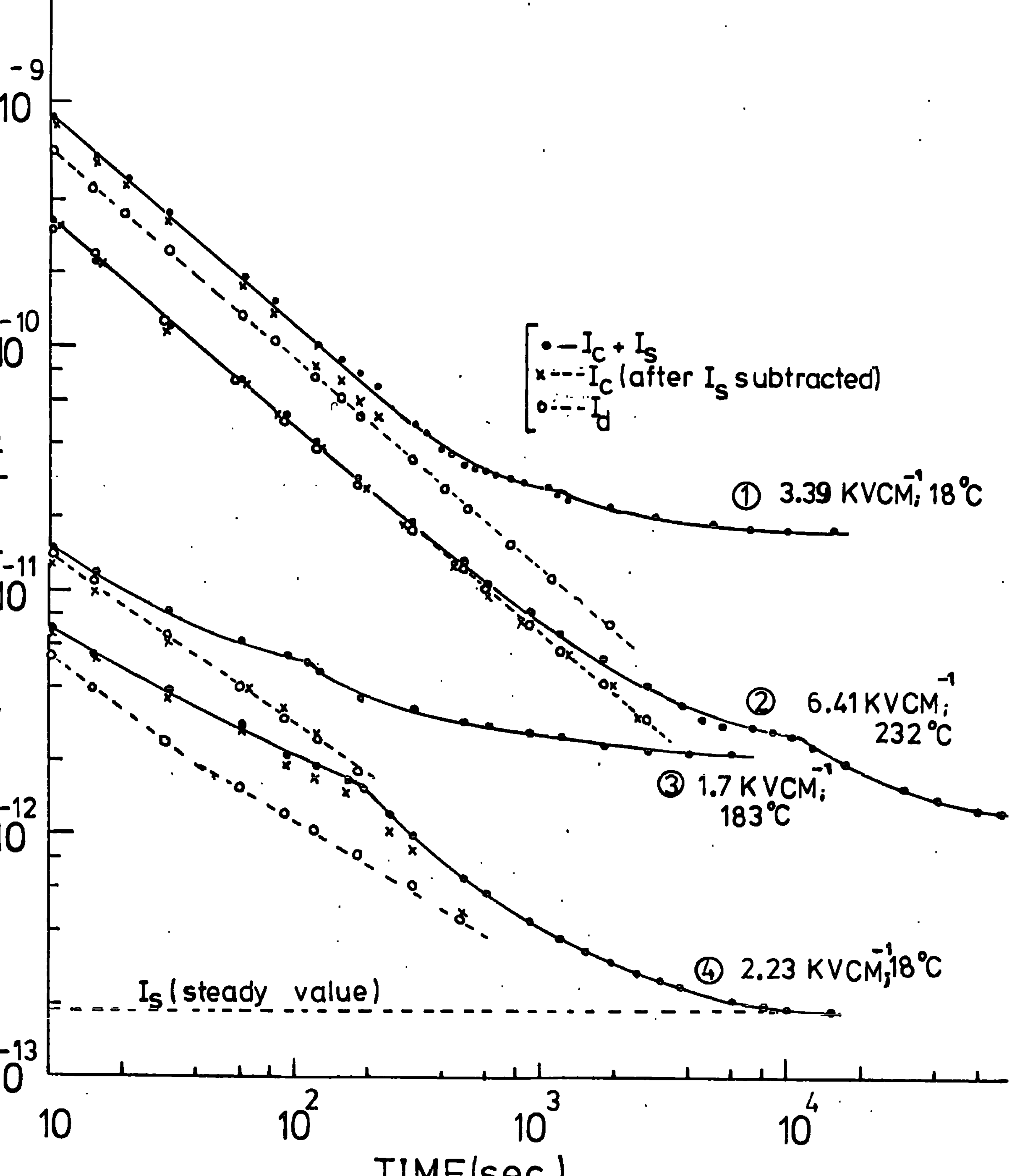

FIG.5.10 Comparison of charging($I_c + I_s$), charging I_c(after I_s subtracted) and discharging I_d currents for ① Si_3N_4, ② 5 w/o MgO/Si_3N_4 ③ Z = 3.2 sialon and ④ Z = 4.0 sialon.

above and below about 550 K, are observed and the activation energies from I_c are 1.4 eV and 0.06 eV respectively. It is relevant to mention that similar temperature dependences of $\sigma'(\omega)$ and $\epsilon'(\omega)$ of the same materials have been observed (Chapter 4, Sect. 4.3.2) and the values of E_A derived from $\log\sigma'(\omega)$ versus T^{-1} above and below T_t = 550 K were very similar ; only at low temperatures were the activation energies found to decrease slowly with increasing frequency. Comparison of Figures 5.2 and 5.8 (b) shows that the slopes of log I_c versus log E and also of log I_d versus log E are very similar to the steady current variation below the transition temperature 550 K. At short times the relation of I_c is linear over the whole field range but at longer times there is a tendency for non-linearity at high fields. The behaviour discussed in this section may be due to the following mechanism. Most available carriers in the system respond initially to the applied field ; later they are impeded by having to make difficult hops over longer distances ; this may lead to "piling up" of other carriers behind those so held up, ultimately giving a steady value after a long time. The tendency for non-linearity at high fields may be due to nearest neighbour correlation between successive hops and increased critical links in the percolation paths (Chapter 2, Fig. 2.3, Sect. 2.3). This evidence indicates further that the origin of the low and high field conduction mechanisms is probably the same.

It seems that the d.c. conduction is likely to be determined by the most difficult hops where bottlenecks occur, while in the increase of conductivity with frequency the carriers hop back and forth over a limited number of "easy hops". On the basis of this the value of σ_{dc} is expected to be lower by some orders of magnitude than that of $\sigma'(\omega)$; this difference is observed in these materials (Chapter 4, Fig. 4.7). The above analysis suggests that the dominant d.c. conduction mechanisms is hopping. Further the correlation between the temperature variations of d.c. and a.c. parameters and especially the similarity between the respective activation energies show strong evidence for the conduction being due to hopping charge carriers rather than dipoles (Chapter 2, Sect. 2.6). If the mechanism were dipolar, the d.c. and a.c. responses would not be expected to correlate at all (82).

Some comments may be made about space charge effects. Jonscher and Careem (112) have suggested that one of the causes of strongly non-linear behaviour in I-V characteristic at high fields is due to injection of space charge from electrodes. They have proved that if these are present the I_c and I_d curves will intersect (under condition of high field and high temperature) so that, at sufficiently short times $I_d > I_c$ violates the condition $I_c(t) = I_d(t) + I_s$. This is observed when a finite amount of injection takes place from the electrodes, so that the discharge current finds initially an additional space charge polarisation superimposed on the average field in the system. This contrasts with the situation when the charging current starts from the fully discharged condition; one may assume that no space charge has been left in the system. In the absence of space-charge there is no intersection and I_c is always greater than I_d. This offers a convenient non-destructive way of testing for the presence of space charge in insulators. In almost all the present experimental data, $I_c > I_d$ and no intersection at high field and high temperature was observed. This confirmed that the heat treatment given to the specimens (Section 5.2) was effective in minimizing space charge and thus it can be assumed that the behaviour is due to dielectric response of a bulk dominated time domain current.

As mentioned earlier slight fluctuations in the decays of I_c are observed (Fig. 5.6, 5.7 and 5.10). The effect has been reported for other materials and several explanations of this behaviour have been given (113). The most recent explanation is a transit time effect for injected carriers (109). It is also mentioned that these currents $(I_c + I_s)$ may be due to the drift of injected electrons. On this assumption the results shown in Figs. 5.6 (a) and (b), Fig. 5.7 and Fig. 5.10, have been used to calculate drift mobilities from the relation

$$\mu_D = {}^{d}/_{t_t \cdot E} \qquad (5.5)$$

where d, t_t and E are the thickness of the specimen in cm ; the transit time in sec. and the applied electric field in v cm^{-1} respectively ; these are listed in Table 5.1. The fluctuation time is almost independent of temperature which implies that μ_D is independent of temperature. Similar effects were noted for other specimens. This very low value of mobility coupled with its temperature independence further supports the concept of conduction in the localized states (Chapter 2, Sect. 2.4). The mobility determined from Hall-effect measurement between 400° C and 1000° C was also less than 10^{-5} cm^2 v^{-1} sec^{-1} (Chapter 3, Sect. 3.4.2). This implies that the carriers are strongly localized in some centres and their motion occurs by hopping from one localized centre to another.

The magnitude and temperature dependence of σ is likely to be determined mostly both by the density of localized carriers (perhaps around imperfections and impurities) in different phases and by their corresponding activation energies. The presence of a glassy phase does not seem to be a dominant factor in determining the conductivity behaviour.

CHAPTER 6

ELECTRICAL PROPERTIES OF 30 m/o Li-SIALON AND 14.3 m/o Y- SIALON GLASS

6.1 INTRODUCTION

As described in previous chapters, sialon ceramics, made by hot-pressing α-Si_3N_4 and α-Al_2O_3, have been established as materials with many potential high temperature engineering applications. The preparative techniques have been further extended to make lithium-sialon and yttrium-sialon (5,114). The β' sialons, produced by reacting silicon nitride and lithium aluminospinel ($LiAl_5O_8$), are isostructural with β-Si_3N_4 and similar to the β'-phase produced in the Si-Al-O-N system. Their compositions have been represented by

$$Li_{x/8}\ Si_{6-\frac{3}{4}x}\ Al_{\frac{5}{8}x}\ O_x\ N_{8-x}$$

where x and (8-x) are respectively the numbers of oxygen and nitrogen atoms in the unit cell, in which x has the limiting value ∿5. Jack (5) has explained the compositions and phases of lithium sialon by a phase diagram (Fig. 6.1). It shows that the reaction of silicon nitride with lithium spinel, $LiAl_5O_8$ gives a β' - lithium sialon in the LiO-Si_3N_4- Al_2O_3 system. Other major phases have structures based on β-eucryptite (Eu'), spinel (S), silicon oxynitride (O' or Ox), tetragonal cristobalite (γ) and the polytype ISR. Spinels in general react with silicon nitride to give β'-phases provided the ratio of metal : non-metal atoms is 3:4. Yttria, Y_2O_3, may also be used as the addition in sialon. The idea of using an yttrium additive to form yttrium sialon has been described in (115). This product is noteworthy in that it is made of almost entirely glassy phase material. This feature distinguishes it

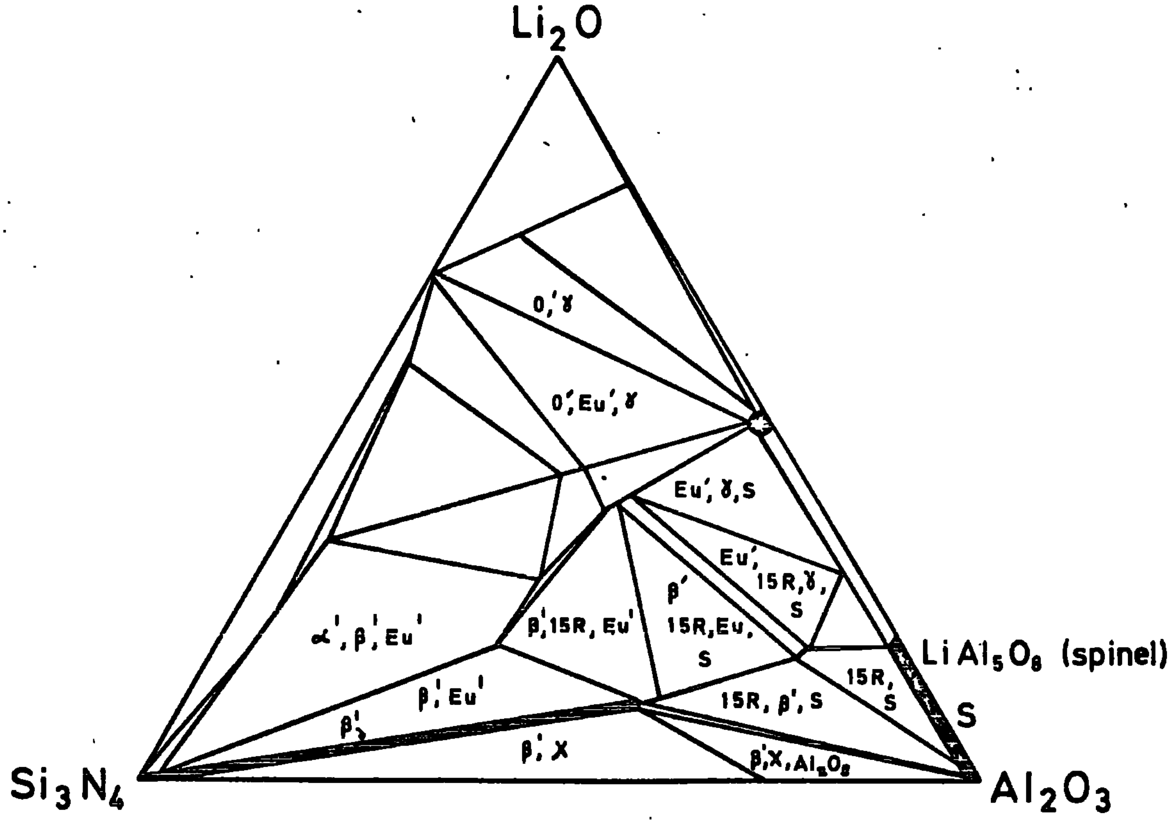

FIG. 6.1 The $Li_2O - Si_3N_4 - Al_2O_3$ section of the Li-Si-Al-O-N system at 1550°C. (after ref. 5)

from pure sialons and lithium-sialons, all of which are predominantly crystalline.

Some physical and chemical properties of lithium and yttrium sialons have been mentioned in (5, 114) and preliminary studies of its electrical properties have been reported in the theses by Kavanagh (116) and by Jama (114). Information about the d.c. electrical conductivity of some lithium compounds such as lithium-aluminium oxide and lithium silico-aluminate glasses is found in (117-118). It is known that some lithium compounds might be suitable as solid electrolytes for high voltage cells if compounds could be formed which exhibit room temperature electrical conductivity values comparable with silver or sodium-substituted beta-alumina. The transport mechanism in some lithium compounds is the hopping type ; in others, d.c. electrical conductivity experiments carried out by Kato (119) show that ionic conduction is present in some lithium compounds coupled with electronic conductivity.

In this Chapter the d.c. field, temperature and frequency dependences of electrical properties for 30 m/o lithium sialon and 14.3 m/o yttrium sialon glass are described. A comparison of the results of pure and doped sialons was made in an attempt to relate the compositions and electrical properties.

6.2 EXPERIMENTAL

The sialon specimens used in this work had nominal compositions 30 m/o lithium and 14.3 m/o yttrium. The structural properties and a knowledge of phases present in the specimens were provided by Jack (5) and Jama (114). The phases identified by x-ray powder analyses showed that the 30 m/o lithium sialon was almost all β' phase with 5% of x-phase and trace amounts of Y-phase. The β'-phase is a hexagonal with an expanded β-Si_3N_4 structure, X-phase is a monoclinic phase (SiO_2 : AlN) and Y-phase is a crystalline phase of unknown composition and distorted wurtzite crystal structure. The 14.3 m/o yttrium sialon contained about 98% glassy phase, the remainder being a crystalline β'-sialon phase. X-ray powder photographs of z = 4.0 sialon, 30 m/o Li-sialon and 14.3 m/o Y-sialon specimens were taken using a standard method ; these are shown in Figure 6.2 for comparison. Clear diffraction patterns are observed for both the pure and lithium-doped sialon specimens, proving the presence of crystalline phases. For the Y-sialon specimen, on the other hand, there are no visible diffraction lines, indicating that the specimen contained almost entirely glassy phase. The unit-cell dimensions of β' for 30 m/o Li-sialon and z = 4.0 sialon are a = 7.64 Å ; c = 2.94 Å and a = 7.72 Å ; c = 2.99 Å respectively (5,7,114).

It is known that most lithium compounds volatilizes at the time of preparation of lithium sialons by hot-pressing. As a result weight losses often occurred in hot-pressing α-"Si_3N_4" - lithium compounds. In (114) weight losses of between 1 and 11% were recorded for lithium sialons in the composition range 20-33 m/o $LiAl_5O_8$: 67-80 m/o Si_3N_4. For this reason chemical analyses of all the lithium sialon products were made. This analytical work was undertaken by Kavanagh (116) using an atomic absorption spectroscopy method outlined briefly below.

The samples were first crushed and put through a 53 micron sieve. It was then necessary to make a solution with the powder. This proved difficult. A solvent consisting of a mixture of HF and HclO was tried. This method was partially successful but usually left a small amount of an insoluble white residue. The fusion approach was also used ; the powdered sample was fused with Na_2CO_3 and then dissolved in Hcl. This gave a clear solution. The solution was then analysed using atomic absorption spectroscopy for lithium, silicon and aluminium. The errors associated with these analyses occurred when trying to get the sialon powder into solution and the estimated error was ± 0.1% in the weight of element. The actual analysis of the 30 m/o $LiAl_5O_8$, 68 m/o Si_3N_4, 2 m/o AlN sialon used was 0.65 w/o lithium whereas starting composition was 1.16 w/o ; the aluminium and silicon analyses agreed closely with the starting composition. No attempt has yet been made to obtain an analysis of the yttrium sialon.

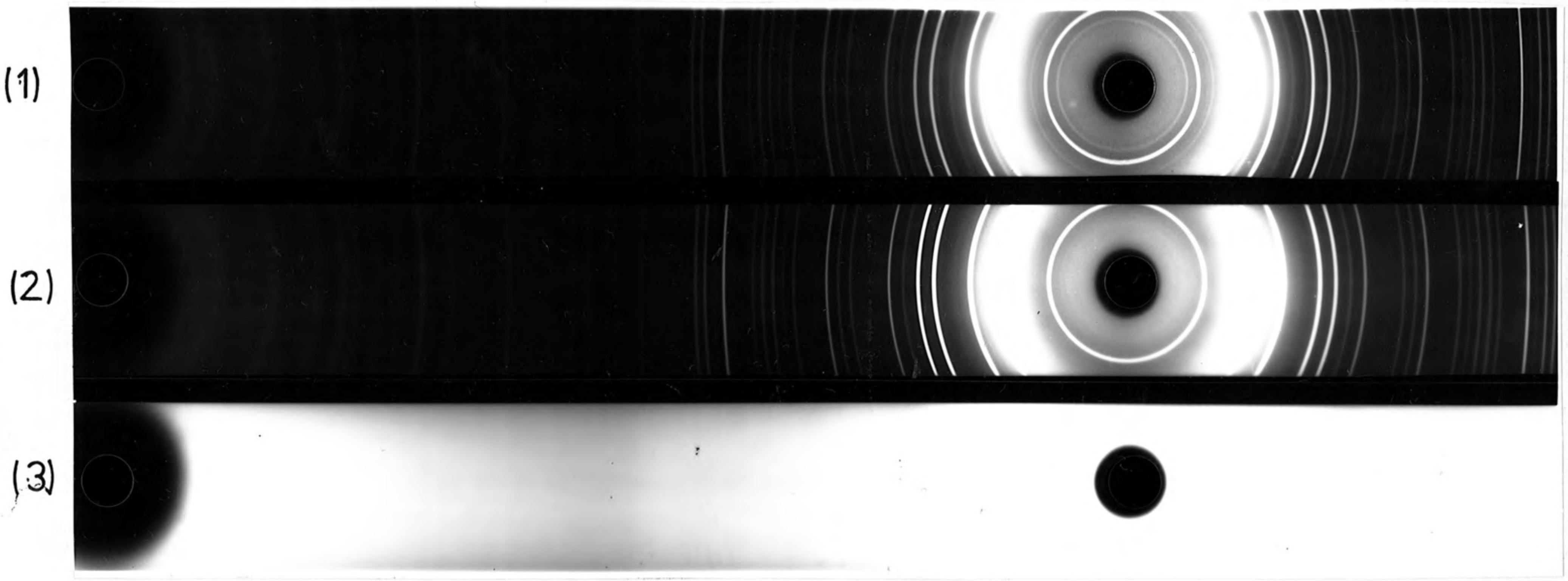

FIG. 6.2 X-ray diffraction patterns of (1) z=4.0 sialon, (2) $30^{m}/_{o}$ Li-sialon and (3) $14.3^{m}/_{o}$ Y-sialon.

All the measurements of conductivity (both d.c. and a.c.), charging/ discharging currents, Hall effect, dielectric constant and dielectric loss were made by the methods described earlier.

6.3 RESULTS

6.3.1 PRELIMINARY CONDUCTIVITY DATA FOR LITHIUM-SIALON

The following results were obtained using methods described in Chapter 3.

In Figure 6.3 the temperature variation of d.c. conductivity for 30 m/o Li-sialon, measured under a low applied field, between 537 K and 1273 K is shown as a log σ versus T^{-1} plot. Readings were taken stepwise both during heating and cooling allowing adequate time at each temperature for the specimen to attain a steady condition. The arrows indicating the sense (heating or cooling) in which the data were taken. After the initial run the specimen was left at room temperature (with no field applied) and three further runs were taken after an interval of 24 hours. The values of conductivity decreased progressively between successive runs and the results were entirely irreversible. In each run the relationship between log σ and 1/T is linear between 700 K and 1273 K. The activation energies obtained from the initial and final runs were 0.79 eV and 1.86 eV respectively. After this series of measurements a colour change in the specimen was observed; the anode became black and the cathode became brown. Electrode polarization effects were observed at high temperatures (but not at low temperatures) and for this reason true values of high temperature conductivity could not be defined.

The temperature variation of complex conductivity, $\tilde{\sigma}_{ac}(\omega)$ over the frequency range 15 Hz to 5 KHz,between 500 K and 1270 K is shown in Figure 6.4. In the lower temperature region, (below about 850 K), $\tilde{\sigma}_{ac}(\omega)$ is strongly dependent on frequency but weakly dependent on temperature ; $\tilde{\sigma}_{ac}(\omega)$ follows a $\tilde{\sigma}_{ac}(\omega) \alpha\ \omega^n$ law with n = 0.9 as observed previously in pure sialons (Chapter 3, Section 3.4). At high temperatures $\tilde{\sigma}_{ac}(\omega)$ was found to be the same at all

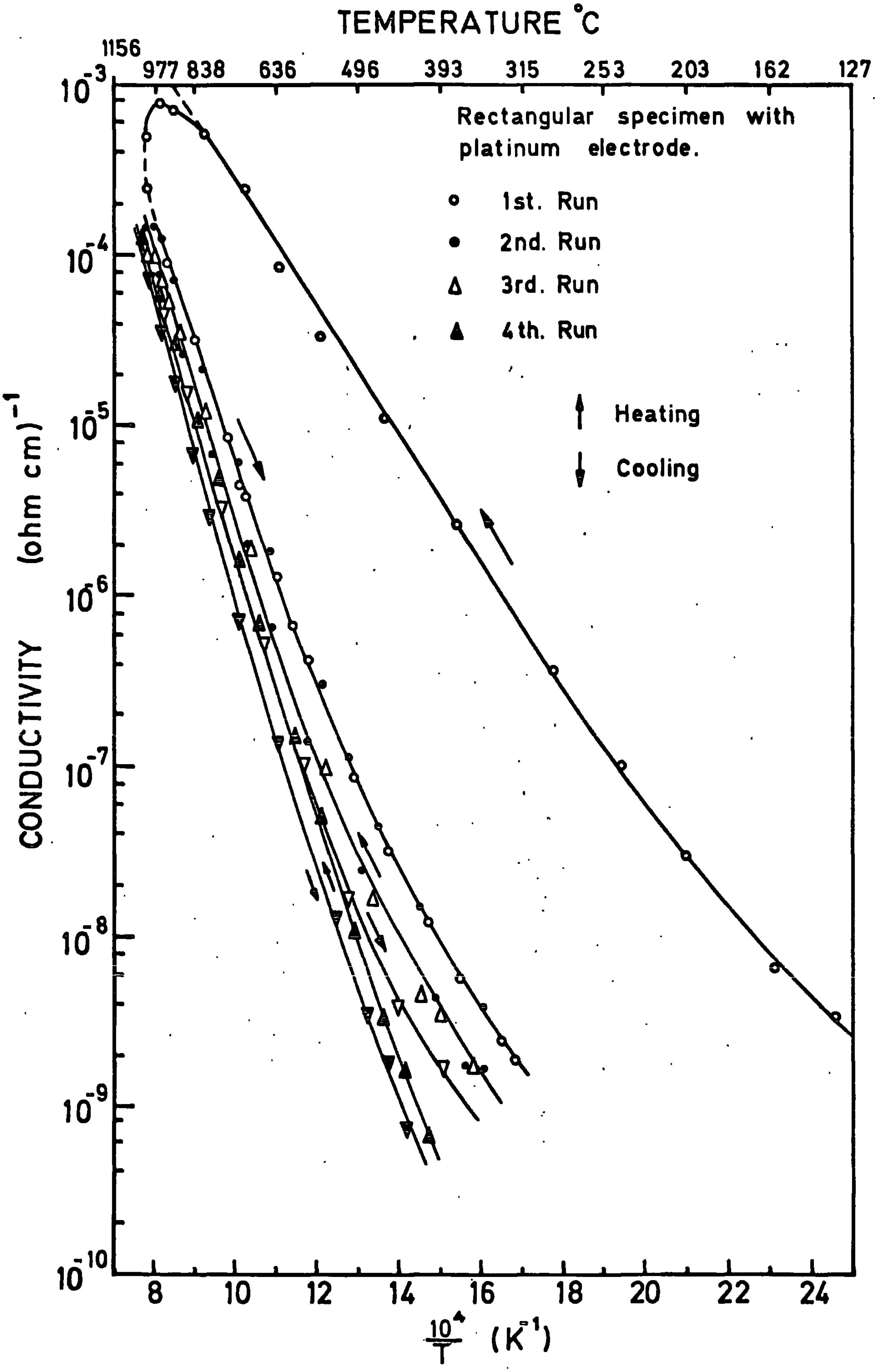

FIG. 6.3 Degradation of dc conductivity from the initial steady value for 30 m/o Li-sialon at high temperature.

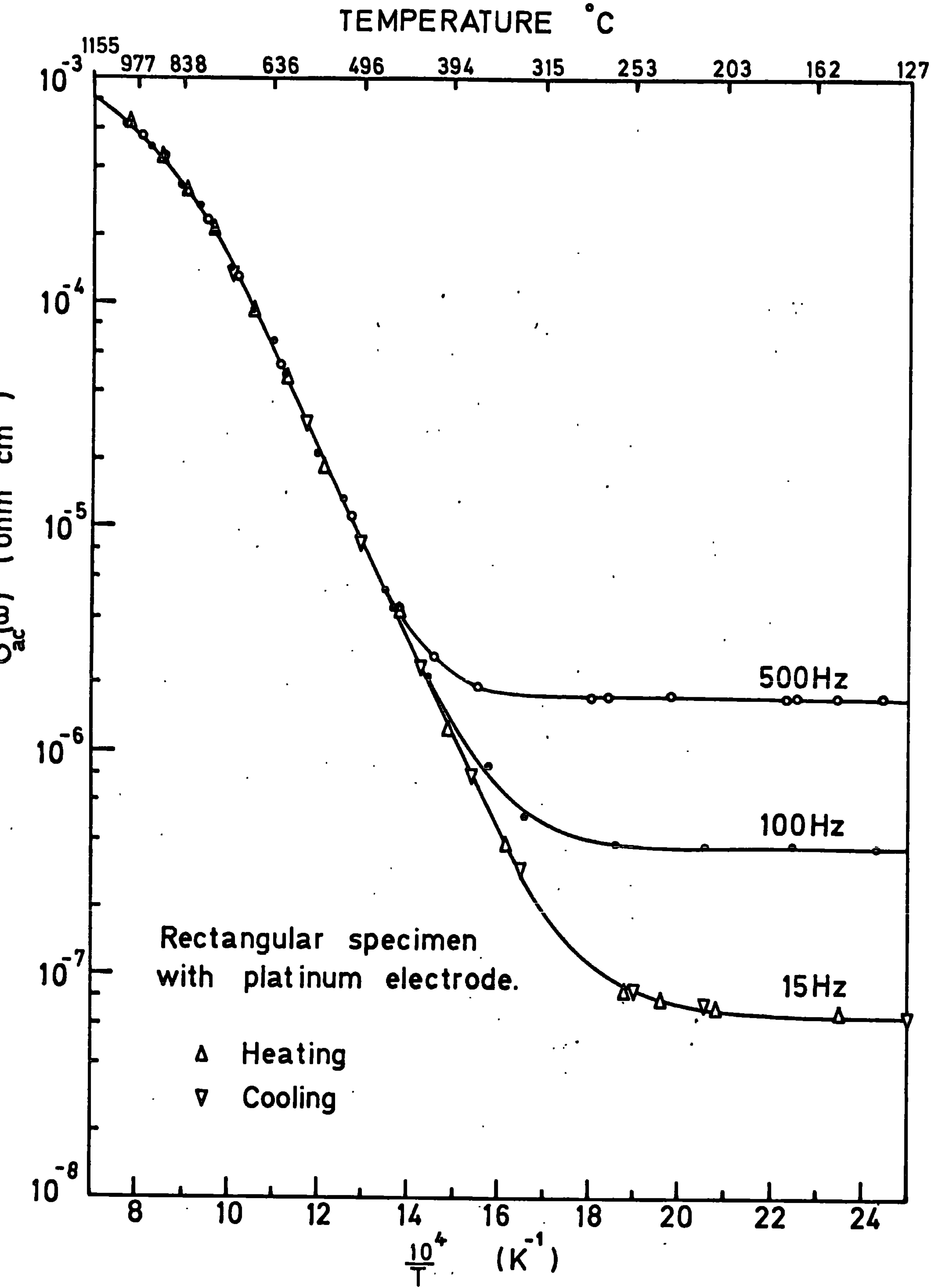

FIG. 6.4 Variation of complex conductivity with reciprocal temperature at different applied frequencies for 30 m/o Li-sialon.

frequencies and became temperature dependent giving a log $\tilde{\sigma}_{ac}(\omega) - T^{-1}$ variation very similar to that found for the initial σ_{dc} at high temperatures. The activation energy derived from these high temperature a.c. results was 0.82 eV, which agreed well with the value obtained from the initial run of σ_{dc} data. Neither polarization effects, nor colour change of the electrodes was observed in the a.c. measurements.

No Hall voltage was observed in the lithium sialon specimen between 573 K and 1200 K under the conditions described in Chapter 3, Sect. 3.3. Thus, the estimated Hall mobility is probably less than 10^{-4} cm^2 v^{-1}sec^{-1}.

6.3.2 D.C. ELECTRICAL PROPERTIES

All the results presented below were made with thin specimens with gold electrodes at temperatures between 291 and about 750 K using a refined technique described in Chapter 5. The nature of the electrical properties was very similar in lithium and yttrium specimens.

The decay of the total charging currents ($I_C + I_S$), the charging currents after subtraction of the steady current I_s and the discharging currents I_D (reverse polarity of I_C) of 30 m/o Li-sialon with time under different applied fields at room temperature are shown in Figure 6.5 in which log I is plotted against log t. The initial charging current I_C and discharging current I_D each follow a $I(t) \alpha t^{-n}$ law, with n = 0.8. The time for the current to decay to a steady value (I_S) was 3 hours and became shorter with increasing applied field. A slight fluctuation in the decay of charging current is observed around, 10^2 sec. The time of occurrence of the fluctuation region decreases with increasing applied field. The discharging current-densities for different applied fields at t = 120 sec are plotted in Fig. 6.6 (a) which shows that the log J_D versus log E plot is linear.

The variation of steady current with applied fields at room temperature is shown in Figure 6.6. In Figure 6.6 (b) the plot of log (J_S) versus log E is linear at low electric fields (< 3 kv cm^{-1}) and becomes non-linear at

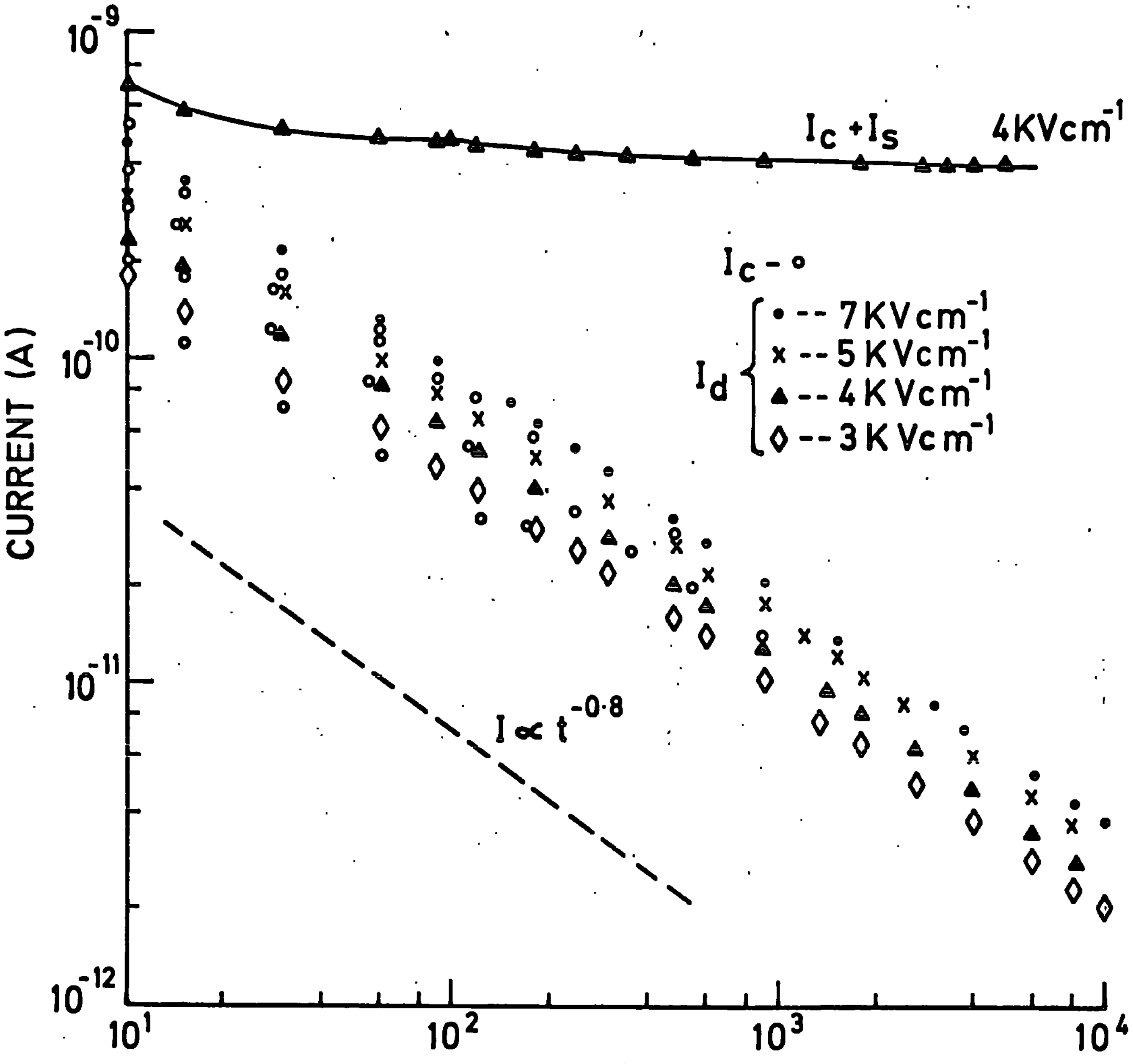

FIG.6.5 Typical charging currents ($I_c + I_s$), charging currents, I_c (after I_s subtracted) and discharge currents, I_d for 30m/o Li-sialon under different applied fields at room temperature.

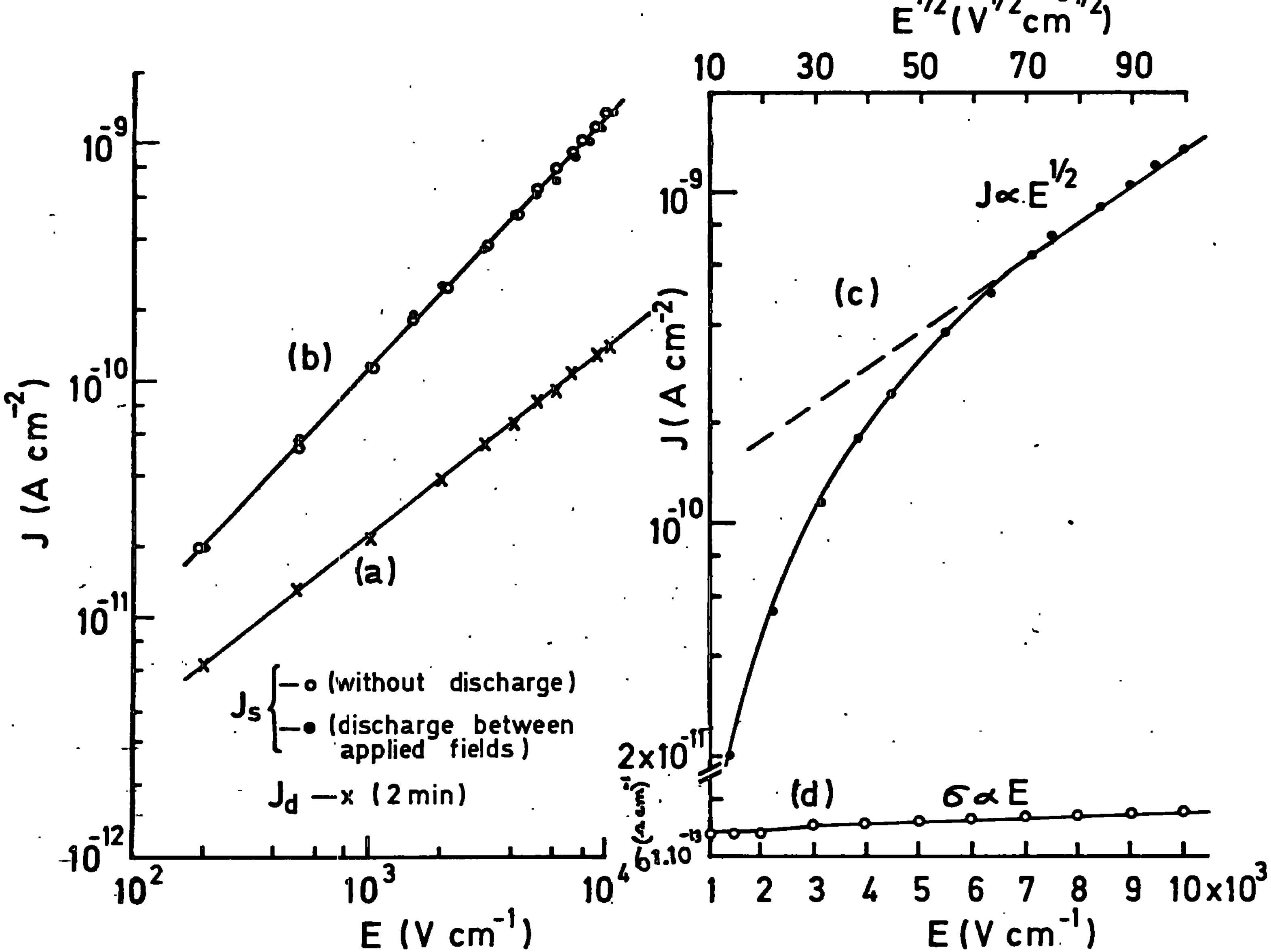

FIG.6.6(b) Log J_s versus log E, (c) Log J_s versus $E^{1/2}$ and (d) Log σ versus E for 30 m/o Li-sialon at room temperature.

moderately high electric fields. The steady currents obtained at different applied fields by the two methods (Chapter 5, Sect. 5.2) are the same within the limit of experimental error (Fig. 6.6 (b)). The same data are replotted in Fig. 6.6 (c) in the form of log (J_s) versus $E^{\frac{1}{2}}$ which is straight line in the high field region. The conductivity is almost independent of E in the low applied fields but in the high field region varies as log $\sigma \alpha E$ (Fig.6.6 (d)) After the same specimen had been used for a very long time no electrode polarization was noticed at room temperature and the results were reproduceable.

The temperature variation of conductivity for 30 m/o Li-sialon and 14.3 Y_2O_3 sialon at a low applied field is shown in Figure 6.7. The relation between log σ and T^{-1} is linear between 725 K and 525 K for lithium specimen and between 825 K and 770 K for yttrium specimen and becomes non-linear at lower temperatures. The values of activation energies (E_A) were calculated from the relation

$$\sigma = \sigma_o \exp \left({}^{-E_A}/_{KT} \right) \qquad (6.1)$$

in the linear higher temperature region and from the slopes of the curves near room temperatures ; these are listed in Table 6.1. The pre-exponential factor was calculated from the linear high temperature region and gives $\sigma_o \sim 1 \text{ ohm}^{-1} \text{ cm}^{-1}$.

In order to study the degradation effects at high temperature, a lithium specimen was kept under constant applied field conditions at 537 K for a long time (e.g. 30 hours). The temperature variation of steady currents was then measured after intervals of 30, 55, 80 and 110 hours at constant applied field. These are illustrated in Figure 6.8 (a) in which log I is plotted against T^{-1}. It was observed that the initial steady currents reduced less than half an order of magnitude after such a long time (110 hours). After this series of measurements the specimen was discharged at 537 K, I_D initially decreased for 10 minutes and became constant. This steady I_D

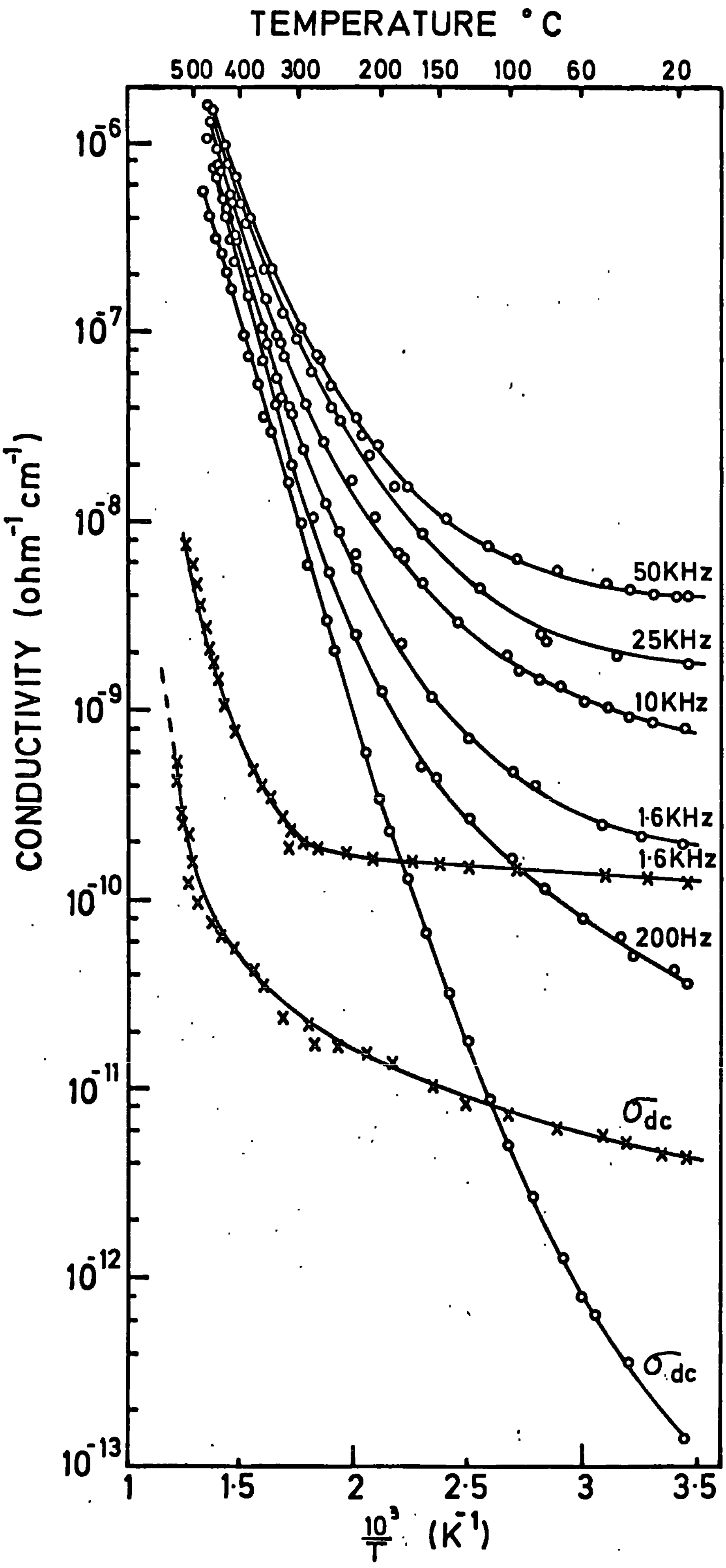

FIG.6.7 Temperature variations of dc and the real part of a.c. conductivities for 30 m/o Li-sialon (∘) and 14.3 m/o Y-sialon glass (×).

Sample	Nominal Composition	Conductivity (Ω^{-1} cm^{-1})		Activation Energy (eV)		σo ($\Omega^{-1}cm^{-1}$) from high temp.	Room Temperature Data		
		18° C	450° C	high temp.	low temp.		Hopping length "a" (Å)	Value of n	Drift mobility $\mu_D(cm^2V^{-1}sec^{-1})$
1.	30 m/o Li-sialon	1.3×10^{-13}	3.2×10^{-7}	0.83	0.30	0.5	32.15	0.8	2×10^{-7}
2.	14.3 m/o Y_2O_3-sialon	4.4×10^{-12}	1.8×10^{-9}	1.40	0.05	0.26	-	-	-
Chapter 4.	$z \simeq 3.2$ sialon	1×10^{-16}	4.0×10^{-12}	1.45	0.05	0.05	65.0	0.7	7.35×10^{-8}

TABLE 6.1: D.C. Electrical Parameters for Sialons (pure and doped).

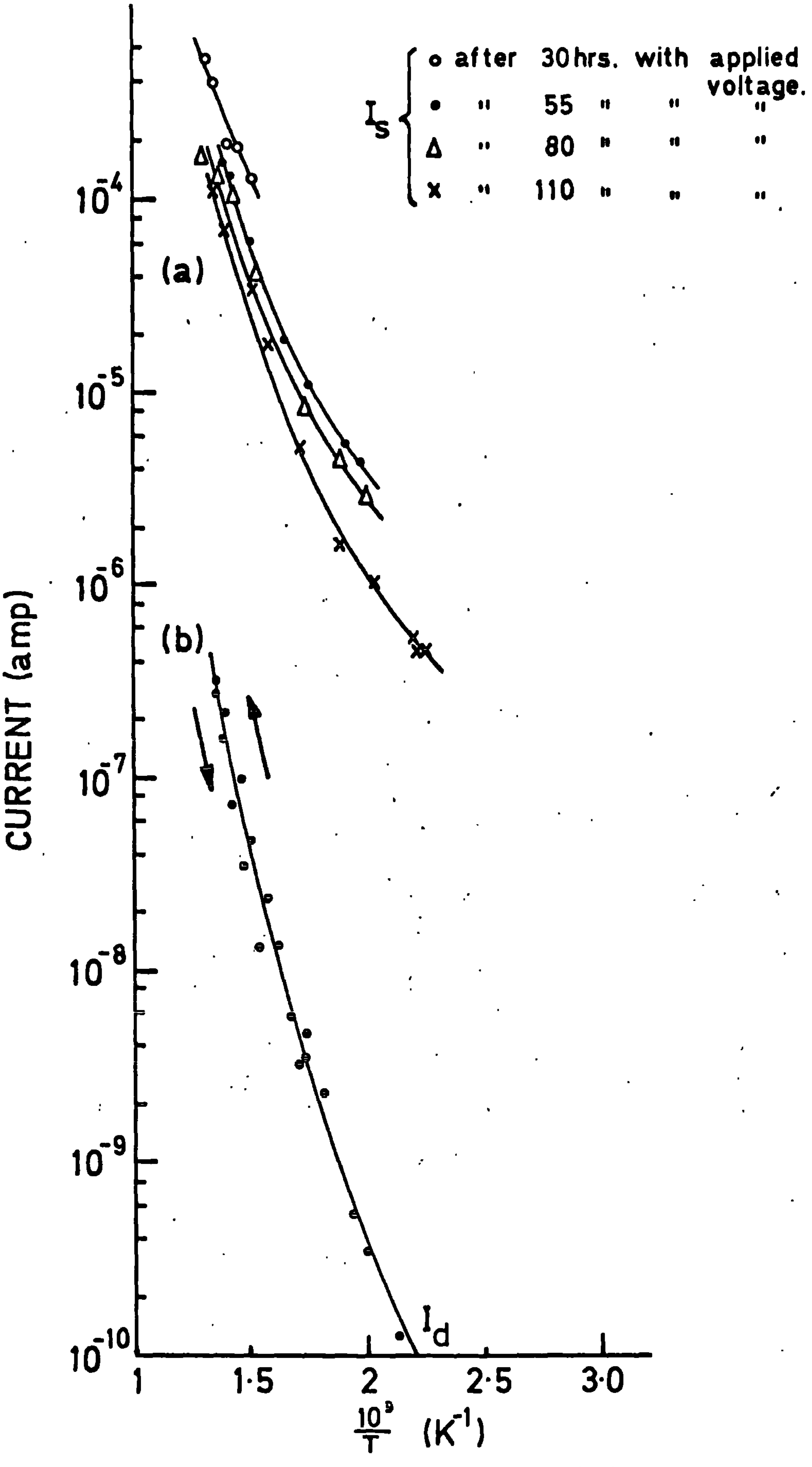

FIG. 6.8 Temperature variations of (a) initial steady currents at different times and (b) steady discharge current for 30 m/o Li-sialon.

(about 10^{-7} amp) did not reduce significantly even after 12 days and varied with temperature (Fig. 6.8 (b)). A colour change of the specimen was observed which was similar to that mentioned above. Black and brown layers were formed as precipitates on the anode and cathode surfaces respectively. After removing the gold electrodes from the specimen by using aqua regia (conc. Hcl/HNO_3) some micrographs of the respective anode and cathode surfaces were taken with a metallurgical microscope (Vickers Ltd). Figure 6.9 demonstrates the black precipitate layer on the anode surface of the specimen (x 600 magnification). This behaviour was not observed in yttrium sialon ; however its conductivity decreased by 10% from initial steady value during thermal treatments. This behaviour is significant and will be discussed in Section 6.4.

It is noticed that σ_{dc} for lithium sialon is less than for yttrium sialon at temperatures below 385 K while the former is much higher above that temperature. The conductivities of both materials are at least two to three orders of magnitude higher than that of pure sialon (Chapter 5, Sect. 5.3.2) throughout the temperature range. The values of conductivity for the three materials (pure and doped sialons) at 291 K and 723 K are listed in Table 6.1 for comparison.

6.3.3 A.C. ELECTRICAL PROPERTIES

The following results were obtained using the methods described in Chapter 4. The frequency variation of the true a.c. conductivity, $\sigma'(\omega)$ (deduced from the difference between the experimental data for the real part of conductivity, $\sigma(\omega)$ and the d.c. conductivity σ_{dc}) at room temperature is shown in Figure 6.10. Over the frequency range 200 Hz to 3 MHz, this fits well with the relation (Chapter 4)

$$\sigma'(\omega) = (\sigma(\omega) - \sigma_{dc}) \quad \alpha \quad \omega^{n} \qquad (6.2)$$

where n has the value 0.78 for yttrium sialon and 0.9 for lithium sialon ;

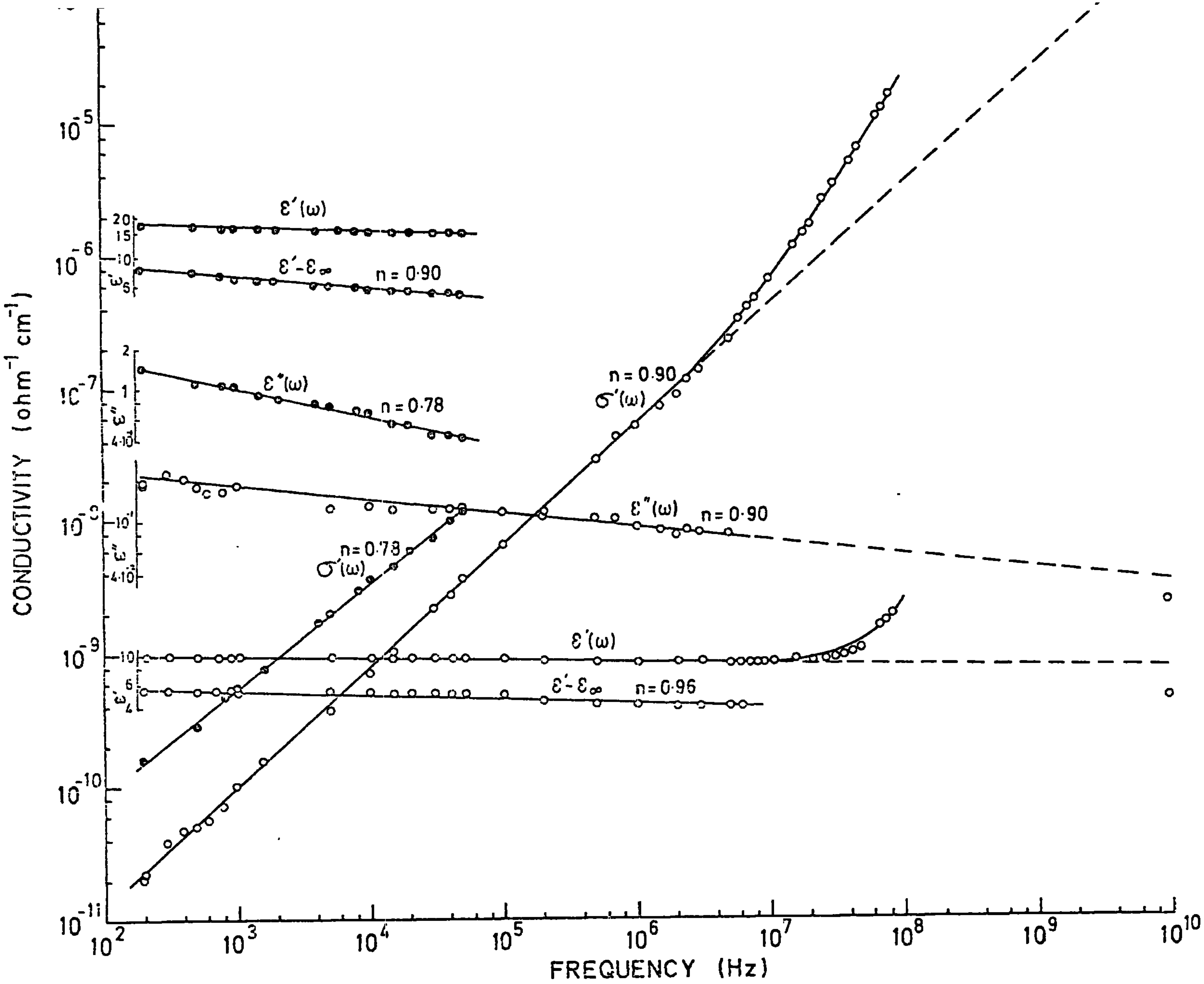

FIG.6.10 Frequency dependance of conductivity, σ′(ω), dielectric loss, ε″(ω), and dielectric constant, ε′(ω) and ε′(ω) - ε∞ for 30 m/o Li-sialon (○) and 14·3 m/o Y-sialon (●) at room temperature

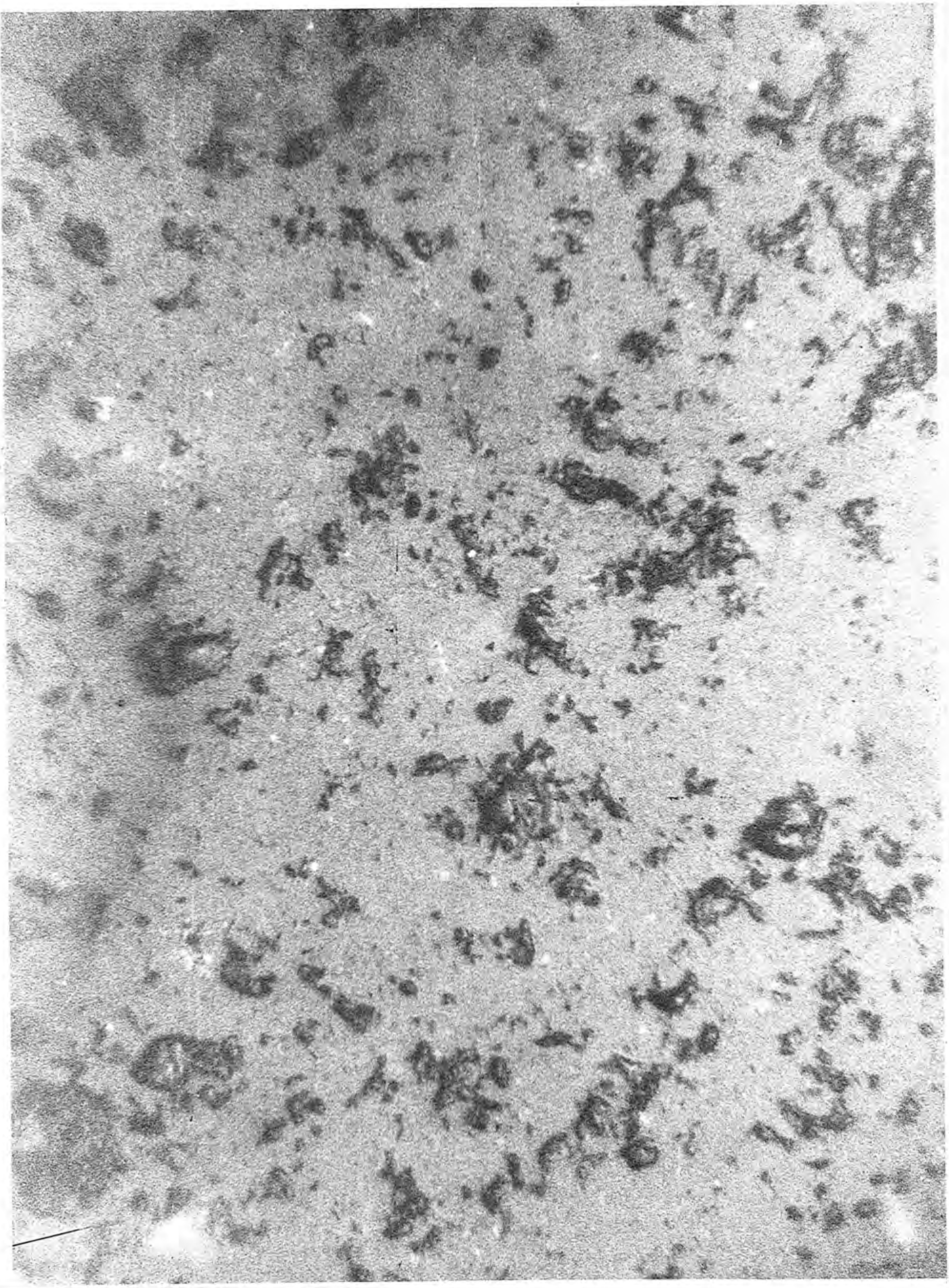

FIG. 6.9 The formation of a black precipitate layer on the anode surface of 30 m/o Li-sialon specimen after electrolysis (× 600 magnification).

these are also listed in Table 6.2. Above about 5 MHz, $\sigma'(\omega)$ for lithium sialon deviated from the linear variation of equation (6.2) and appears to follow $\sigma'(\omega) \alpha \omega^2$. Here it is noticeable that the data obtained by the microwave technique for both specimens falls on the extrapolation of the low frequency variation. Thus the apparent ω^2 variation above 5 MHz seems to be spurious and the linear ω^n variaton is considered to hold over the whole frequency range from 200 Hz to 9.3 GHz. Similar behaviour was observed previously in pure sialon (Chapter 4).

The temperature variation of conductivity $\sigma(\omega)$ at different frequencies (up to 50 kHz) is shown in Figure 6.7 in which log $\sigma(\omega)$ is plotted against the reciprocal of absolute temperature. The temperature variation of conductivity at different frequencies also fits the relation (6.2) where the exponent n varies from 0.9 to 0.3,decreasing slowly with increasing temperature. It is significant to note that the temperature variation of conductivity of lithium sialon at different frequencies does not fit linearly in Arrhenius plots and the activation energy must be defined as the gradient of the plots of log σ against T^{-1}. The activation energy decreases with decreasing temperature and increasing frequency. The highest and lowest values of E_A are in the range of 0.88 - 0.02 eV for lithium sialon and 1.1 - 0.016 eV for yttrium sialon. There is a good correlation between the temperature variations of d.c. and a.c. conductivities. At high temperature the values of E_A deduced from a.c. and d.c. measurements are very nearly the same (Table 6.2). The a.c. conductivity data of lithium sialon fitted log $\sigma(\omega) \alpha T$ rather better than log $\sigma(\omega) \alpha T^{-1}$.

In Figure 6.10 the observed variation of $\varepsilon'(\omega)$ with frequency at room temperature is shown as a log $\varepsilon'(\omega)$ versus log f plot. The value of $\varepsilon'(\omega)$ decreases slightly with frequency up to 6 MHz. Above that frequency, $\varepsilon'(\omega)$ increases and this apparent rise is again thought to be spurious because the microwave data fits reasonably on the extrapolation of the low frequency $\varepsilon'(\omega)$ variations of both the materials. The temperature variation of $\varepsilon'(\omega)$ for lithium sialon at different frequencies is shown in Figure 6.11 in which

Temperature (K)	n from $\varepsilon' - \varepsilon_\infty$		n from ε''		Measured $\varepsilon''/\varepsilon' - \varepsilon_\infty$		Expected value of n $(2/\pi)\cot^{-1}(\varepsilon''/\varepsilon'-\varepsilon_\infty)$	
	Li-sialon	Y -sialon	Li-sialon	Y -sialon	Li-sialon	Y -sialon	Li-sialon	Y-sialon
291	0.96	0.90	0.90	0.78	3.14×10^{-2}	.224	0.98	0.86
400	0.95	-	0.70	-	.274	-	0.83	-
500	0.78	-	0.56	-	.599	-	0.66	-
600	0.65	-	0.44	-	1.20	-	0.44	-
700	0.59	-	0.30	-	2.41	-	0.25	-

Sample reference	Dielectric parameters at 1.6 KHz									Microwave at 9.3 GHz (room temp.)	
	$\sigma(\omega)$ $ohm^{-1}cm^{-1}$		E_A (eV)		$\sigma_o(\Omega^{-1}cm^{-1})$	tanδ		ε'			
	293 K	723 K	high temp	low temp		293 K	723 K	293 K	723 K	tanδ	ε'
Li-sialon	1.5×10^{-10}	7×10^{-7}	0.88	0.05	1.16	3×10^{-2}	6.91	9	140	5.22×10^{-3}	4.41
Y -sialon	8×10^{-10}	1.5×10^{-9}	1.03	0.015	0.05	5.2×10^{-2}	2.1×10^{-1}	17.9	14	2.85×10^{-3}	9.5
Chapter 4. Z= 3.2 sialon	2×10^{-11}	10^{-9}	1.30	0.05	0.05	2×10^{-3}	9×10^{-2}	8.5	12	4×10^{-2}	5.0

TABLE 6.2 : Dielectric parameters for sialons (pure and doped).

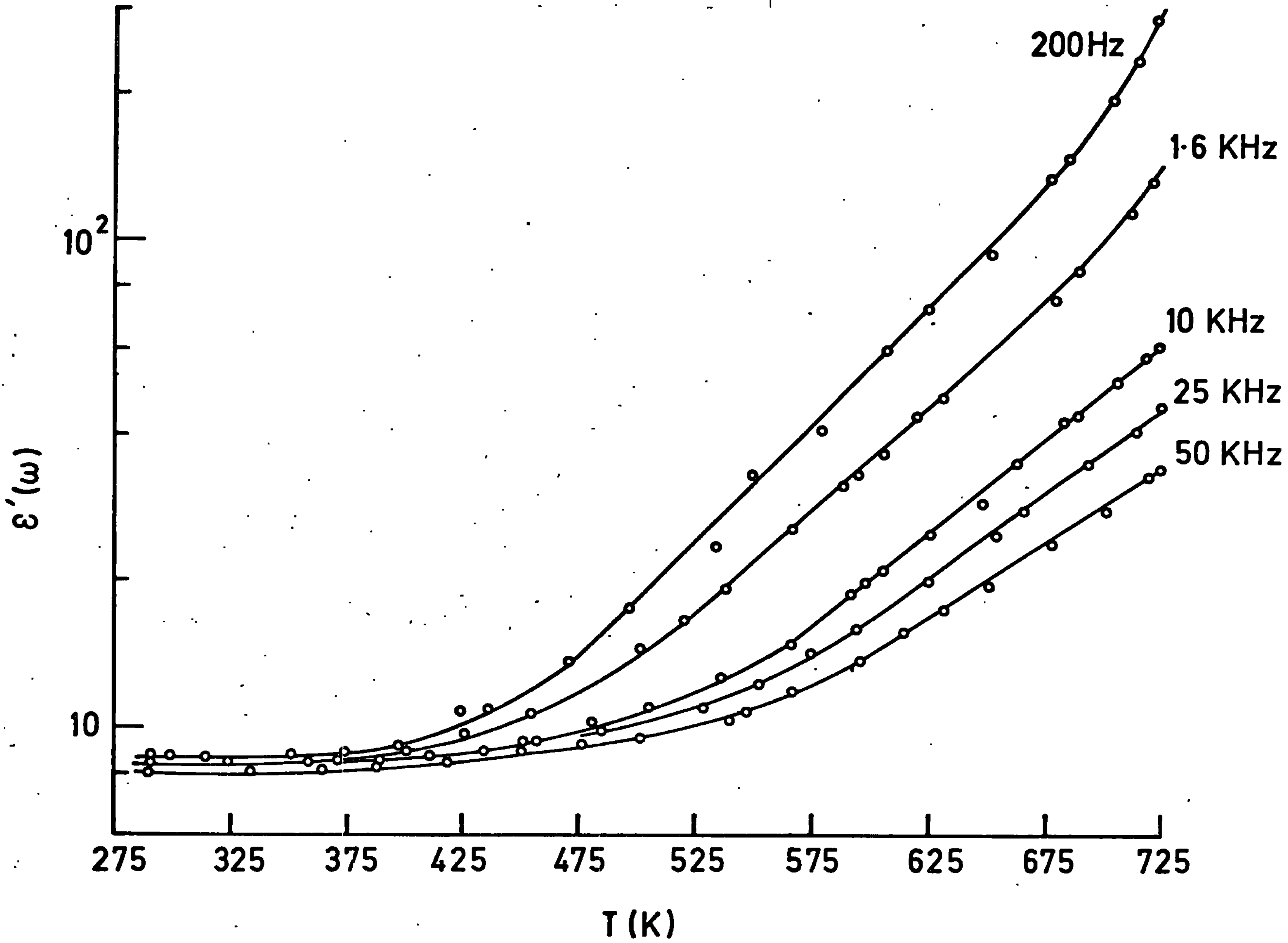

FIG.6.11 Temperature variation of dielectric constant, $\varepsilon'(\omega)$ at different applied frequencies for 30 m/o Li - sialon.

log $\varepsilon'(\omega)$ is plotted against both T and T^{-1}. At low temperatures, below 450 K, $\varepsilon'(\omega)$ increases slowly with temperature, the change being smaller with the increase of applied frequency. Above that temperature $\varepsilon'(\omega)$ increases rapidly with temperature at lower frequencies and less rapidly at higher frequencies. The dielectric constant data also fitted log $\varepsilon'(\omega) \alpha$ T rather better than log $\varepsilon'(\omega) \alpha T^{-1}$. The temperature variation of loss (tanδ) of the same specimen at different frequencies is shown in Figure 6.12 and has a similar form. The values of ε', σ (ω) and tanδ for yttrium sialon decreased by 20% from initial values during thermal treatments. The temperature variation of loss (tanδ) at 1.6 KHz is shown in Figure 6.12. The room temperature value of ε' for yttrium sialon at 1.6 KHz was about 16.5 and reduced to 9 after thermal treatments ; the value of ε' increased to 14 at 725 K. It is noticed that the values of the dielectric parameters of yttrium sialon at room temperature are higher than those of lithium sialon and they appear to be lowered after thermal treatments (Fig. 6.10 and 6.12). This lowering is observed only in yttrium sialon but not in the other nitrogen ceramics used in this work (Chapter 4 and 5). This effect is significant and will be discussed in Section 6.4. Even in high temperature dielectric measurements the electrode polarization effect was not observed for lithium sialon and the results could be reproduced.

There is no major difference between the magnitudes of the frequency variations of σ (ω) and $\varepsilon'(\omega)$ for lithium, yttrium and pure sialons at room temperature but at high temperature, σ (ω) and $\varepsilon'(\omega)$ for pure sialon are at least one to two orders of magnitude lower than that of lithium sialon ; the values of the parameters for yttrium sialon are intermediate between them. Some values are listed in Table 6.2 for comparison.

6.4 DISCUSSION

6.4.1 D.C. BEHAVIOUR

The time dependence of the charging current (after subtracting I_s) and the discharging current at different applied fields follow the Universal

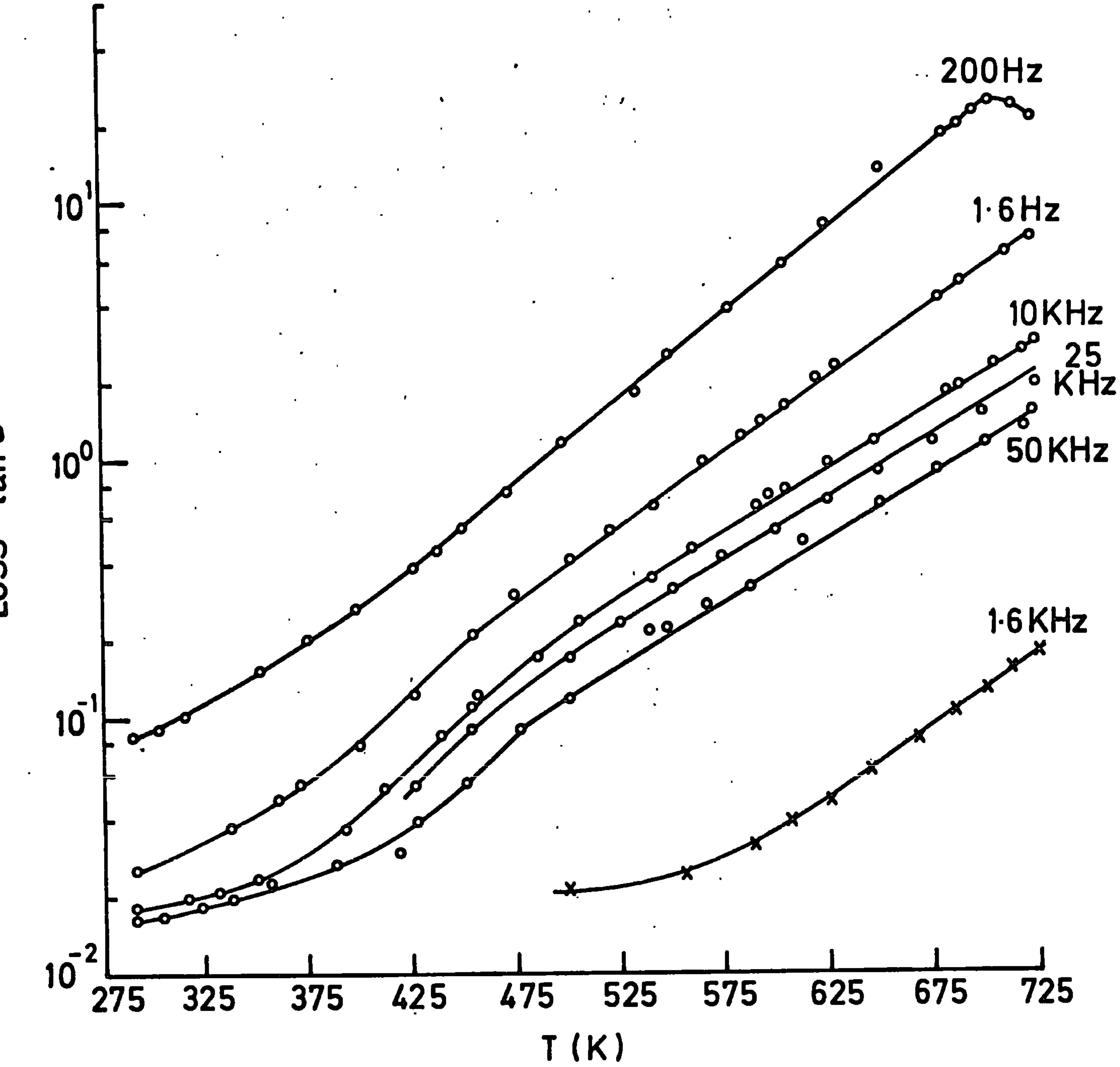

FIG.6.12 Temperature variation of the loss, tan δ at different applied frequencies for 30 m/o Li-sialon (∘) and 14·3 m/o Y-sialon glass (×).

law of dielectric response (Chapter 5, Sect. 5.4.2)

$$I\ (t)\ \alpha\ \ t^{-n} \tag{6.3}$$

with $n < 1$. In case of lithium sialon the value of n derived from I_C and I_D is 0.8 at room temperature. This behaviour is equivalent to the Universal law of dielectric loss $\varepsilon''(\omega)\ \alpha\ \omega^n$ or $\sigma'\ (\omega)\ \alpha\ \omega^n$ (Chapter 4). This type of loss is also observed in this material and will be discussed in Section 6.4.2.

The slight fluctuation in the decay current at 10^2 sec for an electric field of 4 kv cm^{-1} (Fig. 6.5) may be due to transit time effects of injected carriers (Chapter 5, Sect. 5.4.2). On this assumption the drift mobility of lithium sialon is about $2 \times 10^{-7}\ cm^2\ v^{-1}\ sec^{-1}$. The drift mobility for pure sialon obtained previously by this method is listed in Table 6.2 for comparison.

These very low mobility values (both μ_D and μ_H) suggest that the possible transport mechanism is hopping process by localized charge carriers (Chapter 2, Sect. 2.4).

The low field steady current behaviour shows that the log J versus log E characteristic is linear and the magnitude of the slope, (1.03), shows that Ohm's law is obeyed. At high temperatures, the values of E_A and σ_o for the two specimens indicate that the conduction is likely to be hopping by carriers excited into the localized states near the edge of the conduction or valence band (Chapter 2, Section 2.2). Below 588 K, the conductivity data of yttrium sialon fits the relation (Chapter 2, Sect. 2.2)

$$\sigma\ \ \alpha\ \ \exp\ ({}^{-B}/\,T^{1/4}) \tag{6.4}$$

The values of $B \sim 35$ (calculated from the relation 6.4) and $E_A \sim 0.05$ eV support variable range hopping with energies near the Fermi level. At low temperatures, the conductivity of lithium sialon does not fit well with relation (6.4) although it is not linear in the log σ versus T^{-1} plot ;

moreover, the lowest observed activation energy, $E_A \sim 0.3$ eV does not support this process. It is not possible to say whether this process can be observed at very low temperatures for lithium sialon.

The field dependence of conductivity of lithium sialon fits the relation (Chapter 5, Sect. 5.4.2)

$$\sigma \propto \exp\left(eaF/_{KT} \right) \tag{6.5}$$

The value of the characteristic hopping length 'a' calculated from the slope at room temperature was 33 Å.

The conductivity degradation of lithium sialon at high temperature could be attributable to some form of solid state electrolysis or diffusion due to Li^+ ions which may be expected to be relatively highly mobile. Electrolysis is likely to be caused by the migration of Li^+ from anode to cathode, which, in the absence of replenishment, depletes the Li^+ ions and leads to decreased conductivity. After electrolysis, when the specimen was disconnected from the circuit, a voltage of the order of 0.2 v was observed, even after 12 days. This standing voltage and the temperature variation of the steady discharge current are strong evidence for electrolysis. The discolourations of the electrodes may be associated with a solid state electrolytic effect for lithium ions and their corresponding cation vacancies. It may be noted that the crystallographic structures of pure sialon and lithium sialon are very similar and so, if the degradation and colour changes were caused by polarization or densification of the grain boundary glass by thermal treatments or to effects of the electrode materials (gold and platinum), there seems no reason why the effect would only be seen in lithium sialon.

6.4.2 A.C. BEHAVIOUR

The frequency dependence of dielectric loss $\varepsilon''(\omega)$, calculated from the relation $\varepsilon''(\omega) = \frac{\sigma'(\omega)}{\varepsilon o \omega}$ at room temperature, is shown in Figure 6.10. Similarly, the temperature variations of $\varepsilon''(\omega)$ obtained from the experimental data (Fig. 6.7) are shown in Figure 6.13. This fits well with the Universal law of dielectric loss (Chapter 4, Sect. 4.4)

$$\varepsilon''(\omega) \quad \alpha \quad \omega^{n-1} \tag{6.6}$$

with values of n decreasing from 0.9 at room temperature to 0.35 at 725 K for lithium sialon.

The values of $\varepsilon'(\omega) - \varepsilon_\infty$ for the two specimens, obtained after subtraction of ε_∞ at room temperature, is shown in Figure 6.10. Similarly, the temperature variations of $\varepsilon'(\omega) - \varepsilon_\infty$ obtained from Fig. 6.11 are shown in Figure 6.13 as log $(\varepsilon'(\omega) - \varepsilon_\infty)$ versus log f at different temperatures. It is found that these follow (Chapter 4)

$$(\varepsilon'(\omega) - \varepsilon_\infty) \quad \alpha \quad \omega^{n-1} \tag{6.7}$$

with values of n decreasing from 0.95 at room temperature to 0.59 at 700 K for lithium sialon. At temperature the value of n in the $(\varepsilon'(\omega) - \varepsilon_\infty)$ variation is higher than the corresponding value in the $\varepsilon''(\omega)$ α ω^{n-1} law. The ratio of $\varepsilon''(\omega)$ to $\varepsilon'(\omega) - \varepsilon_\infty$ approximately satisfies the Kramers-Kronig relation (Chapter 4, Sect. 4.4)

$$\frac{\varepsilon''(\omega)}{\varepsilon'(\omega)-\varepsilon_\infty} = \cot\left({}^{n\pi}/_{2}\right) \tag{6.8}$$

which can apply to either non-Debe dipolar or to hopping charge carrier (ions or electrons) systems. The values of n obtained at different temperatures from the $\varepsilon''(\omega)$ and $\varepsilon'(\omega) - \varepsilon_\infty$ variations together with those derived from equation (6.8) by substitution of the experimental values of the ratio $\varepsilon''(\omega)/_{\varepsilon'(\omega)} - \varepsilon_\infty$ are shown for comparison in Table 6.2. This behaviour supports conduction by hopping carrier (ions or electrons) system. Furthermore, the temperature variations of $\sigma(\omega)$ and $\varepsilon'(\omega)$ are not of the simple Arrhenius type. This feature is characteristic of the hopping conduction (19,78) ;

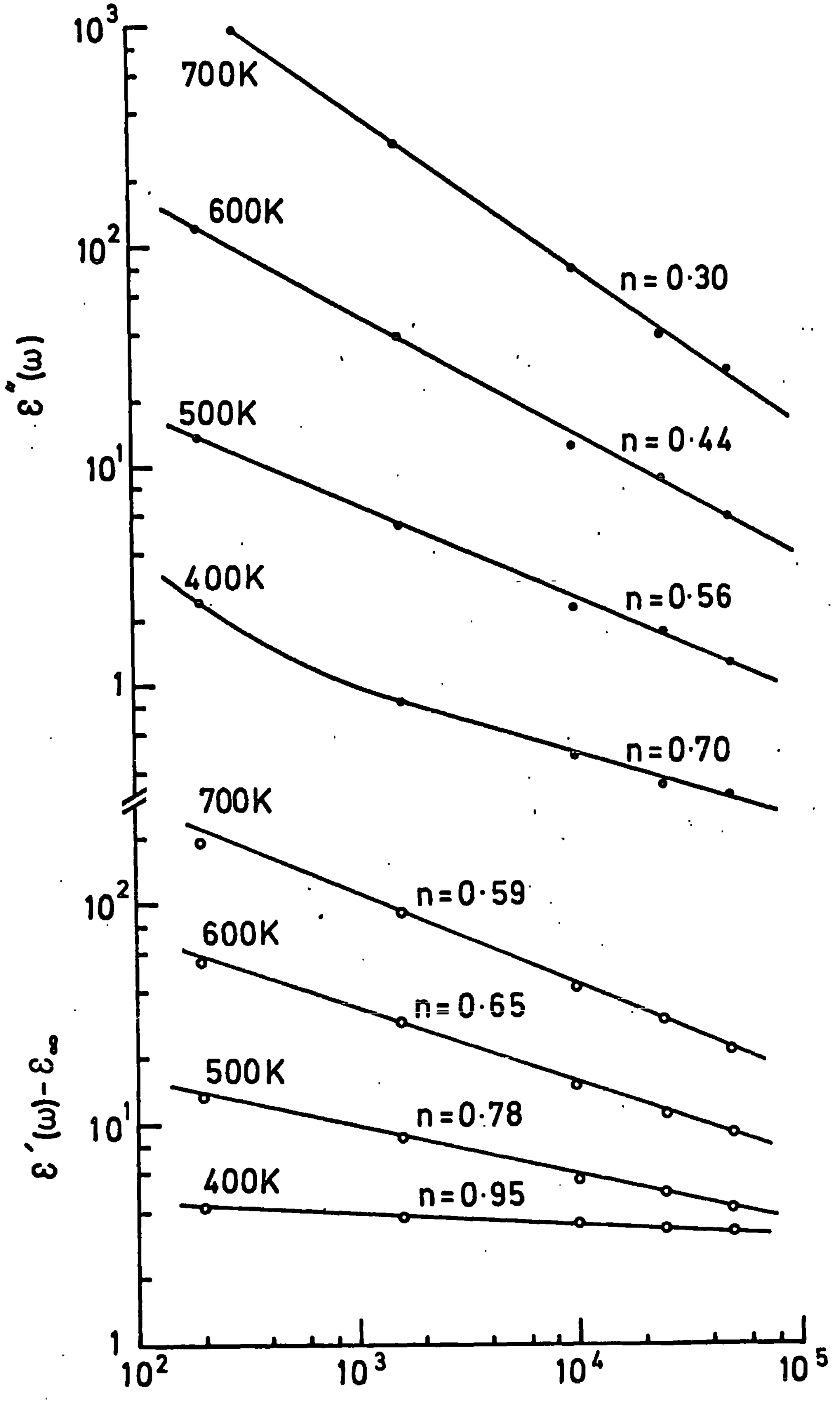

FIG.6.13 Typical temperature variations of the power law characteristics of (a) $\varepsilon''(\omega) \propto \omega^{n-1}$ and (b) $\varepsilon'(\omega)-\varepsilon_\infty \propto \omega^{n-1}$ for Li-sialon.

(Chapter 2, Sect. 2.2).

The decrease of conductivities (both d.c. and a.c.) and dielectric constant for yttrium sialon during thermal treatments is unlikely to be associated with polarization effects ; since no changes of colour or steady discharge current were observed. One possible explanation of this behaviour is the densification of the glass structure leads less void space in the glass and so the conductivities and ε' are reduced during heating prior to the appearance of the equilibrium crystalline phase. This behaviour has been observed in many glasses and glass ceramics (120).

The conductivity (d.c. and a.c.) and dielectric constant of β' sialon phase are lower than that of the lithium sialon and the corresponding values for yttrium sialon glass are intermediate between them ; these are listed in (Table 6.1 and 6.2). This shows that the chemical composition of the sialon has a marked effect on its conductivity, although the mechanism of conduction is probably very similar in all the materials.

CHAPTER 7

MICROWAVE HALL EFFECT

7.1 INTRODUCTION

It is widely known that the d.c. conventional method for determining Hall mobility used in studies of semiconductors have severe limitations for high resistivity materials (111, 121). The influence of the thermal noise that is present where measurements are on materials having low mobilities (as low as 10^{-4} cm^2 v^{-1} sec^{-1}) at elevated temperatures (up to 1200° C) is important because this thermal noise may short out the Hall probes. Furthermore, surface conduction effects including polarisation in the specimens might preclude the observation of the actual signal due to the Hall voltage. These general statements were borne out by the present work, in which the mobility determined by d.c. conventional Hall effect investigation was shown to be less than 10^{-5} cm^2 v^{-1} sec^{-1} between 500° C and 1000° C (Chapter 3, Sect. 3.3). This result was based on estimation of the sensitivity of the apparatus. Thus, in order to obtain reliable values of mobility one must consider alternative methods of investigating the Hall effect for nitrogen ceramics.

Several other techniques have been used to determine the Hall mobility for high resistivity materials. Here three alternative methods, i.e. a.c. Hall effect measurements, Hall current techniques and microwave methods will be considered.

In a.c. Hall effect measurements theremal noise in high resistivity samples and noise associated with high impedance electronic circuitry,can be minimized and the sensitivity of the Hall detection can be greatly improved over the d.c. techniques. Other advantages include the ability to eliminate voltages arising from Hall probe misalignment. Several a.c. Hall effect measurement techniques have been reported in the literature (e.g. 111).

Numerous difficulties are encountered in some of the techniques ; some of these are discussed by McKinzie and Tannhauser (122). Hermann and Ham (123) were able to make a.c. Hall effect measurements on iodine single crystals ($\mu_H \approx 4$ cm^2 V^{-1} sec^{-1}) and the polymereric charge transfer complex iodine-poly-n-vinyl carbazole ($\mu_H = 0.4$ cm^{2}V^{-1}sec^{-1}). If polycrystalline samples are used, problems associated with intercrystalline resistance and interfacial polarization effects can also produce deleterious results. Therefore, this method is not appropriate for nitrogen ceramics.

The Hall current measurement technique provides a useful method of investigating the electronic properties of high resistivity materials. The main advantage of this technique is that with the use of a guard ring, surface conduction effects, which occur for most high resistivity materials, can be separated from the bulk conduction. This method has been used to determine charge carrier mobilities in anthracene single crystals (124). In the measurements on anthracene the magnitude of the Hall currents observed were of the order 10^{-15} amp corresponding to mobility values of around 1 cm^{2}V^{-1}sec^{-1}. Although in general this method is suitable for high resistivity materials it may not be applicable to nitrogen ceramics because of the effect of decaying currents (Chapters 3 and 5).

Hall mobility results have been obtained for various low-mobility materials (e.g. selenium, TCNQ complexes and biological polymers) using a microwave Faraday type rotation measurement technique (125) where the specimen is placed in the centre of a bimodal resonating cavity. In semiconductors at microwave frequencies, the largest contribution to the Faraday effect comes from the presence of conduction electrons (mobile carriers), but an interpretation of the underlying mechanism depends on the mean free relaxation time of these charge carriers. If the charge carriers collision frequency is less than, or of the same order as the incident microwave frequency, the charge carrier will be able to execute orbital motions associated with the cyclotron resonance effect, so providing the desired gyromagnetic action and the resultant Faraday rotation. At normal temperatures, however, charge carrier mean free paths are too small to permit such cyclotron orbital motions and the observed Faraday type rotation arises from a different mechanism, namely the Hall effect. In the experimental method, two degenerate TE modes are excited in the cavity containing the specimen, and the geometry of the input and output waveguides is such that no power is coupled between these waveguides. When a magnetic field is applied along the cavity axis, the resulting Faraday rotation causes power to be transmitted in the output waveguide. Several microwave Hall effect measurement techniques have been reported in the literature (125-128). It has been found that the lowest detectable mobility was of the order 10^{-3} cm^2 V^{-1} sec^{-1} (126). Although this microwave technique appears to have as many problems, if not more, than the more conventional techniques, it has many positive advantages. These advantages include the ability to investigate polycrystalline materials, (since heterogeneities associated with inter-and intra crystalline defect effects are eliminated) and the fact that electrical contact effects are also eliminated since the method is an electrodeless one.

The work described in this Chapter was undertaken to investigate the suitability of the microwave Hall technique for studies on nitrogen ceramics at room temperature and to ascertain their Hall mobility. In order to check the validity of the experimental techniques reference measurements were first made on n-type germanium.

7.2 THEORY OF THE EXPERIMENTAL METHOD

A formula for calculating the mobility can be expressed by the relation (125-126)

$$\bar{\mu} = \left\{ 10^8/_H \right\} \left\{ P'_2/_{P'_1} \right\}^{\frac{1}{2}} \tag{7.1}$$

where $\bar{\mu}$, in $cm^2 V^{-1} sec^{-1}$, is the effective carrier mobility ; H, in gauss, the strength of the applied magnetic field ; P'_1 the Joule loss in the sample due to the current excited by the fundamental mode ; and P'_2 the Joule loss in the sample due to the Hall current. It is however, very difficult to measure these powers directly. Several methods have been used by many authors to determine the power factors for a dual mode cavity. Nishina and Spry (127) have mentioned that microwave power from a stabilized oscillator (P_{in}) was directed through the input of the cavity and excited the first electrical mode of the cavity (Fig. 7.1 (a)). Interaction between the resultant charge motion in the sample and the applied d.c. magnetic field, H, causes a fraction of the incident power to be coupled to mode two of the dual mode cavity. This power leaves the cavity through the output waveguide. In the absence of losses in the sample and in the cavity walls, the carrier mobility $\mu = R\,\sigma = \left\{10^8/_H\right\}\left\{P_{out}/P_{in}\right\}^{1/2}$. However, losses and reflections were not negligible and the corrections were made on the basis of V.S.W.R. measurements at the input and output of the cavity.

It has been shown by Yamagata and Fukuroi (128) that for a bimodal cavity without inbalance, the Hall conductivity is given by

$$\sigma_{ab} \cong \frac{\varepsilon o \omega}{DI} \quad \frac{1}{Q_o} \left(\frac{P^o_{out}}{P^o_{in}} \right)^{1/2} \cdot \frac{1}{2} \left(\frac{\Delta P_{out}}{P^o_{out}} \right) \tag{7.2}$$

where σ_{ab} represents the Hall conductivity, ε_o the dielectric constant of vacuum, ω the angular frequency of microwave, DI the numerical factor depending on the shape and volume of the specimen, and Q_o, the Q-factor of the cavity. The P's indicate the microwave power levels, where the suffixes "out" and "in" mean those outgoing from and incoming to the cavity. The ratio of the output power to the input, P^o_{out}/P^o_{in} was measured before applying the magnetic field. After the application of the magnetic field on the specimen $\Delta P_{out} = P_{out} - P^o_{out}$ was to be determined from the change of the amplitude of the pattern appeared on the cathode-ray oscilloscope. The Hall mobility

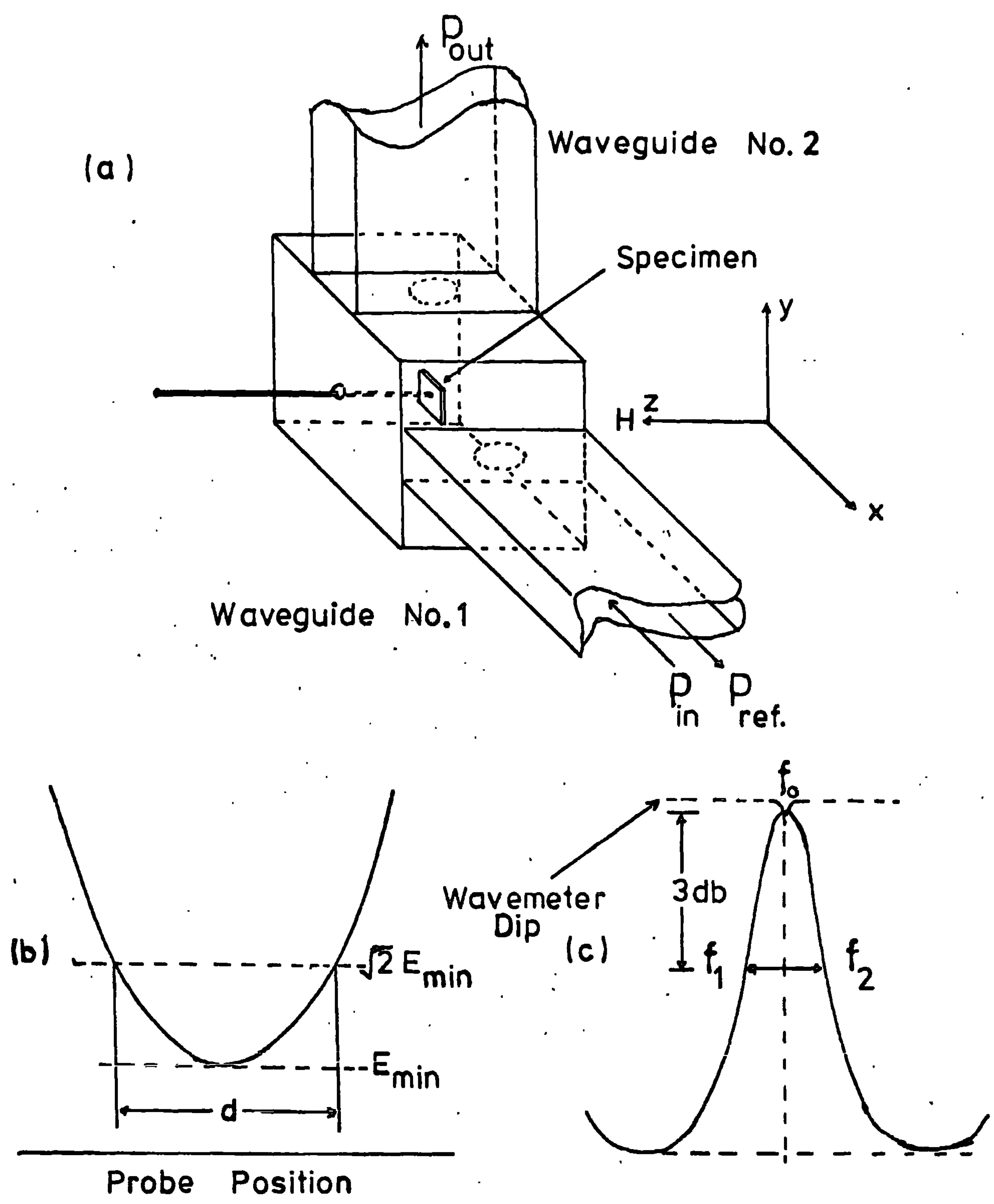

FIG. 7.1(a) Cavity and specimen arrangement for measurement of microwave Hall effect at 9.3 GHz. (b) Width of voltag minimum for determination of VSWR. (c) Resonance curve to determine the Q of the cavity.

can be calculated by the use of the relations

$$\sigma_{ab} \approx \sigma_o^2 . R_H . H, \text{ and } \mu_H = \sigma_o R_H$$

Equation (7.2) is rewritten by using these relations to

$$\mu_H = \frac{10^8}{H} . \frac{\varepsilon\omega}{DI\sigma_o} . \frac{1}{Q_o} . \left\{\frac{P^o_{out}}{P^o_{in}}\right\}^{\frac{1}{2}} . \frac{1}{2} \left\{\frac{\Delta P_{out}}{P^o_{out}}\right\} \tag{7.3}$$

Neglecting the coupling irises assuming $Q_o \approx Q_L$, the loaded Q-factor gives the following apprximation

$$\frac{\Delta\omega_o}{\omega_o} \doteq \frac{1}{Q_o} \approx \frac{DI}{\varepsilon_o\omega} \sigma_o$$

Therefore, equation (7.3) can be reduced to

$$\mu = \frac{10^8}{H} . \left\{\frac{P^o_{out}}{P^o_{in}}\right\}^{\frac{1}{2}} . \frac{1}{2} \left\{\frac{\Delta P_{out}}{P^o_{out}}\right\} \tag{7.4}$$

Equation (7.4) is identical to equation (7.1). The powers term of equation (7.1) can also be obtained experimentally from the relation (assuming equal coupling irises)

$$\mu_1 = \frac{10^8}{H} . \left\{\frac{P^H_{out} - P_{out}}{P^o_{ref} - P^s_{ref}}\right\}^{\frac{1}{2}} \tag{7.5}$$

where $P_{in}^{(1)} = (P^s_{ref} - P^o_{ref})$ refers to the difference of the input reflected powers with and without the sample in the cavity and $P'_{out} = (P^H_{out} - P_{out})$ is to be determined by observing the change of output power with and without magnetic field.

Trukhan (126) has described a method to calculate the mobility by the following relation

$$\mu_2 = 2\left\{1 - \frac{Q_1}{Q_o}\right\}^{-1} \left\{{}^{P_2}/_{P_1}\right\}^{\frac{1}{2}} \left\{1 - \Gamma^2\right\}^{-1} \frac{10^8}{H} \qquad (7.6)$$

where Q_o and Q_1 are the Q's of the empty cavity and the cavity with sample, and Γ is the reflection coefficient of the cavity from input and output (they are considered to be identical). The P_1 and P_2 refer to the incoming power to the cavity and the change of outgoing power with magnetic field respectively. The introduction of a sample effectively reduces the Q factor of the cavity by a certain amount. The change in Q with reflection coefficient of the cavity is given by

$$\frac{Q_1}{Q_o} = \frac{(1-\Gamma_1)\ (1 + \Gamma_o)}{(1+\Gamma_1)\ (1 - \Gamma_o)} \qquad (7.7)$$

here the subscripts O and 1 refer to the situation without and with the sample respectively. If the change in Q factor is small, then equation (7.7) is reduced to

$$\Delta\Gamma = \frac{1}{2} \cdot (1 - \Gamma_o{}^2)\ \frac{\Delta Q}{Q_o} \qquad (7.8)$$

where $\Delta\Gamma = \Gamma_1 - \Gamma_o$. If the change in Q is taken into account throughout, it turns out that instead of measuring the difference between the input reflected powers with and without the specimen as mentioned above, one can directly measure the input power (P_1) when the specimen is actually present in the cavity. If the losses are high, the ratio of the Q's in equation(7.6) will be very small and in such an instance the first term becomes equal to unity (in the limit of course). If the insertion losses are small, so that ${}^{Q_1}/_{Q_o}$ is close to I, then this factor becomes ${}^{Q_o}/_{\Delta Q}$ and is determined by (7.8). In the present work, the value of μ has been calculated using both the equations (7.5) and (7.6) for comparison.

7.3 EXPERIMENTAL

The specimens examined in the present work were nitrogen ceramics of the same compositions as mentioned in (Chapter 1, Table 1.1 and Chapter 6), and a n-type germanium sample. Specimens of typical size 5 mm x 5 mm x 0.2mm were used. The cavity, whose internal dimension was 2.23 cm, was made of copper and had a Q of about 2640. Figure 7.1(a) shows schematically the cavity, the sample, and the input and output waveguides. There were two coupling holes at the input and output sides of the cavity, which were identical. One wall of the cavity was detachable and this feature was used for insertion and removal of the sample with minimum disturbance of the cavity Q and the set-up during the change over of the sample. The sample (mounted on a quartz rod) was placed as centrally as possible in the electric field antinode at the centre of the cavity. The cavity could sustain the modes TE_{101} and TE_{011}. The experimental arrangement of the microwave apparatus is shown in Figure 7.2. The cavity was mounted between the poles of an electromagnet with which magnetic fields of up to 5 kilogauss could be obtained.

The microwave power from a stabilized X-band oscillator (klystron source) was directed through waveguide number one and excited the first electrical mode of the cavity. The resonance pattern was displayed on a dual beam oscilloscope by the crystal detector, X_2 (through a 10 db directional coupler) with the source modulated. The resonant frequency of the cavity was obtained by tuning the mechanical frequency control and reflector voltage of the klystron source. The resonant frequency, f and the frequencies f_1, and f_2 at 3 db points respectively of the resonance curve were measured using a calibrated wavemeter (Fig. 7.1 (c)). The values of Q_o and Q_s of the cavity were determined respectively without and with the specimen, but with the quartz rod in position using the relation, $^{f}/_{f_1-f_2}$. The measurements were then repeated several times. The value of Q_s with the germanium sample was 1000 and with nitrogen ceramics were about 2000 ; the value of Q_o (with the quartz

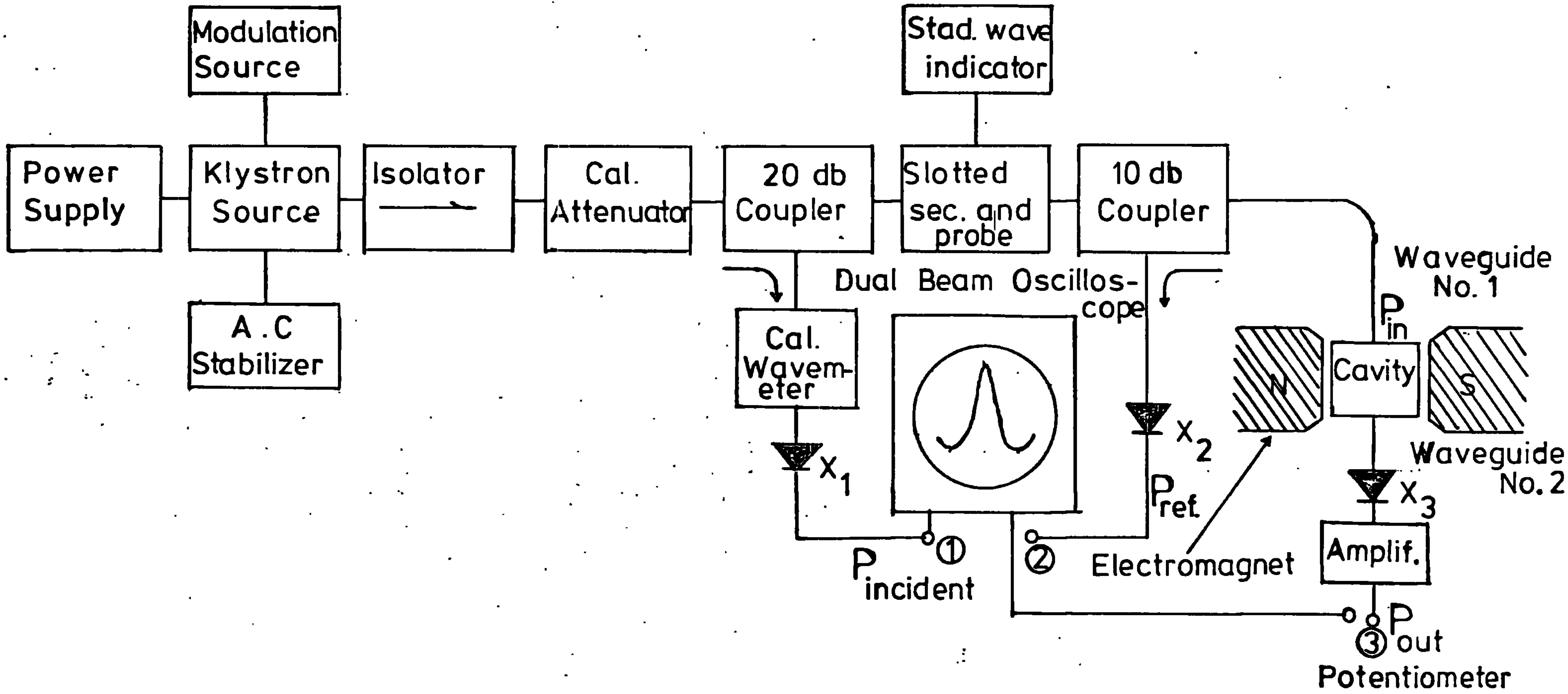

FIG. 7.2 Schematic diagram of microwave Hall effect apparatus at room temperature.

rod only) was 2300. These values were used in equation (7.6).

The reflection coefficient, Γ, was determined using V.S.W.R. measurement techniques suitable for high power levels (129). The Γ and S (V.S.W.R) were calculated from the relations $S = {}^{\lambda g}/_{\pi d}$ and $\Gamma = \frac{S-1}{S+1}$ where λg is the guide wavelength ; d is noted in Fig. 7.1 (b) ; i.e. the electrical distance between $\sqrt{2}\ V_{min}$ points was measured by the slotted line probe, in cm. The value of λg was calculated from the relation

$$\lambda g = \frac{\lambda}{\sqrt{1 - (\lambda/_{2a})^2}}$$ where λ is the free-space

wavelength generated and measured by wavemeter ; a = broad dimensions of guide (here a = 2.29 cm), λ = 9.34 GHz. After substitution these values into the relevant equations, the value of $\Gamma = 0.60$ was obtained. This value was used in equation (7.6).

All the powers were measured after switching off the modulation source. The microwave power, P, generated from the oscillator was directly measured by the crystal detector X_1, whose output, taken through a 20 db directional coupler was observed on either an oscilloscope or a digital millivoltmeter. The 20 db arm was used to ensure that the microwave power reaching the detector was small enough so that operation was guaranteed in the region where $P \alpha V$ (m.v.). All the powers were measured in millivolts. This input power after conversion to an actual value, in milliwatts, was used in equation (7.6). This input reflected powers P^o_{ref} and P^s_{ref} were measured with no sample but with the quartz rod in position and with the sample in the cavity respectively by the crystal detector X_2 joined to a 10 db directional coupler. The difference, $P_{in} = P^o_{ref} - P^s_{ref}$ was used in equation (7.5).

Even in the absence of the static magnetic field, however, a microwave power comparable to the Hall power was coupled out to waveguide No.2, owing to the non-ideal cavity construction. Therefore, the P_{out} and P^H_{out} were measured without and with applied magnetic field respectively, using the crystal detector X_3 at the output of the d.c. amplifier. The difference between $P^H_{out} - P_{out} = P_2$ or P'_{out} as used in both equations (7.5) and (7.6) for the calculation of Hall mobility. The output power was then measured at different applied magnetic fields with the specimen in the same position.

All the measurements were made in air at room temperature.

7.4 RESULTS AND DISCUSSION

Figure 7.3 shows a typical plot of output power, P_{out} versus magnetic field, H, on an n-type germanium sample at room temperature. In high magnetic fields, P'_{out} is seen to deviate from the linear relationship. The data of input and output powers together with the values of mobility obtained under different methods of measurements are listed in Table 7.1. It should be noted that there are two values for the Hall mobility given, due to the different methods of calculation, depending upon the direct and indirect ways of noting the actual power ratios. The value of μ, calculated using equation (7.5) is about 2111 $cm^2 v^{-1} sec^{-1}$ whereas the value of μ_2 obtained using equation (7.6) is 1972 $cm^2 v^{-1} sec^{-1}$. The Hall mobility of the same sample obtained by d.c. conventional method (Chapter 3, Sect. 3.2) was about 2900 $cm^2 v^{-1} sec^{-1}$. The results obtained by two different methods are in close agreement. In (130), the value of μ_H for n-type germanium measured by the microwave Hall effect and the d.c. Hall methods has been found of the order 3300 $cm^2 v^{-1} sec^{-1}$, but a direct comparison is not necessarily valid because of the probable differences in impurity contents of the samples.

No change of output power due to the Hall effect was observed in any of the nitrogen ceramic specimens. As the apparatus would have measured a mobility of greater than 10 $cm^2 v^{-1} sec^{-1}$, this observation implied that the Hall mobility in the specimens was low. The present microwave Hall effect apparatus has not enough sensitivity to determine the value of μ_H for the materials. It needs further improvement ; especially of the output detection system (for which a superheterodyne receiver might be used), elimination of

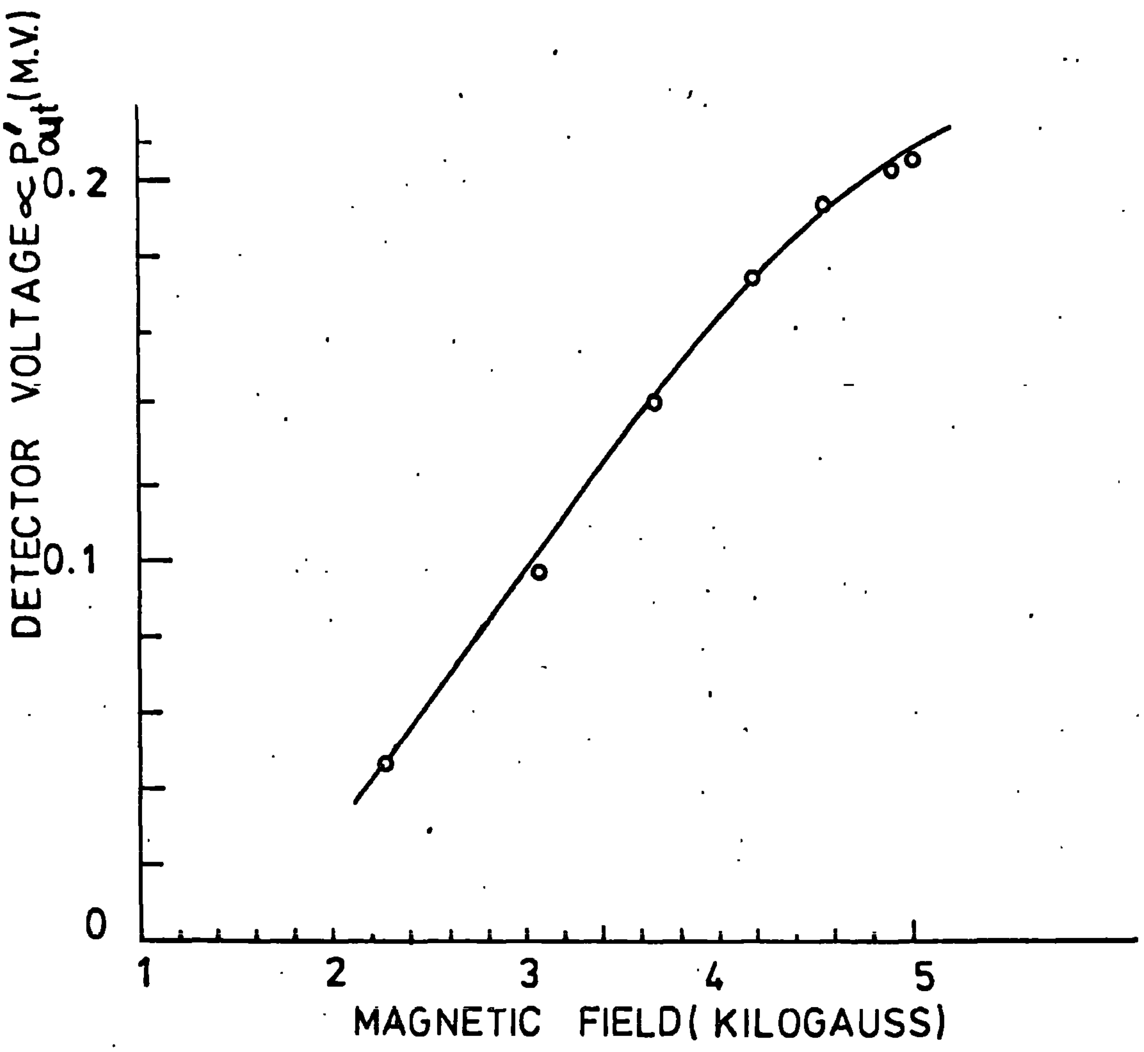

FIG. 7.3 Variation of output power with magnetic field for gemanium specimen.

$P_1^{(2)}$ V α p (mv)	P_{ref}^{o} V α p (mv)	P_{ref}^{s} V α p (mv)	$P_{ref}^{o} - P_{ref}^{s} = P_{in}^{(1)}$ V α p (mv)	P_{out} V α p (mv)	P_{out}^{H} V α p (mv)	$P_{out}^{H} - P_{out} = P_{out}'$ or P_2 V α p (mv)	Magnetic field H in gauss	μ_1 $cm^2v^{-1}sec^{-1}$	μ_2 $cm^2v^{-1}sec^{-1}$
75	62.423	41.846	20.577	5	5.205	.205	5×10^3	1996.25	1865.19
"	"	"	"	"	5.202	.202	4.89	2026.17	1893.14
"	"	"	"	"	5.192	.192	4.575	2111.39	1972.76
"	"	"	"	"	5.173	.173	4.20	2183.15	2039.81
"	"	"	"	"	5.140	.140	3.713	2221.50	2075.65
"	"	"	"	"	5.097	.097	3.08	2229.17	2061.59
"	"	"	"	"	5.048	.048	2.275	2122.99	1963.39

Table 7.1 : Experimental data and Hall mobility for n-type Germanium at 9.3 GHz.

unbalanced signals appearing at the output, design of a cavity of higher Q (cylindrical bimodal cavity) and very good power measuring equipment.

According to the theory presented in (Chapter 2, Sect. 2.4), mobility values above about 1 to 10 $cm^2v^{-1}sec^{-1}$ (for example n-type germanium), can be taken as an indication that the dominant charge carriers are moving in a broad conduction band. Values below about 1 $cm^2v^{-1}sec^{-1}$ could result from hopping or ionic conduction or else indicate an electronic mechanism involving localized electronic states. The evidence from the microwave Hall effect experiments reported here, though somewhat inconclusive, none the less suggests fairly strongly that the Hall mobility values in the nitrogen ceramics are sufficiently low to place them among the category of materials in which conduction mechanisms involving localized electron states are likely.

Finally, it is useful to compare the Hall mobility derived from the conventional d.c. and microwave Hall effect measurements (Chapter 3) and the drift mobility obtained from transit time effects of injected carriers (likely to be electrons) (Chapter 5) for all nitrogen ceramic specimens ; this comparison is shown in Table 7.2. According to theory there must be a difference between the Hall mobility and the drift mobility. In the case of hopping conduction, μ_H is generally higher than the drift mobility, μ_D. Table 7.2 suggests that this holds and indicates further that the drift mobility measurement technique is by far the most promising of the three alternating studied.

Sample reference	Si_3N_4	$5W/oMgO/Si_3N_4$	$Z \gtrsim 3.2$ sialon	$Z \gtrsim 4.0$ sialon	30 m/o Li-sialon
Microwave Hall mobility μ_H, $(cm^2V^{-1}sec^{-1})$ 18° C	< 10	< 10	< 10	< 10	< 10
Conventional Hall mobility μ_H, $(cm^2V^{-1}sec^{-1})$ $500^\circ C - 1000^\circ$ C	$< 10^{-5}$	$< 10^{-5}$	$< 10^{-5}$	$< 10^{-5}$	$< 10^{-4}$
Drift mobility μ_D, $(cm^2V^{-1}sec^{-1})$ 18° C	2×10^{-8}	5×10^{-9}	7×10^{-8}	6×10^{-8}	2×10^{-7}

Table 7.2 : Hall mobilities and drift mobilities for hot-pressed nitrogen ceramics.

CHAPTER 8

CONCLUSIONS

The overall picture of the electrical properties of the nitrogen ceramics investigated, derived from the foregoing Chapters, is that they may be regarded as a class of high resistivity, low mobility materials in which the predominant conduction mechanism at low and medium temperatures is hopping due to impurity (localized) states located near the Fermi level and near the edge of the conduction or valence bands respectively. It is, however, difficult to obtain a completely unambiguous interpretation of the experimental data, not least because of the complexity of the chemical compositions of the materials examined. In conclusion therefore some points may be noted on which further clarification is desirable and some suggestions made of alternative experimental techniques (whose use was precluded by lack of time) which could prove beneficial in this respect. The high temperature d.c. conductivity results up to 1000°C did not support free band or non-localized (extended) states conduction, (Chapters 3 and 5), which implied that the materials did not show intrinsic behaviour even at the highest measured temperature. The thermoelectric power investigation, on the other hand, showed that the sign of the carriers changed above about 900°C (Chapter 3, Sect. 3.4) indicating a change of the conduction mechanism. Therefore, measurement of d.c. conductivity at high temperatures above 1000° C is required to observe the possible presence of other conduction processes. Thin square plate specimens with circular platinum electrodes would be suitable for measurement of conductivity at high temperatures. Measurements of conductivity at high fields above 10^4 V/cm may give further information of the precise nature of the high field conduction mechanisms. The activation energy, E_a obtained from high temperature d.c. conductivity results can for many materials be expressed as $E_a \simeq \frac{1}{2} E_o$. For the sialons $E_a \sim 1.5$ eV so the band gap $E_g \simeq 3$ eV where E_o and E_g are the optical and electrical gaps between conduction and valence bands. Since the gap was not free of states this assumption may not be valid, (Chapter 2, Sect. 2.2), but nevertheless the determination of E_o using optical absorption studies would provide some knowledge about the nature of the band gap and could be compared with electrical band gap. Several experimental techniques and theories for optical absorption studies have been described in (131-132). From the plot of the optical absorption coefficient α versus phonon energy $\hbar\omega$ one can deduce the band gap energy. Therefore, direct studies of the electrical properties of these materials can be complemented by optical absorption studies.

The d.c. conduction results suggested that the charge carriers in the materials examined were predominantly electrons (or holes) rather than ions (except lithium sialon, in which conduction could have been contributed by both electrons and ions). The dielectric parameters suggested that the charge carriers in the conduction processes might be either non-Debye dipolar or charge hopping carriers (electrons or ions) and there was some evidence that the charge carriers were of predominantly electronic nature (Chapter 4, Sect. 4.4). However, conclusive evidence of the nature of charge carriers could not be established from this work. The distinction between electronic and ionic carriers may be a very difficult problem to solve and in some cases it may not be possible to give a conclusive answer to the question. In the case of hopping conduction the problem is even more complicated. Some reliable experiments can be done to know the nature of the charge carriers using the method of galvanic-cell e.m.f. measurements. The theory and the experimental techniques necessary to obtain ionic transport numbers have been described in (133-134). In this technique, a disc or thin plate specimen is used as an electrolyte with platinum electrodes being attached to each side of it. If the two ends of a specimen at a temperature T are in contact with different partial pressures of oxygen P_1 and P_2, then an e.m.f. E_o is generated by the thermodynamic potential difference $E_o = \Delta G/_{NF}$ where N is the number of charges transported by the migrating ions per unit of reaction, F is the Faraday constant, ΔG is the decrease of free enthalpy given by $\Delta G = RT\ln(P_1/_{P_2})$ where R is the gas constant. If the specimen is a mixed conductor, then the cell e.m.f. E is given by $E = t_1 E_o$ where t_1 is the ionic transport number. E_o can be calculated from the measured values of P_1, P_2 and T. The ratio of E, the measured cell e.m.f, to E_o gives the ionic transport number, t_1. For a pure electronic conductor, E_o is zero. Different partial pressures of oxygen can be obtained by using CO_2, O_2 and air atmospheres. One important criterion of ionic conduction is the present of electrolysis. If the electrode does not supply the ionic species slow polarization and a standing potential are observed in the specimen. This behaviour of electrolysis was observed in lithium sialon, and was thought to be due to the migration of lithium mobile ions from anode to cathode, as described in Chapter 6. A further check on the nature of the charge carriers can be made on the specimen by means of an electrolysis experiment (133). In this method three thin square plate specimens with optically polished surfaces are pressed together and heated at a constant high temperature, under which conditions a constant d.c. voltage should be applied for more than 100 hours. The specimens are weighed before and after this treatment. If changes of weight are observed in any of the three specimens the charge carriers would be predominantly ionic.

Some indications of the presence of space charge in the materials were noticed in each type of experiment mentioned in the preceding Chapters. The origin of its occurrence was not clearly understood from this work. Space charge effects are generally observed in many disordered solids and insulators due to their microscopic inhomogeneities (19,82). The space charge may be one of two types :

(i) mobile charge densities injected in excess of thermal equilibrium densities in neutral material - the charge may be free in the sense of many mean free paths of many interatomic spacings or they may be hopping by discontinuous jumps ; they may be ionic or electronic; or

(ii) a fixed charge resulting from the removal of whatever mobile charge may have been presented in the neutral material, leaving behind a fixed background space charge. The presence of space charge was indicated by the fact that the steady current-voltage (I-V) characteristic for an unused specimen (Si_3N_4) showed hysteresis behaviour, Fig. 8.1 ; this was removed by heat treatment after which the I-V characteristic clearly followed Ohm's law. It has been shown by Hill (135) that a sensitive test for the presence of space charge is the presence or absence of a change in voltage at the centre of the specimen when the field is reversed. If space charge is present there is no longer a uniform field and hence the mid-position voltage is not the mean of the voltages at the ends of the specimen. Some evidence of this type of behaviour was obtained for Si_3N_4, Fig. 8.2, by measuring the voltage distribution along the length of a specimen. Furthermore, measurements of both d.c. and a.c. conductivities using specimens of widely different electrode area/thickness ratio will provide direct information of the field distribution in the materials. The occurrence of a dependence of conductivity on the electrode area/thickness ratio indicates the presence of microscopic inhomogeneity in the materials (87). Preliminary measurements of d.c. conductivity on specimen of different thickness, for Z = 3.2 sialon, showed that σ_{dc} did in fact vary with thickness, Fig. 8.3.

It was known from both the conventional d.c. and microwave Hall effect experiments that the Hall mobility of the materials was low. Other methods to determine the Hall mobility may not be suitable for these materials as mentioned in (Chapter 7, Sect. 7.1). Drift mobility techniques will be particularly suitable for these materials. Davies (43) has devised a drift mobility measuring technique which is suitable for highly insulating systems

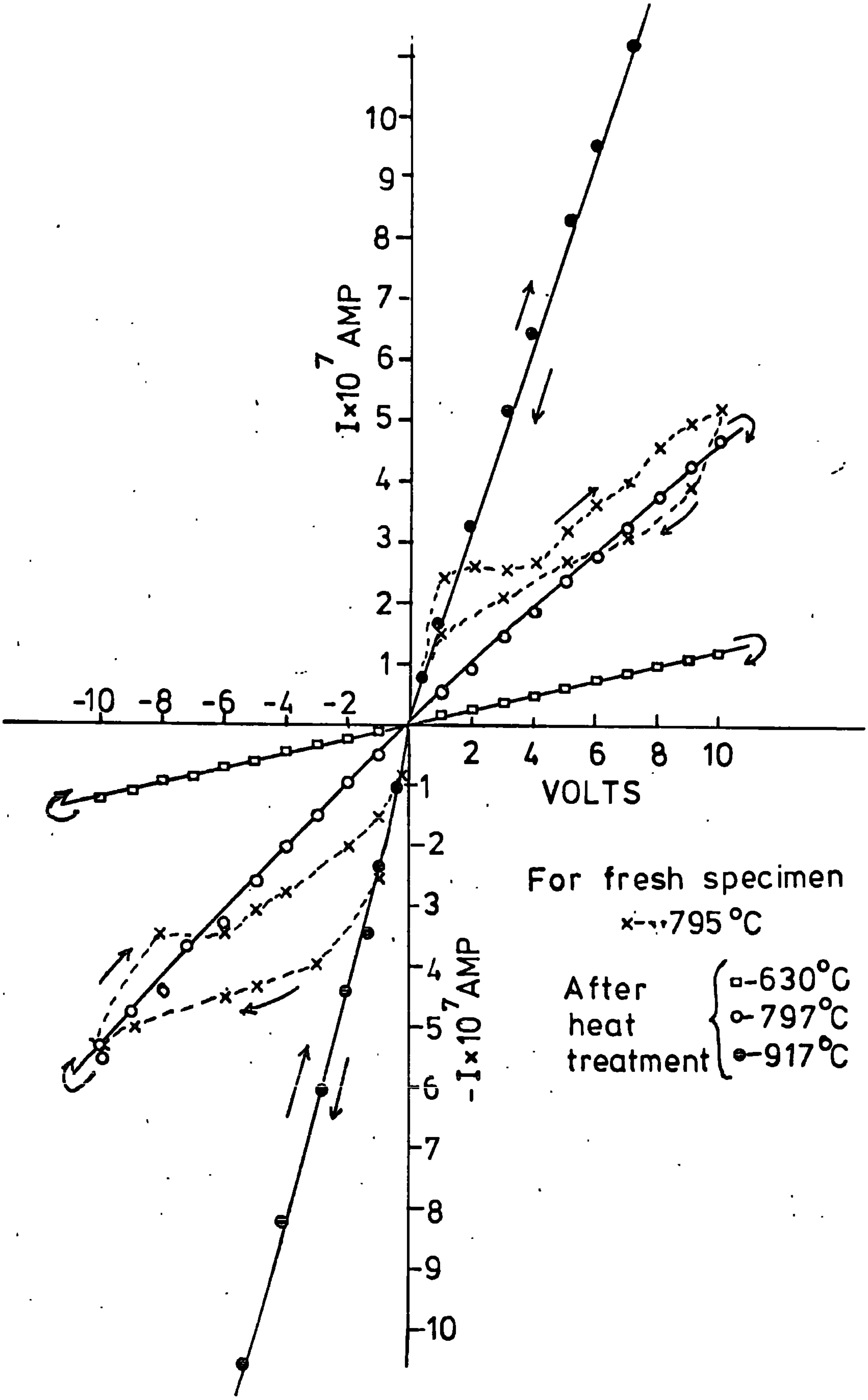

FIG. 8.1 The I-V characteristics of Si_3N_4, observed before and after heat treatment (at 1100 °C for 15 hrs. in air) at various constant temperatures.

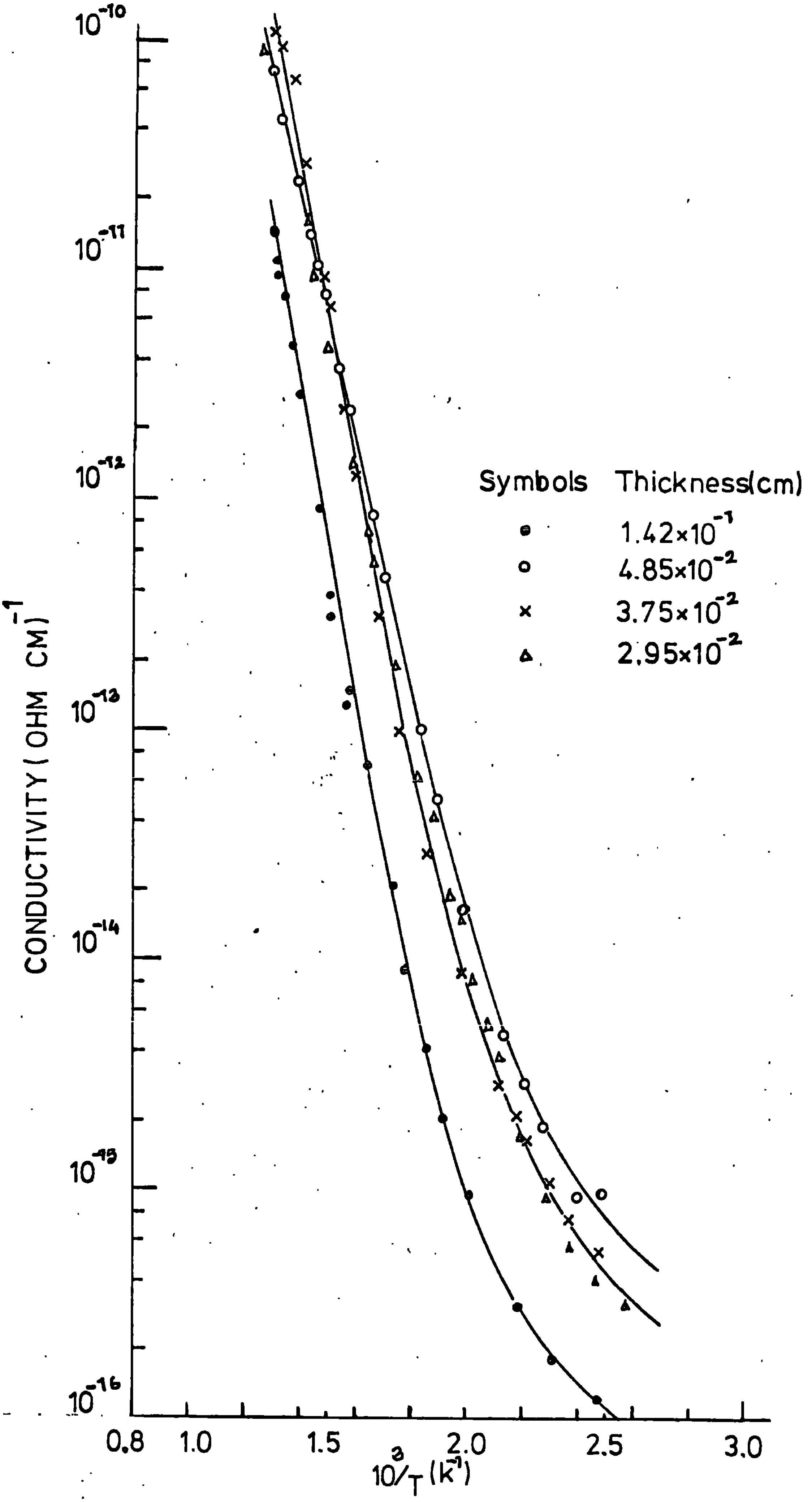

FIG. 8.3 Thickness dependence of conductivity in z=3.2 sialon under a low d.c. field.

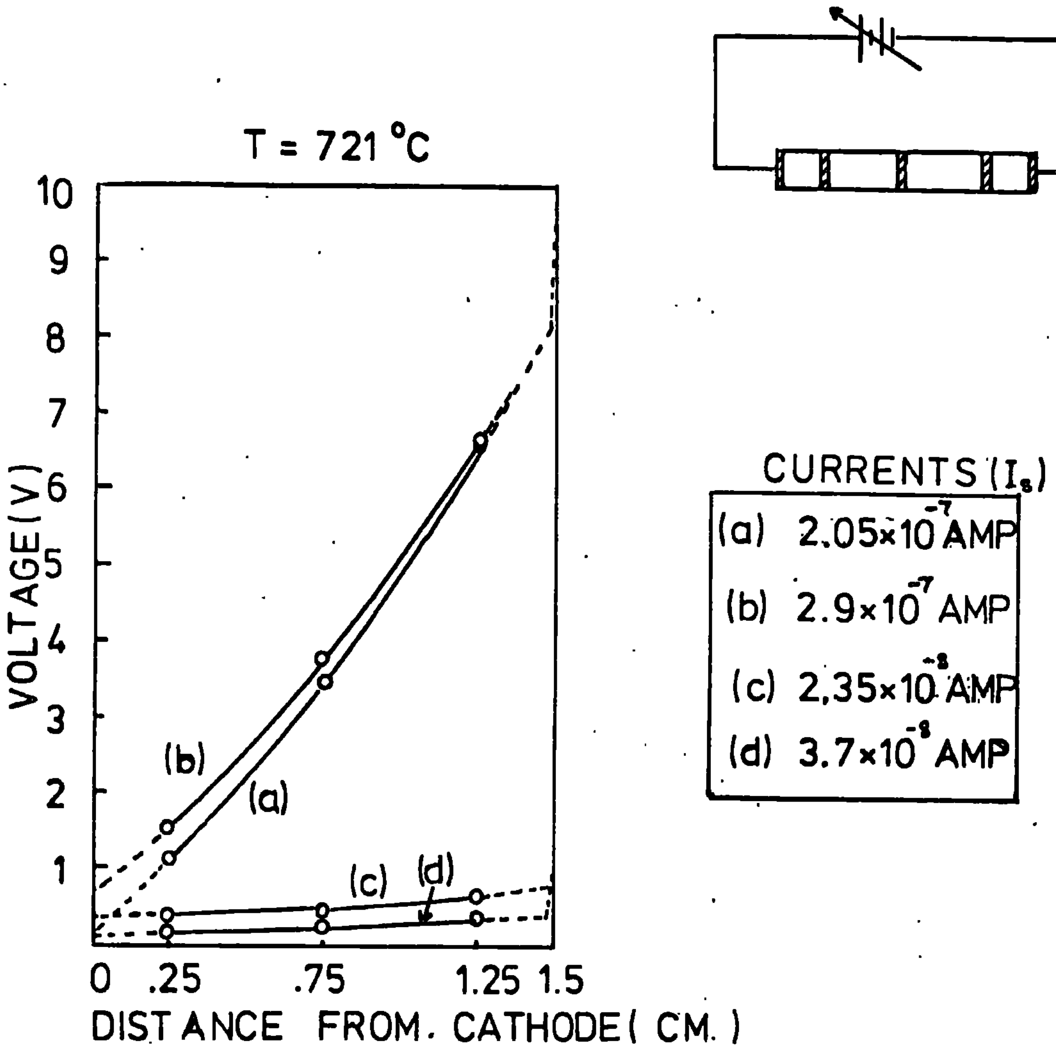

FIG. 8.2 VOltage distribution, observed for Si_3N_4 specimen (a) was the initial result obtained with 10V applied; (b) showed the result on reversal of polarity; (c) was obtained when 1V was applied in the original direction; (d) was obtained when the polarity was reversed.

with very low mobilities (10^{-7}-10^{-9} $cm^2 v^{-1} sec^{-1}$). It consists in allowing an injected space charge to drift under the action of its own electric field. It is better to measure the drift mobility of these materials using the above mentioned method and to compare with the values of μ_D obtained by other methods in ths work.

The loss peaks in some dielectric materials have been observed in the low frequency regions (between 10^{-5} Hz to 10^{2} Hz) and the loss peaks shift to the higher frequencies with increasing temperature (80,82). It has been suggested by Jonscher (80,82) that the frequency variation of loss peaks can be expressed by the relation

$$1/\varepsilon''(\omega) = \left\{\omega/\omega_1(T)\right\}^{-m(T)} + \left\{\omega/\omega_2(T)\right\}^{1-n(T)} \qquad (8.1)$$

where $\omega_{1,2}$ are temperature dependent parameters and the exponents m and 1-n are both smaller than unity and decrease with decreasing temperature. This behaviour is also due to either non-Debye dipolar or hopping charge carrier mechanisms. The temperature variation of dielectric measurements at low frequencies (below 200 Hz), which was omitted in this work, may provide valuable information of the conduction processes.

The temperature variations of tanδ and ε' showed that they became relatively weakly dependent on temperature at higher frequencies. These results give the impression that both tanδ and ε' at 8-10 GHz would be almost temperature independent even at high temperatures. The measurements of tanδ and ε' over the frequency range 8-10 GHz at temperatures up to 600° C may provide significant information about the materials for their possible radome applications. Reaction-bonded Si_3N_4 (100) has been established as a useful material for this purpose.

The results presented in this Thesis show that hot-pressed materials are better insulators than reaction-bonded materials in those instances where a direct comparison with reported data on materials of similar composition could be made. Hot-pressed nitrogen ceramics, especially pure sialons and MgO/Si_3N_4, may be used as high temperature insulators up to 1000° C. Their use may also be possible in high frequency fields, since they have comparatively small losses at microwave frequency.

REFERENCES

1. E GLENNY and T A TAYLOR, Powder Met. 8 (1961) 164.
2. T J BARNBY and R A TAYLOR, part of M.Sc. Dissertation 1971, University of Aston, Birmingham.
3. R KOSSOWSKY, D G MILLER, E S DIAZ, J. Mat.Sci. 10 (1975) 983.
4. S UD-DIN and P S NICHOLSON, ibid 10 (1975) 1375.
5. K H JACK, ibid 11 (1976) 1135.
6. D W RICHERSON, Amer.Ceram.Soc.Bull. 52 (1973) 560.
7. W I WILSON, Ph.D. Thesis, 1974, University of Newcastle-upon-Tyne.
8. Y OYAMA and O KAMIGATTO, Japan, J.Appl. Phys. 11 (1972) 760.
9. A G EVANS and J V SHARP, J.Mat.Sci. 6 (1971) 1292.
10. R KOSSOWSKY, ibid, 8 (1973) 1603.
11. K H JACK and W I WILSON, Nature Phys.Sci.(London) 238 (1972) 28.
12. P DREW and M H LEWIS, J.Mat.Sci. 9 (1974) 1833.
13. R J LUMBY, B NORTH and A J TAYLOR, "Special Ceramics 6", 1975 Stoke-on-Trent ; B.Ceram. R.A., p.283.
14. M H LEWIS, B D POWELL and P DREW, J.Mat.Sci. 12 (1977) 61.
15. J SCHREIBER and W JOHN, Phys.Stat.Sol.78 (1976) 199.
16. N F MOTT, Phil. Mag.19 (196 9) 835 ; Phys. Rev.Lett. 35 (1975) 1293.
17. M H COHEN, H FRITZSCHE and S R OVSHINSKY, Phys. Rev. Letters 22 (1969) 1065.
18. N F MOTT and E A DAVIS, Electronic processes in Non-Crystalline Materials, Clarendon Press,Oxford, 1971.
19. A K JONSCHER and R M HILL, Phys. Thin Films. 8 (1975) 169.
20. H BÖTTGER and V V BRYKSIN, Phys. Stat. Sol. (b) 78 (1976) 9, 415.
21. P W ANDERSON, Phys. Rev.Lett. 34 (1975) 953.
22. A K JONSCHER, J.Vac. Sci. Tech. 8 (1971) 135.

23. R M HILL, Thin Solid Films, 12 (1972) 367.

24. H FRITZSCHE, Electronic and Structural Properties of Amorphous Semiconductors, Edit. P.G.Le Comber (Academic Press,London and New York, 1973) p.55

25. M POLLAK, J.Non-Cryst. Solids, 11 (1972) 1

26. R M HILL, Phys. Stat. Sol (a) 34 (1976) 601.

27. N F MOTT, Electronic and Structural Properties of Amorphous Semiconductors, Edit. P.G Le Comber (Academic Press, London and New York, 1973) p.1

28. J SCHNAKENBERG, Phys. Stat.Sol. 28 (1968) 623.

29. M POLLAK, Phys. Stat. Sol (b) 66, (1974) 483.

30. W BRENIG, G DÖHLER and P WÖLFLE, Z. Phys. 258 (1973) 381.

31. M POLLAK and I RIESS, J. Phys. C9 (1976) 2339.

32. P J ELLIOT, A D YOFFE and E A DAVIS, AIP Conf. Proc. (U.S.A.) No.20 (1974) 311.

33. N F MOTT, Phil. Mag. 24 (1971) 911.

34. R M HILL, Phil. Mag. 24 (1971) 1307.

35. A K JONSCHER, Electronic and Structural Properties of Amorphous Semiconductors, Edit. P.G Le Comber (Academic Press, London and New York 1973) p. 329.

36. S KOC, M ZAVETOVA and J ZEMEK, Thin Films 10 (1972) 165.

37. M H COHEN, J.Non-Cryst.Solids 4 (1970) 391.

38. V V BRYKSIN and YU A FIRSOV, Fiz. tverd. Tela 16 (1974) 811, 1937.

39. R S ALLGAIER, J.Vac. Sci. Tech. 8 (1971) 113.

40. L FRIEDMAN, Electronic and Structural Properties of Amorphous Semiconductors, Edit. P.G Le Comber (Academic Press, London and New York, 1973) p.363.

41. T HOLSTEIN, Phil. Mag. 27 (1973) 255.

42. W E SPEAR, J.Non-Cryst. Solids 1 (1969) 197.

43. D K DAVIES, J. Phys. D. 5 (1972) 162.

44. H FRITZSCHE, Solid State Common. 9 (1971) 1813.

45. D EMIN, Phys. Rev. Letters, 35 (1975) 882.

46. V CAPEK, Phys. Stat. Sol. (b) 57 (1973) 733;

C Zech, J. Phys. B 24 (1974) 1362.

47. H OVERHOF, Phys. Stat. Sol. (b) 67 (1975) 709.

48. C KITTEL, Introduction to Solid State Physics, John Wiley, 1967.

49. M POLLAK and T H GEBALLE, Phys. Rev. 122 (1961) 1745.

50. M POLLAK, Phys. Rev. 133 (1964) A 564,
Phys. Rev. 138 (1965) A 1822,
Phil. Mag 23 (1971) 519.

51. N F MOTT, Phil. Mag. 19 (1969) 835.

52. I G AUSTIN and N F MOTT, Adv. Phys. 18 (1969) 41

53. M POLLAK, Proc. V. Internat. Conf. Amorph. Liquid Semicond.

Garmisch-Partenkirchen I (1973) (Taylor and Francis, London 1974)

p. 127.

54. M KIKUCHI, J. Phys. Soc. Japan 29 (1970) 296.

55. A ALDEA, Z. Phys. 244 (1971) 206.

56. S K LYO and T HOLSTEIN, Phys. Rev. B 8 (1973) 682.

57. H BÖTTGER and V V BRYKSIN, Fiz. tverd. Tela 18 (1976) 1888.

58. H BÖTTGER and V V BRYKSIN, Fiz. tverd. Tela 17 (1975) 2920.

59. P N BUTCHER, J. Phys. C 5 (1972) 1817.

60. P N BUTCHER and P L MORYS, J. Phys. C 6 (1973) 2147.

61. M POLLAK and G E PIKE, Phys. Rev. Lett. 28 (1972) 1449.

62. E J MOORE, J. Phys. C 7 (1974) 1840.

63. H SCHER and M LAX, Phys. Rev. B 7 (1973) 4491, 4502.

64. S TANAKA and H Y FAN, Phys. Rev. 132 (1963) 1516.

65. N F MOTT, Phil. Mag. 22 (1970) 7.

66. J L BEEBY and T H HAYES, J. Phys. C 4 (1970) 1757.

67. H SEGAWA, J. Phys. Soc. Japan 36 (1974) 1087.

68. LE CLEACH and J F PALMIER, J. Non-Crystall. Solids 18 (1975) 265.

69. M KITAO, Japan, J. Appl. Phys. 11 (1972) 1472.

70. S C AGARWAL, S GUHA and K L NARASIMHAN, J. Non-Crystalline Solids 18 (1975) 429.

71. M H GILBERT and C J ADKINS, Phil. Mag. 34 (1976) 143.

72. M ABKOWITZ, et al, Commun. Phys. 1 (1976) 175.

73. P C TAYLOR, et al, Phys. Rev. B. 13 (1976) 1711.

74. M SAYER and A MANSINGH, Phys. Rev. B 6 (1972) 4629.

75. W S CHAN and A K JONSCHER, Phys. Stat. Sol. 32 (1969) 749.

76. S KABASHIMA and T KAWAKUBO, J. Phys. Soc. Japan 24 (1968) 493.

77. A K JONSCHER, J. Phys. C 6 (1973)L 235.

78. A K JONSCHER, Electrets, Charge storage and Transport in Dielectrics ; Edit. by M M Pearlman (Electro-Chem. Soc. Inc. 1973) p. 269.

79. E B IVKIN and B T KOLOMIETS, J. Non-Cryst. Solids 3 (1970) 41.

80. A K JONSCHER, Colloid and Polymer Sci. 253 (1975) 231.

81. Idem, Nature 253 (1975) 719.

82. Idem, Thin Solid Films 36 (1976) 1.

83. E J M KENDALL, Canad. J. Phys. 46 (1968) 2509.

84. P K CHAUDHARI, J M FRANZ and P ACKER, J. Electrochem. Soc. 120 (1973) p.991.

85. K TANABASHI and K KOBAYASHI, Jap. J. Appl. Phys., 12 (1973) 641.

86. J H SANCHEZ-LASSISE and J R YEARGAN, J. Electrochem.Soc. 120 (1973) 423.

87. L SULLIVAN and H C CARD, J. PHys. D : 7 (1974) 1531.

88. A K JONSCHER, Thin Solid Films, 1 (1967) 213.

89. P POPPER and S N RUDDLESDEN, Trans. Brit. Ceram. Soc. 60 (1961) 603.

90. T V ANDREAVA and V K KAZAKOV, High Temp. (U.S.A. English Translation) 5 (1967) 549.

91. P W M JACOBS and J N MAYCOCK, Trans. Met. Soc. AIME 236 (1966) 165.

92. A R ALLNATT and W M JACOBS, Proc. Roy. Soc. (London) A 267 (1962) 31.

93. E A DAVIS and R F SHAW, J. Non-Crystalline Solids, 2 (1970) 406.

94. H K ROCKSTAD, J. Non-Crystalline Solids, 2 (1970) 132.

95. W F PECK and J F DEWALD, J. Electrochem. Soc. 111 (1964) 561.

96. J C MALE, Brit. J. Appl. Phys. 18 (1967) 1543.

97. A K JONSCHER, Proceedings 3rd International Conf. on Thin Films, Budapest, 1975.

98. J VOLGER, Prog. Semicond. 4 (1960) 205.

99. S J GODFREY, J. Brit. Interplanet. Soc. 22 (1969) 353.

100. J D WALTON, Am. Ceram. Soc. Bull 53 (1974) 255.

101. WAYNE KERR CO.LTD, Handbook No. B.224 (1975)

102. A H SCOTT and H L CURTIS, J. Res. Nat. Bur. Stand. 22 (1939) 747.

103. MARCONI INSTRUMENT LTD., Handbook No. OM 1245 (1960).

104. S A E AMMAR, Ph.D., Thesis, University of Durham, 1976.

105. M K MCPHUN and K MEHMET, High Frequency Dielectric Measurement ; Edit. J. Chamberlain and G W Chantry (IPC Science and Technology Press Ltd., U.K., 1972) p. 60, 69.

106. A L LANCE, Introduction to Microwave Theory and Measurements (McGraw-Hill, Inc. 1964) p. 291.

107. S KABASHIMA and T KAWAKUBO, J. Phys. Soc. Japan 24 (1968) 493.

108. M SUCHER and J FOX, Handbook of Microwave Measurements, Vol. II (Polytechnique Press, John Wiley & Sons, Inc., New York : London 1963) p. 495.

109. R LOVELL, J. Phys. D : Appl. Phys. 7 (1974) 1518.

110. T J LEWIS, Dielectric Materials, Measurements and Applications (London, IEE 1975) p. 261.

111. N M TALLAN, Electrical Conductivity in Ceramics and Glass (part A), Marcel Dekker Inc. New York 1974,) p. 95, 153.

112. A K JONSCHER and M CAREEM, Phys. Lett. 55A (1975) 257.

113. R J FLEMING and L F PENDER, Electrets, Charge Storage and Transport in Dielectrics (Edit. by M M Pearlman) p. 474 (Electro-Chem.Soc. Inc. 1973)

114. S A B JAMA, Ph. D. Thesis, 1975, University of Newcastle-upon-Tyne.

115. A W J M RAE, D P THOMPSON, and K H JACK, to be published.

116. S A KAVANAGH, M.Sc. Thesis, 1977, University of Durham.

117. S PIZZINI, J. Appl. Electrochem., 1 (1971) 153.

118. C C LIANG, J. Electrochem. Soc. 120 (1973) 1289.

119. E KATO, Bull. Chem. Soc (Japan), 31 (1958) 108, 113.

120. D L KINSER, Physics of Electronic Ceramics, Part A, Edit. L L Hench and D B Dove (Marcel Dekker, Inc. New York, 1971) p. 523.

121. G HEILMEIER and S E HARRISON, Phys. Rev. 132 (1963) 2010.

122. H L McKINZIE and D S TANNHAUSER, J. Appl. Phys. 40 (1969) 4954.

123. A M HERMANN and J S HAM, Rev. Sci. Instr. 36 (1965) 1553.

124. K MORGAN and R PETHIG, J. Materials Sci. 6 (1971) 179 ; Conduction in Low-Mobility Materials, Edit. N Klein et al (Taylor & Francis Ltd., 1971) p. 391.

125. D D ELEY and R PETHIG, Conduction in Low-Mobility Materials, Edit. N. Klein et al, (Taylor & Francis Ltd., 1971) p. 397.

126. E M TRUKHAN, Fizika tverd. Tela, 4 (1962) 3496 ; Pribory Tekh. Eksp., 4 (1965) 198 ; Biofizika, 11 (1966) 412.

127. Y NISHINA and W J SPRY, J. Appl. Phys. 29 (1958) 230.

128. K YAMGATA and T FUKUROI, Sci. Rep. Res. Inst. Tohoku Univ. A.12 (1960) 247.

129. M SUCHER and J FOX, Handbook of Microwave Measurements, Vol. I (Polytechnic Press, John Wiley & Sons, Inc. New York ; London 1963) p. 98.

130. Y NISHINA and R H GOOD, Rev. Scient. Instrum., 32 (1961) 784.

131. H R PHILIPP, J. Electrochem. Soc. 120 (1973) 295.

132. H FRITZSCHE, J. Non-Crystalline Solids, 6 (1971) 49.

133. T MATSUMURA, Canadian J. Appl. Phys. 44 (1966) 1685.

134. J D MACKENZIE, J. Amer. Ceram. Soc. 47 (1964) 211.

135. R M HILL, Thin Solid Films, 15 (1973) 369.

APPENDIX

PUBLICATIONS

1. "ELECTRICAL CONDUCTIVITY IN HOT-PRESSED NITROGEN CERAMICS"

   J S Thorp and R I Sharif, J. Mat. Sci. 11 (1976) 1494

2. "DIELECTRIC PROPERTIES OF SOME HOT-PRESSED NITROGEN CERAMICS"

   J S Thorp and R I Sharif, J. Mat. Sci. in the press.

3. "D.C. ELECTRICAL PROPERTIES OF HOT-PRESSED NITROGEN CERAMICS"

   J S Thorp and R I Sharif, J. Mat. Sci. in the press.